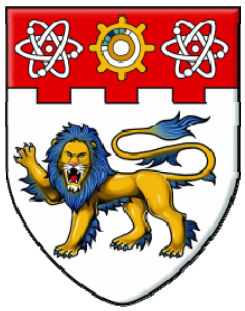

NANYANG TECHNOLOGICAL UNIVERSITY

Induced-Charge Nonlinear Electrokinetic Phenomena and Applications in Micro/Nano Fluidics

ZHAO CUNLU

SCHOOL OF MECHANICAL AND AEROSPACE ENGINEERING

2012

Induced-Charge Nonlinear Electrokinetic Phenomena and Applications in Micro/Nano Fluidics

By

ZHAO CUNLU

A Thesis Submitted to Nanyang Technological University

in Partial Fulfillment of the Requirements for the Degree of Doctor of Philosophy

School of Mechanical and Aerospace Engineering

2012

Abstract

Induced-charge nonlinear electrokinetic phenomena have drawn increasing attention not only due to their fundamental importance but also due to their potential applications for manipulating fluid flows and particles in microfluidics. Such type of nonlinear electrokinetic phenomena is jointly driven by the external electric field and the surface charge induced by the same field on polarizable or conducting surfaces, and is also frequently referred to as induced-charge electrokinetic phenomena. The fluid or particle velocity generated by induced-charge electrokinetics is proportional to the square of the external electric field strength. This is strikingly different from the conventional linear electrokinetics for which the fluid or particle velocity is linearly proportional to the external electric field strength. As a result, the induced-charge electrokinetics can generate larger flow rates and even allows for net flows under AC driving electric fields.

Based on the basic theories of electrokinetics and electrostatics, effective electric boundary conditions between liquid-solid interfaces are derived for induced-charge electrokinetics under two situations. These boundary conditions are capable of predicting the induced zeta potentials over surfaces of solids with finite electric properties which are crucial for theoretical characterization of induced-charge electrokinetics. The applications of these two types of boundary conditions are demonstrated by analyzing the DC field driven induced-charge electroosmosis in a slit microchannel embedded with a pair of dielectric blocks and the AC field driven induced-charge electroosmosis around a leaky-dielectric cylinder, respectively. The calculations show that the basic flow patterns for

induced-charge electroosmosis are the flow vortices which get stronger as the polarizability and /or the conductivity of solids increase.

A complete numerical model is then developed to describe dynamic characteristics of the charging of electric double layer and the associated flows around polarizable dielectrics. The presented model does not invoke various assumptions that can be easily violated in practical applications but usually are made in existing analyses. The comparison with a benchmark solution ensures the validity of the complete model. It is shown that the complete model corroborates the two time scales during the EDL charging revealed in former asymptotic analyses. More importantly, the detailed information inside the EDL during the transient charging is resolved for the first time, which provides insight into the induced-charge electrokinetic phenomena with finite thickness of EDLs.

Furthermore, the concept of induced-charge electrokinetics is extended to nanofluidics. Two nanofluidic systems, i.e., a straight nanochannel and a tapered nanochannel, are proposed for flexible modulations of both ionic transport and fluid flow. For the straight channel, the modulations are achieved by the control of gate voltage (i.e., the voltage applied on the conducting walls of nanochannel). For the tapered channel, the modulations are achieved by varying the direction and magnitude of external electric field and the taper angel of the channel walls. Both systems are advantageous over other nanofluidic systems driven by the conventional linear electrokinetics which usually exhibit poor control of both ionic transport and fluid flow.

Finally, a novel method relying on induced-charge electrokinetics is developed for particle trapping. The proposed technique has been demonstrated experimentally for high-throughput trapping and concentration of particles ranging from submicron to several microns. In addition, a theoretical model is formulated to explain the experimental observations and the trapping mechanisms.

Keywords: Induced-charge electrokinetic phenomena; Micro- and nano-fluidics; Effective electric boundary conditions; Dielectrics and leaky-dielectrics; Charging of electric double layer; Ionic transport; Micro- and nano-fluidic flow control; Particle trapping and concentration; Concentration polarization.

Acknowledgements

This thesis symbolizes the ending of my role as a student and it would not have been possible without the help of many people. First and foremost, I would like to express my deepest gratitude to my advisor, Dr Yang Chun, Charles for his continuous help and guidance during past few years. It is very memorable to retrospect the past with him. In November of 2006, I contacted Dr. Yang about the PhD applications. He was very enthusiastic and patient to give me valuable information regarding the PhD application. Because I did not take TOEFL and GRE exams at that time, he advised me to take two substitute exams held in Beijing during December 2006, which makes my PhD study at Nanyang Technological University (NTU) possible. In August 2007, I joined Dr. Yang's group and then was introduced to an exciting research area-microfluidics and nanofluidics. His dedication and enthusiasm for research impress me and set an example for me. It has been absolutely a great honor and pleasure to work under his mentorship. Other than that, I also would like to extend my special thanks to his wife, Madam Xu Li for her care in the daily life and suggestions in personal matters.

The examination committee of my thesis consists of Professor Huang Xiaoyang (Nanyang Technological University), Professor Martin Z. Bazant (Massachusetts Institute of Technology) and Professor Keh Huan-Jang (National Taiwan University). I appreciate their insightful comments which greatly improve the quality of the thesis.

In addition, I would like to thank all my colleagues in Thermal Fluids Research Lab for their assistance which facilitates the completion of this work.

Specifically, I would thank our group members: Dr. Lewpiriyawong Nuttawut, Mr. Ge Zhengwei, Mr. Liang Qiang, Mr. He Jinhua, Mr. Hon Kar Cherng, Mr. Zhao Yugang, Ms. Zhou Yi and Ms. Jiao Yanmei for the stimulating discussions. Sincere thanks also go to Dr. Wang Wei at Singapore Institute of Manufacturing Technology for his kind help on fabrication of microelectrodes.

This thesis would also not have been possible without the help from Mr. Yuan Kee Hock, a technician in charge of Thermal and Fluids Research Laboratory, who help purchase all experimental items and the staffs from Micromachines Centre who trained me about the microfabrication processes.

Furthermore, the financial support from a NTU Ph.D. scholarship is also sincerely acknowledged.

Last but not least, I am immensely indebted to my family (my parents, two sisters and younger brother). Without their incessant encouragement, love and support, I could not have reached where I am now.

October 12 2012, Singapore

Contents

Figure Legends

Table Legends

Nomenclature

a	Radius of particles or cylinders [m]
c	Concentration of transported species [M]
D	Diffusion coefficient of transported species [m^2/s]
Du	Dukhin number
e	Elementary charge, 1.60×10^{-19} C
E_0	Electric field strength [V/m]
H	Height of the channel [m]
i	Electric current density [A/m^2]
j	Imaginary unit, $j=\sqrt{-1}$
I	Electric current [A]
k_B	Boltzmann constant, 1.38×10^{-23} J/K
n	Number density of ions [$/m^3$]
N_A	Avogadro constant, 6.02×10^{23}/mol
p	Pressure [Pa]
Pe	Peclet number
q	Surface charge density [C/m^2]
Re	Reynolds number
S	Ionic selectivity
Sc	Schimit number

T	Temperature [K]
u, V	Velocity vector [m/s]
u, v	Velocity components [m/s]
x, y	Cartesian coordinates
z	Valence of ions

Greek symbols

β	Ratio of the bulk capacitance to the double layer capacitance
ε	Electric permittivity [F/m]
ε_0	Electric permittivity of vacuum, 8.854×10^{-12} F/m
ε_f	Dielectric constant of the liquid electrolyte
Φ, φ, ϕ	Electric potential [V]
κ	Debye-Hückel parameter [m^{-1}], $\kappa=1/\lambda_D$
λ_D	Debye length [m], $\lambda_D=1/\kappa$
μ	Dynamic viscosity [Pa · s]
σ	Electric conductivity [S/m]
τ	Dimensionless time
ω	Angular frequency of the applied AC electric field [rad/s]
Ω	Dimensionless angular frequency of the applied AC electric field
Ψ, ψ	Stream function [m^2/s]
ζ	Zeta potential [V]

Subscripts

d	Parameters related to the dielectrics
f	Parameters related to the fluid
i	Parameters related to the induced quantities or ions
p	Parameters related to particles
ref	Parameters related to the reference quantities
s	Parameters related to Helmholtz-Smoluchowski velocity or surface
w	Parameters related to solid walls

Overscripts

‾	Dimensionless parameters

Abbreviations

AC	Alternating current
ACEO	AC electroosmosis
DC	Direct current
DCGC	Direct contact gate control
DI	Deionized water
EDL	Electric double layer
FET	Field effect transistor
ICEK	Induced-charge electrokinetics or induced-charge electrokinetic
ICEO	Induced-charge electroosmosis

ICEP	Induced-charge electrophoresis
IHP	Inner Helmholtz plane
OHP	Outer Helmholtz plane
PDMS	Polydimethylsiloxane
PIV	Particle image velocimetry
RC	Resistor-capacitor
SCL	Space charge layer
SP	Shear plane
μTAS	Micro total analysis systems

CHAPTER 1: INTRODUCTION

1.1 BACKGROUND AND MOTIVATION

The manipulation of fluids and particles at microscale is receiving intensive attention due to its relevance to the development of micro total analysis systems (μTAS) for drug screening and delivery, environmental and food monitoring, biomedical diagnoses and chemical syntheses etc. Unfortunately, the widely-accepted fluid manipulation techniques at macroscale cannot be directly adopted at microscale due to the inherently small Reynolds number involved at microscale. One example is that the fluid instabilities caused by inertial effects at macroscale disappear at microscale due to the strong viscous effects. Thus, the microfluidic mixing is dictated by diffusion alone, without the benefit of the flow instabilities. For fluidic devices with nanometric scales, molecular diffusion is relatively rapid and the mixing is achieved instantaneously; however, in fluidic devices with micrometer scales (10-100 μm), it takes relatively long time (e.g., about 100s for molecules with diffusivity of 10^{-10} m^2/s) to achieve a good mixing. Another inherent limitation at microscale is that the pressure-driven flow becomes inefficient to achieve satisfactory flow rates. Various techniques are thus being proposed for manipulating (pumping, mixing, and separating etc.) solutes and particles at microscales. Owing to the large surface to volume ratios in typical microfluidic devices, surface phenomena naturally are among the most preferred ones. Electrokinetic phenomena are one type of such surface phenomena, and certainly the most popular non-mechanical techniques in microfluidic devices. The popularity of electrokinetic techniques is ascribed to their numerous advantages: no moving parts and thus immune to mechanical

failure; electronically controlled and thus easily automated; flat velocity profiles of liquid sample which minimize the sample dispersion; fluid or particle velocity does not depend on the microchannel dimensions etc.

The basic physics behind conventional electrokinetic phenomena is as follows: when an electrolyte solution is brought into contact with a charged solid surface, a charged diffuse layer develops near the charged solid surface due to the Coulombic attraction between the charge on the solid surface and the counterions inside the solution. Once an external electric field is applied tangentially along the charged surface, the charged diffuse layer experiences an electrostatic body force which gives rise to a fluid flow relative to the charged surface. The liquid motion relative to the stationary charged surfaces is known as electroosmosis, and the motion of charged particles relative to the stationary liquid solution is known as electrophoresis. The classic electroosmosis occurs around surfaces with fixed surface charge (or, equivalently, zeta potential ζ) and then the effective liquid slip at the solid surface is linearly related to the external electric field strength by Helmholtz-Smoluchowski equation, i.e., $u_s = -\varepsilon\zeta E_0 / \mu$ (Here, ε is the electric permittivity of the electrolyte solution, ζ is the zeta potential of the solid surface, E_0 is the external electric field strength and μ is the dynamic viscosity of the electrolyte solution). When a charged particle is freely suspended in the fluid, electroosmotic slip on the particle surface causes the particle itself to move electrophoretically with velocity $U = \varepsilon\zeta E_0 / \mu$ (Here, ζ denotes the zeta potential of particle). More comprehensive descriptions of electrokinetics are provided in textbooks and reviews (Anderson, 1989; Ghosal, 2004; Hunter, 1981; Masliyah and Bhattacharjee, 2006; Probstein, 1994; Russel

et al., 1989). Owing to the linear relationship with the external electric field strength, the conventional electrokinetic phenomena are also termed as linear electrokinetic phenomena. The linearity of classic electrokinetic phenomena, however, has some drawbacks (Bazant and Squires, 2004): (i) the resulting velocity for liquid or particle is somewhat low, e.g., u_s =70 μm/s in aqueous solution with E_0=100 V/cm and ζ=10 mV and (ii) AC electric fields, which reduce undesirable Faradaic reactions, produce no net motion of liquid or particle. On the other hand, nonlinear electrokinetic phenomena refer to electrically driven fluid flows or particle motions which depend nonlinearly on the externally applied electric field strength (Bazant, 2008). A typical example of nonlinear electrokinetic phenomena is the electroosmotic flows around conducting or polarizable surfaces. The electric charge induced on the conducting surface by the external electric field itself results in a non-uniform zeta potential whose magnitude is linearly proportional to the strength of external electric field. Subsequently, the resultant Helmholtz-Smoluchowski slip velocity at the conducting surface is proportional to the square of the external electric field strength., namely $u_s \propto E_0^2$ (Bazant and Squires, 2004; Squires and Bazant, 2004). Such nonlinear electrokinetic phenomenon is usually referred to as induced-charge electrokinetic phenomena to emphasize the central role played by the induced electric charge.

Owing to the nonlinearity caused by polarizable surfaces, the induced-charge electroosmotic flow can be much stronger than the traditional fixed charge electroosmotic flow, and also can permit the non-zero time average flow under AC electric fields. Furthermore, nonlinear induced-charge electrokinetics

exhibits a high level of controllability because of the actively controlled surface charge or zeta potential. Then nonlinear electrokinetics naturally lends itself to microfluidic and nanofluidic applications due to various advantages mentioned above. However, nonlinear electrokinetic phenomena are relatively new in the family of electrokinetics. Some underlying mechanisms of induced-charge nonlinear electrokinetics are still not well understood, and its applications in microfluidics and nanofluidics are still scarce. Fundamental characterizations are thus required to promote the undemanding of this class of electrokinetics and its applications in microfluidics and nanofluidics also need further extension and exploration.

1.2 RESEARCH OBJECTIVES AND SCOPE

The aim of this dissertation is to advance the fundamental theory of nonlinear induced-charge electrokinetic phenomena and further explore their possible applications in micro- and nano-fluidics. It is known that the zeta potential is a very important parameter in theoretical prediction of conventional electrokinetics. Similarly, theoretical analyses of induced-charge electrokinetics require efficient evaluation of the induced zeta potentials of polarizable surfaces. Moreover, as will be shown in the literature review in Chapter 2, much attention has been focused on ideally polarizable surfaces (i.e., conductors with good conductivities). More general situations with finitely polarizable or leaky-dielectric surfaces need to be addressed.

The driving force for the nonlinear electrokinetics originates from the induced electric double layer. Thus, the transient formation of electric double layer around a polarizable medium is of crucial importance to better understand

the dynamic aspects of induced-charge electrokinetics. Previous analyses have addressed this issue based on a simple physical picture or various assumptions, and thus the existing models are inadequate for a general characterization of transient induced-charge electrokinetics. No general complete model has been developed to resolve the detailed transient charging characteristics of the electric double layer and the associated electrokinetic flows.

Nanofluidics, an extension of microfluidics to nanoscale, promises the sensing and detection of single molecules or ions. The control of transport of molecules and ions in nanofluidic systems usually requires the modification of surface charge on the nanofluidic channel walls. The conventional way to achieve this is by surface treatment with chemical additives. This method, however, is not convenient to use during the operation of nanofluidic systems. The induced-charge electrokinetics provides an active and robust way for the surface charge modulation. Obviously, the application of induced-charge electrokinetics at the present stage is mainly limited to microfluidics. In view of this, the extension of induced-charge electrokinetics to nanofluidics is much required.

Particle manipulation is also an important subject in microfluidics because of its high relevance to cells handling, colloid assembly, virus detection and macromolecule analyses. The classical picture for induced-charge electrokinetics is the formation of microvortices near polarizable surfaces, which naturally makes the induced-charge electrokinetics quite suitable for microfluidic mixing. Only very recently, the induced-charge electrokinetics is used to achieve particle transportation, which indicates that induced-charge electrokinetics is a potential technique for particle manipulations.

Consequently, the objectives and scope of this thesis include the following:

(1) To derive effective electric boundary conditions for evaluation of induced zeta potential on dielectric and leaky-dielectric surfaces. In addition, the application of the proposed generalized electric boundary conditions is demonstrated by investigating the induced-charge electroosmosis around dielectric and leaky-dielectric surfaces.

(2) To develop a complete model for resolving the detailed charging characteristics of electric double layers around polarizable dielectrics and the associated transient induced-charge electrokinetic flows. The developed model features the full coupling of ionic species transport, fluid flow and electric potential and thus gives a general description of induced-charge electrokinetics.

(3) To develop novel nanofluidic systems for flexible control of both ionic transport and fluid flow via induced-charge nonlinear electrokinetics. Specifically, two prototypes of nanofluidic system for control of both ionic transport and fluid flow are presented and their operating characteristics are investigated in details.

(4) To develop a novel technique for trapping submicron and nanoparticles by using induced-charge nonlinear electrokinetics. The proposed experimental scheme is shown to be effective for trapping submicron and nanoparticles. Furthermore, a theoretical model based on the proposed effective electric boundary conditions is used to throw light on the complex trapping mechanisms.

1.3 ORGANIZATION OF THE THESIS

This thesis entitled “Induced-Charge Electrokinetic Nonlinear Phenomena and Applications in Micro/Nano Fluidics” consists of seven chapters and covers both fundamental aspects and practical applications of induced-charge electrokinetic phenomena. Chapter 1 introduces the background of electrokinetic techniques and the motivation of this study, followed by the proposed objectives and scope of the present research. Chapter 2 presents an overview of the classic electrokinetic techniques and the recent development on electrokinetic phenomena. In addition, the previous investigations are commented and the research directions for this thesis is identified and highlighted. In Chapter 3, two types of general effective electric boundary conditions between a solid and an electrolyte solution are proposed to evaluate the induced zeta potentials over the surfaces of dielectric and leaky-dielectric solids, which bridges the gap between the induced-charge electrokinetics generated on perfectly polarizable surfaces and the classic fixed charge electrokinetics generated on insulating (non-polarizable) surfaces. Theoretical analyses of the induce-charge electroosmosis under DC and AC electric fields are presented to demonstrate the applications of these two effective boundary conditions. In Chapter 4, a complete numerical model is developed to fully describe the transient charging of the electric double layers around dielectrics and the associated induced-charge electrokinetic flows. Chapter 5 extends the induced-charge electrokinetics to the nanofluidic regime for the first time. Two prototypes of nanofluidic systems which have flexible control of both flow and ionic transport are also proposed and analyzed. Chapter 6 reports a novel technique which takes advantage of induced-charge electrokinetics for the manipulation of submicron and nanoparticles. The experimental results

demonstrated that the proposed method is particularly effective for trapping submicron and nanoparticles. At last, Chapter 7 provides a summary of contributions from this thesis research and also includes the proposed work for the future studies.

CHAPTER 2: LITERATURE REVIEW

2.1 CLASSIC ELECTROKINETIC PHENOMENA

2.1.1 THE CLASSIC THEORY OF ELECTRIC DOUBLE LAYERS

Solid surfaces acquire electrical surface charge when they are brought into contact with a polar solvent (Hunter, 1981), in particular, with an electrolyte solution. The origins of this charge are diverse, and include several popular mechanisms (Delgado and Arroyo, 2002): (1) preferential adsorption of ions in the solution; (2) adsorption–desorption of lattice ions; (3) direct dissociation or ionization of surface groups; (4) charge-defective lattice: isomorphous substitution.

To maintain the electroneutrality of the system, the electric double layer (EDL) with an excess of counterions must form to counterbalance the surface charge. Although it is traditionally termed “double’’ layer, its structure can be very complicated and may contain three or more layers in most instances. Figure 2.1 below illustrates schematically the Stern model for an electrical double layer. For example, consider in this case that the surface charge is negative and some anionic species in the solution are specifically absorbed (as shown by the green species). Counterions are attracted to the surface by the coulombic force. However, they are not all situated in one plane and form a diffuse layer. The concentration of counterions in the diffuse layer decreases as the distance is away from the surface.

For the Stern model shown in Figure 2.1, the structure of electric double layer can be identified as (Delgado and Arroyo, 2002):

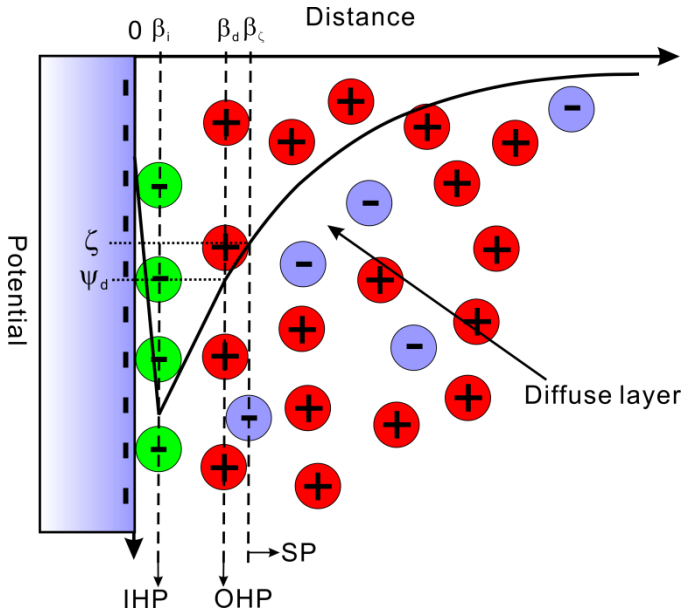

Figure 2.1 Schematic illustration of the Stern model for electric double layer at a negatively charged interface.

(i). The plane at $x=\beta_i$ is the inner Helmholtz plane (IHP) and the plane at $x=\beta_d$ is called the outer Helmholtz plane (OHP). The IHP is the plane cutting through the center of the adsorbed species. The OHP is the plane cutting through the counterions at their position of closest approach.

(ii). The region between $x=0$ and $x=\beta_d$ is often named the Stern layer or sometimes the dense part of the double layer.

(iii). The portion extending from $x=\beta_d$ is called the diffuse layer or sometimes the diffuse part of the double layer.

(iv). The plane at $x=\beta_\zeta$ is the shear plane (SP). The well-known zeta potential is defined as the potential drop between this plane and the bulk solution. Generally, SP is not co-planar with OHP. At the SP, it is assumed that the liquid viscosity drops discontinuously from infinity in the Stern layer to a finite value in the diffuse layer. SP is the boundary that separates the electric double layer into a mobile part and an immobile part. For the sake of convenience, the zeta

potential is taken to be equivalent to the potential at the OHP in most circumstances, i.e. $\psi_d = \zeta$. See page 201-216 in Hunter (1981) for more detailed discussion.

The diffuse layer begins from the OHP, and can be mathematically described in terms of the equilibrium condition for ions as

$$-ez_i \nabla\psi - k_B T \nabla \ln n_i = 0 \tag{2.1}$$

where the first term corresponds to the electrostatic force on ions of type i (ez_i is ionic charge and ψ is the potential) and the second term denotes the thermodynamic force because of the ionic diffusion (k_BT denotes the thermal energy and n_i is number concentration). The solution of equation (2.1) under the condition $n_i = n_i^0(\infty)$ for $\psi = 0$ leads to the famous Boltzmann distribution

$$n_i(\mathbf{r}) = n_i^0(\infty) exp\left[-\frac{ez_i\psi(\mathbf{r})}{k_B T}\right] \tag{2.2}$$

where $n_i^0(\infty)$ is the bulk number concentration of ions of type *i* (far from the charged surface), and **r** is the position vector. Finally, the Poisson equation relates the potential and the ionic concentrations by

$$\nabla^2\psi(\mathbf{r}) = -\frac{1}{\varepsilon_0\varepsilon_f}\rho(\mathbf{r}) = -\frac{1}{\varepsilon_0\varepsilon_f}\sum_{i=1}^{N} ez_i n_i^0(\infty)\exp\left[-\frac{ez_i\psi(\mathbf{r})}{k_B T}\right] \tag{2.3}$$

where $\varepsilon_0\varepsilon_f$ is the electric permittivity of the solution medium. Equation (2.3) is the so-called Poisson–Boltzmann equation which is the mathematical presentation of Gouy-Chapman theory describing the physics of the diffuse part of electric double layer.

Usually, equation (2.3) cannot be analytically solved due to its nonlinearity. But in certain cases, we can obtain analytical solutions:

1. For a flat interface with a low potential ψ_d, equation (2.3) can be linearized based on the Debye-Hückel approximation and then the solution can be sought as

$$\psi = \psi_d e^{-\kappa x} \tag{2.4}$$

where κ^{-1} is the Debye length, and it is a measure of the thickness of the electric double layer. It can be formulated as

$$\lambda_D = \kappa^{-1} = \sqrt{\frac{\varepsilon_0 \varepsilon_f k_B T}{\sum_{i=1}^{N} e^2 z_i^2 n_i^0 (\infty)}} \tag{2.5}$$

The typical values of the Debye length κ^{-1} for different electrolyte concentrations for the case of binary monovalent electrolytes are shown in Table 2.1. It is clearly shown that the Debye length decreases with the increase of the electrolyte concentration. At high molarity, the thickness of electric double layer is very small. However, the double layer thickness in a solution without electrolytes can be regarded as infinitely thick (i.e., a large distance from the surface).

Table 2.1 Relationship between molar concentration and Debye length for binary monovalent electrolytes at 25 °C

Ionic concentration, M	Debye length κ^{-1}, nm
10^{-6}	304
10^{-4}	30.4
10^{-2}	3.04

2. For a flat interface with an arbitrary potential ψ_d and a symmetric, binary electrolyte (z_1=-z_2 =z), the Poisson–Boltzmann equation (2.3) has the famous Gouy-Chapman solution

$$Y(x) = 2\ln\left[\frac{1+e^{-kx}\tanh(Y_d/4)}{1-e^{-kx}\tanh(Y_d/4)}\right] \tag{2.6}$$

where Y is the dimensionless potential

$$Y = \frac{ze\psi}{k_B T} \tag{2.7}$$

3. For a spherical surface (radius a) with low potentials, equation (2.3) can be solved as

$$\psi(r) = \psi_d\left(\frac{a}{r}\right)e^{-\kappa(r-a)} \tag{2.8}$$

otherwise either numerical or analytical solutions have to be applied in other cases.

2.1.2 FIXED-CHARGE ELECTROKINETIC PHENOMENA

Generally speaking, electrokinetic phenomena are the consequences of the interaction between an external electric field and the EDL. In the classic electrokinetics, the surface charge is solely determined by the physiochemical properties of the surface and the solution. Therefore, with given surface and electrolyte solution, the surface charge is fixed and independent of the external electric field.

2.1.2.1 SMALL ZETA POTENTIALS

A solid surface submerged in aqueous solutions acquires a charge density q

which attracts counterions and repels coions to form the electric double layer (effectively a surface capacitor). The diffuse ionic charge in the EDL gradually screens the electric field generated by the surface charge, resulting in an electric potential drop across the EDL (which effectively represents the zeta potential). Under the Debye–Hückel linear approximation (small surface charge or potential), the potential in the diffuse part of double layer is given by equation (2.4) from which one can obtain a linear relationship between the surface charge density and the zeta potential as

$$q = \varepsilon_0 \varepsilon_r \kappa \zeta \tag{2.9}$$

Two popular electrokinetic phenomena are electroosmosis and electrophoresis which both find myriads of microfluidic applications for chemical analyses, biomedical diagnostics, colloidal particle manipulations and so on. Electroosmotic flows occur along charged solid walls subject to tangential electric fields. Generally, the externally applied electric field exerts an electrostatic body force on the net charge density in the diffuse part of EDL, driving the ions and then the liquid in the EDL into motion. Subsequently, the momentum generated inside the EDL gradually diffuses to the bulk liquid due to the viscous coupling. At the steady state, the velocity of the bulk liquid reaches a uniform value and the resulting fluid flow appears to slip at the outer edge the EDL of thickness λ_D (as shown in Figure 2.2(a)). Such slip velocity is given by the Helmholtz–Smoluchowski equation

$$u_s = -\frac{\varepsilon_0 \varepsilon_f \zeta}{\mu} E_0 \tag{2.10}$$

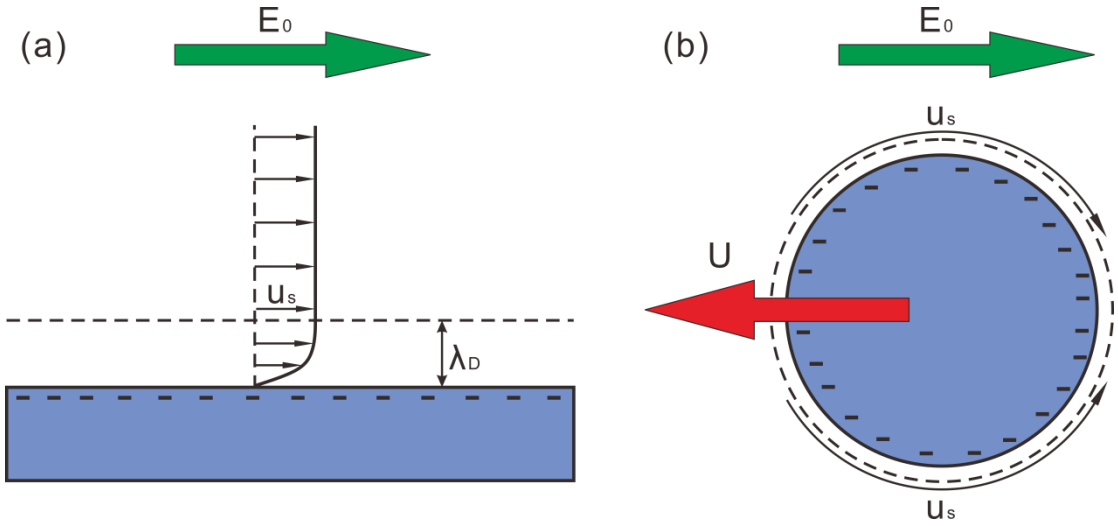

Figure 2.2 (a) Electroosmosis: an electric double layer (EDL) of thickness λ_D develops over a negatively charged solid surface submerged in an electrolytic solution. A tangentially applied electric field exerts electrostatic forces on the mobile ions in the EDL to drive electroosmotic slip flow over the charged surface. (b) Electrophoresis: electroosmotic slip velocity on the surface of a charged particle moves this particle phoretically with a velocity equal in magnitude and opposite in direction to such electroosmotic slip velocity.

where μ is the fluid viscosity and E_0 is the electric field strength of bulk electric field. In microfluidic applications (the thin EDL assumption applies), it is evident that the velocity of electroosmosis does not depend on the channel dimensions. This unique feature is strikingly different from the pressure-driven flow in which the velocity depends strongly on channel dimensions. Consequently, the electroosmotic pumping has long been an efficient and popular technique for fluid transportation in microchannels. On the other hand, for a freely suspended particle with charged surface, the electroosmotic slip velocity over the particle surface gives rise to a particle motion opposite to the electroosmotic slip velocity, known as electrophoresis (as shown in Figure 2.2(b)). Under the thin double layer limit, the electrophoretic velocity of the particle is given by the Smoluchowski equation

$$U = \frac{\varepsilon_0 \varepsilon_f \zeta}{\mu} E_0 = \mu_{EP} E_0 \tag{2.11}$$

where E_0 is the strength of external electric field, and $\mu_{EP} = \varepsilon_0 \varepsilon_f \zeta/\mu$ is called the electrophoretic mobility of the particle (Note that ζ is the zeta potential of particles).

2.1.2.2 LARGE ZETA POTENTIALS

If the solid surface is so heavily charged that the zeta potential becomes comparable to or much larger than the so-called thermal voltage, $k_BT/(ze)$, the exponential profile of EDL potential given by equation (2.4) and the linear voltage–charge relation given by equation (2.9) become invalid. The potential in the diffuse part of double layer satisfies the nonlinear Poisson–Boltzmann equation and the solution is given by equation (2.6). Under the thin double layer limit, one can obtain a nonlinear surface charge density–zeta potential relation for the double layer of a symmetric, binary electrolyte from equation (2.6) as

$$q = 4n_0 ze\lambda_D \sinh\left(\frac{ze\zeta}{2k_BT}\right) \tag{2.12}$$

It should be noted here that q generally grows exponentially with $ze\zeta/(k_BT)$. For heavily charged surfaces, the result predicted from equation (2.12) significantly deviates from that predicted from equation (2.9). For weakly charged surfaces, it is not surprising that equation (2.12) can reduce to equation (2.9) by using the famous Debye-Hückel linear approximation ($\sinh\left[ze\zeta/(2k_BT)\right] \approx ze\zeta/(2k_BT)$). It also has been pointed out that this nonlinearity described in equation (2.12) would have important implications for double layer relaxation (Bazant et al., 2004).

In such nonlinear regime, the Helmholtz–Smoluchowski equation (2.10) for the electroosmotic slip is still valid on condition that (Squires and Bazant, 2004)

$$\frac{\lambda_D}{a}\exp\left(\frac{ze\zeta}{2k_BT}\right)\ll 1 \tag{2.13}$$

where a denotes the radius of surface curvature. For the situations with very thick electric double layers and/or large zeta potentials, equation (2.13) is violated and concentrations of ions in the electric double layer are significantly different from those in the bulk. Then surface conduction inside the electric double layer becomes significant and its effects on electrokinetics must be accounted for. For example, the electrophoretic mobility, μ_{EP}, becomes dependant nonlinearly on the dimensionless Dukhin number

$$Du=\frac{\sigma_s}{\sigma a} \tag{2.14}$$

which characterizes the ratio of the surface conductivity, σ_s, to the bulk conductivity, σ (Lyklema, 1995).

Both electromigration and convective transport of ions in the electric double layer contribute to the surface conductance, σ_s. The relative importance of convective transport is characterized by another dimensionless number $m=2\varepsilon_0\varepsilon_f\left[k_BT/(ze)\right]^2/(\mu D)$ and the Du of a symmetric binary electrolyte can be formulated as (Squires and Bazant, 2004)

$$Du=\frac{2\lambda_D(1+m)}{a}\left[\cosh\left(\frac{ze\zeta}{2k_BT}\right)-1\right]=4\frac{\lambda_D(1+m)}{a}\sinh^2\left(\frac{ze\zeta}{2k_BT}\right) \tag{2.15}$$

In the extreme case of infinitely thin double layers ($\lambda_D\to 0$), the condition in

equation (2.13) is satisfied and the Dukhin number disappears naturally, so the electrophoretic mobility is exactly given by the Smoluchowski equation (2.11). For highly charged particles (with $\zeta \gg k_B T/(ze)$) with finite double layer thickness, however, the Dukhin number is generally finite and the surface conduction plays significant roles. The direct consequences of surface conduction are the generation of bulk concentration polarization and a nonuniform diffuse charge distribution around the particle, which would add diffusiophoretic and concentration polarization contributions to electrophoretic mobility of the particle. One can referred to Dukhin (1993) and Lyklema (1995) for more detailed accounts and discussion of surface conduction.

2.2 RECENT DEVELOPMENT ON ELECTROKINETIC PHENOMENA

In the classic electrokinetic phenomena, solid surfaces possess a homogeneous constant surface charge (or zeta potential). When the solid surfaces acquire inhomogeneous zeta potentials, interesting and useful phenomena can occur. According to the polarizability of surfaces over which electrokinetic phenomena take place, we generally divide the development of electrokinetics into two categories: electrokinetics involving non-polarizable surfaces and electrokinetics involving polarizable surfaces. Furthermore, in respective categories, the development is further subcategorized and reviewed according to different mechanisms.

2.2.1 NON-POLARIZABLE (INSULATING) SURFACES

Although the application of the external driving electric field does not influence the surface charge on insulating surfaces in classic linear electrokinetic phenomena, variation of the surface charge still can be realized through

different techniques.

2.2.1.1 PATTERNING SURFACE WITH FIXED NONUNIFORM CHARGE

In the classical electrokinetic phenomena, a fixed, homogeneous surface charge (or, equivalently, zeta potential ζ, defined as the potential drop across the electric double layer) is widely assumed. Note that electrokinetic phenomena over surfaces with inhomogeneously patterned surface charge/potential also have been reported in the literature. Teubner (1982) first investigated the electroosmotic flow over surfaces with inhomogeneous zeta potentials. However the details of flow characteristics were not elaborated. Anderson and Idol (1985) found that flow circulations exist in the electroosmotic flow through inhomogeneously charged pores. By modulating the surface charge density on the walls of a microchannel, it was shown that a net electroosmotic flow can be controlled to be either parallel or perpendicular to the externally applied field (Ajdari, 1995; Stroock et al., 2000). Figure 2.3 schematically illustrates the principle of electroosmotic flow control in microchannels by surface charge modulation. These ideas have been further realized to fabricate a "transverse electrokinetic pump" which has a advantageous feature that it can be powered by low voltages applied across a narrow channel (Gitlin et al., 2003).

To visualize the flow patterns of electroosmosis, a caged-fluorescence technique was developed to measure the fluid velocity and sample-dispersion rate of electroosmosis in cylindrical capillaries with a noncontinuous distribution of zeta potential (Herr et al., 2000). The adsorption of analyte molecules also can cause the channel wall to be inhomogeneously charged, and the resulting electroosmosis has been shown to increase the analyte

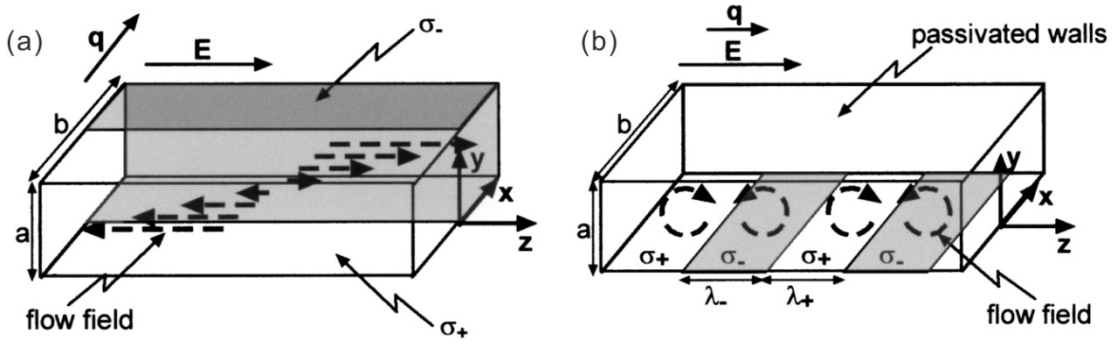

Figure 2.3 Mechanisms for surface charge modulation in microchannels. σ_+ and σ_- represent the surface charge densities. q represents the direction of surface charge variation. The dotted arrows represent the electroosmosis generated in the channel. (a) $\mathbf{q} \perp \mathbf{E}$: The direction of surface charge variation is perpendicular to the applied electric field: positive surface charge density σ_+ on one half domain ($x < 0$) and negative surface charge density σ_- on the other half domain ($x > 0$). (b) $\mathbf{q} \parallel \mathbf{E}$: The direction of surface charge variation is parallel to the applied electric field (Stroock et al., 2000).

dispersion that can decrease the resolution in capillary electrophoresis (Ghosal, 2003; Long et al., 1999). Brotherton and Davis (2004) elaborated the effects of step changes in both zeta potential and cross section on electroosmosis in slit channels with arbitrary shapes of cross section. Their analyses indicated that the flow pattern in each region is a combination of a uniform electroosmotic flow and a nonuniform pressure-driven flow. Halpern and Wei (2007) theoretically examined the electroosmotic flow in a microcavity patterned with nonuniform surface charge. The results show that the flow demonstrates various patterns, depending on the aspect ratio of the cavity and the distribution of zeta potential. Zhang and Qiu (2008) demonstrated both experimentally and numerically the generation of 3D vortices by patterning surface with discrete charge patches on the inner surface of a round capillary tube. Lee et al. (2011) conducted a 3-D numerical study to investigate how the solute dispersion during electroosmotic migration is affected by the variation of surface and solution properties in

microchannels. It was found that the dispersion rate of a solute plug is increased by shear flows generated by zeta potential variations across and along the microchannel.

The surface charge modification can also be used to tune the electrophoretic motion of particles. For a colloidal particle with spatially inhomogeneous zeta potentials, Anderson (1985) demonstrated interesting and counter-intuitive effects that not only the total net charge but also the distribution of surface charge affects electrophoretic mobility of the colloidal particle. Long and Ajdari (1998) theoretically examined the electrophoresis of colloids with patterned shape and surface charge, and found that patterned colloids undergo a pure motion of rotation or move transversely to the applied electric field. Figure 2.4 presents an example with both patterned shape and surface charge. The patterned shape and surface charge in this case are defined by $a(\theta) = a_0\left[1 + \alpha\cosh(4\theta)\right]$ and $q(\theta) = q_0\cos(4\theta + \pi/2)$, respectively. a_0 is the cylinder radius at $\theta = \pi/8$ (i.e. the radius for the original circular cylinder denoted by the dash line), α is a small perturbation to the original circular cross-section, and q_0 represents the surface charge density at $\theta = -\pi/8$.

2.2.1.2 ACTIVE MODULATION OF CHARGE ON INSULATING SURFACES BY USING FLOW FIELD-EFFECT TRANSISTORS

Another variation of surface charge can be achieved actively by an electric field applied perpendicularly to the solid surface. Lee et al. (1990) first applied this technique to manipulate zeta potential of capillary wall for improving the separation efficiency in capillary electrophoresis. In their system, an auxiliary side electrode was embedded inside the capillary wall to set up the electric field

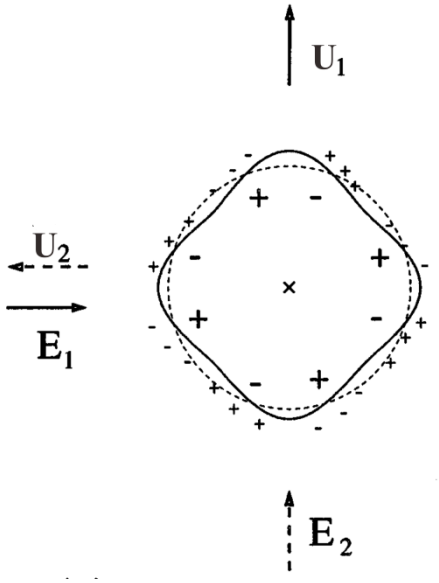

Figure 2.4 Electrophoretic motion of a cylinder with both patterned shape ($a(\theta)=a\left[1+\alpha\cosh(4\theta)\right]$) and surface charge ($q(\theta)=q_0\cos(4\theta+\pi/2)$). The direction of the cylinder motion is always perpendicular to the direction of applied electric field (Long and Ajdari, 1998).

that modifies the wall zeta potential. Ghowsi and Gale (1991) demonstrated the feasibility of electroosmosis control in a similar configuration. By analogy with the electronic field-effect transistor (FET), Schasfoort et al. (1999) further developed microfluidic flow FETs based on the same concept. Flow FETs, whose working mechanism is illustrated in Figure 2.5, employ an additional electrode embedded behind the insulating channel wall to establish a modulating electric field which maintains a nonzero potential difference between this auxiliary electrode and the bulk fluid. Active control of this nonzero potential difference modifies the potential drop across the electric double layer (so-called effective zeta potential), which in turn alters the electroosmotic flow. Van Der Wouden et al. (2006) demonstrated that directional flow can be induced in an AC field driven microfluidic FET by the synchronized switching of the gate potential and the channel axial potential.

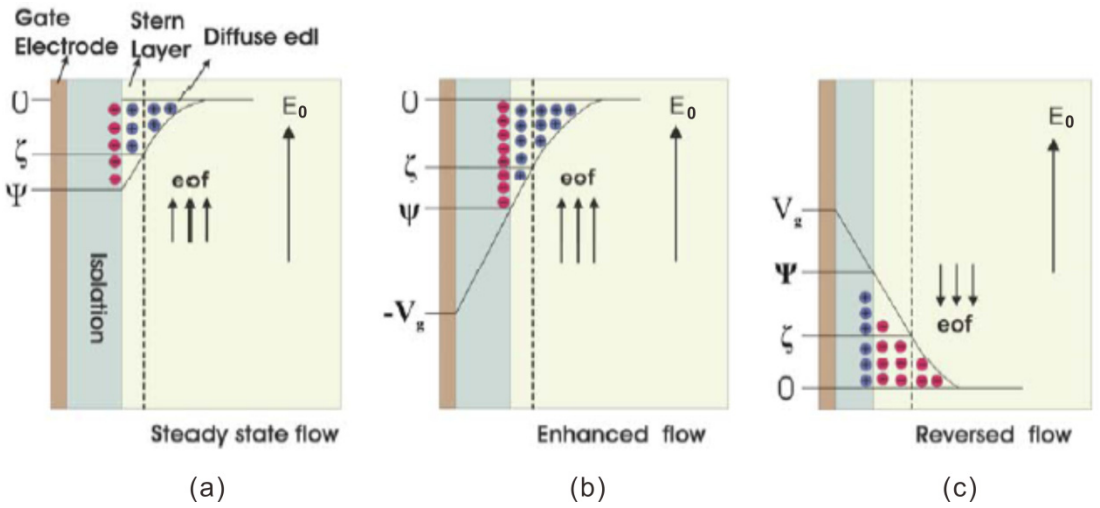

Figure 2.5 Schematic representation of the operating principle of a flow FET. Although the driving electric field E_0 is fixed, direction and intensity of the electroosmotic flow can be adjusted by a gate voltage which modulates the local zeta potential. In Case (a), there is no applied gate voltage and the velocity of electroosmotic flow is proportional to the natural zeta potential. In case (b), an applied negative gate voltage V_g enhances the negative zeta potential and thus the electroosmotic flow. In case (c), a positive gate potential reverses the charge in the electric double layer and thus the electroosmotic flow (Schasfoort et al., 1999).

Following the applications of FET to manipulate electroosmotic flows in microchannels, Daiguji et al. (2003) and Daiguji et al. (2005) theoretically extended the field-effect control to nanofluidics. They showed that FET technique can be used to regulate ionic transport by locally modifying the surface charge density on the nanochannel walls when the EDLs are overlapped. Karnik et al. (2005) experimentally demonstrated the use of field effect control in nanofluidics. They showed that the gate voltage modulates the charge on the nanochannel walls and then ionic conductance, which holds the promises for fabricating integrated nanofluidic circuits for the manipulation of ions and biomolecules in sub-femtoliter volumes. Later, transports of protein through nanochannels (Karnik et al., 2006) and proton inside silica films (Fan et al.,

2008) and ionic conductance in nanochannels (Fan et al., 2005; Joshi et al., 2010) were also modulated by utilizing the same gate control technique.

The effectiveness of FET flow control methods has been demonstrated with both fused-silica capillaries and microfabricated devices. This method demonstrates a higher level of controllability because of its ability to modify surface charge or zeta potential dynamically and electrically. However, in the typical FET configuration, an insulation layer usually separate the gate electrode from the fluid, and high gate voltages are required to modulate zeta potential or surface charge on the channel wall for observable FET effects. Such as in Sniadecki et al. (2004), for modification of the surface charge density of the channel, a gate voltage in the range of −120V to +120V was applied across the parylene C layer of 1.22μm thickness sandwiched between the fluid and the gate electrode. Similarly, Schasfoort et al. (1999) applied a transverse voltage of 50V across a 390nm thick insulation layer made of silicon nitride to modify the surface charge density for control of the electroosmotic flow.

Another active way for controlling surface charge relies on the use of wall coated with TiO_2, whose zeta potential can be modified by the UV light exposure (Moorthy et al., 2001).

2.2.2 POLARIZABLE (CONDUCTING) SURFACES

When polarizable surfaces are subject to external electric fields, the external driving electric field induces surface polarization charge in addition to the physiochemical bond charge on the surfaces, which would bring extra effects on classic electrokinetic phenomena. Depending on the locations where the phenomena arise (either on energized electrodes or around conductors floating

in an electric field), this category of electrokinetic phenomena can be classified as (i) AC electric field driven electrokinetic phenomena and (ii) induced-charge electrokinetic phenomena. Furthermore, another type of related electrokinetic phenomena termed as electrokinetic phenomena of the second kind caused by the induced bulk charge because of conducing surfaces is also reviewed here.

2.2.2.1 AC ELECTRIC FIELD DRIVEN ELECTROKINETIC PHENOMENA

A typical phenomenon in this subcategory allows steady electroosmotic flows to be driven by AC electric fields over two coplanar electrodes (see Figure 2.6). This "AC electroosmosis (ACEO)" was first theoretically and experimentally explored around a pair of adjacent, flat electrodes deposited on a glass slide and subjected to AC driving fields, and the basic flow patterns involve two counter-rotating vortices (Ramos et al., 1998, 1999). In the later serial papers (González et al., 2000; Green et al., 2000, 2002), detailed experimental, theoretical and numerical analyses of ACEO on microelectrodes were performed. Figure 2.6 shows a classical configuration of ACEO system and a comparison between the experimental result and the theoretical prediction.

Meanwhile, ACEO was also implemented to achieve various microfluidic applications. Ajdari (2000) theoretically predicted the AC electroosmosis over asymmetric electrodes and pointed out that the pumping effect can be induced due to the symmetry breaking of electrode arrangement. Based on the same idea, prototypes of AC electrokinetic micropumps were constructed and analyzed (Mpholo et al., 2003; Ramos et al., 2003). AC electroosmosis was also utilized to achieve rapid concentration of bioparticles (Wu et al., 2005), which can significantly reduce the transport time to detector and thus leads to an

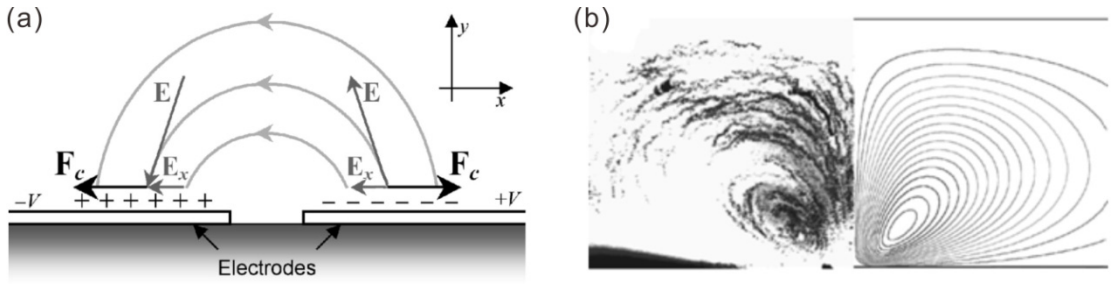

Figure 2.6 AC electroosmosis over two symmetric coplanar electrodes. (a) An electric double layer is induced over each electrode when coplanar electrodes are powered by the AC electric field with a particular frequency, and then induced electric double layers modify the external driving field. The electrostatic interaction of electric double layers with the local driving field gives rise to two opposite body forces which drive the AC electroosmosis. (b) A comparison between the measured streamlines on the left and the calculated streamlines on the right for the steady AC electroosmotic flow. If the electric field oscillates too slow, electric double layers fully screen the external driving field and there is no external field to drive AC electroosmosis. On the other hand, if the electric field oscillates too fast, there is not enough time for electric double layers to form and AC electroosmosis disappears. Consequently, the strongest AC electroosmosis occurs at a given field frequency (Green et al., 2002).

enhanced sensitivity. Sasaki et al. (2006) introduced the AC electroosmotic flow into a microchannel by applying an AC voltage to a pair of coplanar meandering electrodes, which can significantly improve the microfluidic mixing. Morin et al. (2007) simulated the AC electroosmosis with an equivalent electric circuit. They identified two distinct mechanisms for the AC electroosmosis: the diffusion of ionic species from the bulk to the electric double layer and the electrochemical reactions on the electrode surface. More recently, AC electroosmotic flows were adopted to manipulate microtubules in solution (Uppalapati et al., 2008), which provides a new tool to investigate and control the interaction between microtubules and microtubule motors in vitro. García-Sánchez et al. (2008) experimentally investigated the pumping performance of the traveling wave AC electroosmosis. They found the flow reversal when the voltage is above a

threshold, which was attributed to conductivity gradients generated in the bulk liquid due to Faradaic reactions. Ng et al. (2009) reported a novel approach using the AC electroosmosis with DC biases to significantly enhance mixing of two laminar streams flowing in microchannels. This approach provides a new way to break the symmetry of the AC electroosmosis by using a DC bias. Chen et al. (2009) gave a comprehensive assessment of micromixing performance for three different AC electroosmotic flow protocols, namely capacitive charging, Faradaic charging and asymmetric polarization. The results revealed that the Faradaic charging produces much stronger vortices than the other two protocols, and therefore enhances the species mixing. The generation of in-plane microvortices, and pumping flow in a microchannel was achieved recently with the benefit of AC electroosmotic flow (Huang et al., 2010b). The rotational direction of in-plane microvortices and pumping flow direction can be readily controlled by reversing the polarity of applied voltages.

Time-varying AC electric fields also can induce a rich variety of colloidal particle assembly around microelectrodes. Under AC electric fields, colloidal particles can achieve self-assembly to form two dimensional colloidal crystal near electrodes (Trau et al., 1996, 1997; Yeh et al., 1997). Figure 2.7 shows the transient formation of two-dimensional colloidal crystal under AC electric fields. This effect was attributed to a rectified electroosmotic flow directed radially toward the particle, which results from the interaction of an induced inhomogeneous electric double layer with the nonuniform applied electric field. Later, experiments were conducted to investigate the effects of AC electric field, particle size and surface charge on the latex particle aggregation on a conducting

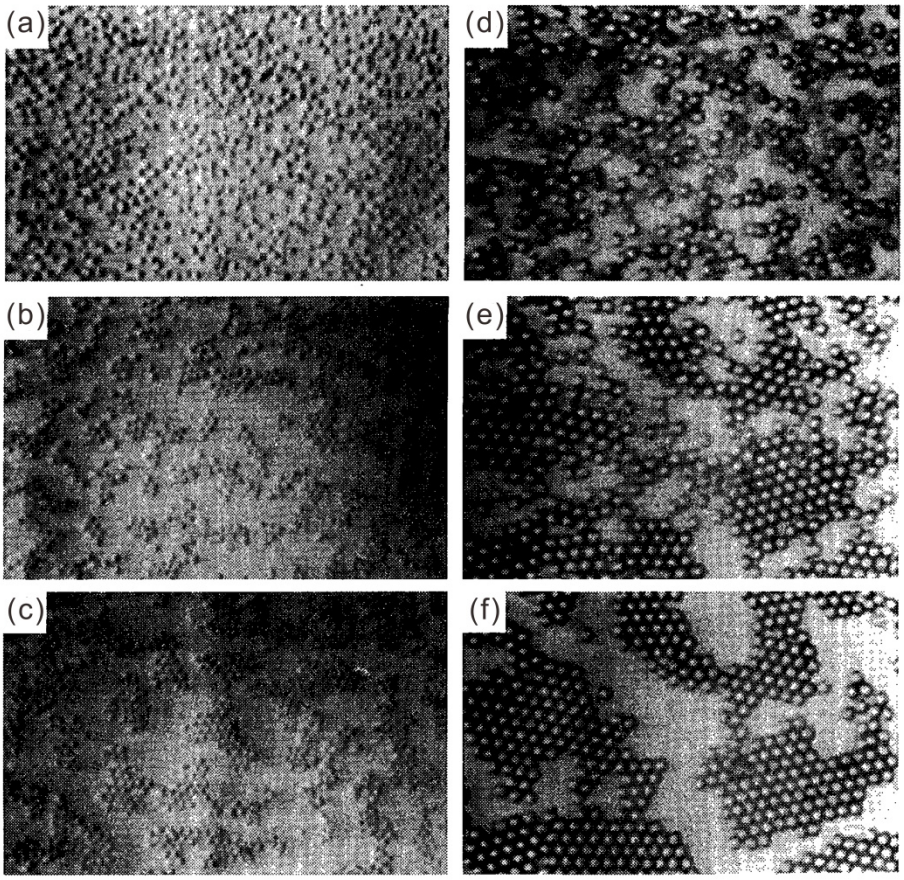

Figure 2.7 Transient formation of two-dimensional colloid crystal over the electrode surface under AC electric fields. The first column from (a) to (c) presents the formation process for 900nm colloidal particle and the second column from (d) to (f) presents the formation process for 2μm colloidal particle. The electric field in (a) and (d) was turned off and the time interval between each frame is 15s (Trau et al., 1996).

surface under AC electric fields (Nadal et al., 2002a). It was argued that the competition between electrohydrodynamic attraction and electrostatic dipolar repulsion plays important roles in the particle aggregation. Ristenpart et al. (2003) showed that various patterns of particle assembly can be formed around electrodes when bidisperse colloidal suspensions are under the influence of AC electric fields. Kumar et al. (2005) observed a reversible aggregation of particles in microchannels under AC electric fields. They further demonstrated that such reversible aggregation of particles can be tuned by varying the amplitude and

frequency of the applied AC electric field. Since the electrohydrodynamic flow around particles plays important roles in particle assembly, Ristenpart et al. (2007) performed a detailed analysis for such flows near an electrode with the AC electric forcing. Their analysis ascribed the flow to the thin double layer induced around the particle by AC electric fields. Mittal et al. (2008) reported an experiment to measure dipolar forces between micrometer sized polystyrene latex particles in AC electric fields. The conclusions showed that the dipolar interactions decrease with the increase of the background salt concentration, which is mainly attributable to a reduction in the difference between particle and medium conductivities.

The two AC field driven electrokinetic phenomena discussed above, AC electroosmosis and AC particle self-assembly, share some common features. They both occur around electrodes which are actively energized with AC electric fields. Both effects are strongest when AC frequency takes a particular value, and both effects vanish in DC electric fields. In addition, both are proportional to the square of the applied voltage. Therefore, AC field driven electrokinetic phenomena can be categorized as a type of nonlinear electrokinetic phenomena as compared with classic linear electrokinetic phenomena in which the resulting fluid or particle velocity is linearly scaled with the applied voltage. This nonlinear dependence can be intuitively understood as follows: The one power of electric field is used to induce charge inside the electric double layer, and another power of electric field is used to drive this induced charge to generate hydrodynamic flows or particle motion.

2.2.2.2 INDUCED-CHARGE ELECTROKINETICS (ICEK)

Nonlinear induced-charge electroosmotic flows are originally observed and discussed in colloid science. Levich (1962) first discussed the induced-charge double layer around a metallic colloidal particle in an external electric field and analyzed the induced flow field around the particle. Later, extensive studies ware carried out by the Ukrainian school (Dukhin, 1986; Dukhin and Murtsovkin, 1986; Dukhin and Shilov, 1969; Gamayunov et al., 1992; Gamayunov et al., 1986; Murtsovkin, 1996; Simonov and Dukhin, 1973) several decades ago. Such nonlinear flows arise when the applied electric field interacts with the nonelectroneutral electric double layer that has been induced by the applied field itself. Recently, several similar nonlinear electroosmotic flows driven by both AC and DC electric fields around polarizable objects have draw attention from the microfluidic community. Nadal et al. (2002b) performed a theoretical and experimental study of the microflow patterns produced around a polarizable dielectric stripe deposited on a planar electrode. The analyses showed that there are two counter-rotating vortices over the dielectric stripe, which is similar to the flow pattern of AC electroosmosis. In rather different situations, Thamida and Chang (2002) examined a DC nonlinear electrokinetic flow around a corner in a microchannel made of dielectric materials which can be weakly polarized. Takhistov et al. (2003) experimentally found that nonlinear electrokinetic vortices can be induced near microchannel junctions due to the finite polarizability of channel material (as shown in Figure 2.8). These examples of nonlinear electrokinetic phenomena indicate that polarizable surfaces in microfluidic devices can add new perspectives on the conventional linear electrokinetics. The detailed discussion and review of this type of nonlinear

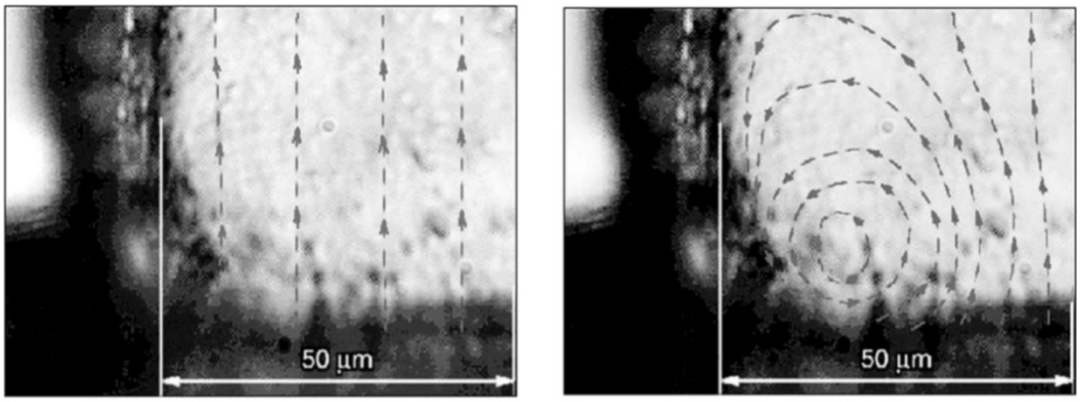

Figure 2.8 The flow patterns at the junction of a microchannel. (a) The sharp corner cannot be polarized by a low electric field strength (20V/cm) and the irrotational flow pattern of linear electroosmosis is maintained. (b)The sharp corner is polarized by a high electric field strength (50V/cm) and the irrotational characteristics of linear electroosmotic flow is violated (Takhistov et al., 2003).

electrokinetics can be found in Bazant et al. (2009) and Bazant and Squires (2010).

One should note that electrokinetic phenomena around polarizable surfaces are driven by a same physical mechanism: all feature a nonlinear electrokinetic flow which results from the interaction of the applied field with the double layer charge induced by the applied field itself. To highlight the essential role of induced charge in EDL, the term 'induced-charge electroosmosis' (ICEO) is then suggested for the description of such nonlinear electrokinetic flows (Squires and Bazant, 2004). Squires and Bazant (2004) also explored its relation to widely studied nonlinear electrokinetic phenomena, e.g., AC electroosmosis (Ajdari, 2000; Ramos et al., 1999). It was also suggested that ICEO generated around asymmetric conducting objects could perform a number of microfluidic applications, such as pumping, mixing and particle manipulations. Figure 2.9 schematically shows the evolution of an external DC electric field around a conducting patch immersed in an electrolyte solution, the formation of

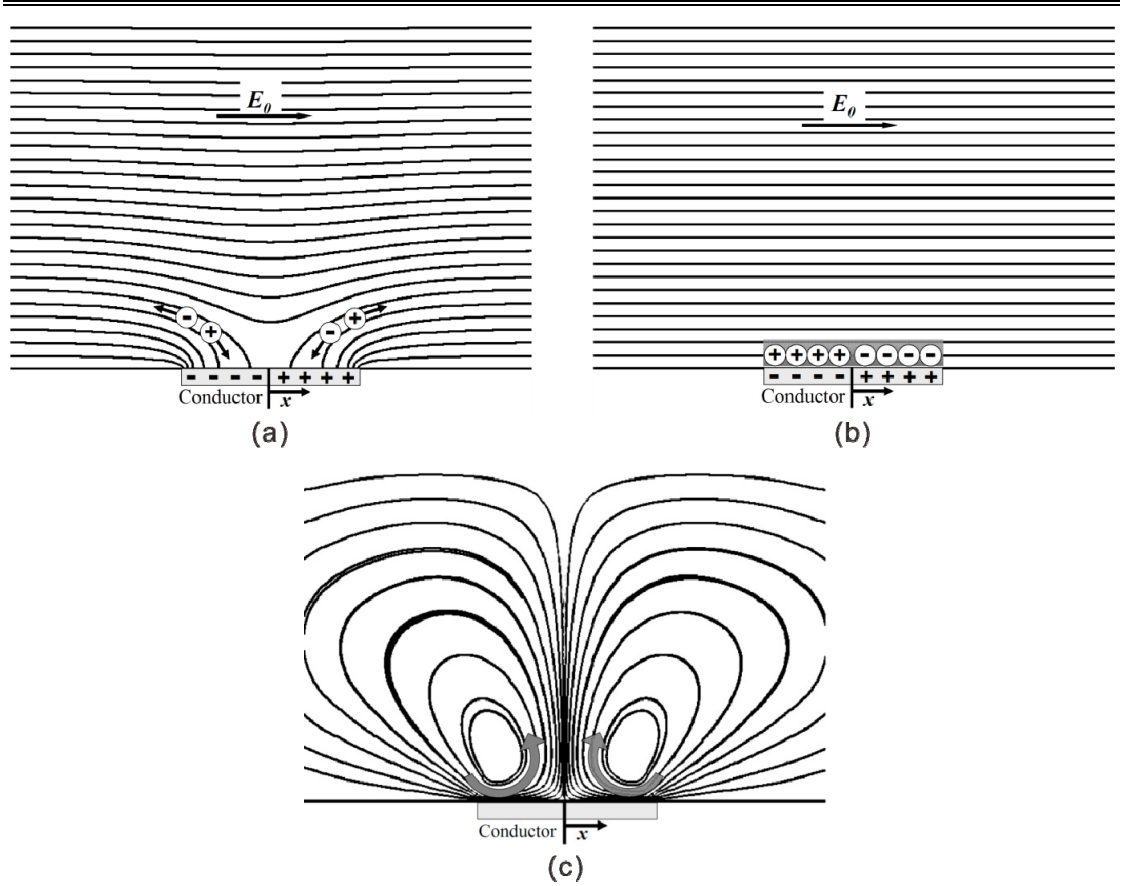

Figure 2.9 Illustration of the generation of induced-charge electroosmosis over a conducting patch. (a) Initially, the conducting patch immersed in an electrolytic solution is subjected to an external DC electric field, and the conducting patch is instantaneously polarized with the electric field lines intersecting the surface at right angles. The right (left) half of the surface acquires positive (negative) charge after polarization. (b) Then such surface charge distribution drives positive ions towards one half of the surface (x<0) and negative ions to the other half (x>0). This process charges up the electric double layer on the conducting surface. At the steady state, the double layer is fully charged and all the electric field lines become tangential to the surface of conductor. The induced zeta potential is ζ_i=-E_0x at the steady state. (c) Finally, the interaction of the external field and the induced double layer causes two nonlinear electroosmotic slip velocities (proportional to E_0 squared) directed from both edges toward the center, giving rise to two symmetric vortices above the surface. Since the polarity of the induced charge inside electric double layer is reversed by reversing the direction of electric field, an AC electric field drives an identical flow (Soni et al., 2007).

induced electric double layer and the corresponding ICEO above the conducting patch. It is evident that the basic flow pattern of ICEO is a pair of symmetric counter-rotating vortices above the conducting patch. Compared with

conventional linear electroosmosis associated with nonpolarizable surfaces of fixed zeta potentials, ICEO flows around polarizable surfaces are largely unnoticed. However, direct control of the shape, position, and potential of conducting or polarizable surfaces in ICEO can introduce lots of interesting and useful effects that do not exist in the conventional linear electrokinetics. It is obvious that ICEO flows promote conventional electrokinetic flows to a higher level of controllability and naturally lend themselves for use in microfluidic devices.

Another aspect of ICEK dubbed induced-charge electrophoresis (ICEP) was also proposed for the case of freely suspended polarizable particles, and can be a potential tool for particle manipulations. Although ICEP cannot induce motion of perfectly spherical particles in uniform electric fields, broken symmetries (such as shape asymmetry, nonuniform surface properties, or nonuniform applied fields) in ICEP do result in particle motions (Squires and Bazant, 2006). Figure 2.10 presents a simple strategy for inducing the ICEP motion of a conductor by shape asymmetry. The direction of particle motion can be either parallel or perpendicular to the external electric field, depending on shape asymmetry. Another fundamental discovery of their work is that shape asymmetry can yield quite interesting behaviors, such as the rotation and alignment of the particle in the direction of the electric field, and the migration of a particle carrying no net charge, which all are absent for the case of perfectly spherical particles.

Attention also has been paid to explore ICEK phenomena for microfluidic applications. Levitan et al. (2005) experimentally demonstrated the ICEO around a platinum wire immersed in a KCl solution under an external AC electric field. It

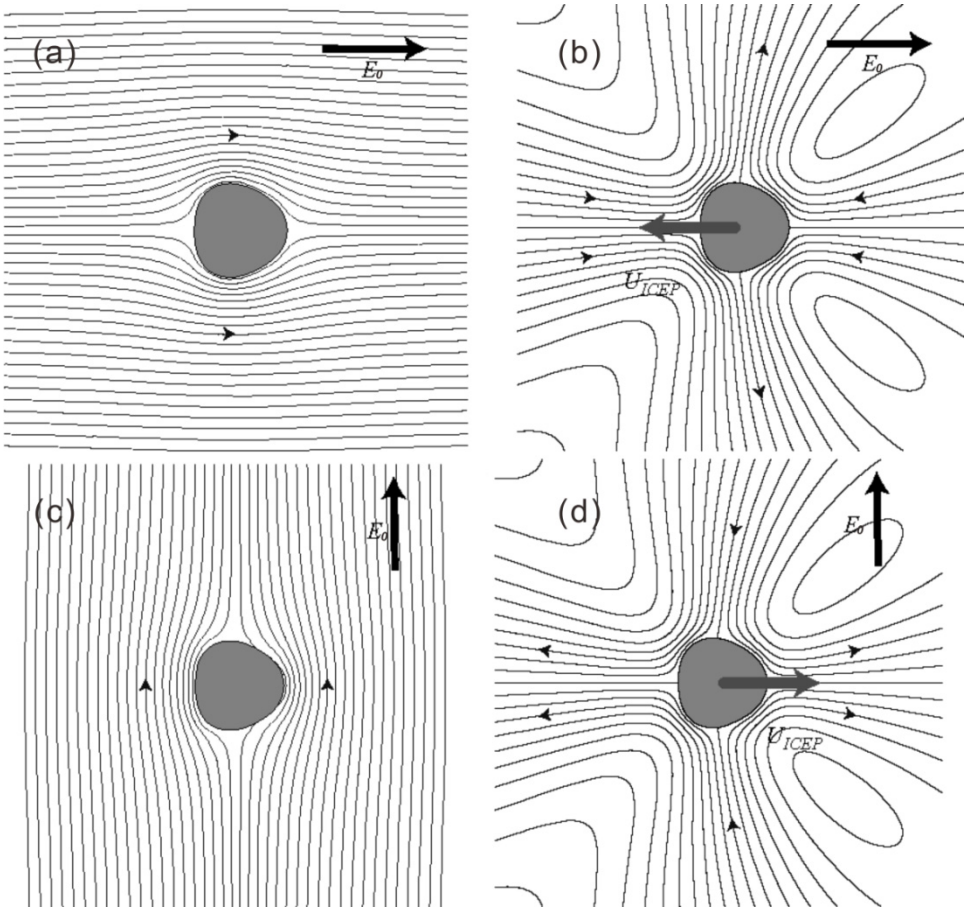

Figure 2.10 Translocation of asymmetric conductors with zero net charge in uniform applied electric fields. The upper row denotes ICEP induced motion due to the broken fore-aft symmetry of the conductor, and the conductor move by ICEP towards its wide end. The direction of ICEP motion is opposite to the direction of electric field. (a) Electric field lines and (b) streamlines of the ICEO flow for the broken fore-aft symmetry. The lower row denotes ICEP induced motion due to the broken left-right symmetry of the conductor, and the conductor move by ICEP towards its narrow end. The direction of ICEP motion is perpendicular to the direction of electric field (c) Electric field lines and (d) streamlines of the ICEO flow for the broken left-right symmetry (Squires and Bazant, 2006).

was shown that the ICEO driven by weak AC electric fields has more general frequency dependence in comparison with the ACEO, even allowing a steady flow under a DC electric field (since the platinum wire is not an electrode supplying the driving electric field). Bazant and Ben (2006) presented some new guidelines for designing high-flowrate 3D AC electroosmotic pumps relying on the concept of ICEO, and the creation of ICEO flow conveyor belt over a stepped electrode

array was identified to be one of the most effective guidelines. Later, these guidelines were adopted by Huang et al. (2010a) to achieve a state-of-the-art AC electroosmotic pump. Leinweber et al. (2006) utilized the ICEK to realize a continuous demixing process in a microfluidic devices. The process relies on noble metal posts floating in high external electrical fields. It was shown that the presented microfluidic demixer can achieve the efficient demixing of a homogeneous electrolyte into concentrated laminae and depleted laminae. Zhao and Bau (2007) utilized ICEO to construct a stir which simply consists of a single, cylindrical conductor enclosed by a square domain. It was also demonstrated that the stir operates with low driving voltages and can achieve chaotic mixing. A mixer for microfluidic sample preparation was also designed and tested (Harnett et al., 2008). In the mixer, they applied an AC electric field to create ICEO microvortices within a microfluidic channel. In addition, their proposed design of mixers prevents sample dilution and thus maintains detection sensitivity. Wu and Li (2008a) patterned PDMS microchannels with platinum conducting surfaces for the generation of ICEO. Furthermore, this strategy can achieve mixing enhancement which was validated both experimentally and numerically. More recently, the localized control of bulk pressure driven flow near conductive surfaces was presented with the use of ICEO (Sharp et al., 2011). They demonstrated that the ICEO flows introduced by conducting structures enable an on/off switch of fluid flow in a microfluidic device.

The idea of induced-charge electrokinetics is also extended for particle manipulations. Yariv (2005) theoretically analyzed the ICEP motion of non-spherical conducting particles. It was demonstrated that unlike the conventional

linear electrophoresis, nonspherical particles with zero net charge can translate and/or rotate in response to the imposed electric field because of the ICEP. Saintillan et al. (2006) examined the hydrodynamic interaction in the ICEP of infinitely polarizable slender rods. Particularly, they showed that the nonlinear ICEO flow on the particle surfaces causes the alignment of the rods in the direction of the electric field and induces linear distributions of point-force singularities. Then the stresslet disturbance flows are induced by such distribution of point forces to produce hydrodynamic interactions between the rods. Later, experimental verifications of these ICEO and ICEP effects were recently reported (Rose et al., 2007). The motion of Janus microparticles with one dielectric and one metal-coated hemisphere due to ICEP was reported experimentally (Gangwal et al., 2008). It was found that the direction of particle motion is perpendicular to the external driving field, which differs from the conventional linear electrophoresis. Recently, such experimental observation was supported by an theoretical analysis by Kilic and Bazant (2011). Miloh (2008) gave a systematic analysis of the motion of conducting particles with arbitrary shape under both DC and AC nonuniform electric fields. It was highlighted that the dipolophoresis (combination of dielectrophoresis and ICEP) is the driving mechanism for particle motion. More recently, Daghighi et al. (2011) constructed a 3D numerical model to investigate the transport of Janus particles in microchannels via ICEP. This study reveals that ICEO vortices produced on the polarizable side of the Janus particle push the Janus particle to move faster than the non-polarizable particles and the entirely polarizable particles (see Figure 2.11). The direction of the Janus particle motion can be tuned by adjusting the orientation of the polarizable part of Janus particle.

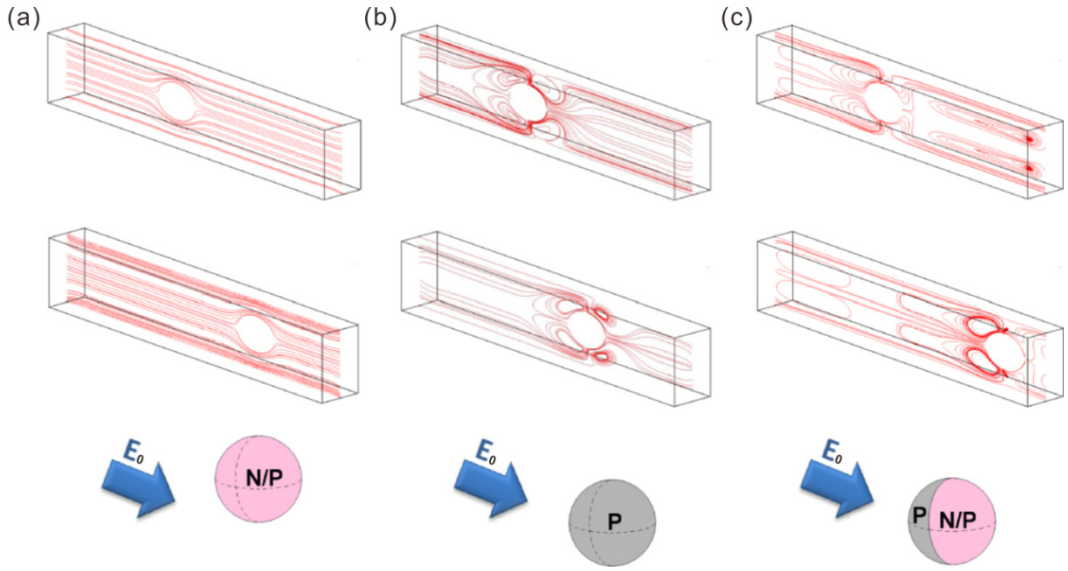

Figure 2.11 Comparison among electrophoretic motion of three different types of particles in microchannels. (a) A non-polarizable particle with a natural zeta potential of 60 mV, (b) an entirely polarizable particle with zero net charge, (c) a Janus particle. "P" represents "polarizable" and "N/P" represents "non-polarizable". For all cases the zeta potential on the microchannel wall and the external electric field are set to be the same. The top row shows the initial locations of particles in microchannels, the middle row shows particle locations after a same period of time. The bottom row shows the orientation of the particles with respect to the external field.

At last, we point out the differences between induced-charge electrokinetic phenomena and AC field driven electrokinetic phenomena reviewed in previous section. The AC field driven electrokinetic phenomena occur around conducting electrodes with actively applied voltages, and the induced-charge electrokinetic phenomena occur around polarizable materials (not necessarily conducting) floating in a external electric field. The AC field driven electrokinetic phenomena disappear at the DC limit, while the induced-charge electrokinetic phenomena should be strongest at the DC limit in principle.

2.2.2.3 SECOND-KIND ELECTROKINETICS

Second-kind electrokinetic flows usually occur around conducting porous materials under the influence of very large applied electric fields. Under a large

electric field, strong concentration polarization and space charge are produced in the bulk electrolyte due to strong currents of certain ions through the conducting surface. Then the fluid motion due to electrokinetics of the second kind is triggered by the interaction of the space charge with the applied field (Dukhin, 1991). This mechanism also can explain the similar phenomena which occur near the nonporous conducting surfaces with very large Faradaic currents because of strong electrochemical reactions (Barany et al., 1998). Another fundamental phenomenon due to second-kind electrokinetic flows is the electroosmotic instability on membrane surfaces (Zaltzman and Rubinstein, 2007), which also has been observed in experiments (Rubinstein et al., 2008; Yossifon and Chang, 2008).

A classical picture for the second-kind electrokinetic flow is depicted by Dukhin's model which characterizes an "electroosmotic whirlwind" around a highly conductive spherical particle subject to a strong electric field and a corresponding bulk charge layer induced in the electrolyte solution, as shown in Figure 2.12. This effect could be incorporated in electrochromatographic systems to greatly facilitate rapid separations (Rathore and Horvath, 1997). Second-kind electrokinetics and space charge formation also can occur in systems with microchannel-nanochannel junctions, as interpreted in Figure 2.13. In nanochannels with overlapping double layers, counterions predominate over coions to neutralize the charge on nanochannel walls. Under an external electric field, the nanochannel then mainly conducts a current of counterions, which could be strong enough to deplete the bulk salt concentration in the microchannel. At the steady state, a space charge layer of counterions is induced

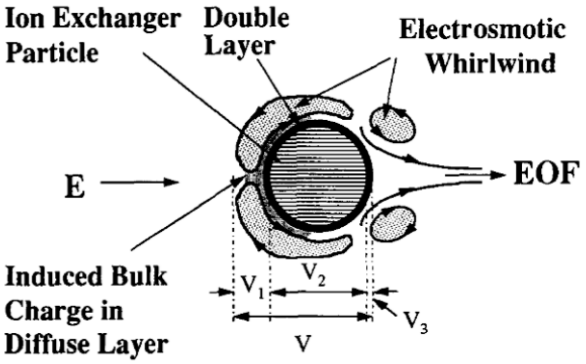

Figure 2.12 Schematic illustration of Dukhin's model in which an induced bulk charge layer and electroosmotic whirlwind form around a highly conductive ion-exchange particle subject to high electric fields. V is the total potential drop across the entire domain, and is composed of V_1 (potential drop across the bulk charge layer), V_2 (potential drop across the particle itself), and V_3 (potential drop across the electric double layer) (Rathore and Horvath, 1997).

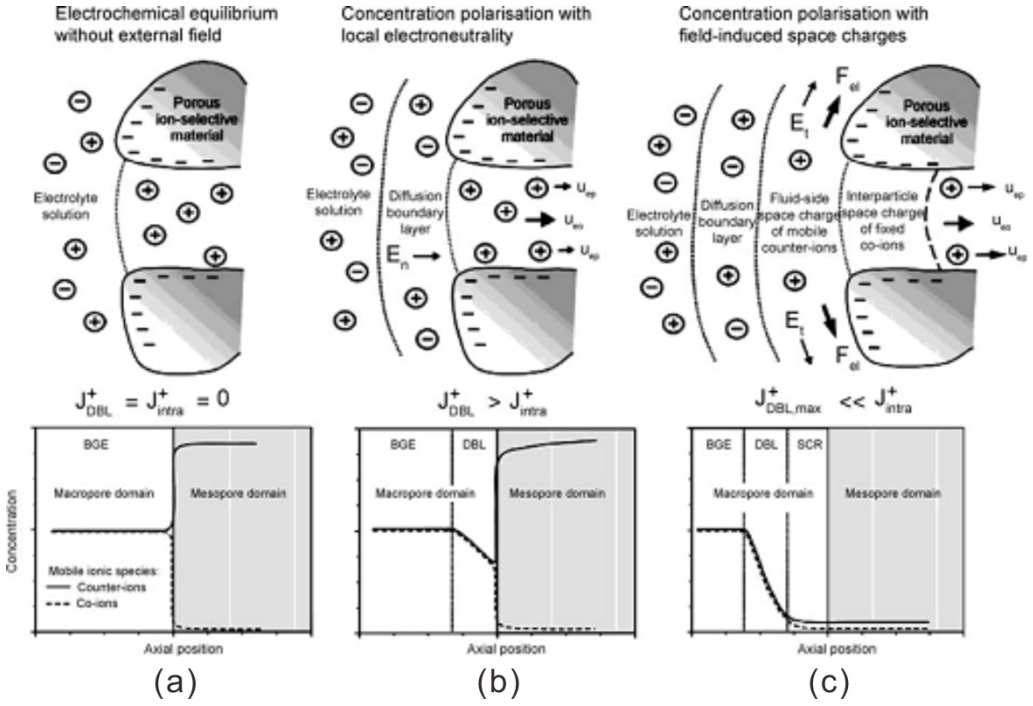

Figure 2.13 Schematic show of the mechanism for the formation of space charge and second-kind electroosmosis at the microchannel-nanochannel junction. (a) In the absence of external electric field, the microchannel contains neutral electrolyte and the nanochannel mainly contains counterions due to the overlapping of electric double layers. (b) After an electric field is applied, the counterions are mainly conducted through the nanochannel. Then the nearby salt concentration in the microchannel is depleted, which introduces a bulk diffusion layer. (c) The bulk concentration can be depleted completely under a strong electric field, which leads to the formation of space charge and second-kind electroosmosis around the microchannel-nanochannel junction (Leinweber and Tallarek, 2004).

near the microchannel-nanochannel junction. The second-kind electrokinetic flows thus occur because of the interaction of the tangential electric fields near the junction with the space charge layer surrounding the junction.

Mishchuk et al. (2001) analyzed both theoretically and experimentally the phenomena of limiting current and strong concentration polarization around flat and curved interfaces. They found out that the current through the curved interface grows rapidly, while the current tends to saturate for the case of flat surface. This is mainly due to an important change of characteristics of concentration polarization generated by electroosmosis of the second kind near the curved interface. Ben and Chang (2002) theoretically predicted the generation of microvortices around an ion-exchange porous granule and attributed it to electrokinetic phenomena of the second kind. Based on electroosmosis of the second kind, a low-voltage micropump was developed (Heldal et al., 2007). This kind of micropumps presents several advantages: no moving parts; small power/voltage and dimensions; situated inside the flow channel. These advantages make the pump suitable for portable, embedded and implantable microfluidic devices. Micropumps utilizing electroosmosis of the second kind was also successfully tested using AC electric fields (Mishchuk et al., 2009), which was also shown to be in good agreement with the theoretical prediction. The AC field eliminates the possibility of bubble generation in the operation of microfluidic and lab-on-a-chip systems. More Recently, Kivanc and Litster (2011) presented a micropump made of mesoporous silica skeletons with electroosmosis of the second kind. The focus of the study was to clarify the effect of pressure loads on the pumping performance, and particularly the reverse

pressure-driven flow under a critical pressure load was found to significantly reduce electroosmosis of the second kind.

Other than fluid motion, second-kind electrokinetics also can induce particle motion. Dukhin et al. (1989) established the existence of electrophoresis of the second kind for metallic particles. Barany et al. (1998) demonstrated that electrophoretic velocities of the conducting particles are much higher than those expected for non-conducting particles. They attributed this to electrokinetics of the second kind. Usually, a bulk charge layer is induced outside the primary electric double layer when the externally applied electric is high enough to produce the over limit current through the particle. This extra induced bulk charge layer interacts with the external electric field, leading to the enhancement of electrophoretic velocities. In a later independent work (Ben et al., 2004), the above reasoning for electrophoretic velocity enhancement due to electrophoresis of the second kind was corroborated.

However, second-kind electrokinetics requires large applied electric field and thus triggers strong surface and bulk chemical reactions, which are usually unwanted in most biomedical-related microfluidic applications. Furthermore, one should note that there are distinct differences between the ICEK and the second-kind electrokinetics. Second-kind electrokinetic phenomena are driven by space charge in the bulk solution, not in the electric double layer. In contrast, ICEK relies on relatively small induced charge in the electric double layer induced around polarizable surfaces, rather than bulk space charge. Particularly, ICEK does not induce Faradaic reactions because of relatively low driving

voltages, which thus makes the ICEK a possible candidate for biomedical applications.

2.3 SUMMARY AND COMMENTS ON PREVIOUS STUDIES

Based on the literature review, it has been identified that electrokinetics can happen around both insulating (nonpolarizable) and polarizable media. The linear electrokinetics or fixed charge electrokinetics generally occurs around insulating media and the nonlinear electrokinetics occurs around polarizable or conducting media. The linear electrokinetics is well understood and its applications in microfluidics and nanofluidics are well established. However, nonlinear electrokinetics is a relatively new class of electrokinetic phenomena. Consequently, some of its fundamental aspects still lack thorough understanding and its applications in microfluidics and nanofluidics need to be further explored.

AC electric field driven electrokinetics, induced-charge electrokinetics and electrokinetics of the second kind are reviewed under the category of nonlinear electrokinetics. In AC field driven electrokinetics, all electrodes are powered to supply the driving electric fields. Then complicated electrode designs are indispensable for highly integrated microfluidic devices. Due to inherent surface and bulk chemical reactions, electrokinetics of the second kind is not suitable for microfluidics which frequently handles biosamples. In comparison with the above two types of nonlinear electrokinetics, induced-charge electrokinetics, however, utilizes electrically polarizable surfaces floating in one global driving electric field. This global driving field can be simply set up by two electrodes, which requires a much simpler electrode design. Moreover, induced-charge

electrokinetics relies on the double layer charge induced by low voltages and thus does not suffer from surface and bulk electrochemical reactions.

In addition, induced-charge electrokinetics is a relatively new member in the family of nonlinear electrokinetics, and the fundamental understanding of induced-charge electrokinetics is still poor in several aspects: First, most existing studies assumed ideally polarizable surfaces (metal). Actually, induced-charge electrokinetics can be more general to occur around any finitely polarizable surfaces. Second, the charging of electric double layer around polarizable solids is a key to understanding the induced-charge electrokinetics. Previous analyses are based on models with various assumptions that can be easily violated in real microfluidic applications. It is obvious that no complete mathematic model has been presented to describe the transient behaviors of the electric double layer and the associated liquid flows in details.

Other than the aforementioned fundamental aspects, applications of induced-charge nonlinear electrokinetics at the present stage are very limited as compared to conventional linear electrokinetics. To the best of our knowledge, there is only one well-established application for induced-charge electrokinetics in the literature, i.e., microfluidic mixing. The applications of induced-charge electrokinetics in microfluidics need to be further explored. On the other hand, nanofluidics-an extension of microfluidics to nanometer scale-mainly involves manipulations of charged molecules and ions in nanochannels. In nanochannels with overlapping electric double layers, transport of charged species is dominated by the surface charge density on the nanochannel walls. Then active control of nanofluidic systems needs the direct modulation of surface charge

density on the walls of nanochannel. It is clear that induced-charge electrokinetics is a natural choice for such purpose, in which the surface charge density can be actively controlled by adjustment of the external electric field strength or the orientation of surface with respect to the external electric field. Consequently, the extension of induced-charge electrokinetics from microfluidics to nanofluidics is necessary.

CHAPTER 3: INDUCED-CHARGE ELECTROKINETIC PHENOMENA OVER DIELECTRIC AND LEAKY-DIELECTRIC SURFACES: EFFECTIVE ELECTRIC BOUNDARY CONDITIONS AND THEIR APPLICATIONS*

3.1 INTRODUCTION

Electrokinetics, including electroosmosis and electrophoresis, plays important roles in manipulation of liquid flow and particles in microfluidic contexts. General description of classical electrokinetic flows in microfluidic channels with thin electric double layer (EDL) utilizes a slip velocity approximate approach to avoid the need of solving the detailed profiles of the EDL potential and fluid velocity. Such slip velocity can be described by the Helmholtz-Smoluchowski equation ($V_s = -\varepsilon\zeta E / \mu$) which is associated with the electric permittivity ε and dynamic viscosity μ of the liquid, the applied local electric field E and the zeta potential of the channel wall ζ, thereby providing an appropriate boundary condition for the hydrodynamic problems in microfluidics. For a uniform prescribed zeta potential, the resulting flow is irrotational (Morrison, 1970). Nonetheless, the preceding description is adequate for perfectly insulating channel surfaces that usually bear natural

* This chapter is a combination of two published papers: Cunlu Zhao and Chun Yang, Analysis of induced-charge electro-osmotic flow in a microchannel embedded with polarizable dielectric blocks. Physical Review E, 2009. **80**(4):046312; Cunlu Zhao and Chun Yang, ac electrokinetic phenomena over semiconductive surfaces: Effective electric boundary conditions and their applications. Physical Review E, 2011. **83**(6): 066304.

electric charges (or natural zeta potential) fixed due to the physiochemical bonds. Consequently, the surface charge density is independent of the externally applied electric field. However, for electrokinetic phenomena around polarizable or conducting solids, it has been demonstrated that in the presence of an external electric field, extra electric charge can be induced on polarizable or conducting solid surfaces immersed in an electrolyte solution, thereby triggering the charging of EDL inside the electrolyte solution. This is represented by a zeta potential which depends on the external electric field, and is not a fixed equilibrium material property anymore. The resulting dependence of the surface charge density (and consequently the ζ potential) upon the externally applied field strength gives rise to a nonlinear Helmholtz-Smoluchowski relation for the slip velocity.

The reviewed works about ICEK in Chapter 2 mostly focus on ideally polarizable surfaces or particles. Under this circumstance, the solid floating in an external electric field is equipotential and thus evaluation of the induced zeta potential does not require the details of potential distribution inside the solid. Of more general interest, solid objects generally possess finite electric properties and thus cannot be simply approximated as either perfectly polarizable or completely insulating (Flores-Rodriguez and Markx, 2006). When dealing with electrokinetic phenomena on the surface of a solid object with finite electric properties (dielectric constants and conductivities), electrical potential distributions inside such solids must be known to calculate the induced zeta potential, and thus extra electric boundary conditions at the liquid-solid interface are needed to link the bulk electric potentials inside both solid and

electrolyte solution. Therefore, the present chapter aims at generalizing the electrical boundary conditions for the ICEK phenomena at liquid-solid interfaces.

Although Squires and Bazant (2004) considered the reduction of induced zeta potential due to a thin dielectric coating on a conducting cylinder, they assumed that the electric field strength does not vary inside the thin dielectric coating. Under more general conditions, Yossifon et al. (2006) and Yossifon et al. (2007) obtained a Robin-type boundary condition to link the bulk potential in electrolyte solution and the potential in dielectric body (not a thin dielectric surface). Later, these boundary conditions were reproduced with consideration of the physics of induced-charge electrokinetics (Zhao and Yang, 2009, 2011b). Such boundary conditions can be used to evaluate the potential drop across the EDL around arbitrarily polarizable dielectrics subjected to small electric fields. Notably, similar Robin-type boundary conditions have been used to describe the compact Stern layer on electrodes (Bazant et al., 2005; Biesheuvel et al., 2009; Bonnefont et al., 2001) or the membrane (Lacoste et al., 2009; Ziebert et al., 2010). These models however predict the potential drop across a thin electroneutral layer, while Yossifon's model more generally predicts the potential drop across a charged EDL (namely the induced zeta potential). In the first part of this chapter, generalized electric boundary conditions are derived for ideally dielectric surfaces by extending the model of Yossifon et al. (2006) and Yossifon et al. (2007) to the situation of arbitrary induced zeta potential. Under this circumstance, there are no free charge carriers inside the dielectrics and only the surface charge due to electric polarization contributes to the zeta potential. Theoretically, such derived electric boundary conditions can be

applicable within the entire range of dielectric constant; namely the dielectric constant of materials spans from zero (nonpolarizable) to infinity (perfectly polarizable). Furthermore, with aid of the proposed electrical boundary conditions, the ICEO flows driven by a DC electric field over two symmetric polarizable dielectric blocks embedded in the walls of a microchannel will be analyzed. The ICEO flow field will be obtained analytically by solving a biharmonic equation that governs the stream function. Finally, the effects of dielectric constant of the polarizable dielectric block and the natural zeta potential of the insulating channel walls on such ICEO flow will be examined.

However, from a practical viewpoint, a solid can have both finite dielectric constant and conductivity and is leaky dielectric (semiconductive) in nature. Under this circumstance, free charge carriers are present inside both the solid and the liquid. Consequently, the space charge layer (SCL) forms in the solid and the EDL forms in the electrolyte liquid under the influence of external electric fields, and these two layers constitute the interface between a leaky-dielectric solid and an electrolyte solution. Other than the polarization surface charge, free charge stored in the SCL because of electric conduction also contributes to the induced zeta potential. On the other hand, AC electric field is more desirable in microfluidic applications since it introduces another control parameter of frequency and also reduces possible negative effects, such as electrolysis and dissolution of electrodes. Therefore, the second part of this chapter presents effective electrokinetic boundary conditions for AC field driven ICEK to correlate the bulk electrical potentials across the EDL and the SCL at a leaky-dielectric solid-electrolyte solution interface. Such effective electrokinetic boundary

conditions allow for determining the induced zeta potentials on the surface of leaky-dielectric solids subjected to an AC electric field of arbitrary wave forms. Furthermore, the derived electrokinetic boundary conditions are implemented for analyzing the AC field driven ICEK flow around a leaky-dielectric cylinder.

3.2 DC FIELD DRIVEN INDUCED-CHARGE ELECTROKINETICS: EFFECTIVE BOUNDARY CONDITIONS AND THEIR APPLICATIONS

3.2.1 GENERAL ELECTRICAL BOUNDARY CONDITIONS ON A POLARIZABLE DIELECTRIC–LIQUID INTERFACE

To illustrate the process of generating the induced charges at a liquid-dielectric surface in ICEK phenomena, we can envisage a simple case: a dielectric object of arbitrary shape with a polarizable surface immersed in an aqueous solution as shown in Figure 3.1 (a). When an electric field is applied over the object, the object surface is polarized with negative surface charge facing towards the anode of the electric field and positive surface charge facing towards the cathode of the electric field. Such induced charge on polarizable object surface attracts counterions and repels coions in the solution to form a screening cloud (i.e., EDL) around the surface. Such screening cloud in turn causes the electric field lines to be expelled and the ionic flux into the charge cloud to be reduced. At the steady state, once the EDL is fully charged, the external electric field is completely screened off from the solid. Then the externally applied field exerts an electrostatic body force on the ions in the screening cloud, driving the ions and thus the liquid into motion (see Figure 3.1 (b)). It should be pointed out here that the following derivations are based on two assumptions (Squires and Bazant, 2004): (i) The surface conduction is negligible compared to the bulk

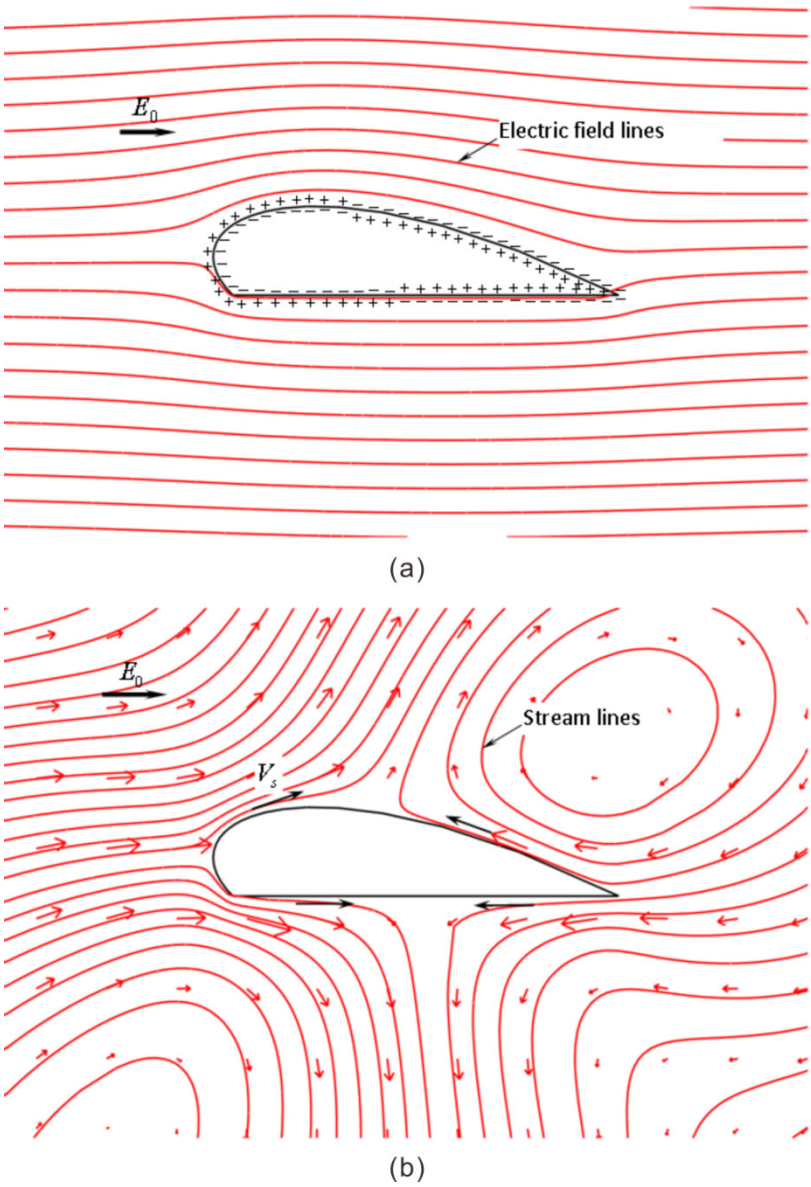

Figure 3.1 Schematic diagram illustrating the mechanism of ICEO. (a) Steady-state electric field distributions around a polarizable dielectric object immersed in an electrolyte solution, where the charge distribution on the surface of the solid is due to the polarization of the dielectric block and the charge inside the EDL is due to the corresponding coulombic attraction, (b) Steady-state stream lines of ICEO flow driven by the Smoluchowski velocities V_s on the surfaced of the polarizable dielectric block.

conduction of the electrolyte. This is true for the cases of small Dukhin numbers where the EDL is thin and no electrochemical reaction occurs at the dielectric–liquid interface. (ii) The induced zeta potential is small so that the Debye-Hückel linear approximation is applicable. With these assumptions, Figure 3.1 (a)

illustrates that under the steady state, the polarizable object behaves like an insulator because an induced EDL around the polarizable surface is formed and the normal component of electric field does not conduct ions into the EDL anymore. This steady-state electrostatic configuration effectively represents the no-flux electrostatic boundary condition assumed in conventional electrokinetic analysis. In the absence of electrical conductivity gradient in the bulk, the externally applied electric potential outside the EDL at the steady state is governed by the Laplace equation which is expressed as

$$\nabla^2 \Phi_f = 0 \tag{3.1}$$

with an insulating boundary condition specified at the outer edge of the EDL (the detailed boundary structure is shown in Figure 3.2)

$$\mathbf{n} \bullet \nabla \Phi_f \Big|_{n=\lambda_D} = 0 \tag{3.2}$$

where **n** represents a unit vector along n axis (i.e., perpendicular to the polarizable dielectric surface), and λ_D is the Debye screening length that is related to properties of a symmetric electrolyte (*z*:*z*) solution through

$$\lambda_D = \sqrt{\frac{\varepsilon_0 \varepsilon_f k_B T}{2 n_0 e^2 z^2}} \tag{3.3}$$

where e is the fundamental charge, z is the valence of the electrolyte ions, n_0 is the bulk number concentration of the electrolyte, k_B is the Boltzmann constant and T is the absolute temperature of the electrolyte solution. This Debye screening length is normally referred to as the EDL thickness (Squires and Quake, 2005). The EDL is typically of about nanometers in size, which is why the

thin EDL assumptions is usually invoked (and in most cases justified) in microfluidics.

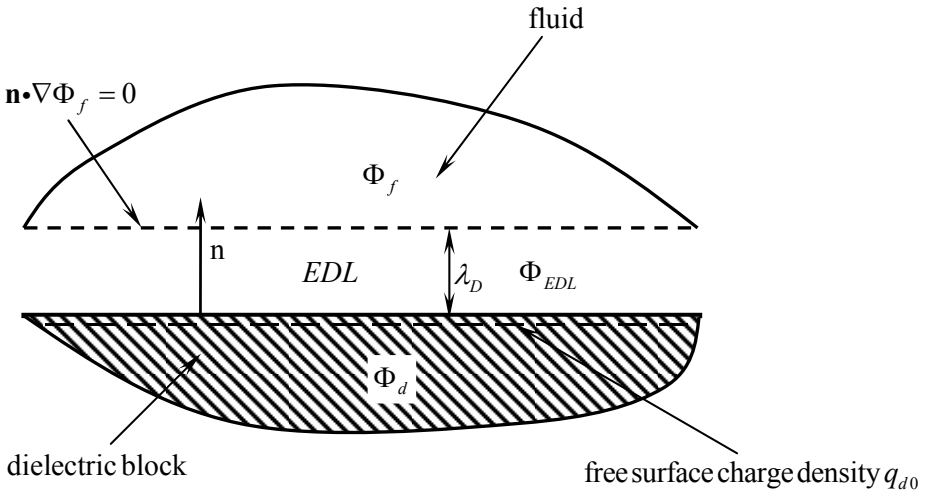

Figure 3.2 Schematic diagram for the electric boundary condition for the induced-charge electrokinetic phenomena at the interface between an electrolyte solution and a polarizable dielectric object.

Following Squires and Bazant (2006), we also define the induced zeta potential as the potential difference between the potential of fluid at the outer edge of the EDL and the potential on the polarizable dielectric surface. Recall that the potential in the fluid domain is governed by equations (3.1) and (3.2). The potential inside the polarizable dielectric body is also governed by Laplace's equation

$$\nabla^2\Phi_d = 0 \tag{3.4}$$

It is noted that before the external electric field is imposed, there already exists natural surface charges of density q_{d0} on the dielectric surface. Then the normal component of the electric displacement across the dielectric surface is not continuous, instead with a step jump by amount of q_{d0} (Paris and Hurd, 1969)

$$\varepsilon_0\varepsilon_f \mathbf{n}\bullet\nabla\Phi_{EDL}\Big|_{n=0} - \varepsilon_0\varepsilon_d \mathbf{n}\bullet\nabla\Phi_d\Big|_{n=0} = -q_{d0} \tag{3.5}$$

where ε_0 is the permittivity of vacuum and has a value of 8.854×10^{-12} F/m, and ε_f and ε_d are respectively the dielectric constants of the liquid and the dielectric block. Φ_{EDL} represents the potential inside the EDL, and it matches the bulk potential Φ_f at the outer edge of the EDL through $\Phi_{EDL}\big|_{n=\lambda_D} = \Phi_f\big|_{n=\lambda_D}$ and $\mathbf{n}\bullet\nabla\Phi_{EDL}\big|_{n=\lambda_D} = \mathbf{n}\bullet\nabla\Phi_f\big|_{n=\lambda_D}$. Inside the EDL, the potential is governed by Poisson's equation

$$\nabla^2\Phi_{EDL} = -\frac{\rho_e}{\varepsilon_0\varepsilon_f} \tag{3.6}$$

where ρ_e is the net charge density inside the EDL. Then with an assumption of thin EDL, the EDL can be approximated as a local planer geometry as shown in Figure 3.2, and hence equation (3.6) is reduced to

$$\varepsilon_0\varepsilon_f \frac{\partial^2\Phi_{EDL}}{\partial n^2} = -\rho_e \tag{3.7}$$

Integrating equation (3.7) from the polarizable dielectric surface to the outer edge of the EDL, we can write

$$\varepsilon_0\varepsilon_f \int_0^{\lambda_D} \frac{\partial^2\Phi_{EDL}}{\partial n^2} dn = -\int_0^{\lambda_D} \rho_e dn \tag{3.8}$$

Note that the upper limit of the integration, $n = \lambda_D$ physically represents the outer edge of the EDL. The right-hand side of equation (3.8) gives the total amount of charges stored in the EDL capacitor which can be related to the potential drop across the EDL (equivalent of the induced zeta potential),

$\Phi_f\big|_{n=\lambda_D} - \Phi_d\big|_{n=0}$, by equation (2.12) . For the left-hand side of equation (3.8), it is readily to show that $\partial\Phi_{EDL}/\partial n$ vanishes at the outer edge of the EDL (see equation (3.2)). Hence, based on equation (3.8), the electric displacement at the fluid-solid interface on the fluid side can be approximated as

$$\varepsilon_0\varepsilon_f \mathbf{n}\bullet\nabla\Phi_{EDL}\big|_{n=0} = 4n_0 ze\lambda_D \sinh\left[\frac{ze\left(\Phi_f\big|_{n=\lambda_D} - \Phi_d\big|_{n=0}\right)}{2k_BT}\right] \tag{3.9}$$

which represents the amount of charges (including both natural and induced parts) stored in the EDL capacitor near a polarizable dielectric surface. These charges induce same amount of opposite surface charges on the dielectric block surface which are responsible for the ICEK phenomena.

Utilizing equations (3.5) and (3.9), we can obtain a boundary condition that connects the potentials in the dielectric domain and the bulk fluid domain

$$\lambda_D \frac{\varepsilon_d}{\varepsilon_f}\mathbf{n}\bullet\nabla\Phi_d\Big|_{n=0} = 2\frac{k_BT}{ze}\sinh\left[\frac{ze\left(\Phi_f\big|_{n=\lambda_D} - \Phi_d\big|_{n=0}\right)}{2k_BT}\right] + \zeta_{d0} \tag{3.10}$$

where ζ_{d0} is the zeta potential corresponding to natural surface charges q_{d0}, and is related to q_{d0} by

$$\zeta_{d0} = \frac{\lambda_D q_{d0}}{\varepsilon_0\varepsilon_f} \tag{3.11}$$

Due to the nonlinear hyperbolic sine function involved in equation (3.10), it is only possible to use numerical methods to evaluate the induced zeta potential. However, when the potential drop across the EDL is small (for a small electric

field), one obtains a linearized boundary condition of Robin type from equation (3.10) for the potential distribution inside the polarizable dielectric object

$$\Phi_d\big|_{\mathrm{n}=0} + \lambda_D \frac{\varepsilon_d}{\varepsilon_f} \mathbf{n}\bullet\nabla\Phi_d \bigg|_{n=0} = \Phi_f\big|_{n=\lambda_D} + \zeta_{d0} \tag{3.12}$$

which exactly recovers the result of Yossifon et al. (2006) and Yossifon et al. (2007) who obtained the same boundary condition for small induced zeta potentials by using the asymptotic matching method. The advantage of this boundary condition is its linearity which helps to evaluate the induced zeta potential analytically. In the next section, a case study is presented to show the applications of the boundary condition (3.12).

Through the boundary condition (3.12), the potential inside the polarizable dielectric object and the potential in the bulk fluid domain (namely outside the EDL) are coupled together, and thus the potential inside the dielectric object can be obtained by solving equation (3.4) since the electrical potential distribution in the bulk fluid domain has already been determined by equations (3.1) and (3.2). Finally, the total zeta potential can be found as the difference between the potential at the outer edge of the EDL and the potential on the dielectric object surface, and it takes the following form

$$\zeta_d = \Phi_d\big|_{n=0} - \Phi_f\big|_{n=\lambda_D} = -\lambda_D \frac{\varepsilon_d}{\varepsilon_f} \mathbf{n}\bullet\nabla\Phi_d \bigg|_{n=0} + \zeta_{d0} \tag{3.13}$$

Besides the conventional zeta potential ζ_{d0} due to natural charges on the dielectric surface, it is revealed by equation (3.13) that an extra zeta potential $\zeta_{di} = -\lambda_D \varepsilon_d \mathbf{n}\bullet\nabla\Phi_d\big|_{n=0} / \varepsilon_f$ is induced due to the presence of external electric field.

Obviously, the induced zeta potential ζ_{di} is no longer a constant; instead it varies with local electric field strength at the polarizable dielectric object surface.

The proposed electric boundary condition shown in equation (3.12) is general because two important limiting cases can be obtained from it. For the case of insulating surfaces (i.e., $\varepsilon_d \to 0$), the electric boundary condition for conventional electrokinetic flows can be recovered when the induced part of the zeta potential ζ_{di} drops off and only the natural zeta potential ζ_{d0} remains. On the other hand, when an object has excellent electric conductibility (i.e., $\varepsilon_d \to \infty$), a perfect conductor should be equipotential, that is $\Phi_d = \zeta_{d0}$. Utilizing equation (3.12), we can show that the induced zeta potential is just the opposite potential at the outer edge of the EDL in the liquid domain, i.e., $-\Phi_f\big|_{n=\lambda_D}$; this is consistent with the analysis by Squires and Bazant (2004) for perfectly polarizable surfaces (i.e., $\varepsilon_d \to \infty$).

3.2.2 INDUCED ZETA POTENTIAL ON THE SURFACE OF TWO POLARIZABLE DIELECTRIC BLOCKS EMBEDDED IN THE WALL OF A SLIT MICROCHANNEL

Consider an electrolyte solution in a parallel-plate slit channel of height 2H as shown in Figure 3.3. Two symmetric polarizable dielectric blocks are embedded in the microchannel walls, and they have an arbitrary dielectric constant ε_d and geometric dimensions of aH × bH (where a and b respectively are length and height scale factor of the polarizable dielectric block with respect to the half height of the channel H). Once in contact with electrolyte solution, the polarizable dielectric surface is charged with a uniform natural zeta potential ζ_{d0}. The rest of the channel wall is electrically insulating and also has a uniform

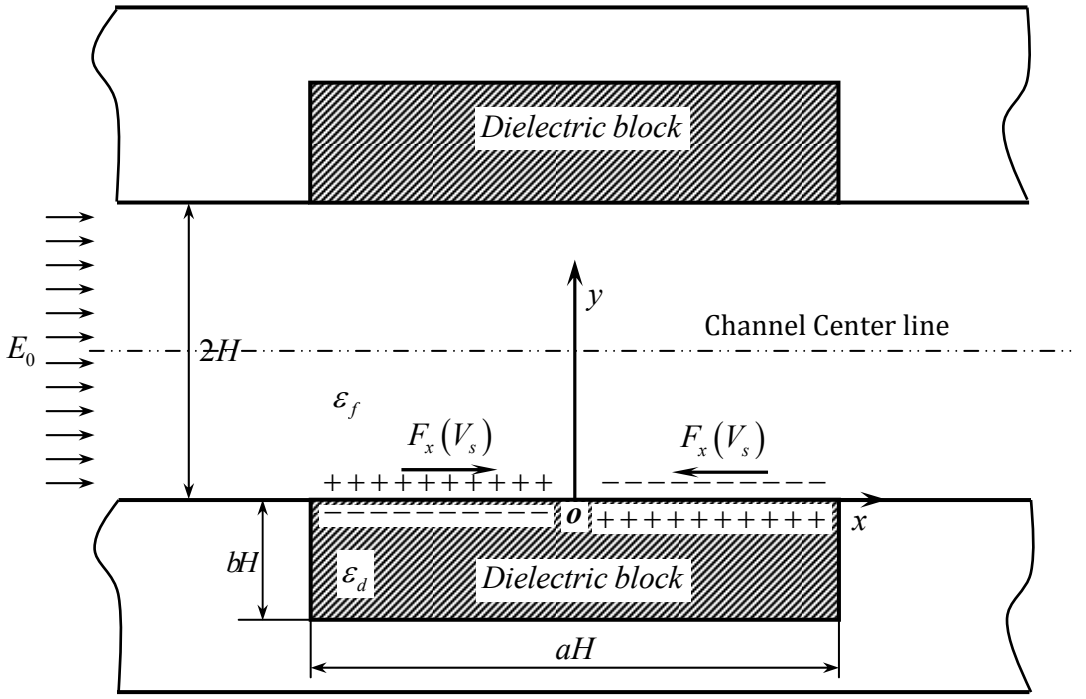

Figure 3.3. Schematic of two symmetric polarizable dielectric blocks embedded in the two walls of an infinitely long insulating slit microchannel. After application of an external electric field E_0, the dielectric block is polarized so that the left-hand side of the object's surface acquires negative surface charges and the right-hand side of its surface acquires positive surface charges. In order to maintain the electrical neutrality in the entire system, the net charge density in the EDL near the left-hand side of the surface should be positive ($\rho_e>0$) and the net charge density in the EDL near the right-hand side of the surface should be negative ($\rho_e<0$). Obviously, the interaction of the external electric field and these two charge densities generates two electric body forces F_x ($=\rho_e E_0$) (with opposite directions inside the EDL), thereby resulting in two Smoluchowski slip velocities V_s (with opposite directions) which are responsible for the flow patterns generated above the dielectric block surface.

natural zeta potential ζ_0. With the thin EDL approximation, the electric field in the fluid domain is one-dimensional, i.e., $\mathbf{E}=E_0\mathbf{e}_x$, which gives a linear profile of the applied electrical potential in the bulk fluid domain, $\Phi_f = -E_0 x + C$ (here C is a constant). Due to symmetry, analyses of both the electric problem and the flow problem in the next section are restricted in the lower half of the channel domain. Hence, to determine the induced zeta potential on the dielectric surface,

we need to know the electrical potential distributions inside the dielectric block. Since there is no free charge inside the dielectric block, the electric potential in the dielectric block domain is governed by the Laplace equation

$$\nabla^2 \Phi_d = 0 \tag{3.14}$$

The appropriate boundary conditions are specified as

$$\Phi_d\big|_{y=0} + \frac{\varepsilon_d}{\varepsilon_f}\lambda_D \left.\frac{\partial \Phi_d}{\partial y}\right|_{y=0} = -E_0 x + \zeta_{d0} \tag{3.15}$$

$$\left.\frac{\partial \Phi_d}{\partial y}\right|_{y=-bH} = 0 \qquad \left.\frac{\partial \Phi_d}{\partial x}\right|_{x=-aH/2} = 0 \qquad \left.\frac{\partial \Phi_d}{\partial x}\right|_{x=aH/2} = 0 \tag{3.16}$$

Defining the following non-dimensional groups:

$$\bar{\Phi}_d = \frac{\Phi_d}{E_0 H} \qquad \bar{\zeta}_{d0} = \frac{\zeta_{d0}}{E_0 H} \qquad \bar{x} = \frac{x}{H} \qquad \bar{y} = \frac{y}{H} \tag{3.17}$$

we can nondimensionalize equation (3.14) and expressed it in the Cartesian coordinate as

$$\frac{\partial^2 \bar{\Phi}_d}{\partial \bar{x}^2} + \frac{\partial^2 \bar{\Phi}_d}{\partial \bar{y}^2} = 0 \tag{3.18}$$

The dimensionless boundary conditions can be rewritten as

$$\bar{\Phi}_d\big|_{\bar{y}=0} + \frac{\varepsilon_d}{\varepsilon_f}\frac{\lambda_D}{H} \left.\frac{\partial \bar{\Phi}_d}{\partial \bar{y}}\right|_{\bar{y}=0} = -\bar{x} + \bar{\zeta}_{d0} \tag{3.19}$$

$$\left.\frac{\partial \bar{\Phi}_d}{\partial \bar{y}}\right|_{\bar{y}=-b} = 0 \qquad \left.\frac{\partial \bar{\Phi}_d}{\partial \bar{x}}\right|_{\bar{x}=-a/2} = 0 \qquad \left.\frac{\partial \bar{\Phi}_d}{\partial \bar{x}}\right|_{\bar{x}=a/2} = 0 \tag{3.20}$$

Without otherwise specification, the other potentials and geometric dimensions are also scaled by E_0H and H, respectively. Using the separation of

variables method, we can show that the electric potential inside the polarizable dielectric block takes the form

$$\overline{\Phi}_d\left(\overline{x},\overline{y}\right)=\overline{\zeta}_{d0}+\sum_{n=1}^{\infty}\left(A_n e^{\mu_n \overline{y}}+B_n e^{-\mu_n \overline{y}}\right)\cos\left[\mu_n\left(\overline{x}+\frac{a}{2}\right)\right] \tag{3.21}$$

where the coefficient A_n and B_n are given by

$$A_n=\frac{2\left[1-(-1)^n\right]}{a\mu_n^2}\frac{e^{2\mu_n b}}{(1-\beta\mu_n)+(1+\beta\mu_n)e^{2\mu_n b}} \tag{3.22}$$

$$B_n=\frac{2\left[1-(-1)^n\right]}{a\mu_n^2}\frac{1}{(1-\beta\mu_n)+(1+\beta\mu_n)e^{2\mu_n b}} \tag{3.23}$$

Here β is a dimensionless parameter defined as

$$\beta=\frac{\varepsilon_d/\varepsilon_f}{H/\lambda_D} \tag{3.24}$$

which physically characterizes the relative importance of the associated electrical properties ($\varepsilon_d/\varepsilon_f$) and the channel size ($H/\lambda_D$). The dimensionless parameter β may also be viewed as a ratio of capacitances: namely, the ratio of the block capacitance ε_d/H to the double-layer capacitance ε_f/λ_D. The physical interpretation is that for an ideally polarizable dielectric $\beta\to\infty$ (i.e. a conductor with infinite capacitance) there is zero potential dropped over the dielectric and hence all potential is dropped over the double layer, giving the maximal induced zeta potential and thus ICEK phenomena. For a dielectric with finite ε_d, then β is finite and hence certain potential is dropped across the dielectrics, thereby reducing the induced zeta potential and hence ICEK phenomena. The eigenvalues μ_n are determined from

$$\mu_n = \frac{n\pi}{a} \qquad n = 1,2,3\cdots \tag{3.25}$$

As mentioned early, the total zeta potential $\overline{\zeta}_d$ on a polarizable dielectric surface can be found as the difference between the potential on the polarizable dielectric surface and the potential at the outer edge of the EDL. Furthermore, the total zeta potential can be decomposed into two parts: (i) $\overline{\zeta}_{d0}$ due to the natural surface charges, and (ii) $\overline{\zeta}_{di}$ due to the induced charges, and thus is given by

$$\overline{\zeta}_d = \overline{\Phi}_d\Big|_{\overline{y}=0} - \overline{\Phi}_f\Big|_{\overline{y}=\lambda_D/H} = \overline{\zeta}_{d0} + \overline{\zeta}_{di} \tag{3.26}$$

where $\overline{\zeta}_{di}$ can be determined with aid of equation (3.21) as

$$\overline{\zeta}_{di} = -\beta \frac{\partial \overline{\Phi}_d}{\partial \overline{y}}\bigg|_{\overline{y}=0} = -\beta \sum_{n=1}^{\infty} \mu_n \left(A_n - B_n\right) \cos\left[\mu_n \left(\overline{x} + \frac{a}{2}\right)\right] \tag{3.27}$$

For completely insulating blocks (i.e., β=0), it can be readily shown from equation (3.27) that the induced zeta potential $\overline{\zeta}_{di}$ is zero, and thus the zeta potential on the electrically insulating block surface contains $\overline{\zeta}_{d0}$ only. This is the case for the classical linear electrokinetic phenomena with natural fixed charges. On the other hand, for perfectly conducting (or polarizable) blocks (i.e., $\beta \to \infty$), it also can be shown that equation (3.27) can be simplified to

$$\overline{\zeta}_{di} = \sum_{n=1}^{\infty} \frac{2\left[(-1)^n - 1\right]}{a\mu_n^2} \cos\left[\mu_n \left(\overline{x} + \frac{a}{2}\right)\right] \tag{3.28}$$

Note that the right-hand side of equation (3.28) in fact is the Fourier series expansion of the function $\overline{x}$. Hence, we can obtain that $\overline{\zeta}_{di} = \overline{x} = -\overline{\Phi}_f$. This result

is exactly the same as the analytical result of Squires and Bazant (2004) for perfectly polarizable surfaces.

3.2.3 FLOW FIELD OF INDUCED-CHARGE ELECTROOSMOSIS IN A SLIT MICROCHANNEL EMBEDDED WITH TWO POLARIZABLE DIELECTRIC BLOCKS

With a DC electric field, E_0 applied along the axial direction of an infinitely long slit microchannel as shown in Figure 3.3, the electrolyte in the microchannel experiences an electrostatic body force $\rho_e E_0$ (i.e., Lorentz force), where ρ_e is the net charge density due to the EDL of the channel. However, as this electrostatic body force is present only within the EDL which is very thin compared to the channel depth, the flow can be considered as triggered by a moving boundary wall. Therefore, the fully-developed flow field for low Reynolds number creeping flows (i.e., $\mathrm{Re} \ll 1$) of an incompressible Newtonian fluid is two-dimensional and is governed by the continuity equation and the Stokes equation (Deen, 1998)

$$\nabla \bullet \mathbf{V} = 0 \tag{3.29}$$

$$-\nabla p + \mu \nabla^2 \mathbf{V} = 0 \tag{3.30}$$

with an implicit slip boundary condition given by the Helmholtz-Smoluchowski equation

$$\mathbf{V} = -\frac{\varepsilon_0 \varepsilon_f \zeta}{\mu} \mathbf{E} \tag{3.31}$$

where $\mathbf{V}$ is the velocity vector expressed as $\mathbf{V} = u\mathbf{e}_x + v\mathbf{e}_y$, $\mathbf{E}$ is the electric field strength vector and it can be expressed as $\mathbf{E} = E_0 \mathbf{e}_x$, p is the hydrodynamic pressure, ζ is the zeta potential of the channel wall, and μ is the dynamic viscosity

of the electrolyte solution. As shown in Figure 3.3, along the channel wall the zeta potential can be modeled by three segments: (i) when $x < -aH/2$ and (ii) when $x > aH/2$, the wall is completely electrically insulating, and has a uniform natural zeta potential of ζ_0. (iii) when $-aH/2 \le x \le aH/2$, the channel wall is a polarizable dielectric surface. Besides the conventional zeta potential ζ_{d0}, there is an extra induced zeta potential ζ_{di} under applied external electric field. It is evident that the zeta potential exhibits step change at two conjunction points: $x = -aH/2$ and $x = aH/2$, which will result in a jump in the Helmholtz-Smoluchowski slip velocity along the microchannel according to equation (3.31).

It can be readily shown that the governing equation equations (3.29) and (3.30) can be transformed into a biharmonic equation in terms of the stream function(Deen, 1998)

$$\nabla^4 \Psi = 0 \tag{3.32}$$

which can be further expressed in Cartesian coordinates as

$$\frac{\partial^4 \Psi}{\partial x^4} + 2\frac{\partial^4 \Psi}{\partial x^2 \partial y^2} + \frac{\partial^4 \Psi}{\partial y^4} = 0 \tag{3.33}$$

The two velocity components can be expressed as two spatial derivatives of the stream function

$$u = \frac{\partial \Psi}{\partial y} \qquad v = -\frac{\partial \Psi}{\partial x} \tag{3.34}$$

Assuming that the flow far away from the polarizable dielectric patch is undisturbed, the magnitude of the velocity is given by the Helmholtz-Smoluchowski velocity expressed by

$$V_\infty = -\frac{\varepsilon_0 \varepsilon_f \zeta_0 E_0}{\mu} \tag{3.35}$$

With aid of equations (3.34) and (3.35), the proper boundary conditions can be prescribed for the stream function as

$$\left.\frac{\partial \Psi}{\partial x}\right|_{y=0} = 0 \qquad |x| < \infty \tag{3.36}$$

$$\left.\frac{\partial \Psi}{\partial y}\right|_{y=0} = \begin{cases} -\dfrac{\varepsilon_0 \varepsilon_f \zeta_0 E_0}{\mu} & x < -\dfrac{aH}{2} \text{ and } x > \dfrac{aH}{2} \\ -\dfrac{\varepsilon_0 \varepsilon_f \zeta_d E_0}{\mu} & -\dfrac{aH}{2} \le x \le \dfrac{aH}{2} \end{cases} \tag{3.37}$$

$$\left.\frac{\partial \Psi}{\partial x}\right|_{y=H} = 0 \qquad \left.\frac{\partial^2 \Psi}{\partial y^2}\right|_{y=H} = 0 \qquad |x| < \infty \tag{3.38}$$

$$\Psi \to V_\infty y \text{ as } |x| \to \infty \tag{3.39}$$

where ζ_d denotes the dimensional total zeta potential on the polarizable dielectric surface and its dimensionless counterpart is $\overline{\zeta}_d$.

Because of linearity, we can decompose the total stream function as

$$\Psi = \Psi_\infty + \Psi_d \tag{3.40}$$

where $\Psi_\infty = V_\infty y$, which is the stream function for the far away flow field. Ψ_d is the stream function due to the disturbance of the polarizable dielectric patch and it also satisfies the biharmonic equation.

Nondimensionalizing all stream functions (Ψ, Ψ_∞ and Ψ_d) with respect to $V_\infty H$, we can rewrite the governing equation for the induced stream function

Ψ_d in dimensionless form $\bar{\Psi}_d$ as

$$\frac{\partial^4 \bar{\Psi}_d}{\partial \bar{x}^4} + 2\frac{\partial^4 \bar{\Psi}_d}{\partial \bar{x}^2 \partial \bar{y}^2} + \frac{\partial^4 \bar{\Psi}_d}{\partial \bar{y}^4} = 0 \tag{3.41}$$

The corresponding boundary conditions can be formulated as

$$\left.\frac{\partial \bar{\Psi}_d}{\partial \bar{x}}\right|_{\bar{y}=0} = 0 \qquad |\bar{x}| < \infty \tag{3.42}$$

$$\left.\frac{\partial \bar{\Psi}_d}{\partial \bar{y}}\right|_{\bar{y}=0} = \begin{cases} 0 & \bar{x} < -\frac{a}{2} \text{ and } \bar{x} > \frac{a}{2} \\ \frac{\bar{\zeta}_d}{\bar{\zeta}_0} - 1 & -\frac{a}{2} \le x \le \frac{a}{2} \end{cases} \tag{3.43}$$

$$\left.\frac{\partial \bar{\Psi}_d}{\partial \bar{x}}\right|_{\bar{y}=1} = 0 \qquad \left.\frac{\partial^2 \bar{\Psi}_d}{\partial \bar{y}^2}\right|_{\bar{y}=1} = 0 \qquad |x| < \infty \tag{3.44}$$

$$\bar{\Psi}_d \to 0 \text{ as } |\bar{x}| \to \infty \tag{3.45}$$

Furthermore, with the Fourier transform (Debnath and Bhatta, 2007)

$$\bar{\Psi}_d^k(k, \bar{y}) = \frac{1}{\sqrt{2\pi}} \int_{-\infty}^{+\infty} \bar{\Psi}_d(\bar{x}, \bar{y}) e^{-ik\bar{x}} d\bar{x} \tag{3.46}$$

the biharmonic equation (3.41) then can be converted into a fourth-order ODE

$$\frac{d^4 \bar{\Psi}_d^k}{d\bar{y}^4} - 2k^2 \frac{d^2 \bar{\Psi}_d^k}{d\bar{y}^2} + k^4 \bar{\Psi}_d^k = 0 \tag{3.47}$$

The boundary conditions are also transformed into the Fourier domain accordingly, and they become

$$\left.\bar{\Psi}_d^k\right|_{\bar{y}=0} = 0 \qquad \left.\frac{d\bar{\Psi}_d^k}{d\bar{y}}\right|_{\bar{y}=0} = Z(k) \tag{3.48}$$

$$\bar{\Psi}_d^k\Big|_{\bar{y}=1} = 0 \qquad \left.\frac{d^2\bar{\Psi}_d^k}{d\bar{y}^2}\right|_{\bar{y}=1} = 0 \tag{3.49}$$

where the auxiliary function $Z(k)$ is defined by

$$Z(k) = \frac{1}{\sqrt{2\pi}} \int_{-\frac{a}{2}}^{+\frac{a}{2}} \left(\frac{\bar{\zeta}_d}{\bar{\zeta}_0} - 1 \right) e^{-ik\bar{x}} dx \tag{3.50}$$

Substitution of equations (3.26) and (3.27) into equation (3.50) gives an explicit expression for Z(k)

$$Z(k) = -\frac{1}{\sqrt{2\pi}} \frac{\beta}{\bar{\zeta}_0} \sum_{n=1}^{\infty} \mu_n (A_n - B_n) \frac{ik\left[-e^{\frac{iak}{2}} + (-1)^n e^{-\frac{iak}{2}} \right]}{k^2 - \mu_n^2} + \frac{1}{\sqrt{2\pi}} \frac{\bar{\zeta}_{d0} - \bar{\zeta}_0}{\bar{\zeta}_0} \frac{2\sin\left(\frac{ak}{2}\right)}{k} \tag{3.51}$$

The solution of the stream function in the k domain is

$$\bar{\Psi}_d^k(k, \bar{y}) = C_1(k)\sinh(k\bar{y}) + C_2(k)\,\bar{y}\cosh\left[k(\bar{y} - 1)\right] \tag{3.52}$$

where two coefficients are determined by

$$C_1(k) = \frac{-2}{\sinh(2k) - 2k} Z(k) \tag{3.53}$$

$$C_2(k) = \frac{2\sinh(k)}{\sinh(2k) - 2k} Z(k) \tag{3.54}$$

Finally, the induced stream function can be obtained by using the inverse Fourier transform

$$\bar{\Psi}_d(\bar{x}, \bar{y}) = \frac{1}{\sqrt{2\pi}} \int_{-\infty}^{+\infty} \bar{\Psi}_d^k(k, \bar{y}) e^{ik\bar{x}} dk \tag{3.55}$$

and the total stream function is constructed through equation (3.40)

$$\bar{\Psi}\left(\bar{x},\bar{y}\right)=\bar{y}+\frac{1}{\sqrt{2\pi}}\int_{-\infty}^{+\infty}\bar{\Psi}_d^k\left(k,\bar{y}\right)e^{ik\bar{x}}dk \tag{3.56}$$

Likewise, the dimensionless velocity field is obtained by substituting equation (3.56) into equation (3.34)

$$\bar{u}\left(\bar{x},\bar{y}\right)=1+\frac{1}{\sqrt{2\pi}}\int_{-\infty}^{+\infty}\frac{d\bar{\Psi}_d^k\left(k,\bar{y}\right)}{dy}e^{ik\bar{x}}dk \tag{3.57}$$

$$\bar{v}\left(\bar{x},\bar{y}\right)=-\frac{1}{\sqrt{2\pi}}\int_{-\infty}^{+\infty}\left(ik\right)\bar{\Psi}_d^k\left(k,\bar{y}\right)e^{ik\bar{x}}dk \tag{3.58}$$

where $\bar{u}=u/V_\infty$ and $\bar{v}=v/V_\infty$.

The remaining task is to evaluate the integrations with respect to k. To obtain analytical solutions for the integrations in equations (3.56), (3.57) and (3.58), the residue theorem (Jeffrey, 2006) is invoked, where the infinite integral of an analytic function can be converted to an summation of residues at all singularity points of this function. One can readily show that integrands in equations (3.56), (3.57) and (3.58) are analytic functions. Then we can respectively show that the solutions for the dimensionless stream function, the horizontal velocity component and the vertical velocity component are

$$\bar{\Psi}\left(\bar{x},\bar{y}\right)=\bar{y}+\left(-1\right)^c\sqrt{2\pi}i\sum_{m=1}^{\infty}\frac{Z\left(k_m\right)e^{ik_m\bar{x}}}{\cosh\left(2k_m\right)-1}\left\{-\sinh\left(k_m\bar{y}\right)+\sinh\left(k_m\right)\bar{y}\cosh\left[k_m\left(\bar{y}-1\right)\right]\right\} \tag{3.59}$$

$$\bar{u}\left(\bar{x},\bar{y}\right)=1+\left(-1\right)^c\sqrt{2\pi}i\sum_{m=1}^{\infty}\frac{Z\left(k_m\right)e^{ik_m\bar{x}}}{cosh\left(2k_m\right)-1}\left\{-\cosh\left(k_m\bar{y}\right)k_m+\sinh\left(k_m\right)\cosh\left[k_m\left(\bar{y}-1\right)\right]+k_m\sinh\left(k_m\right)\bar{y}\sinh\left[k_m\left(\bar{y}-1\right)\right]\right\} \tag{3.60}$$

$$\bar{v}\left(\bar{x},\bar{y}\right)=\left(-1\right)^{c}\sqrt{2\pi}\sum_{m=1}^{\infty}\frac{Z\left(k_m\right)k_m e^{ik_m\bar{x}}}{\cosh\left(2k_m\right)-1}\left\{-\sinh\left(k_m\bar{y}\right)+\sinh\left(k_m\right)\bar{y}\cosh\left[k_m\left(\bar{y}-1\right)\right]\right\}$$

(3.61)

where k_{m} is the complex root of the eigenfunction $\sinh\left(2k_m\right)-2k_m=0$. When $\bar{x}>0$, c=0 and the summation is taken for all k_m with positive imaginary part; when $\bar{x}<0$, c=1 and the summation is carried out for all k_m with negative imaginary part. Table 3.1 provides the first five complex roots of the above eigenfunction computed using Mathematica 6.0 with high accuracy of 10^{-10}. Moreover, as $\bar{x}\to 0$ from both domains (i.e., $\bar{x}>0$ and $\bar{x}<0$), we can check that an identical value is obtained, which ensures that the present analytical solutions are continuous at $\bar{x}=0$. In the calculation, we used 1000 terms to evaluate all the above infinite series solutions with an accuracy of 10^{-8}.

Table 3.1 First five eigenvalues determined form the eigenfunction, $\sinh\left(2\mathbf{k_m}\right)-2\mathbf{k_m}=0$

m	k_m
1	±1.3843391414+3.7488381388i
2	±1.6761049424+6.9499798569i
3	±1.8583838398+10.1192588539i
4	±1.9915708201+13.2772736327i
5	±2.0966257352+16.4298705025i

Note: the complex conjugates of k_m are another half of eigenvalues

3.2.4 RESULTS AND DISCUSSION

In this section, a special case study is presented to show the basic flow patterns of ICEO flow above the polarizable block embedded in the channel wall. Then by using the analytical solutions, parametric studies are carried out to

examine the effects of the dielectric constant of the polarizable dielectric block and the natural zeta potential of the electrically insulating part of the channel wall on flow patterns of ICEO flows. In all calculations, the polarizable dielectric blocks are assumed to have fixed dimensionless dimensions of a=5 and b=5. Moreover, since the focus of this study is placed on the induced charge effects, the effect of the natural surface charges on the polarizable dielectric block surface is excluded by assuming $\overline{\zeta}_{d0} = 0$.

3.2.4.1 BASIC FLOW PATTERNS OF ICEO FLOWS

To our best knowledge, no analytical solutions of ICEO flows are available in this geometry in the literature. Hence a specific case study is conducted to present the basic flow patterns of ICEO flows above the polarizable dielectric block. In this special case, we consider a limiting case of $\beta \to \infty$ when the polarizable dielectric block is a perfect conductor and thus has greatest polarizability. The dimensionless natural zeta potential on both upstream and downstream of the insulating microchannel $\overline{\zeta}_0$ is set as -0.1, which may represent a practical situation where E_0 =100 V/cm, H= 50 μm and ζ_0 =-50 mV.

The calculated results are shown in Figure 3.4 which includes the horizontal velocity component $\overline{u}$, the vertical velocity comment $\overline{v}$ and the velocity vector field. It is seen from Figure 3.4 (a) that the fluid near the channel wall moves to the block center (i.e., $\overline{x} = 0$ and $\overline{y}$=0) with large velocity from two sides; however the velocity decreases as approaching to the block centerline (i.e., $\overline{x} = 0$). Near the block centerline, the flow changes its direction with flow moving towards the block centerline near the channel wall region (i.e., $\overline{y}$=0) and flow leaving away

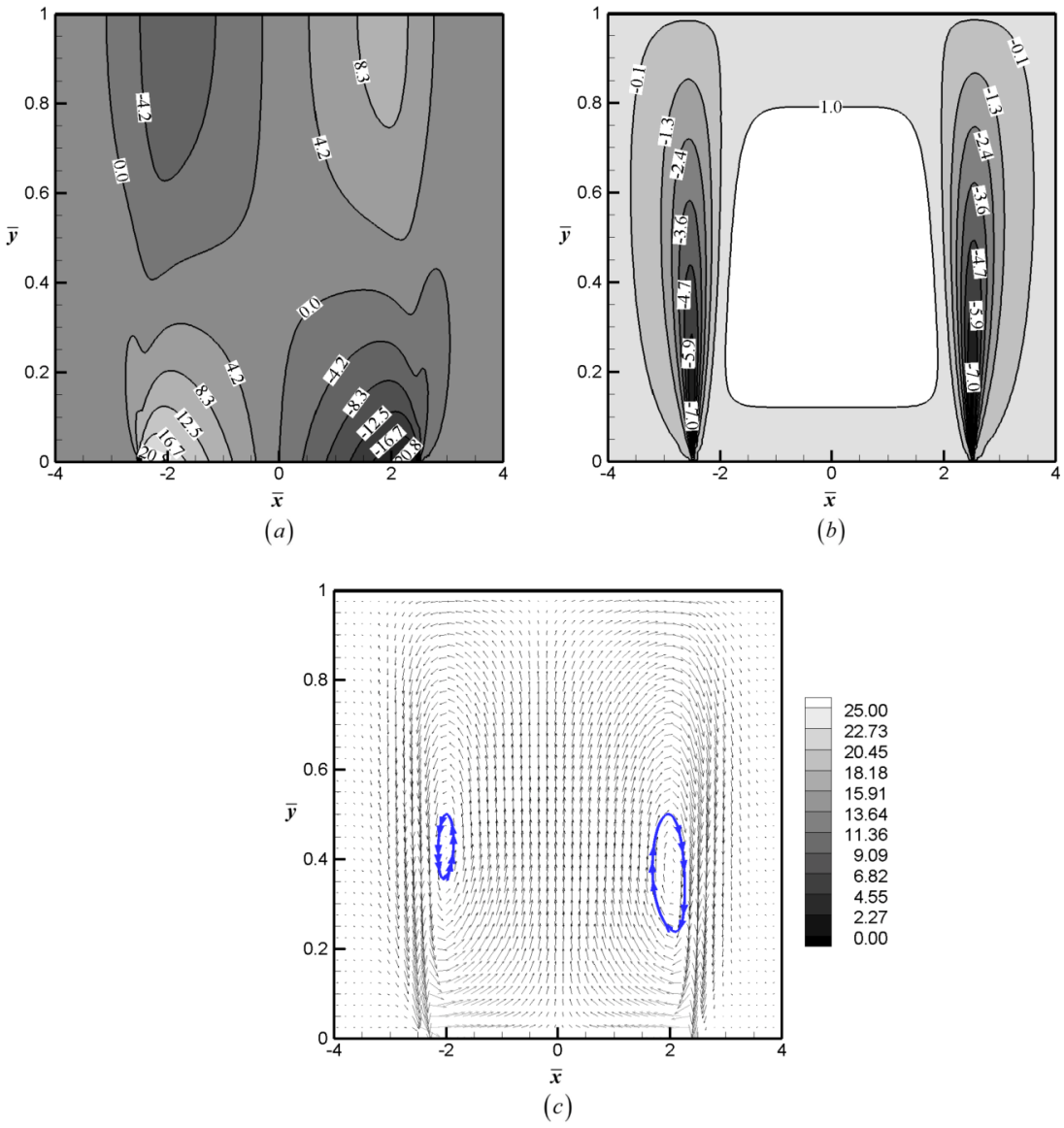

Figure 3.4 Analytical solutions derived in the present study for (a) horizontal component of velocity $\bar{u}$, (b) vertical component of velocity $\bar{v}$ and (c) velocity vector field. Calculations are conducted for the ICEO flow above a perfectly polarizable ($\beta \to \infty$) block with a=5, b=5, and the dimensionless natural zeta potential for the perfectly polarizable block $\bar{\zeta}_{d0}$ =0, and the insulating wall $\bar{\zeta}_0$ = -0.1.

from the block centerline in the channel center line region (i.e., $\bar{y} = 1$). As shown in Figure 3.3, on the left side of the block surface (i.e., $\bar{x} < 0$), the external electric field induces negative surface charges (also negative induced zeta potential); while on the right side of the block (i.e., $\bar{x} > 0$), the positive surface charges (also positive induce zeta potential) are induced. Accordingly the resultant slip

velocity is positive on the left side and is negative on the right side of the block based on the expression of the Smoluchowski velocity given by equation (3.35). In addition, on the block surface, the magnitude of the horizontal velocity component can reach twenty times larger than that of the insulating channels regions. This is attributed to the fact that the Helmholtz-Smoluchowski slip velocity on conducting surfaces is proportional to E_0^2 (Bazant and Squires, 2004), whiles the Smoluchowski slip velocity driven by natural charges is just proportional to E_0. Since the flow rate is determined by the natural charge driven electroosmotic flow in the regions of insulating channel, in order to fulfill the mass conservation there must be velocity reversal on both sides of the channel centerline (i.e., $\bar{y}$=1). For a sufficiently large natural zeta potential on the insulating wall, the ICEO flow over the polarizable blocks may not dominate the electroosmotic flow over the insulating walls; i.e. it is only because the natural zeta is not too large that the dominance of ICEO is observed. From the vertical velocity distributions shown in Figure 3.4 (b), it is noted that the fluid in a large portion around the block centerline region moves upwards to the channel centerline at a velocity comparable to the incoming flow from infinity ($\bar{x} \to \pm\infty$). Above the two edges of the polarizable block, the fluid flows down very fast to the polarizable surface. All these features are resulted from the fact that there should be no net flow along y direction. Figure 3.4 (c) shows the analytical solution computed using equations (3.60) and (3.61), which gives high resolution of the velocity vector field. It is shown that there is a pair of counter-rotating vortices above the polarizable surface. The generation of a vortices pair

on a planar polarizable surface due to induced-charge electrokinetics was also conceptualized in the work by Soni et al. (2007).

3.2.4.2 PARAMETRIC STUDY OF ICEO FLOW PATTERNS

Figure 3.5 shows the effect of β on the flow patterns over the bottom polarizable dielectric block. The normalized stream function has a value of zero on the channel walls and unit one at the channel centerline. The difference of the stream function between two locations in the flow field represents the steady-state volumetric flow rate passing through the cross-section line determined by theses two locations. Since there exists a uniform velocity profile at both upstream and downstream of the channel, the stream function should be linearly proportional to y and the stream lines are exactly in parallel with x axis in the two insulating regions of the channel. Showing in Figure 3.5(a) corresponds to the case of β=0, indicating that the block is not polarizable. Furthermore, with the assumption of no natural surface charges on the block surface, $\zeta_{d0} = 0$, no driving force is present for the fluid over the block. Hence, no slip boundary condition on the block surface causes velocity profile to exhibit a parabolic shape and the stream function depends on y^3, which explains the stream line distributions above the dielectric surface shown in Figure 3.5(a). As β increases, the dielectric block becomes more polarizable. Then, a small clockwise vortex is formed above the right portion of the polarizable dielectric surface as shown in Figure 3.5 (b). With such magnitude of β, the induced zeta potential on the left portion of the block is of the same order and also the same sign as the natural zeta potential on the insulating channel wall. The resultant two Helmholtz-

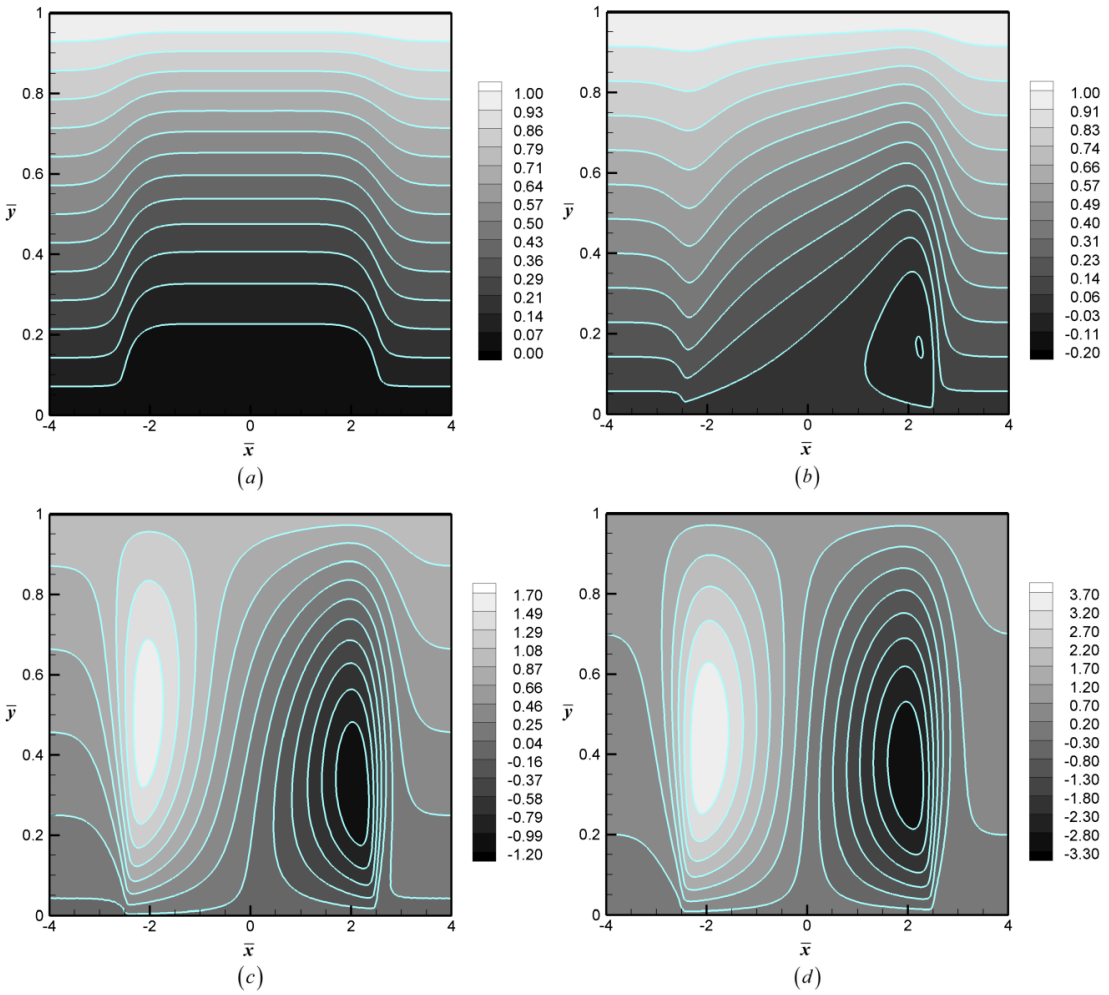

Figure 3.5 Dimensionless stream function $\bar{\Psi}$ contour above a polarizable dielectric block for four different β values, (a) β=0, (b) β=0.1, (c) β=1 and (d) β→∞. Other parameters in the calculations are a=5, b=5 and the dimensionless natural zeta potential for the perfectly polarizable block $\bar{\zeta}_{d0}$ = 0 , and the insulating wall $\bar{\zeta}_0$ =-0.1.

Smoluchowski slip velocities on the left portion of the polarizable surface and the upstream insulating surfaces are of similar magnitude and also in the same direction. Hence, the flow speeds up near the polarizable dielectric block and slows down near the channel centerline to fulfill the mass conservation of fluid, but no circulating flow is developed on the left portion of the block. However, on the right portion of the polarizable dielectric surface, non-zero value of β always produces a negative slip velocity (in opposite to the main flow stream), thereby

giving rise to the development of a vortex. As shown in Figure 3.5 (c), further increasing β causes the dielectric surface to be more polarizable, and consequently induces a larger zeta potential on the left surface which in turns produces a larger slip velocity (compared to the slip velocity from the infinitely far upstream flow in the insulating channel region). The large difference in these two slip velocities makes the flow reversal occur over the left portion of the block. As a result, a pair of two counter-vortexes is formed. In the limiting case of $\beta \to \infty$ as shown in Figure 3.5 (d), the induced zeta potential on the perfectly conductive surface is the highest, and so is the Helmholtz-Smoluchowski velocity, resulting in the strongest pair of two counter-rotating vortices. At this situation, the liquid transportation in the vortices is several times faster than that in the insulating channel regions. This can be reflected from the values of stream function in the two vortex centers, which are 3.70 and -3.30, respectively.

Figure 3.6 shows the effect of the dimensionless natural zeta potential of the insulating microchannel walls on the flow patterns above a perfectly conductive block. For the case of $\overline{\zeta}_0$ = -0.3 shown in Figure 3.6 (a), a pair of counter-rotating vortices are formed due to a large difference between the induced zeta potential on the block surface and the natural zeta potential on insulating channel walls. With the increase of natural zeta potential (as indicated in Figure 3.6 (b)), the vortex above the left side of the polarizable surface is gradually distorted, even disappears as shown in Figure 3.6 (c). In these two cases, the velocity of the incoming flow from upstream has almost the same order of magnitude as the induced slip velocity on the left-side of the polarizable surface. Thus, similar to

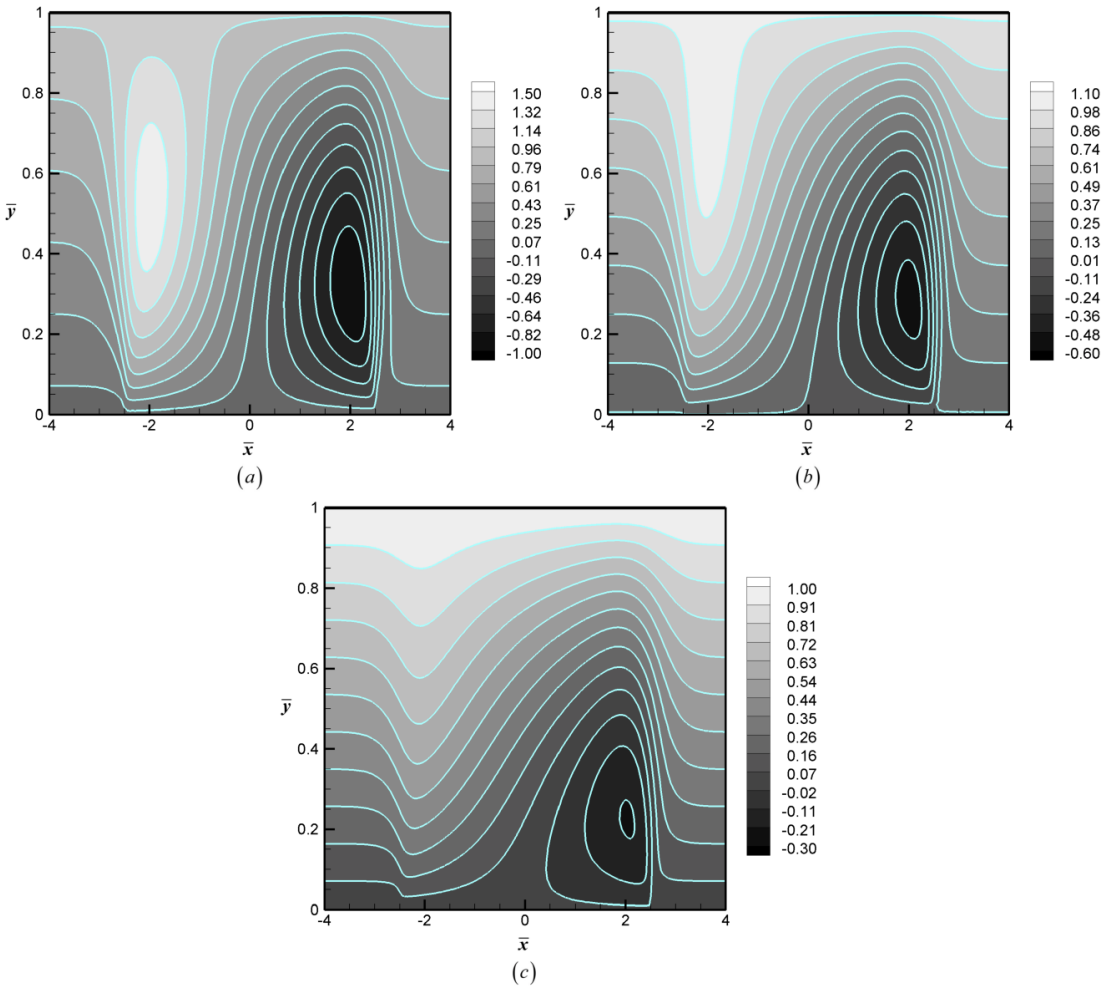

Figure 3.6 Dimensionless stream function $\bar{\Psi}$ contour above a perfectly polarizable block ($\beta \to \infty$) for three different $\bar{\zeta}_0$ values, (a) $\bar{\zeta}_0$ =-0.3, (b) $\bar{\zeta}_0$ =-0.5 and (c) $\bar{\zeta}_0$ =-1.0. Other parameters in the calculations are a=5, b=5, and the dimensionless natural zeta potential for the insulating wall $\bar{\zeta}_0$ = -0.1 .

the cases of Figure 3.5 (a) and Figure 3.5 (b), the flow reversal near the block centerline does not happen. However, on the right-side of the polarizable surface, there always exists a negative induced Smoluchowski velocity which counteracts with the incoming flow from upstream of the channel. Thus a vortex is present to fulfill the mass conservation. It is expected that the vortex on the right side of the block surface can disappear only when $\bar{\zeta}_0 \to -\infty$.

It should be noted that generation of this kind of microvortices is very useful. For example, the presence of vortical flow structure can enhance micromixing - which is always a challenging task because mixing in low Reynolds flows is intrinsically poor. Additionally, pumping and/or separating bioparticles are also other potential applications (Green, 2005; Lee et al., 2007; Takhistov et al., 2003).

3.3 AC FIELD DRIVEN INDUCED-CHARGE ELECTROKINETICS OVER LEAKY-DIELECTRIC SURFACES: EFFECTIVE BOUNDARY CONDITIONS AND THEIR APPLICATIONS

3.3.1 EFFECTIVE ELECTRIC BOUNDARY CONDITIONS

It is known that there is usually a SCL (i.e., an "EDL" in the solid) in the leaky-dielectric solid adjacent to the EDL in the liquid electrolyte (Bardeen, 1947; Bockris and Reddy, 2004; Bockris et al., 2002; King and Freund, 1984). The thicknesses of EDL and SCL have the same order of magnitude and typically range from 1nm to 100nm, and thus both of them need to be considered simultaneously. Then we need to model the transport (by diffusion and migration) of both types of charge carriers (i.e., electrons and holes) in the solid as what we usually do for both cations and anions in the liquid. We restrict our analysis under the following three assumptions (i) thin EDL and SCL, (ii) negligible Peclet number and (iii) small induced electric field (i.e. $\Psi = \mathrm{ze}\Phi_0 / \left(k_B \mathrm{T}\right) \ll 1$, wherein z denotes the valence of charge carriers inside the electrolyte solution, e the elemental charge, k_B the Boltzmann constant and T the absolute temperature). These assumptions were also made in previous studies (Squires and Bazant, 2004; Swaminathan and Hu, 2009; Yossifon et al., 2009).

The thin EDL and SCL assumption requires that the EDL thickness and the SCL thickness are much smaller than the characteristic dimension of the leaky-dielectric solid wall, a, that is $\delta_1 = \lambda_{D1}/a \ll 1$, $\delta_2 = \lambda_{D2}/a \ll 1$. The EDL thickness for a symmetric electrolyte (z:z) can be defined as $\lambda_{D1} = \sqrt{\varepsilon_0 \varepsilon_f k_B T / \left(2 n_{01} z^2 e^2\right)}$, and the SCL thickness is similarly defined as $\lambda_{D2} = \sqrt{\varepsilon_0 \varepsilon_w k_B T / \left(2 n_{02} e^2\right)}$, where n_{0i} denotes the bulk concentration of charge carriers inside the liquid and solid domains (i=1 for the electrolytic solution and i=2 for the leaky-dielectric solid, this convention is complied with in the whole work), ε_0 is the electric permittivity of vacuum. ε_f and ε_w are the dielectric constants of the electrolyte and the leaky-dielectric solid, respectively.

From a microfluidic application viewpoint, the aforementioned three assumptions are valid. Therefore, in the model development, the hydrodynamic problem and the electrostatic problem can be decoupled (Squires and Bazant, 2004; Swaminathan and Hu, 2009; Yossifon et al., 2009; Zhao and Yang, 2011a). Furthermore, as shown in Figure 3.7, the electrostatic problem can be divided into four sub-domains: the two domains for the electroneutral bulk solid wall and bulk electrolyte solution with their harmonic dimensionless electric potentials Φ_w and Φ_f, respectively, and the two 'inner' domains of the charged EDL and the SCL whose dimensionless electric potentials, Φ_{EDL} and Φ_{SCL}, should satisfy Poisson's equation. Note that all these dimensionless potentials are scaled with respect to the reference potential Φ_0. To obtain the effective electrokinetic conditions connecting Φ_w and Φ_f on the leaky-dielectric solid–electrolyte interface, the focus is placed on the inner domains which (for $\delta_1 << 1$ and $\delta_2 <<$

1) can be seen locally one-dimensional in the direction of the y' axis perpendicular to the solid surface. Then, the corresponding 'outer' (y) and 'inner' (Y_1, Y_2) dimensionless spatial variables can be defined as $y' = ay = \lambda_{D1} Y_1 = \lambda_{D2} Y_2$.

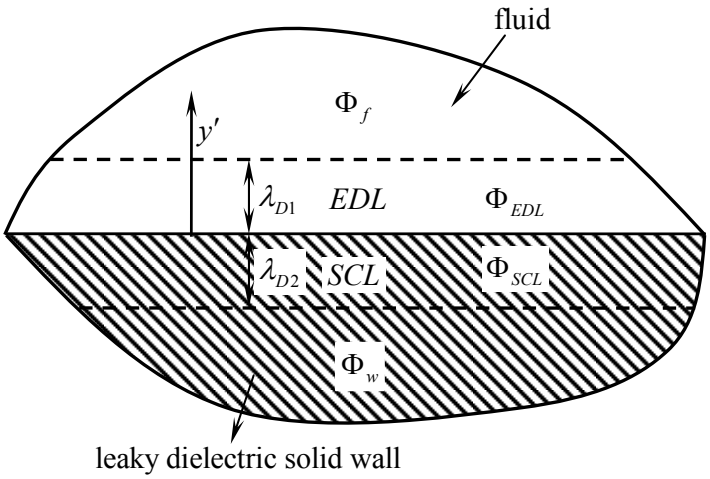

Figure 3.7 A schematic representation of the electrostatic problem in four sub-domains, namely, (i) the bulk electrolyte fluid domain Φ_f, (ii) the bulk leaky dielectric solid wall domain Φ_w, (iii) the EDL domain Φ_{EDL} inside the liquid and (iv) the SCL domain Φ_{SCL} inside the solid. The dash lines inside the electrolyte fluid and solid wall respectively represent the outer edges of the EDL and SCL where Φ_{EDL} matches Φ_f and Φ_{SCL} matches Φ_w. λ_{D1} and λ_{D2}denote the thicknesses of EDL and SCL, respectively.

In our analysis, the dimensionless net charge densities inside the liquid and solid domains due to the difference between the concentration of positive charge carriers and that of negative charge carriers, i.e., $n_p - n_n$, is expressed as $\rho_i = \left(n_{pi} - n_{ni}\right) / \left(2\Psi n_{0i}\right)$. To the leading order (in the limit of small δ_1, δ_2 and Ψ), Φ_{EDL} and Φ_{SCL} respectively satisfy Poisson's equations

$$\frac{\partial^2 \Phi_{EDL}}{\partial Y_1^2} = -\rho_1 \quad \text{and} \quad \frac{\partial^2 \Phi_{SCL}}{\partial Y_2^2} = -z\rho_2 \tag{3.62}$$

and the continuity equations for electric current (that is obtained from the Nernst–Planck equations for positive and negative carriers in both fluid and solid domains)

$$\frac{\partial \rho_1}{\partial \tau} = \frac{\partial^2 \rho_1}{\partial Y_1^2} - \rho_1 \quad \text{and} \quad \frac{t_w}{t_f}\frac{\partial \rho_2}{\partial \tau} = \frac{\partial^2 \rho_2}{\partial Y_2^2} - \rho_2 \tag{3.63}$$

where τ is the dimensionless time normalized with the reference time $t_f = \lambda_{D1}^2 / D_f$ and in equation (3.63), $t_w = \lambda_{D2}^2 / D_w$ (where D_f stands for the mass diffusivity for free charge carriers in liquid, and for a dilute symmetric binary electrolyte it is usually assumed that positive and negative free charge carriers have the same diffusivity, namely $D_{p1} = D_{n1} = D_f$. In the solid wall we also assume that both charge carriers have the save diffusivities, i.e., $D_{p2} = D_{n2} = D_w$). Such reference time t_f also can be expressed as $t_f = \varepsilon_0 \varepsilon_f / \sigma_f = 1/\omega_D$, which denotes the charge relaxation time in the electrolytic solution, and also can be viewed as the time that ions take to travel a Debye length by diffusion. ω_D is the Debye frequency of the electrolytic solution (Ajdari, 2000), and σ_f is the bulk electric conductivity of the electrolytic solution and can be formulated as $\sigma_f = 2n_{0I} z^2 e^2 D_f / (k_B T)$. Similarly, the charge relaxation time t_w inside the leaky-dielectric solid wall has the same physical interpretation as t_f.

On the solid surface, Φ_{EDL} and Φ_{SCL} satisfy the electrostatic boundary conditions (Paris and Hurd, 1969)

$$\Phi_{EDL} = \Phi_{SCL} \quad \text{and} \quad \frac{\partial \Phi_{EDL}}{\partial Y_1} - \beta \frac{\partial \Phi_{SCL}}{\partial Y_2} = -q \quad \text{at } Y_1 \text{ or } Y_2 = 0 \tag{3.64}$$

which respectively describe the continuity of the electric potential and the discontinuity of the electric displacement due to the presence of free charges at the interface between two different media. In equation (3.64), $\beta = (\varepsilon_w \lambda_{D1})/(\varepsilon_f \lambda_{D2})$ and q is the dimensionless free surface charge density which is scaled by $\varepsilon_0 \varepsilon_f \Phi_0 / \lambda_{D1}$.

Under the widely adopted assumptions - the solid surface is totally blocking and there is no Faradaic reaction on the leaky-dielectric surface, namely no charge carrier fluxes are allowed to penetrate through the solid wall. The vanishing of normal components of the positive carriers flux and the negative carrier flux inside both domains leads to the boundary conditions for ρ_1 and ρ_2 respectively as

$$\frac{\partial \rho_1}{\partial Y_1} = -\frac{\partial \Phi_{EDL}}{\partial Y_1} \text{ at } Y_1=0 \tag{3.65}$$

$$z\frac{\partial \rho_2}{\partial Y_2} = -\frac{\partial \Phi_{SCL}}{\partial Y_2} \text{ at } Y_2=0 \tag{3.66}$$

At the outer edges of the EDL and the SCL, we have the following asymptotic matching conditions

$$\Phi_{EDL}\big|_{Y_1\to\infty} = \Phi_f\big|_{y\to 0} \quad \text{and} \quad \Phi_{SCL}\big|_{Y_2\to -\infty} = \Phi_w\big|_{y\to 0} \tag{3.67}$$

and the following electroneutrality conditions

$$\rho_1 \to 0 \text{ as } Y_1 \to \infty \tag{3.68}$$

$$\rho_2 \to 0 \text{ as } Y_2 \to -\infty \tag{3.69}$$

We consider time periodic electrokinetic phenomena under an externally applied AC electric field with arbitrary wave forms, e.g., triangle, rectangle, and sinusoid etc. It is assumed that the AC electric field and its first-order time derivative are continuous over the period T_0. As such, its value at $\tau = \tau + kT_0$ is identical for any integer *k*. In addition, a general periodic field quantity, X , can be expressed as a form in complex Fourier series, $X(\tau) = \sum_{k=-\infty}^{+\infty} X^{(k)} \exp(jk\Omega\tau)$, where $j = \sqrt{-1}$, Ω is the normalized frequency with respect to the Debye frequency ω_D of electrolyte solution and it can be determined from $\Omega = 2\pi / T_0$. Here, $X^{(k)} = \left[\int X(\tau) \exp(-jk\Omega\tau) d\tau \right] / T_0$ represents the complex amplitude of the AC electric field, and $X^{(-k)}$ is its corresponding complex conjugate**.** Therefore, the sum of aforementioned complex Fourier series always gives rise to a real function.

Due to its linearity, the present problem can be obtained as a superposition of an induced part satisfying the homogenous version of equation (3.64) and an equilibrium part solely contributed by the natural surface charge density *q*. We focus on the induced part of the problem. Similar Fourier decompositions are then assumed for the electric potentials (Φ_{EDL}, Φ_{SCL}, Φ_w and Φ_f) and the net charge densities ρ_i (i=1,2) in terms of their corresponding complex amplitudes $\Phi_{EDL}^{(k)}$, $\Phi_{SCL}^{(k)}$, $\Phi_w^{(k)}$, $\Phi_f^{(k)}$ and $\rho_i^{(k)}$. Note that the component k=0 corresponds to a steady DC electric forcing. The solutions of transformed problems resulting from equation (3.63) together with the boundary conditions given by equations (3.65) and (3.66) give the complex amplitudes for net charge densities $\rho_i^{(k)}$. By

substitution of these two results into the right-hand side of transformed equation (3.62), one can obtain two equations that respectively govern potentials in the two inner domains, and the solutions to these equations would be

$$\Phi_{EDL}^{(k)} = \left.\frac{d\Phi_{EDL}^{(k)}}{dY_1}\right|_{Y_1=0}\left[\left(1-\frac{1}{\gamma_1^2}\right)Y_1 - \frac{1}{\gamma_1^3}e^{-\gamma_1 Y_1}\right] + A_1 \tag{3.70}$$

$$\Phi_{SCL}^{(k)} = z\left.\frac{d\Phi_{SCL}^{(k)}}{dY_2}\right|_{Y_2=0}\left[\left(1-\frac{1}{\gamma_2^2}\right)Y_2 + \frac{1}{\gamma_2^3}e^{\gamma_2 Y_2}\right] + A_2 \tag{3.71}$$

with $\gamma_1^2 = 1 + jk\Omega$ and $\gamma_2^2 = 1 + t_w jk\Omega / t_f$. At the outer edges of the two inner regions, i.e., $Y_1 \to \infty$ and $Y_2 \to -\infty$, the solutions given by equations (3.70) and (3.71) are to be matched with the solutions outside the EDL and SCL to determine the unknown coefficients. Hence we have

$$\Phi_f^{(k)} = A_1 \text{ and } \frac{d\Phi_f^{(k)}}{dy} = \frac{1}{\delta_1}\left.\frac{d\Phi_{EDL}^{(k)}}{dY_1}\right|_{Y_1=0}\left(1-\frac{1}{\gamma_1^2}\right) \text{ as } y \to 0 \tag{3.72}$$

$$\Phi_w^{(k)} = A_2 \text{ and } \frac{d\Phi_w^{(k)}}{dy} = \frac{z}{\delta_2}\left.\frac{d\Phi_{SCL}^{(K)}}{dY_2}\right|_{Y_2=0}\left(1-\frac{1}{\gamma_2^2}\right) \text{ as } y \to 0 \tag{3.73}$$

The coefficient of the exponential term on the right-hand side of equation (3.70) can be viewed as the complex amplitude for the effective induced zeta potential that is the potential drop across the EDL, i.e.

$$\zeta_i^{(k)} = -\left(d\Phi_{EDL}^{(k)} / dY_1\Big|_{Y_1=0}\right) / \gamma_1^3 = -\delta_1\left(d\Phi_f^{(k)} / dy\Big|_{y=0}\right) / \left[\gamma_1\left(\gamma_1^2 - 1\right)\right] \tag{3.74}$$

Utilizing equations (3.72) and (3.73), one can eliminate A_1, A_2, $d\Phi_{EDL}^{(k)} / dY_1\big|_{Y_1=0}$

and $d\Phi_{SCL}^{(k)}/dY_2\big|_{Y_2=0}$ from the transformed boundary conditions equation (3.64) to obtain the following two equations

$$\Phi_f^{(k)} - \Phi_w^{(k)} = \frac{d\Phi_f^{(k)}}{dy}\frac{\delta_1}{\gamma_1\left(\gamma_1^2 - 1\right)} + \frac{d\Phi_w^{(k)}}{dy}\frac{\delta_2}{\gamma_2\left(\gamma_2^2 - 1\right)} \text{ at y=0} \tag{3.75}$$

$$\delta_1 \frac{\gamma_1^2}{\left(\gamma_1^2 - 1\right)}\frac{d\Phi_f^{(k)}}{dy} - \beta\delta_2 \frac{\gamma_2^2}{\left(\gamma_2^2 - 1\right)}\frac{d\Phi_w^{(k)}}{dy} = 0 \text{ at y=0} \tag{3.76}$$

Equations (3.75) and (3.76) are the effective electrokinetic boundary conditions that directly connect the complex amplitudes of two bulk potentials ($\Phi_w^{(k)}$ and $\Phi_f^{(k)}$) across a leaky-dielectric solid-electrolyte interface. These derived electrokinetic boundary conditions are of practical significance for evaluating induced zeta potentials over leaky-dielectric surface. They are applicable to the AC field driven induced-charge electrokinetics over solids of any dielectric constants and conductivities under an electric field with arbitrary wave forms. For all finite values of β and t_w/t_f, the solution of the electrostatic problem requires the simultaneous determination of two bulk harmonic potentials (governed by Laplace's equation), $\Phi_f^{(k)}(\mathbf{r})$ and $\Phi_w^{(k)}(\mathbf{r})$ (where $\mathbf{r}$ is the position vector), which satisfy the boundary conditions (3.75) and (3.76) on the surface of leaky-dielectric solids as well as the far-field conditions for $\Phi_f^{(k)}(\mathbf{r})$.

For conventional electrokinetic phenomena, solid walls are considered as perfect insulators, suggesting that both β and t_f/t_w are equal to zero. Then it can be obtained from equations (3.75) and (3.76) that there is no induced zeta potential (since in this case there is no electric field inside the solid, and

$\Phi_f^{(k)} - \Phi_w^{(k)}$ is the effective induced zeta potential drop across the EDL), and the bulk electrostatic potential inside the liquid domain satisfies the homogeneous Neumann condition, i.e., the electrically insulating condition ($d\Phi_f^{(k)} / dy = 0$).

For ideal dielectric objects under a DC electric field, the conductivity of the solids is zero ($t_f / t_w = 0$). Then there is no SCL effect inside the solid and the frequency of external electric field is zero ($\Omega = 0$). Hence equations (3.75) and (3.76) can reduce to

$$\Phi_w^{(k)} + \frac{\varepsilon_w \lambda_{D_1}}{\varepsilon_f a} \frac{d\Phi_w^{(k)}}{dy} = \Phi_f^{(k)} \text{ at } y=0 \tag{3.77}$$

$$\frac{d\Phi_f^{(k)}}{dy} = 0 \text{ at } y=0 \tag{3.78}$$

which shows the Robin-type and Neumann-type boundary conditions of the steady electrostatic problems for the solid wall and the bulk liquid, respectively. The detailed derivation of equations (3.77)and (3.78) was provided in the work by Yossifon et al. (2007) and Zhao and Yang (2009) [see their equations (2) and (9)].

To gain further physical insights into the two boundary conditions given in equations (3.75) and (3.76), we substitute equation (3.74) into equation (3.75) to obtain the charging equations for the EDL and the SCL, respectively as

$$\frac{d\Phi_f^{(k)}}{dy} = -\frac{\zeta_i^{(k)}}{\delta_1}\left(\gamma_1^2 - 1\right)\gamma_1 \text{ at y=0} \tag{3.79}$$

$$\frac{d\Phi_w^{(k)}}{dy} = -\frac{\Phi_w^{(k)} - \Phi_f^{(k)} - \zeta_i^{(k)}}{\delta_2}\left(\gamma_2^2 - 1\right)\gamma_2 \text{ at y=0} \tag{3.80}$$

In equations (3.79) and (3.80), the left-hand sides respectively represent the charging currents of the EDL and SCL, which are equal to the growth rates of their total charge shown on the right-hand sides of equations (3.79) and (3.80). It is noted that $\Phi_w^{(k)} - \Phi_f^{(k)} - \zeta_i^{(k)}$ in equation (3.80) denotes the potential drop across the SCL and is the counterpart of induced zeta potential $\zeta_i^{(k)}$ in the solid. If the EDL and SCL are to be considered as effective capacitors, we also can obtain frequency dependent capacitances (in dimensional form) for the EDL as $\varepsilon_0 \varepsilon_f \gamma_1 / \lambda_{D1}$ and the SCL as $\varepsilon_0 \varepsilon_w \gamma_2 / \lambda_{D2}$. Therefore, the present study provides a rigorous alternative to the widely used equivalent RC circuit models for the EDL in AC electrokinetic phenomena, where the capacitance of EDL reads $\varepsilon_0 \varepsilon_f / \lambda_{D1}$ which is independent of frequency (Ajdari, 2000; Castellanos et al., 2003; Ramos et al., 1999). Based on the equivalent RC-circuit model, the parameter $\beta = (\varepsilon_w \lambda_{D1}) / (\varepsilon_f \lambda_{D2})$ in the above conditions represents the ratio of the capacitance of the SCL ($\varepsilon_0 \varepsilon_w / \lambda_{D2}$) and that of the EDL ($\varepsilon_0 \varepsilon_f / \lambda_{D1}$). When $\beta \gg 1$, it is expected that the potential drop across the leaky-dielectric solid-electrolyte interface, $\Phi_w^{(k)} - \Phi_f^{(k)}$, is mainly composed of the induced zeta potential $\zeta_i^{(k)}$ and becomes comparable to $-\Phi_f^{(k)}$. In the limit case of $\beta \to \infty$ (i.e. a perfectly polarizable solid) $\Phi_w^{(k)} = 0$ (also $d\Phi_w^{(k)} / dy = 0$ since electric field does not exist inside a perfectly polarizable solid) and our derived equation (3.79) then precisely reproduces the model presented in the work by Squires and Bazant (2004) for perfectly polarizable solids [see their equations (7.48) and (7.50)].

Furthermore, equation (3.79) can be rearranged to obtain

$$\frac{d\Phi_f^{(k)}}{dy} = -\zeta_i^{(k)} jk\omega \frac{\lambda_{D1} a}{D_f} \sqrt{1 + jk\frac{\omega}{\omega_D}} \text{ at y=0} \qquad (3.81)$$

from which one can identify the time scale for the charging of EDL is $\lambda_{D1}a/D_f$ when the frequency of external electric field (ω in dimensional form) is much less than the Debye frequency ω_D. This time scale ($\lambda_{D1}a/D_f$) is of critical importance for characterization of AC field driven induced-charge electrokinetics. When the frequency of external field is much higher than $D_f/(\lambda_{D1}a)$, there is no induced EDL and the induced zeta potential also vanishes, while when the frequency of external field is much lower than $D_f/(\lambda_{D1}a)$, there is enough time for the charging of EDL, and the induced zeta potential and the associate electrokinetic phenomena are significant. It also should be noted from equations (3.75) and (3.76) that for a leaky-dielectric solid-electrolyte interface two time scales ($\lambda_{D1}a/D_f$ for the charging of EDL and $\lambda_{D2}a/D_w$ for the charging of SCL) compete under AC electric fields. When $\lambda_{D1}a/D_f$ is much smaller than $\lambda_{D2}a/D_w$, the potential drop across the interface is mainly on the liquid electrolyte side, while when $\lambda_{D1}a/D_f$ is much larger than $\lambda_{D2}a/D_w$, the potential drop across the interface is mainly on the leaky-dielectric solid side.

3.3.2 AC FIELD DRIVEN INDUCED-CHARGE ELECTROOSMOTIC FLOW AROUND A LEAKY-DIELECTRIC CYLINDER

In this section, we will demonstrate the implementation of the effective boundary conditions derived in section 3.3.1 for an AC field induced-charge flow around a leaky-dielectric cylinder (see Figure 3.8). Such leaky-dielectric cylinder with a radius of R immersed in an electrolyte solution is put (electrically floating) in an AC electric field of sinusoidal wave form, expressed as $E = \mathrm{Re}\left[E_0 \exp\left(j\Omega\tau\right)\right]$

with Re ( ) denoting the real part of the complex number. Then the EDL inside the liquid domain and the SCL inside the solid domain develop near the leaky-dielectric surface. It is already mentioned that the complex amplitudes of potentials inside bulk electroneutral liquid and solid domains, Φ_f and Φ_w , are all governed by Laplace's equation. The boundary conditions connecting these two domains are described by equations (3.75) and (3.76), which in polar coordinates can be reformulated as

$$\Phi_f - \Phi_w = \frac{\partial \Phi_f}{\partial r}\frac{\delta_1}{\gamma_1\left(\gamma_1^2 - 1\right)} + \frac{\partial \Phi_w}{\partial r}\frac{\delta_2}{\gamma_2\left(\gamma_2^2 - 1\right)} \text{ at r=1} \tag{3.82}$$

$$\delta_1 \frac{\gamma_1^2}{\left(\gamma_1^2 - 1\right)}\frac{\partial \Phi_f}{\partial r} - \beta\delta_2 \frac{\gamma_2^2}{\left(\gamma_2^2 - 1\right)}\frac{\partial \Phi_w}{\partial r} = 0 \text{ at r=1} \tag{3.83}$$

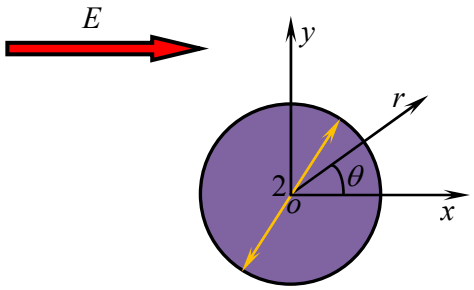

Figure 3.8 A leaky-dielectric cylinder immersed in an unbounded electrolyte solution is under an AC electric field with sinusoidal wave form. The external electric field E is applied along the x direction. Coordinates are normalized with respect to the radius of cylinder (R) and the electric field strength is normalized with respect to Φ_0 / R.

For the RC-circuit model, the effective electric boundary conditions can be formulated as

$$\Phi_f - \Phi_w = \frac{\partial \Phi_f}{\partial r}\frac{\delta_1}{\left(\gamma_1^2 - 1\right)} + \frac{\partial \Phi_w}{\partial r}\frac{\delta_2}{\left(\gamma_2^2 - 1\right)} \text{ at r=1} \tag{3.84}$$

$$\delta_1 \frac{\gamma_1^2}{\left(\gamma_1^2 - 1\right)} \frac{\partial \Phi_f}{\partial r} - \beta \delta_2 \frac{\gamma_2^2}{\left(\gamma_2^2 - 1\right)} \frac{\partial \Phi_w}{\partial r} = 0 \text{ at r=1} \tag{3.85}$$

which are to be compared against our present model in equations (3.82) and (3.83). For simplicity, the following derivations are carried out only for the boundary conditions presented in equations (3.82) and (3.83), but not for the boundary conditions in equations (3.84) and (3.85).

In addition, we also need a far field condition for Φ_f

$$\Phi_f = -E_0 x = -E_0 r\cos\theta \text{ as r} \rightarrow \infty \tag{3.86}$$

In equations (3.82), (3.83), (3.84), (3.85) and (3.86), the potentials, electric field strength and radial coordinate are respectively normalized with respect to Φ_0, Φ_0 / R and R. Referring to the definitions of two electrokinetic parameters, δ_1 and δ_2, in the previous section , one can write $\delta_1 = \lambda_{D1} / R$ and $\delta_2 = \lambda_{D2} / R$ in this case. For the given sinusoidal AC electric field, $\gamma_1^2 = 1 + j\Omega$ and $\gamma_2^2 = 1 + jt_w\Omega / t_f$.

The electrostatic potentials satisfy the Laplace equation in both bulk liquid and solid domains, and the solutions for complex amplitudes of the potentials inside the bulk electrolyte domain, Φ_f, and inside the bulk leaky-dielectric cylinder, Φ_w, are assumed as (Selvadurai, 2000)

$$\Phi_f = -E_0 \cos\theta \left(r + \frac{A}{r} \right) \tag{3.87}$$

$$\Phi_w = -BE_0 r\cos\theta \tag{3.88}$$

Substitution of equations (3.87) and (3.88) into equations (3.82) and (3.83) gives two expressions for

$$A = 1 - \frac{2\beta G_2 \gamma_2^3}{G_1 \gamma_1^3 \left(1 + G_2\right) + \beta G_2 \gamma_2^3 \left(1 + G_1\right)} \tag{3.89}$$

$$B = \frac{2 G_1 \gamma_1^3}{G_1 \gamma_1^3 \left(1 + G_2\right) + \beta G_2 \gamma_2^3 \left(1 + G_1\right)} \tag{3.90}$$

where G_1 and G_2 are two complex groups related to the liquid domain and solid domain, respectively

$$G_1 = \frac{\delta_1}{\gamma_1 \left(\gamma_1^2 - 1\right)} \tag{3.91}$$

$$G_2 = \frac{\delta_2}{\gamma_2 \left(\gamma_2^2 - 1\right)} \tag{3.92}$$

Furthermore, the tangential electric field strength on the leaky-dielectric surface reads

$$E_\theta = -\frac{1}{r}\frac{\partial \Phi_f}{\partial \theta} = -E_0 \sin\theta \left(1 + A\right) \text{ at r=1} \tag{3.93}$$

In this particular case, the complex amplitude of the induced zeta potential defined by equation (3.74) can be formulated as

$$\zeta_i = -\frac{\partial \Phi_f}{\partial r}\frac{\delta_1}{\gamma_1 \left(\gamma_1^2 - 1\right)} = G_1 \left(1 - A\right) E_0 \cos\theta \text{ at r=1} \tag{3.94}$$

It is evident from equation (3.94) that the induced zeta potential is linearly proportional to the external electric field strength. For a conducting cylinder with ideal polarizability under a DC forcing, i.e., $\beta \to \infty$ and $\Omega \to 0$, we can obtain the induced zeta potential as

$$\zeta_i = 2 E_0 \cos\theta \tag{3.95}$$

which is identical to the result given by equation (3.5) in the work by Squires and Bazant (2004).

Utilizing the well-known Smoluchowski equation, the AC induced-charge electroosmotic slip velocity on the surface of such leaky-dielectric cylinder can be determined by

$$\mathbf{u}_s = U_0 E_0^2 \sin\theta\cos\theta\,\hat{\boldsymbol{\theta}} \tag{3.96}$$

where $\hat{\boldsymbol{\theta}}$ denotes the unit vector along the azimuthal direction, and U_0 can be determined as

$$U_0 = \mathrm{Re}\left[G_1\left(1-A\right)\exp\left(j\Omega\tau\right)\right]\mathrm{Re}\left[\left(1+A\right)\exp\left(j\Omega\tau\right)\right] \tag{3.97}$$

The Smoluchowski slip velocity approach is strictly valid when the induced EDL is in quasi-equilibrium ($\Omega \ll 1$), and it however was also shown to be a good approximation even for relatively high frequencies ($\Omega \sim 1$) (Ramos et al., 2007).

After obtaining the slip velocity $\mathbf{u}_s$ from the above solution of the electrostatic problem, we now proceed to solve the flow field around the leaky-dielectric cylinder. Because the Reynolds number is very small in microfluidics, the liquid flow in the bulk electroneutral electrolyte domain is governed by the dimensionless continuity equation and Stokes equation

$$\nabla\cdot\mathbf{u} = 0 \text{ and } -\nabla p + \nabla^2\mathbf{u} = 0 \tag{3.98}$$

respectively, which are subjected to the slip boundary condition

$$\mathbf{u} = \mathbf{u}_s \text{ at } r = 1 \tag{3.99}$$

and the far field boundary condition

$$\mathbf{u} = 0 \text{ as } r \to \infty \tag{3.100}$$

where $\mathbf{u}$ and p respectively represent the fluid velocity vector and the pressure, and they are normalized by $\varepsilon_0 \varepsilon_f \Phi_0^2 / (\mu R)$ and $\varepsilon_0 \varepsilon_f \Phi_0^2 / R^2$, respectively.

It is straightforward to adopt the stream function formulation to solve such hydrodynamic problem. First, the radial (u_r) and azimuthal (u_θ) velocity components can be expressed in terms of the stream function ψ as

$$u_r = \frac{1}{r}\frac{\partial \psi}{\partial \theta} \qquad u_\theta = -\frac{\partial \psi}{\partial r} \tag{3.101}$$

where the stream function is normalized with respect to $\varepsilon_0 \varepsilon_f \Phi_0^2 / \mu$.

Then substituting equation (3.101) into equation (3.98), we can obtain the following biharmonic equation that governs the flow field

$$\nabla^2 \left(\nabla^2 \psi \right) = 0 \tag{3.102}$$

where operator ∇^2 in polar coordinate can be expressed as

$$\nabla^2 = \frac{1}{r}\frac{\partial}{\partial r}\left(r \frac{\partial}{\partial r} \right) + \frac{1}{r^2}\frac{\partial^2}{\partial \theta^2} \tag{3.103}$$

The boundary conditions given by equations (3.99) and (3.100) can be transformed to

$$\frac{1}{r}\frac{\partial \psi}{\partial \theta} = 0 \text{ and } \frac{\partial \psi}{\partial r} = -U_0 E_0^2 \sin\theta\cos\theta \text{ at r=1} \tag{3.104}$$

as well as the far-field boundary conditions

$$\frac{1}{r}\frac{\partial \psi}{\partial \theta} = 0 \text{ and } -\frac{\partial \psi}{\partial r} = 0 \text{ as } r \to \infty \tag{3.105}$$

Squires and Bazant (2004) derived the solutions for the fluid motion around a perfectly polarizable cylinder immersed in an electrolyte solution under a DC field (see their Table 1). By analogy, we can find the stream function and the corresponding velocity components of the fluid flow outside the leaky-dielectric cylinder to be

$$\psi = \frac{1-r^2}{4r^2} U_0 E_0^2 \sin 2\theta \tag{3.106}$$

$$u_r = \frac{1-r^2}{2r^3} U_0 E_0^2 \cos 2\theta \tag{3.107}$$

$$u_\theta = \frac{1}{2r^3} U_0 E_0^2 \sin 2\theta \tag{3.108}$$

which reveal that the flow field scales nonlinearly with respect to the external electric field strength. This feature differs from classic electrokinetic flows over insulating surfaces where the flow field is linearly proportional to external electric field strength. Again, for the limiting case of an ideally polarizable cylinder under the DC forcing, equations (3.106)–(3.108) are shown to be identical to those results given in ref. (Squires and Bazant, 2004)

$$\psi = \frac{1-r^2}{r^2} E_0^2 \sin 2\theta \tag{3.109}$$

$$u_r = \frac{2\left(1-r^2\right)}{r^3} E_0^2 \cos 2\theta \tag{3.110}$$

$$u_\theta = \frac{2}{r^3} E_0^2 \sin 2\theta \tag{3.111}$$

3.3.3 RESULTS AND DISCUSSION

Calculations are performed by using the derivations presented in section 3.3.2 to show the induced-charge electrokinetic flow patterns around a leaky-dielectric cylinder under various AC phases. For simplicity, we first consider a special cylindrical conductor with ideal polarizability ($\beta \to \infty$). The stream function contours (normalized with respect to E_0^2) of induced-charge electrokinetic flow at four different AC phases are plotted in Figure 3.9. In the calculation, the reference zero stream function is chosen on the cylinder surface. Then the stream function value at a given point in the flow field denotes the volumetric flow rate through a line connecting that point and the leaky-dielectric surface. Usually, the magnitude of the stream function value can be seen as a measure of the flow strength. It is evident from Figure 3.9 (a) that the flow is strongest at the phase $\Omega\tau=0$. Basic flow field involves four vortices symmetric with respect to both x and y axes. These flow circulations are the consequence of induced slip velocities on four segments of the cylinder surface which all direct towards the line x=0. With time evolving, both the external field strength and the induced zeta potential decrease, which then leads to a reduction in the flow strength (see the phase $\Omega\tau= \pi/4$ shown in Figure 3.9 (b)). To the phase $\Omega\tau= \pi/2$ in Figure 3.9 (c), although the external electric field further decrease to zero, the tangential electric field strength on the cylinder surface given by equation (3.93) and the induced zeta potential given by equation (3.95) are not zero due to the essential phase lags between these two and the external field. Consequently, the fluid slip velocity on the cylinder surface and thus the weak circulations still persist. After the phase $\Omega\tau= \pi/2$, the external electric field changes its direction

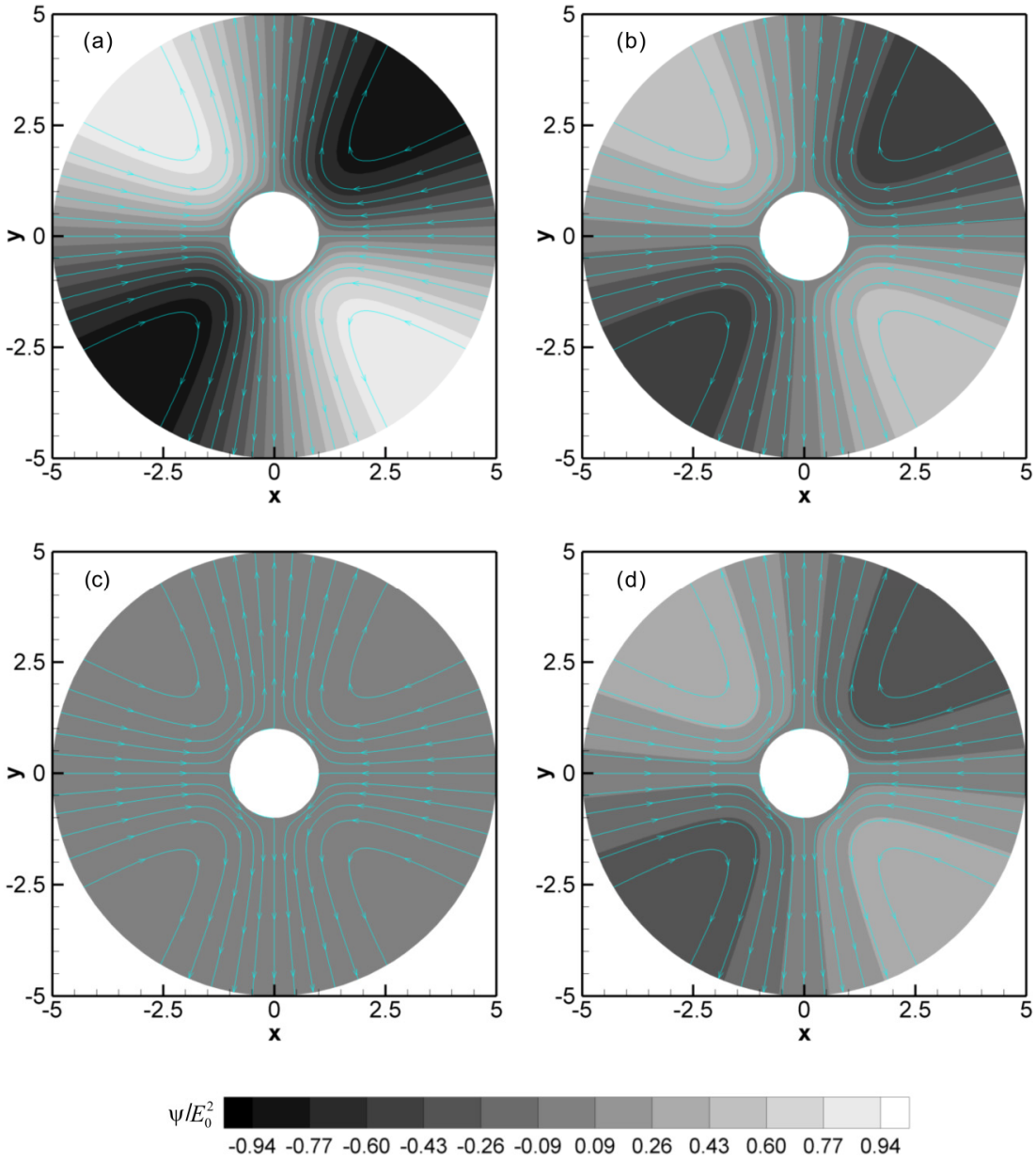

Figure 3.9 Contours for the stream function of an AC induced-charge electrokinetic flow at four different AC phases for the case of a conducting cylinder with perfect polarizability ($\beta \to \infty$): (a) $\Omega\tau=0$, (b) $\Omega\tau=\pi/4$, (c) $\Omega\tau=\pi/2$ and (d) $\Omega\tau=3\pi/4$. The arrowed lines are stream lines. In the calculations, the electrokinetic parameter is $\delta_1=1/100$ and the frequency is $\Omega=0.001$.

and the local induced zeta potential on the cylinder surface also reverses its sign. Thus the direction of the induced slip velocity (as a product of the tangential electric field strength and the induced zeta potential) on cylinder surface still remains the same as that in the first half period (namely, $\Omega\tau$ from 0 to $\pi/2$), and

so does the direction of flow circulations. With the magnitude of electric field strength increasing, the flow becomes intensified as shown in Figure 3.9 (d) for the phase of $\Omega\tau = 3\pi/4$. Till the phase $\Omega\tau=\pi$ (not shown here), the flow is enhanced to reach the same situation as for the phase $\Omega\tau=0$. Finally, it is also worth mentioning that the frequency of induced-charge flow oscillation is doubled to 2Ω since both driving electric field and induced zeta potential oscillate at the frequency of Ω.

If the case of an ideally polarized cylinder under the DC forcing is taken as a reference, the induced-charge electrokinetic flow field around a leaky-dielectric cylinder can be found by multiplying the solutions given by equations (3.109), (3.110) and (3.111) with a scale factor of $U_0/4$. This scale factor is important since the parameters affecting the dynamics of the induced-charge oscillating flow around the leaky-dielectric cylinder are included in such factor, such as the period, amplitude and phase. Figure 3.10 characterizes the dependence of $U_0/4$ on AC phase for a leaky-dielectric cylinder under various frequencies of external field (Ω) and ratios of the free charge relaxation times (t_w/t_f). It is seen that the amplitude of the flow oscillation increases with decreasing Ω or t_w/t_f. It is also noted that the phase lag between the induced-charge flow and the external electric field also reduces with the decrease of Ω or t_w/t_f. These features can be interpreted as follows: when Ω is low, there is sufficient time for free charge carriers to diffuse into the EDL and SCL to charge them up. On the other hand, with decreasing t_w/t_f, the cylinder becomes more conducting and the free charges inside such leaky-dielectric cylinder can respond quickly to form the SCL which effectively represents a surface charge density on the cylinder surface.

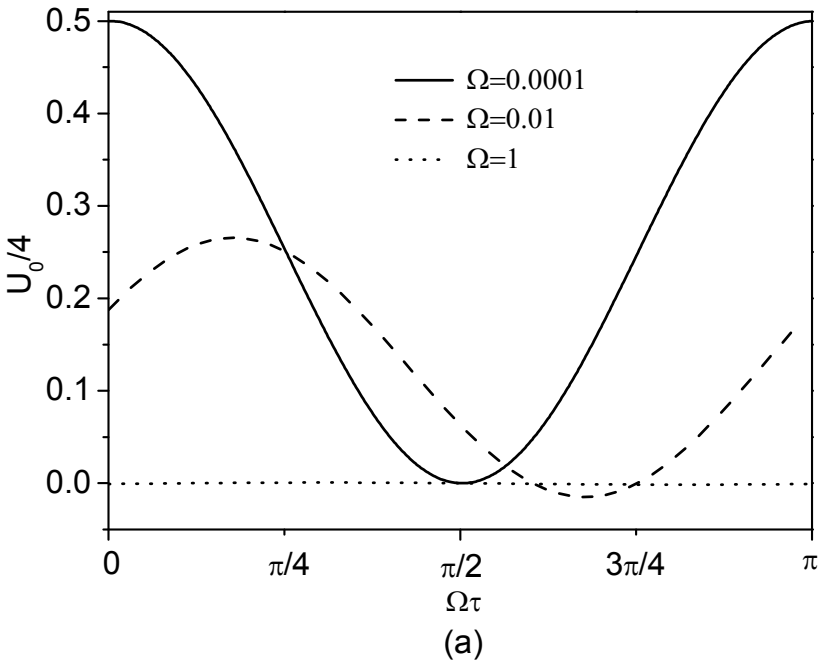

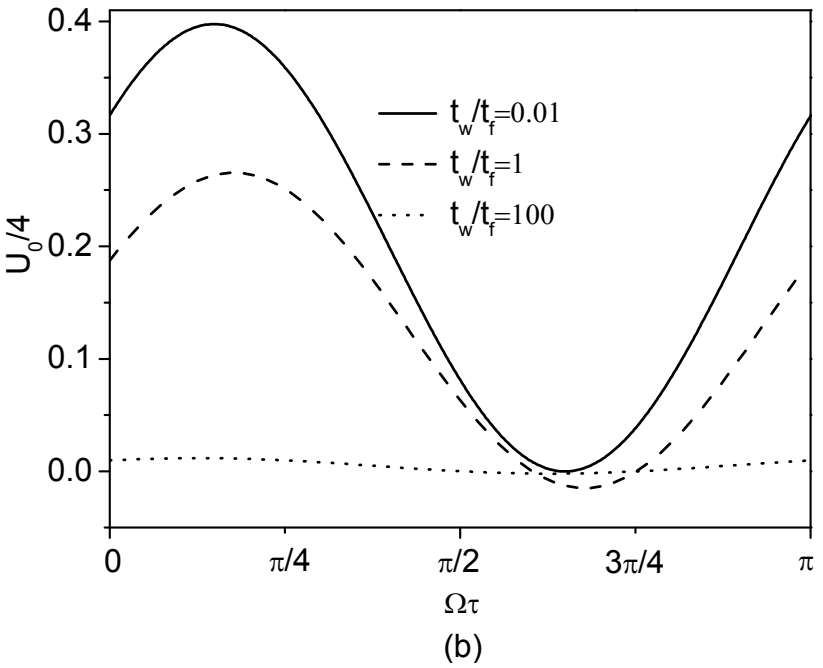

Figure 3.10 Variation of $U_0/4$ for an AC induced-charge electrokinetic flow around a leaky-dielectric cylinder with AC phase angle (here the expression for U_0 is given by equation (3.97)). (a) Dependence of $U_0/4$ on the frequency of AC field, Ω, when t_w/t_f=1.0. (b) Dependence of $U_0/4$ on the free charge relaxation time ratio, t_w/t_f, when Ω =0.01. In all calculations, β=1 and $\delta_1 = \delta_2$=1/100 are chosen.

In addition, it is known that the RC circuit model is widely used in the literature. To illustrate the difference between our present model and the conventional RC circuit model, the ratio of the complex amplitude for induced zeta potential obtained from our model (ζ_i) to that predicted from the RC model ($\zeta_{i,RC}$) is presented in Figure 3.11. ζ_i and $\zeta_{i,RC}$ are evaluated by using our derived boundary conditions (equations (3.82) and (3.83)) and boundary conditions for the RC model (equations (3.84)and (3.85)), respectively. Since $\zeta_i / \zeta_{i,RC}$ is a complex number, its modulus represents the ratio of the magnitude of the induced zeta potential evaluated from our model to that evaluated from the RC model, and its argument represents the phase lag between our model and the RC model. It is noted that our model and the RC model become identical only under the case of DC electric forcing ($\Omega \rightarrow 0$). However, as the frequency of applied field increases, our model predicts smaller induced zeta potentials, and the phase lag between our model and the RC model becomes larger. Similarly, it also can be readily found that both the tangential electric field strength given by equation (3.93) and the resultant Smoluchowski slip velocity given by equation (3.96) are smaller than those predicted by the RC model. As pointed out in a review paper by Bazant et al. (2009), the RC model was shown to overestimate existing experimental results for the ICEK flow velocity. Therefore, the model presented in this study could partially reduce such discrepancy to some extent.

Considering the fact that the SCL is actually an equivalent EDL in the solid, the derived effective boundary conditions can be extended to describe dynamic behavior of an interface between two immiscible electrolyte solutions under AC

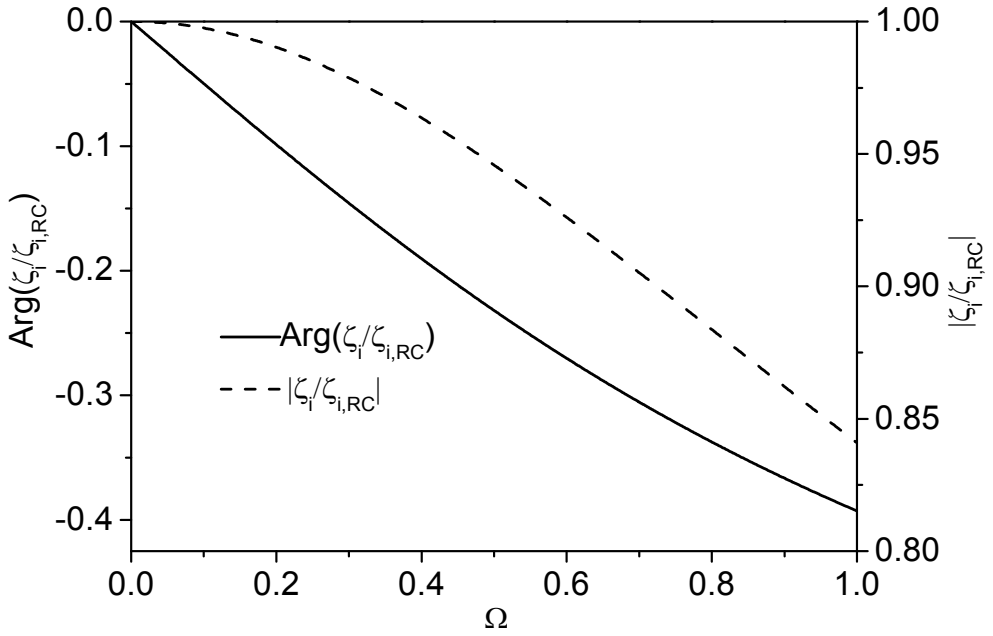

Figure 3.11 Ratio of the complex amplitude of the induced zeta potentials predicted by the present model (ζ_i) to that predicted by the conventional RC circuit model ($\zeta_{i,RC}$) for the case of a conducting cylinder with perfect polarizability ($\beta \to \infty$) and $\delta_1=1/1000$. The left vertical axis represents the argument for the complex ratio $\zeta_i/\zeta_{i,RC}$ and the right vertical axis represents the corresponding modulus.

electric forcing. Interfaces between two immiscible electrolyte solutions are widely used for biomimetics, catalysis, surface cleaning, and assembly of nanoparticle arrays (Girault and Schiffrin, 1985; Su et al., 2003). Monroe et al. (2006) and Monroe et al. (2009) investigated the behavior of an interface between two immiscible electrolyte solutions under the DC forcing, and they pointed out that two EDLs forming near the interface between two immiscible electrolyte solutions play an essential role. Another potential application of the present boundary conditions is to modify the classic dielectrophoresis theory for leaky-dielectric particles in electrolyte solutions. It is known that EDL and SCL are not considered in the conventional theories of dielectrophoresis. Usually, an assumption of the continuity in both electric potential and electric displacement

should be made when deriving the dielectrophoretic force and torque acting on a particle. This assumption however is not valid for a leaky-dielectric particle in which the SCL of finite thickness develops. Under this case, obviously the continuity of electric potential does not hold anymore (see equation (3.75)) due to the charging of EDL and SCL. Then the local electric field around the particle should be modified accordingly. Ultimately, the effective dipole moment and therefore the dielectrophoretic force and torque on a leaky-dielectric particle need to be modified by taking into account the dynamic charging of EDL and SCL. Although some researchers (Basuray and Chang, 2007; Hoffman and Zhu, 2008; Swaminathan and Hu, 2009; Zhao and Bau, 2009) noticed this problem and already addressed the EDL charging effect on dielectrophoretic force, the SCL effects have yet been addressed. Furthermore, no one has ever provided any simple formulae for the dielectrophoretic force and torque on a spherical particle to include both EDL and SCL effects. With our derived effective boundary conditions, it can be expected that the modification of conventional dielectrophoretic theory can be included in a modified Clausius-Mossoti factor. This will be our next effort.

3.4 SUMMARY

This chapter presents two types of effective electric boundary conditions for evaluation of induced zeta potentials on solid surfaces in ICEK. These boundary conditions are of fundamental significance in ICEK since the prediction of induced zeta potential is necessary for theoretical characterization of ICEK. The following summarizes the main conclusions from this chapter.

Firstly, general electric boundary conditions describing DC field driven ICEK at liquid-dielectric interfaces are proposed within the frame work of electrostatics. By utilizing the proposed boundary conditions, the ICEO flow in an infinitely long microchannel patterned with two symmetric polarizable dielectric blocks is investigated analytically. Fourier transform method is invoked to solve a biharmonic equation which governs the ICEO flow field described by the stream function. Dimensionless parameters are introduced, and their effects on flow characteristics are analyzed. It is found that an increase in polarizability of the dielectric block enhances the slip velocity on the block surface and thus induces a pair of counter-rotating vortices. Moreover, increasing the natural zeta potential on the upstream and downstream of the insulating microchannel walls leads to extinction of the vortex near the upstream insulating microchannel and suppression of the vortex near the downstream insulating microchannel.

Secondly, effective electric boundary conditions for AC field driven ICEK phenomena around floating leaky-dielectric solids are derived for an AC electric field with arbitrary wave forms. The general electric boundary conditions take into account the contributions from both the electrical polarization and the electrical conduction to induced zeta potentials. We have demonstrated that our general boundary conditions can recover two well-known limiting cases, (i) the conventional electrokinetic phenomena with perfectly insulating (nonpolarizable) surfaces and (ii) the induced-charge electrokinetic phenomena with perfectly polarizable surfaces. The effective electric boundary conditions allow for analyses of AC field driven ICEK phenomena with induced EDL and SCL effects while without the need of resolving trivial details of the EDL and SCL.

Furthermore, a case study of the AC induced-charge electrokinetic flow around a leaky-dielectric cylinder is presented to demonstrate the implementation of the derived boundary conditions. Our analyses showed that four flow circulations are induced around the leaky-dielectric cylinder. Furthermore, the intensity of these circulations can be modulated by adjusting the parameters associated with the EDL and SCL. Particularly, when decreasing the frequency of applied electric field (Ω) or the ratio of the free charge relaxation times (t_w/t_f), the amplitude of the induced-charge flow oscillation increases and the phase lag between the induced-charge electrokinetic flow and the external electric field decreases. In addition, a comparison between our present model and the conventional RC circuit model showed that the RC model predicts larger values for the induced zeta potential, and thus stronger induced-charge electrokinetic flows. This could partially explain the finding reported by some studies that the RC model usually overestimates the experimental data of induced-charge electrokinetic flows.

CHAPTER 4: DYNAMIC CHARGING OF ELECTRIC DOUBLE LAYERS AROUND POLARIZABLE DIELECTRICS

4.1 INTRODUCTION

The development of electric double layers around polarizable objects is crucial for understanding the induced-charge electrokinetics. Physically, it was already established that the dielectric solid surface acquires surface charge when it is polarized by the external electric field, and these induced surface charge repels the coions and attracts the counterions in the electrolyte solution to charge the EDL around the solid surface. Then the interaction of the external field with this induced EDL drives the induced-charge nonlinear electrokinetics. At the steady state, the charged EDL around the polarizable dielectrics completely screens the external driven field and the dielectric surface behaves like a perfect insulator. Although the physical picture is simple, no complete mathematical model has yet been developed to describe the above physical reasoning.

In Chapter 3, two types of boundary conditions are derived to link the potentials in two bulk domains (the bulk liquid and the bulk solid). Although such boundary conditions can predict the potential drop across the EDL, the detailed information of EDL (such as flow field, electric field and ionic concentration field inside the EDL) is not available from the model presented in Chapter 3. In addition, the analysis presented in Chapter 3 is only applicable to situations with low induced zeta potentials and thin EDLs. These two

assumptions allow for neglecting both surface conduction and bulk concentration polarization which however will be shown to have important implications on the transient charging of electric double layer. Moreover, the thin double layer assumption also limits the models in Chapter 3 to microfluidic regime where the thickness of EDL is much smaller than the characteristic dimension of the solid object, and certainly the models presented in Chapter 3 are not applicable to relatively thick EDLs, such as in nanofluidic regime where the thickness of EDL is comparable to the characteristic dimension of the solid.

Previously, Bazant et al. (2004) and Chu and Bazant (2006) conducted asymptotic analyses for the charging of EDL around planar and cylindrical conductors, and they identified two important time scales for the charging process. At a so-called smaller *RC* time scale, $\lambda_D L_{ref}/D$, (where λ_D is the Debye length, L_{ref} is the characteristic dimension of the system, and D is the diffusivity of the ions), the EDL gets charged due to preferential adsorption of counterions. As the charging process continues, concentration gradient is generated in the bulk solution, and thus the bulk diffusion process at a larger time scale, L_{ref}^2/D, appears to stabilize and slow down the charging process. However, their asymptotic analyses are not general due to several assumptions involved, such as thin EDL approximation; the perfectly polarizable solid; the neglect of the coupling of charging process to fluid flow which is however highly relevant for microfluidic and nanofluidic devices driven by induced-charge electrokinetics.

This chapter presents a complete model for describing the transient behaviors of EDL charging and induced-charge electrokinetic flows around arbitrarily polarizable solids. Such model does not contain assumptions invoked

in previous theoretical investigations and thus gives the most accurate information of dynamic aspects of the EDL charging. The theoretical model comprises of a Poisson equation for the electric potential in electrolyte domain, a Navier-Stokes equation for the liquid velocity and a Nernst-Planck equation for ionic concentration inside the electrolyte domain and a Laplace equation for the conjugate electric potential inside the dielectric solid domain. With the complete model, the detailed information inside the EDL during the charging process is revealed for the first time, and more importantly, the flow field accompanying the transient charging process is also investigated.

4.2 GOVERNING EQUATIONS AND MODEL DESCRIPTIONS

4.2.1 GOVERNING EQUATIONS

To nondimensionalize the governing equations, we introduce the following reference parameters respectively for electric potential, velocity, time, pressure, surface charge density

$$\varphi_{ref} = \frac{k_B T}{e},\ u_{ref} = \frac{\varepsilon_0 \varepsilon_f \varphi_{ref}^2}{\mu L_{ref}},\ t_{ref} = \frac{\kappa^{-1} L_{ref}}{D_{ref}},\ p_{ref} = \mu \frac{u_{ref}}{L_{ref}},\ q_{ref} = \varepsilon_0 \varepsilon_f \frac{\varphi_{ref}}{L_{ref}} \qquad (4.1)$$

and Peclet number and Schmidt number

$$Pe = \frac{u_{ref} L_{ref}}{D_{ref}} \qquad Sc = \frac{\mu}{\rho D_{ref}} \qquad (4.2)$$

where L_{ref} , c_{ref} and D_{ref} denote the reference length scale, the reference ionic concentration and the reference ionic diffusion coefficient, respectively. All of them are to be specified in the next section. In equation (4.1), e is the elementary charge, k_B is the Boltzmann constant, T is the absolute temperature. ε_0 and ε_f

represent the permittivity of free space and the dielectric constant of electrolyte solution, respectively.

In equation (4.1) the reference time t_{ref} stands for the characteristic time of the EDL charging (MaCdonald, 1970). It can be understood as the RC time for the circuit with a double-layer capacitor, $C = \varepsilon_0 \varepsilon_f / \lambda_D$ in series with a bulk resistor, $R = L_{ref} / \sigma$ where σ represents the bulk electric conductivity and can be expressed as $\sigma = 2 c_{ref} N_A D_{ref} e^2 / \left(k_B T \right)$, where N_A is the Avogadro constant. The above RC time scale of EDL charging is only applicable to polarizable objects subjected to weak electric fields, and thus surface conduction and bulk diffusion at the global scale L_{ref} can be safely neglected. For large applied fields or large induced double layer charge, significant surface conduction and bulk diffusion occurs at a much larger time scale, L_{ref}^2 / D_{ref}, which would invalidates the former simple circuit approximation.

For the electric problem, there are two domains, electrolyte solution domain and dielectric solid domain. Inside the electrolyte domain, the electric potential is governed by the Poisson equation which can be written nondimensionally as

$$\nabla^2 \varphi_f = -\frac{1}{2} \left(\kappa L_{ref} \right)^2 \left(z_1 c_1 + z_2 c_2 \right) \tag{4.3}$$

where c_i and z_i are respectively the dimensionless concentration and the valence of ions (i=1 for cations and i=2 for anions) in the electrolyte solution. The right hand side of equation (4.3) represents the free charge density in the electrolyte solution domain. κ is the inverse of Debye length given by

$$\kappa = \sqrt{\frac{2 c_{ref} N_A e^2}{\varepsilon_0 \varepsilon_f k_B T}} \tag{4.4}$$

Inside the dielectric solid, the free charge carriers are absent and the electric potential is governed by the dimensionless Laplace equation

$$\nabla^2 \varphi_s = 0 \tag{4.5}$$

Ionic transport is described by the Nernst-Planck equation which can be written for two ionic species in the electrolyte solution domain as

$$\kappa L_{ref} \frac{\partial c_i}{\partial t} + Pe\left(\mathbf{u} \bullet \nabla c_i\right) = D_i \nabla^2 c_i + D_i z_i \nabla \bullet \left(c_i \nabla \varphi_f\right) \tag{4.6}$$

The flow problem only exists in the liquid electrolyte domain where the transient flow field is governed by the continuity and Navier–Stokes equations. These equations, in their dimensionless forms, are

$$\nabla \bullet \mathbf{u} = 0 \tag{4.7}$$

$$\frac{\kappa L_{ref}}{Sc} \frac{\partial \mathbf{u}}{\partial t} = -\nabla p + \nabla^2 \mathbf{u} - \frac{1}{2}\left(\kappa L_{ref}\right)^2 \left(z_1 c_1 + z_2 c_2\right) \nabla \varphi_f \tag{4.8}$$

4.2.2 DESCRIPTIONS OF THE SIMULATION DOMAIN AND THE INITIAL AND BOUNDARY CONDITIONS

We consider a dielectric cylinder of radius a immersed an unbounded electrolyte solution domain. To numerically model the dynamics of the electrolyte around the dielectric cylinder floating in an external electric field, we envisage a square domain with the dielectric cylinder located at its center, as shown in Figure 4.1. In order to avoid the influence of the size of imaginary square domain on the simulation results, we compared the results for several sizes of the square domain and found out that the size effect is trivial. In the

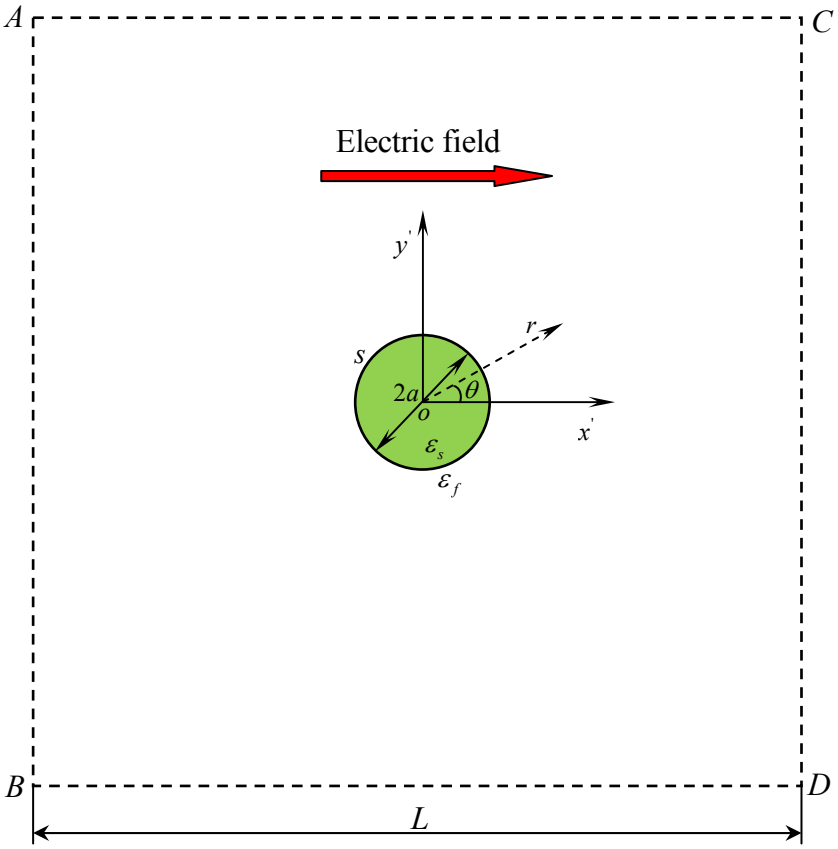

Figure 4.1 Sketch of the simulation domain and the coordinate systems. A cylinder with radius of a is located at the center of the imaginary square domain with dimensions of L×L. The four dashed lines represent the imaginary boundaries where far field boundary conditions are imposed for the Poisson equation, the Nernst-Planck equation and the Navier-Stokes equation. The length of each boundary measures L set to be at least 25 times of the cylinder radius to eliminate the boundaries effects on the charging process of EDL around the cylinder. The dielectric cylinder with dielectric constant of ε_s is surrounded by the electrolyte solution with dielectric constant of ε_f. The external electric field is applied along the x' direction.

present study, we set each boundary of the square domain with lateral length 25 times of the cylinder radius. Symmetric electrolyte KCl with z_1=-z_2=1 is considered in the simulation and the reference ionic diffusion coefficient D_{ref} is chosen as 10^{-9} m^2/s. Then the normalized ionic diffusion coefficient for cationic and anionic species are D_1=1.957 and D_2=2.032 (Masliyah and Bhattacharjee, 2006), respectively. c_{ref} is set to be the bulk ionic concentrations and L_{ref} is chosen as the radius of the cylinder, a. The physical properties of the electrolyte

solutions are identical to those of the room temperature (T=298K) water, and then we can calculate the Peclet number as Pe=0.51 and the Schmidt number as Sc=906.

At last, proper boundary conditions and initial conditions are prescribed as follows for the aforementioned Poisson equation, Nernst-Planck equation and Navier-Stokes equation.

Along the plane AB shown in Figure 4.1, the boundary condition for the electric potential is

$$\varphi_f = \varphi_0 \text{ on the plane AB} \tag{4.9}$$

and the potential, φ_0, is adjustable through a power source. The plane CD is taken as the reference and thus the potential is set to be zero

$$\varphi_f = 0 \text{ on the plane CD.} \tag{4.10}$$

The surfaces of BD and AC are in the bulk electrolyte solution, and hence carry no charge

$$\mathbf{n} \bullet \nabla \varphi_f = 0 \text{ on the planes AC and BD.} \tag{4.11}$$

where **n** denotes the unit outward normal to the corresponding surfaces. To determine the potential inside the dielectric solid, the proper boundary conditions linking the potentials inside the electrolyte domain and the solid domain are required on the surface of the dielectric solid. According to the electrostatics, we have two boundary conditions on the surface of the dielectric solid which respectively describe the continuity of electric potential and the discontinuity of electric displacement across the solid surface

$$\varphi_s = \varphi_f \tag{4.12}$$

$$D_r \mathbf{n} \bullet \nabla \varphi_s = q + \mathbf{n} \bullet \nabla \varphi_f \tag{4.13}$$

where D_r represents the ratio of dielectric constant of the dielectric solid to that of the electrolyte solution, i.e., $D_r = \varepsilon_s / \varepsilon_f$. q can be regarded as the dimensionless physiochemical surface charge density on the dielectric surface.

For the ionic transport, the segments AB, AC, CD and BD are assumed to be in the bulk electrolyte solution. Accordingly, the concentrations of the positive and negative ions are the same as the bulk concentration of the electrolyte solution

$$c_i = 1 \text{ on the plane AB, AC, CD and BD} \tag{4.14}$$

On the surface of the cylinder s, since ions cannot penetrate the solid surface, the net ionic fluxes normal to the rigid wall is zero

$$\mathbf{n} \bullet \left(\mathbf{u} c_i - D_i \nabla c_i / Pe - D_i z_i c_i \nabla \varphi / Pe \right) = 0 \text{ on the cylinder surface s} \tag{4.15}$$

For the fluid flow problem governed by equations (4.6), (4.7) and(4.8), the nonslip boundary condition (i.e., $\mathbf{u}$ =0) is used on the surface of the dielectric cylinder, s. At boundaries AB and BD AC and CD, because they are far away from the cylinder and there is no pressure gradient applied externally, normal pressure with p = 0 is used at the boundaries AB, BD, AC and CD.

Initially, the whole electrolyte domain is completely neutral and both cations and anions have the same scaled concentration, i.e., c_i=1. Electrolyte solutions is quiescent at the beginning, i.e., $\mathbf{u}$=0. When a DC voltage φ_0 is suddenly applied at t=0, the cylinder is instantaneously polarized while the whole electrolyte domain still remains electroneutral and quiescent. We numerically solve equation (4.3)

by using the initial conditions for ionic concentrations and velocity field, and the electric potential obtained is prescribed as the initial condition for electrostatic problem.

The above model differs from most of previous studies on transient induced-charge electrokinetic phenomena, which are based on assumptions of the thin EDLs, the Debye-Hückel linearity and negligible convective transport of ions and surface conduction. In the present work, we start from basic governing equations for electrokinetics and dispense with all these assumptions. The model presented here features the full coupling of electric potential, ionic transport and liquid flow, and thus is a general description of the dynamic behaviors of EDL and liquid flow around dielectrics. Appendix A details the model validation which ensures the correctness and accuracy of the present model.

4.3 RESULTS AND DISCUSSION

4.3.1 TRANSIENT CHARGING OF EDL AROUND A CYLINDER

Figure 4.2 shows the transient charging process of the EDL around a floating cylinder with ideal polarizability (conductor with $Dr \rightarrow \infty$). In the plots, (x, y) are the corresponding dimensionless coordinates for (x', y'). Initially, when an external electric field is imposed across the uncharged cylindrical conductor immersed in an electrolyte solution, the conductor is polarized instantaneously with the surface on the anode side of the electric field bearing negative surface charges and that on the cathode side of the electric field bearing positive surface charges. These surface charges are redistributed over the conducting surface to make sure that the conductor is equipotential, which requires the electric field

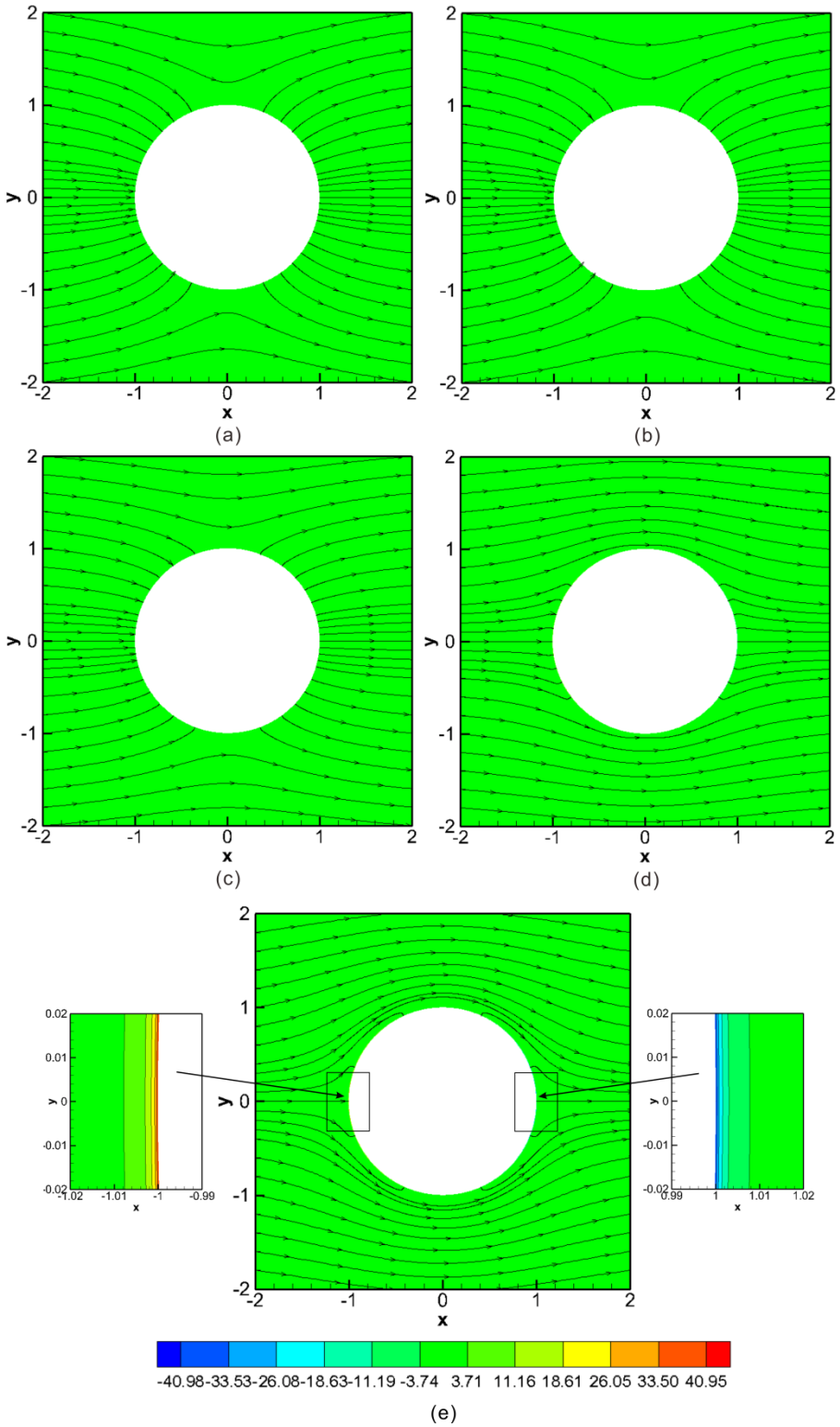

Figure 4.2 Transient charging process of the EDL around an uncharged floating conducting cylinder ($D_r \to \infty$) under the conditions of an applied bias of $\varphi_0=50$ and $\kappa a=100$, (a) t=0, (b) t=0.01, (c) t=0.1, (d) t=1, (e) $t \to \infty$. The contours show the normalized net charge density, c_1-c_2, inside the electrolyte domain, and the arrowed lines denote the electric field lines.

lines to intersect the conducting surface at right angles (Stratton, 1941). This feature can be clearly seen from Figure 4.2 (a). Subsequently, induced surface charge on the conducting surface attracts counterions and repels coions in the electrolyte solution, which triggers the charging process of EDL around the conductor. As the charging process continues, the local electroneutrality inside the electrolyte domain is broken, with positive net charge density induced inside EDL near the cylinder surface on the anode side of the electric field and negative net charge density induced inside EDL near the cylinder surface on the cathode side of the electric field. In turn, this induced ionic charge inside the EDL begins to counteract the external electric field and slightly distort the electric field lines as shown in Figure 4.2 (b) and Figure 4.2 (c). As time evolves further to t=1 (or a dimensional RC charging time, $\lambda_D a / D_{ref}$), the EDL continues to be charged with much higher net charge density around the cylinder. At this stage, the charged density inside the EDL is high enough to distort the local electric field lines significantly at the outer edge of the EDL, as depicted in Figure 4.2 (d). Till steady state (Figure 4.2(e)), the conductor seems like shielded from the external electric field by an EDL "shell". At the steady state, the charge density inside the EDL exactly counteracts the local external electric field, and thus the charging process stops. It also should be noted that the electric field lines must always intersect the cylinder surface at right angles during the charging of EDL to constrain the net charge on the cylinder surface to be zero. In this case study, a thin EDL case (κa=100) is simulated, so the details of net charge density inside the EDL are not clearly displayed in Figure 4.2(a)-Figure 4.2 (d). Consequently, a magnified view of local net charge density distribution inside the EDL is shown in Figure 4.2(e).

It is clear that at the steady state the positive net charge density is induced inside the EDL near the left half of the cylinder surface and the negative net charge density is induced inside the EDL near the right half of the cylinder surface.

The time evolution of the corresponding normalized surface charge density is characterized in Figure 4.3. $\varepsilon_0\varepsilon_r\varphi_{ref}/a$ is chosen as the reference surface charge density for nondimensionalization. It is seen from Figure 4.3 that the magnitude of the surface charge density at a fixed locus on the conducting surface increases as time evolves from t=0 to t=10. This is quite understandable when retrospecting the dynamic charging of EDL presented in Figure 4.2. In process of the EDL charging, the charge density inside the EDL grows, which also needs to be neutralized by the growing surface charge density on the conducting surface. After t=10, the surface charge density gradually decreases a bit to its steady state value. This nonmonotonicity in time characteristics is due to the generation of concentration polarization in the bulk electrolyte solution which is to be elaborated in section 4.3.3. Unlike the physiochemical bond surface charge in conventional electrokinetics which usually does not depend on the external electric filed, the surface charge here is induced by the polarization of the surface and thus is dependent on the external electric fields. In addition, the net surface charge must be always maintained to be zero during the charging of the EDL.

4.3.2 TRANSIENT DEVELOPMENT OF FLOW FIELD AROUND THE CYLINDER

The characteristics of transient development of the corresponding velocity field around the cylindrical conductor ($Dr\rightarrow\infty$) for $\kappa a=100$ and $\varphi_0=50$ is presented in Figure 4.4. Initially (t=0), the whole solution domain is stationary

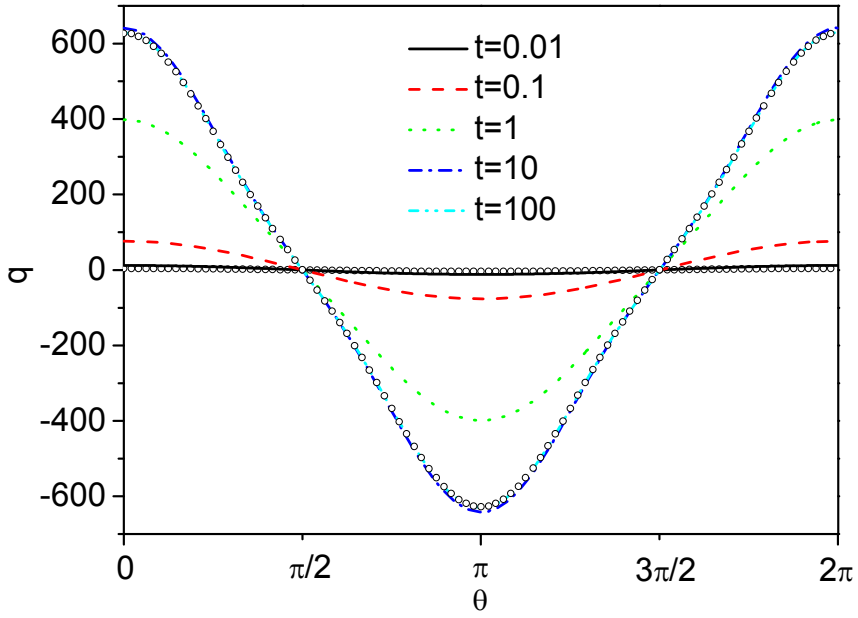

Figure 4.3 The transient development of induced charge density on the conducting cylinder (ideally polarizable $D_r \to \infty$) surface for $\kappa a=100$ with the applied bias of $\varphi_0=50$. The results for two extreme time instants are also included in the plot, the circles with a smaller amplitude is for initial state (t=0) and that with a larger amplitude is for steady state ($t \to \infty$).

(not shown in Figure 4.4), because the solution is electroneutral everywhere in the electrolyte and the external electric field does not exert any driving force on the liquid solution. As the EDL near the cylinder surface gets charged, the external electric field induces electrostatic body force which drives the solution to move. Because the electrostatic driving force only exists inside the EDL very near the cylinder surface, the liquid inside the EDL starts to move first. Then the momentum generated inside the EDL diffuses to the bulk solution, which results in the bulk motion of the solution, as shown in Figure 4.4 (a). Since the driving force is only present inside the nonneutral EDL near the cylinder, it is expected that the velocity attains its maximum value very near the cylinder surface at the outer edge of EDL where the driving force vanishes. With further charging of the

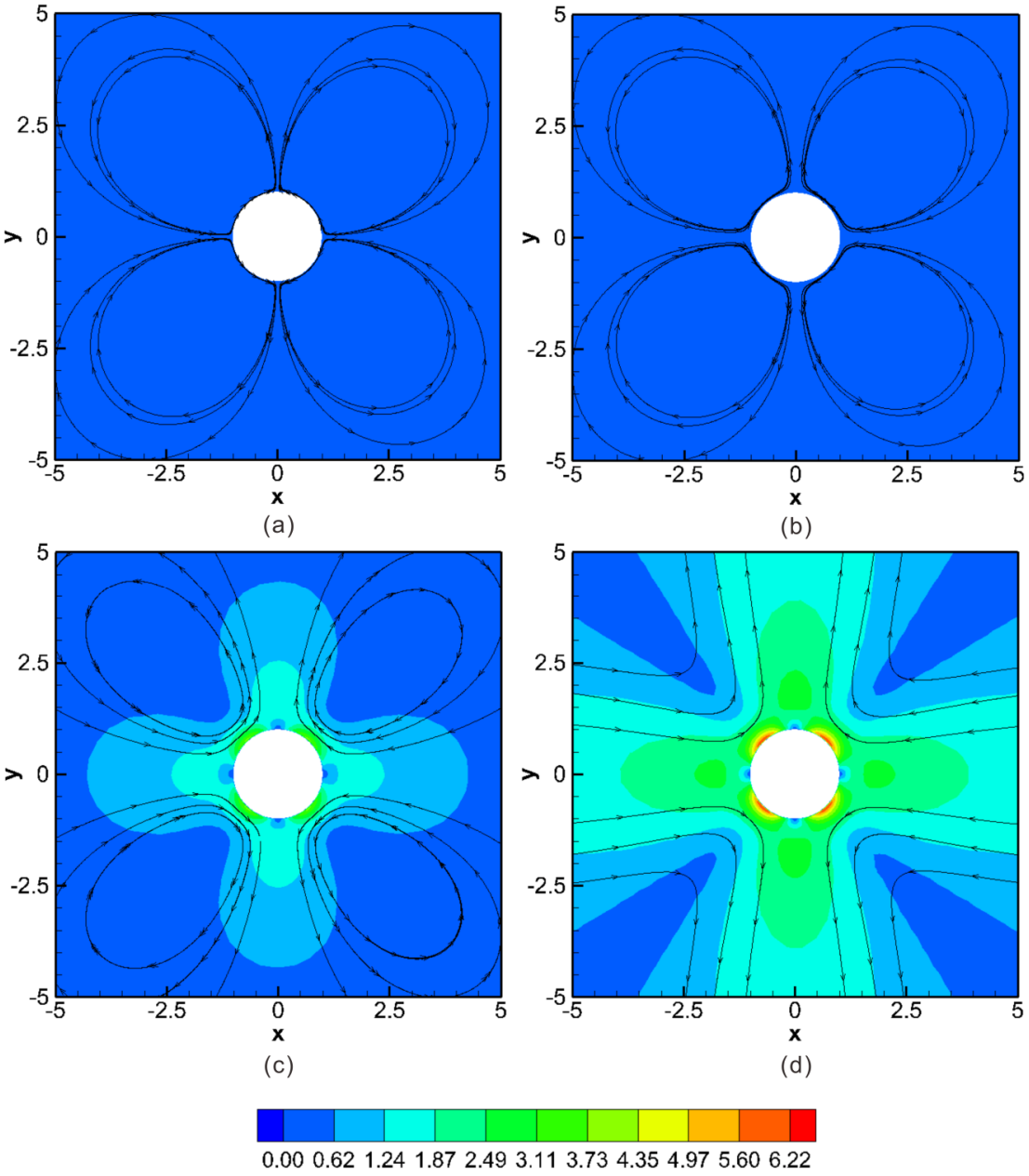

Figure 4.4 Contours for the magnitude of velocity around the ideally polarizable cylinder (Dr→∞) for κa=100 with the applied bias of φ_0=50 at four instants, viz., (a) t=0.01, (b) t=0.1, (c) t=1 and (d) t→∞. The arrowed lines are the stream lines.

EDL, the magnitude of electrostatic body force increases, so does the magnitude of maximum velocity as consecutively shown in Figure 4.4 (b), Figure 4.4 (c) and Figure 4.4 (d). At the same time, the momentum generated inside the EDL continues to diffuse to the bulk liquid domain due to the viscous coupling between the electrolyte solution inside EDL and the bulk electrolyte solution.

Therefore, larger portion of solution gets activated as time evolves. It is also identified that the distribution of velocity magnitude around the cylinder at any instant of time is symmetric with respect to both x axis and y axis. At the steady state ($t\rightarrow\infty$), the EDL is fully charged and then the magnitude of velocity reaches its maximum at the outer edge of EDL as shown in Figure 4.4 (d). Simultaneously, the momentum generated inside the EDL fully diffuse to the bulk liquid with a maximal portion of liquid around the cylinder actuated. It is also worth noting that the flow patterns in Figure 4.4 are similar to those presented in Figure 3.9 because of the same mechanism of induced-charge electrokinetics involved.

Actually, basic flow patterns around the cylinder are four symmetric vortices. The two vortices at the upper left corner and at the lower right corner rotate counter-clockwise while the other two at the upper right corner and at the lower left corner rotate clockwise. As the positive (negative) charge density is induced inside the EDL near the surface on the anode (cathode) side of the electric field, the interaction of which with the local tangential electric field induces electrostatic body forces all directing towards x=0 along the cylinder surface. Correspondingly, the fluid is also dragged towards x=0 along the conducting surface to form such vortical flows around the cylinder.

4.3.3 TRANSIENT DEVELOPMENT OF BULK CONCENTRATION POLARIZATION

It has been confirmed that significantly charging of EDL around conductors can induce bulk electrolyte concentration gradient (Bazant et al., 2004; Chu and Bazant, 2006). In addition, they also indentified two competing time scales, $\lambda_D a / D_{ref}$ for RC charging of EDL and a^2 / D_{ref} for bulk diffusion, for this transient process. The detailed characteristics of the formation and spreading of

concentration gradient in the present system are also shown in Figure 4.5. Once the external field is turned on, the bulk electrolyte concentration just outside the EDL is depleted to supply counterions for the charging of EDL. As time evolves to t=1 (or at the dimensional time of $\lambda_D a / D_{ref}$), more counterions are needed for charging the EDL and the bulk concentration of electrolyte is further reduced and simultaneously the zone of reduced electrolyte concentration is expanded. It also should be noted that at this stage the surface conduction also becomes important due to enhanced ionic concentration in the EDL. Additionally, such enhanced surface conduction needs to be balanced with enhanced normal fluxes of ions into EDL, which provides a boost for the formation of bulk concentration gradients. As time evolves further (from $\lambda_D a / D_{ref}$ to a^2 / D_{ref}), bulk neutral electrolyte slowly diffuses back to the depleted zone, leading to a slightly increase in the electrolyte concentration outside the EDL. During replenishment of the depleted zone, concentration polarization gradually spreads away from the cylinder surface to the bulk electrolyte, at the same time the EDL gradually relaxes to its steady state. Figure 4.5 (b) depicts the ionic concentrations of both ions at t =100, the portion with different concentrations of cations and anions represents the nonelectroneutral EDL, and the portion with equal concentrations of both ions represents the bulk concentration polarization. When the equilibrium state is reached, a steady state concentration polarization zone is established in the bulk electrolyte. The above characteristics for the concentration polarization play an important role in the charging process of the EDL. As revealed by Bazant et al. (2004) and Chu and Bazant (2006), the bulk diffusion was first induced by the EDL charging which requires the preferential

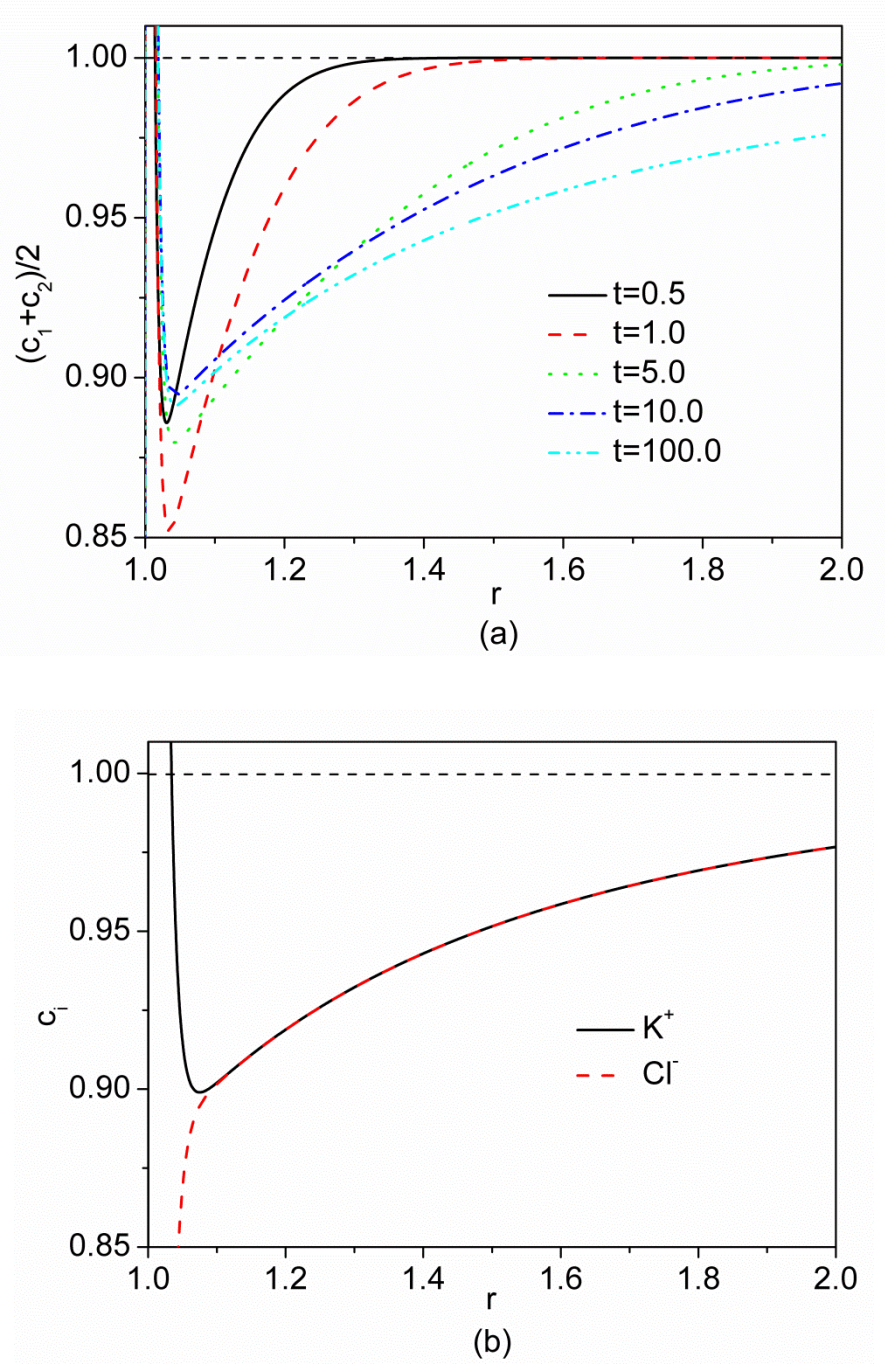

Figure 4.5 Formation and spreading of the bulk concentration polarization along radial direction at θ=π when $D_r \to \infty$, φ_0=50 and κa=100. (a) Transient development of concentration polarization; (b) Concentration distributions for cations and anions at t=100.

adsorption of counterions, and then in turn helps to relax and stabilize the EDL charging process. The coexistence of two time scales leads to nonmonotonic time evolutions of relevant quantities, which has the generic manifestation that the

relevant quantities increase quickly to their maximums after the RC time scale, and then gradually relax to the steady state at a much larger bulk diffusion time scale. This would explain the nonmonotonic time characteristics of surface charge density presented in Figure 4.3.

Figure 4.6 shows the effects of relevant model parameters on the steady state concentration polarization inside the bulk electrolyte solution. As shown in Figure 4.6 (a) and (b), the concentration polarization is enhanced with the

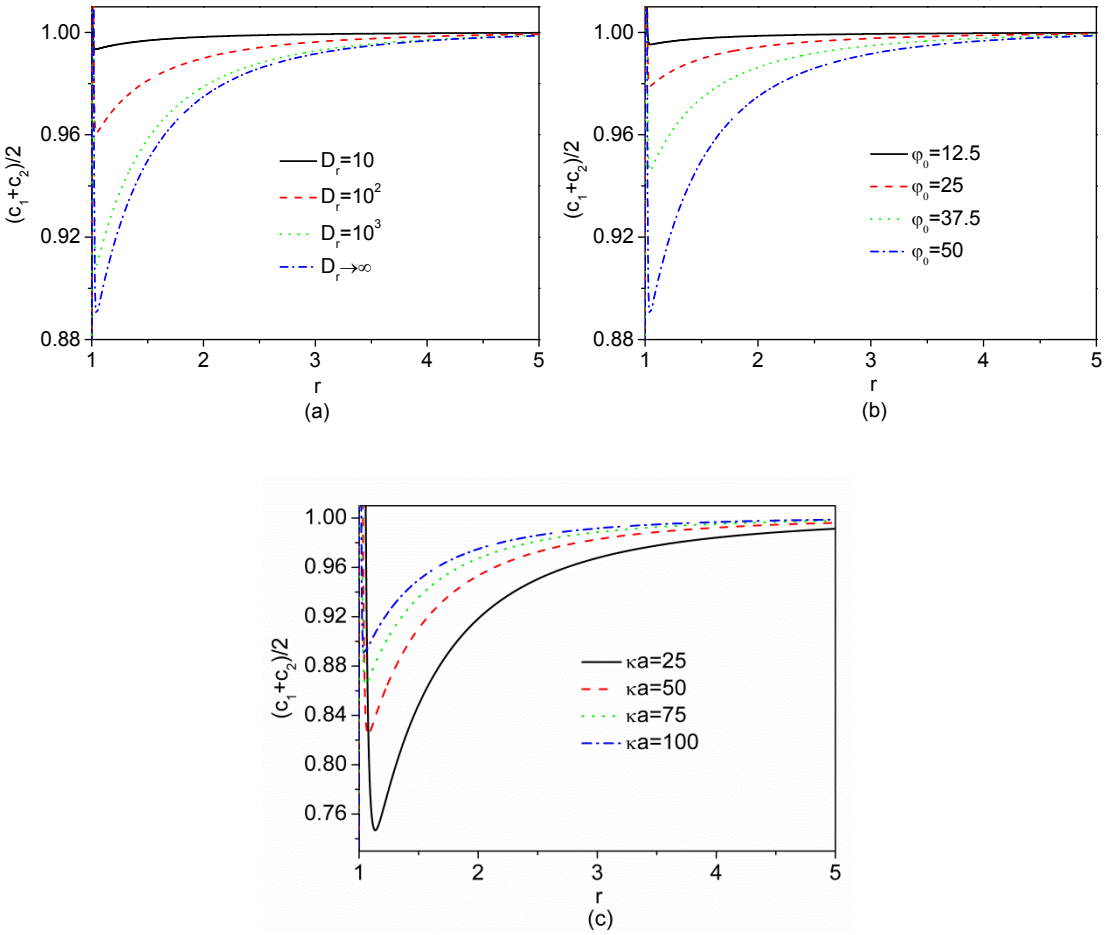

Figure 4.6 Effect of relevant model parameters on the steady state bulk concentration polarization along radial direction at θ=π. (a) Effect of D_r on the bulk concentration polarization when φ_0=50 and κa=100; (b) Effect of φ_0 on the bulk concentration polarization when $D_r\to\infty$ and κa=100; (c) Effect of κa on bulk concentration polarization when φ_0=50 and $D_r\to\infty$.

increase of polarizability of the cylinder and/or the externally applied voltage. For situations of low polarizability (D_r=10) and low voltage (φ_0=12.5), the bulk concentration polarization is insignificant, because the induced surface charge on the cylinder surface is not high enough to attract sufficient counterions from the bulk to create bulk concentration gradients. For the effect of κa shown in Figure 4.6(c), it is evident that the cylinder with a thicker EDL (such as κa=25) produces more significant concentration polarization. The surface conduction is more pronounced for the thicker EDL. At the steady state, the larger surface conduction also needs to be balanced with a larger normal flux of ions into EDL which depletes the electrolyte concentration near the cylinder surface more significantly, and consequently produces a larger concentration polarization. Our conclusions here certainly extend those of Bazant et al. (2004) and Chu and Bazant (2006) to a more general situation. In their work, only the effect of the applied voltage is elucidated, and they concluded that for weak applied fields, the bulk concentration polarization only appears as a first-order correction to the uniform background concentration, and thus can be negligible. However, for strong applied fields, it should be noted that the bulk concentration polarization becomes comparable to the background concentration, and therefore cannot be ignored.

4.3.4 EFFECTS OF RELEVANT PARAMETERS ON TRANSIENT CHARGING CHARACTERISTICS OF ELECTRIC DOUBLE LAYER

Figure 4.7 presents the effects of relevant model parameters on the transient charging of EDL around polarizable dielectrics. As indicated in Figure 4.7 (a), the net charge density in the EDL is higher for cylinders with higher dielectric

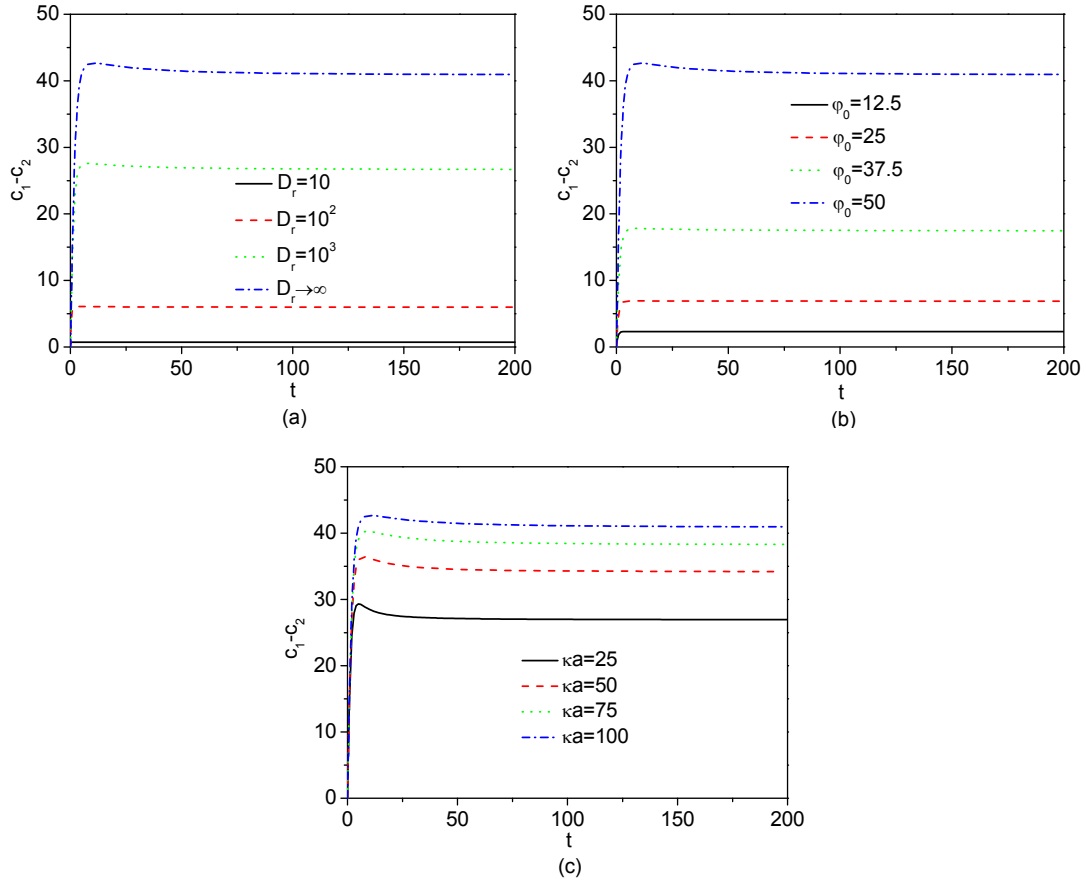

Figure 4.7 Effect of relevant model parameters on transient charging of EDL around dielectric cylinders. (a) Effect of D_r on the net charge density on cylinder surface at r=1, θ=π when φ_0=50 and κa=100; (b) Effect of φ_0 on the net charge density on cylinder surface at r=1, θ=π when D_r→∞ and κa=100; (c) Effect of κa on the net charge density on cylinder surface at r=1, θ=π when φ_0=50 and D_r→∞.

constants. For a dielectric cylinder with relativity low polarizabilities (D_r=10 and 10^2), the charge density on the cylinder surface at r=1, θ=π increases monotonically from zero to its steady state value. While for a dielectric cylinder with relatively high polarizabilities (D_r=10^3 and ∞), the net charge density rapidly reaches a maximum value after the initial *RC* charging process, and then slowly decays toward its limiting value during the spreading of bulk concentration polarization. For the low driving voltages (φ_0=12.5 and 25), the time characteristics of net charge density are similar to those of low

polarizabilities, and the time characteristics of net charge density at high voltages (φ_0=37.5 and 50) are similar to those of high polarizabilities. Actually, the influence of the two model parameters, D_r and φ_0, on the transient charging of EDL is inherently the same. For high values of D_r and φ_0, the cylinder surface is strongly polarized with high surface charge density, which needs to be neutralized by the higher net charge density inside the EDL. In addition, the higher charge density and associated surface conduction inside the EDL can induce larger bulk concentration polarization which is responsible for the nonmonotonic time characteristics of the net charge density. For low voltages and polarizabilities, the induced concentration polarization is insignificant and the nonmonotonic time characteristics of the net charge density disappear. For the effect of κa, it is seen from Figure 4.7 (c) that there is more significant reduction of net charge density for the thick EDL after the initial RC charging process, which is again due to the more significant concentration polarization for the thick EDL.

4.3.5 EFFECTS OF RELEVANT PARAMETERS ON STEADY STATE FLOW FIELD

Figure 4.8 details the effects of relevant model parameters on the magnitude of induced-charge electroosmotic velocity at the steady state. It is seen from Figure 4.8 (a) and Figure 4.8 (b) that the magnitude of velocity increases with the increase of the applied voltage and/or the dielectric constant of the cylinder. It is understandable that the surface charge density on the cylinder surface increases with the increase of the polarizability and/or the externally applied voltages. Then the enhanced surface charge induces much higher double layer charge density which in turn interacts with the external field to produce stronger flows.

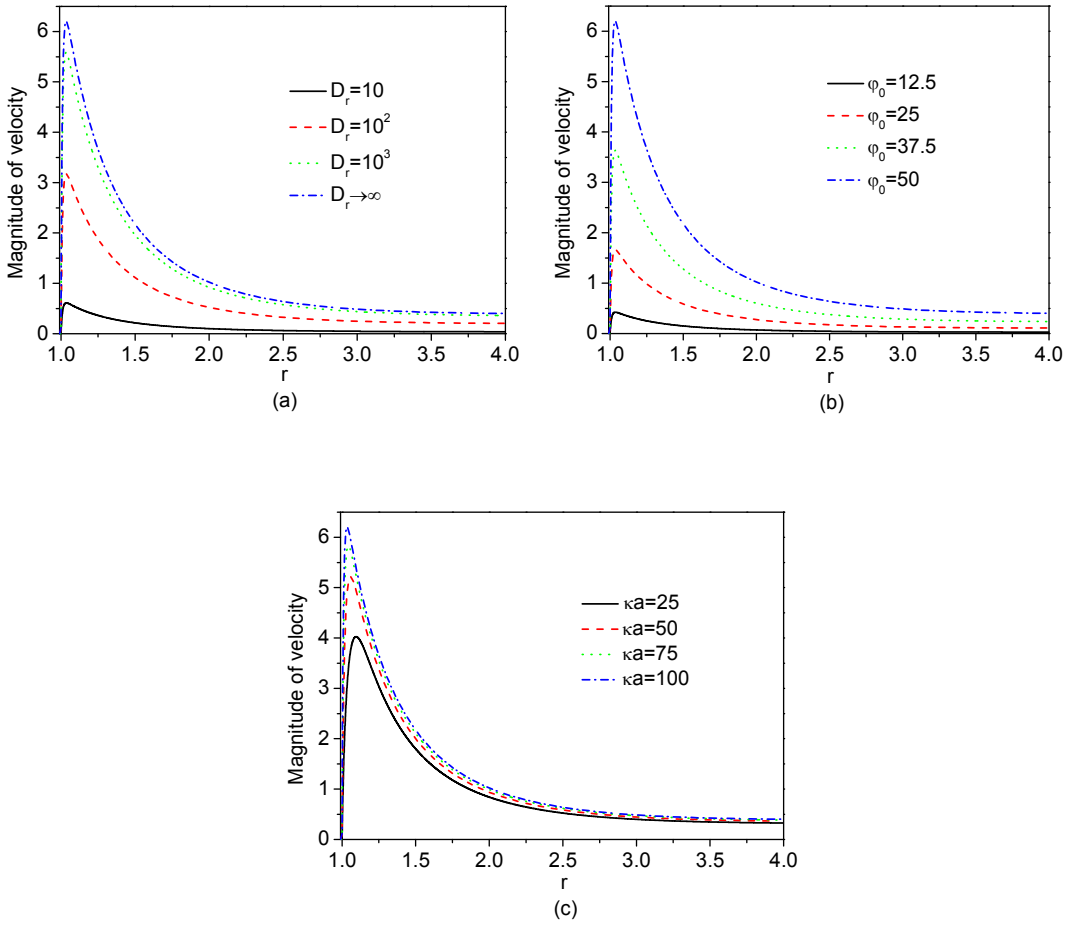

Figure 4.8 Effect of relevant model parameters on the magnitude of velocity at the steady state along the radial direction at θ=π/4. (a) Effect of D_r on the steady state velocity when φ_0=50 and κa=100; (b) Effect of φ_0 on the steady state velocity when D_r→∞ and κa=100; (c) Effect of κa on the steady state velocity φ_0=50 and D_r→∞.

For a perfectly polarizable dielectric cylinder (Dr→∞), the velocity at the outer edge of EDL reaches a maximum value of around 6.2. The studies reported in the literature mainly focused on the perfectly polarizable solids. Here, we consider a more general case which includes the solids spanning the entire spectrum of dielectric constant. In addition, a careful examination of the dependence of fluid velocity on the external electric field shown in Figure 4.8 (b) suggests that the maximum velocity at the outer edge of EDL is proportional to φ_0^2. This feature is the typical behavior of induced-charge electrokinetics and defines the

nonlinearity of induced-charge electrokinetics. As indicated in Figure 4.8 (c), the dimensionless velocity increases with the increase of κa, especially inside the EDL near the cylinder surface. This is because a larger κa induces a larger net charge density in the EDL as indicated in Figure 4.7 (c), then the larger net charge density is driven by the external field to generate stronger flows.

We note that for thin EDL situations, such as κa= 500 in the model validation presented in Appendix A, the velocity attains the maximum very near the conducting surface (at the outer edge of the EDL). It is shown that the numerical results agree well with those from the slip velocity model which is based on the assumption of vanishingly small EDL (κa→∞). In the practical microfluidic applications with large values of κa (usually in order of about 1000), the flow field only in the bulk electrolyte domain is relevant and usually the velocity distribution inside the thin EDLs becomes less important. Then in modeling of the flow field of induced-charge electroosmosis under thin EDL situations, a slip velocity boundary condition on the conducting surface is usually prescribed for the momentum equation and the velocity variation inside the EDL is neglected. However, this picture is not true for cases with relatively thick EDLs (such as κa=25, 50, and even 75 and 100) for which the location with the maximum velocity leaves away from the cylinder surface. Consequently, the thickness of EDL cannot be neglected, and also the velocity change inside the EDL becomes crucial when determining of the whole flow field inside the electrolyte domain. Thus, the slip velocity approximation is no longer valid under such circumstance. The complete model presented here is valid for arbitrary EDL thickness and certainly resolves this difficulty.

4.4 SUMMARY

The transient dynamics of EDL charging and fluid flow around polarizable dielectrics are addressed numerically. The modeling relies on the solution of basic equations governing electrokinetics in a fully coupled manner, and thus negates the need for invoking the popular assumptions made on induced-charge electrokinetic phenomena. Different from the classic linear electrokinetics in which the surface charge density (or zeta potential) is due to pure physiochemical mechanism, the surface charge density in induced-charge electrokinetics around dielectrics is induced by the polarization of dielectrics by external electric fields. Here we focus on the induced-charge effect and the physiochemical bond charge is taken to be zero (q=0 in equation (4.13)), so the left hand of equation (4.13) represents the amount of induced surface charge density which is responsible for induced-charge electrokinetics around dielectrics. If the dielectrics are completely nonpolarizable ($D_r \rightarrow 0$), equation (4.13) reduces to the electric boundary condition used in conventional linear electrokinetics. Our model is valid for arbitrary thickness of EDL and can resolve details inside the EDL which are necessary for understanding induced-charge electrokinetic phenomena around polarizable dielectrics with nanometer scales.

A case study is performed to investigate the dynamics of induced-charge electrokinetics around a floating conductive cylinder ($Dr \rightarrow \infty$). At the initial state, the cylinder is polarized symmetrically with the conducting surface on the anode side of external electric field acquiring negative surface charges and that on the cathode side of external electric field acquiring positive surface charges. These surface charges trigger the charging of the EDL around the conducting cylinder.

The transient charging of EDL can be generally divided into two stages because of the two time scales inherent to the system. At the first stage (the so-called RC charging), surface charge density on the conducting surface increases to neutralize the increasing net charge density inside the EDL. At the second stage (the so-called bulk diffusion), surface charge density gradually decrease a bit to its steady sate value due to the decrease of EDL charge density, which is caused by the bulk diffusion of neutral electrolyte. At steady state, the charge density stored in the EDL is high enough to screen the external electric field and the charging process stops. For a particular case of floating conductive cylinder, our results show that the basic flow pattern for induced-charge electroosmosis around the conducting cylinder involves four symmetric vortices which start very near the conducting surface and diffuse into bulk electrolyte solution during the EDL charging.

According to Appendix A, our numerical model substantiates the classic description of induced-charge electroosmosis around conductors with thin EDLs using the slip velocity approach. However, the validity of the slip velocity approach is limited to the situations where the condition (2.13) holds, i.e. thin EDL and low induced zeta potentials. These conditions in real microfluidic applications can be easily violated, and significant surface conduction and bulk diffusion render the slip velocity approach invalid. The complete numerical model presented in this chapter provides a general description of induced-charge electrokinetics.

Although the complete model is quite general for characterization of induced-charge electrokinetics, the numerical solution of this model at very large κa

poses challenges. For very large values of κa (very thin EDLs), the gradients of electric potential, velocity and ionic concentration are extremely drastic inside EDLs, which then requires extremely dense mesh system inside the EDL to capture such gradients. Therefore, the computational load is increased significantly, and the numerical model becomes inefficient and sometimes unusable. Fortunately, as suggested by equation (2.13), the slip velocity approach is valid as long as the EDL is thin enough. Our numerical model is efficient for the situations where thicker EDLs are involved.

At last, it is evident from the mathematical formulation that induced-charge electrokinetics is also electrolyte dependent. However, existing theoretical work assumed that the electrolyte is symmetric and has the same diffusion coefficient of cations and anions. These assumptions make their predictions only applicable to limited electrolytes, such as KCl. Our complete model can be applicable to any binary electrolytes (symmetric or asymmetric), though KCl is chosen in our case study. A promising direction for the future reach is to investigate the effects of electrolyte on transient behaviors of EDL charging and the induced electrokinetic flow. With the asymmetric electrolyte and the mismatch of the diffusion coefficients of cations and anions, it should be expected that the symmetric characteristics of EDL charging and fluid flow around the cylinder are to be violated.

CHAPTER 5: INDUCED-CHARGE ELECTROKINETIC PHENOMENA IN CONDUCTING NANOFLUIDIC CHANNELS*

5.1 INTRODUCTION

Nanofluidics offers promising opportunities for the control of ionic and molecular species transport and the detection/sensing of single biomolecules (Duan and Majumdar, 2010; Kovarik and Jacobson, 2009; Schoch et al., 2008; Sparreboom et al., 2009). As one of channel dimensions shrinks down to nanometric scale, forces and phenomena that are absent or negligible in larger microchannels, may play dominant roles. Then fluidic devices integrated with nanometer-sized channels can provide new analytical functions. To successfully design nanofluidic devices, one needs to consider several critical effects including localized enhancement of electric field, double-layer overlap and the resulting ion selectivity, enhanced diffusion as well as increased influence of surface-to-volume ratio, surface charge, and entropy. Based on these effects, nanofluidic devices can improve routine processing and add new functionalities to microfluidic devices (Kovarik and Jacobson, 2009).

A characteristic length scale for the electric double layer (EDL), the Debye length, κ^{-1} (usually in the range of 1 to 100 nm) is responsible for difference between microfluidics and nanofluidics. For microfluidic channels, the Debye

* This chapter is a combination of two electronic preprints submitted to **arXiv**: Cunlu Zhao and Chun Yang, Electroosmosis in conducting nanofluidic channels, arXiv:1007.1216v3 ; Cunlu Zhao and Chun Yang, Induced charge electrokinetic phenomena in tapered conducting nanochannels, arXiv:1008.1310v1.

length is much thinner than the channel height h ($\kappa h \gg 1$), the ion concentration inside the majority of channel domain is the same as the bulk concentration. For nanofluidic channels, the channel height becomes comparable to or much smaller than the Debye length, where $\kappa h \ll 1$, counterions predominates over coions inside the channel and the average concentration of counterions in a nanochannel c was found to mainly depend on the surface charge density q of the channel walls: $c = 2|q|/(N_A e h)$ (Yan et al., 2009), N_A being the Avogadro constant. Thus the transport of ions in nanofluidic channels is dominated by the surface charges (Plecis et al., 2005; Stein et al., 2004).

In conventional electrokinetic phenomena, the intrinsic surface charge is determined by physiochemical properties of the surface and the solution. The control of surface charge is only possible by changing the physiochemical properties of the surface (the density/chemical composition of the groups on the solid surface) and the solution (the pH, ion type and ionic concentration of the bulk solution). When a solid surface is conductive, the surface charge however can be actively controlled by applying a potential difference between the electrolyte solution and the solid surface (Mruetusatorn et al., 2009; Nishizawa et al., 1995). Squires and Bazant (2004) adopted the similar idea to modify zeta potential (an indicator of surface charge) on the conducting surface by applying a potential difference between the conducting surface and electrolyte solution, and they named this technique as fixed potential induced-charge electrokinetics. In this method of surface charge modification, since the gate electrode is in direct contact with the electrolyte solution, it is also termed direct contact gate control (DCGC) technique in this thesis. The DCGC technique bears similarity to flow FET

reviewed in Chapter 2. Nevertheless, gate electrodes in DCGC are deposited on the walls and thus are in direct contact with electrolyte solutions, and gate electrodes in the FET technique are separated from electrolyte solutions by insulating layers. In DCGC technique, the gate voltage induces the electric double layer on the gate electrode (assumed to be ideally polarizable). Such electric double layer can be effectively seen as a charged capacitor at small DC voltages (Mruetusatorn et al., 2009). In analogy to the capacitor charging, the quantity and polarity of the ionic charges inside EDL at the gate can be modulated by changing the gate voltage, thus adjusting electroosmotic velocity at that location. Because the gate electrode directly contacts the fluid, the DCGC technique operates at much lower voltages as compared with the FET method which usually encounters the large voltage drop over the insulation layer. Very recently, the modulation of the zeta potential in microfluidics using DCGC for electroosmotic flow control was experimentally demonstrated by Mruetusatorn et al. (2009) and Plecis et al. (2010), and the voltages they applied on the gate are much lower than those used in the FET method and the highest voltage is only 2V. Like the flow FET technique, the DCGC technique also can be naturally extended to control nanofluidic systems.

In the first part of this chapter, a novel DCGC technique for nanofluidics is developed by virtue of induced-charge electrokinetics, and its flexibility in manipulating both ionic transport and fluid flow through the straight nanochannels is demonstrated. While in practical applications the channels typically have asymmetrical shapes, and hence there is also increasing interest in transport through asymmetrical nano pores or channels (Perry et al., 2010; Siwy

et al., 2004; Vlassiouk and Siwy, 2007; White and Bund, 2008; Yusko et al., 2009). In the second part of this chapter, a fundamental study of the ICEK inside a tapered conducting nanochannel is performed, and its applications for manipulating both ionic species transport and fluid flow are theoretically investigated. Qualitative as well as quantitative changes in the ionic transport and flow characteristics due to varying degrees of the applied electric bias and the taper angel of channel walls are studied, and further insights into mechanisms of the relevant phenomena are discussed.

5.2 ELECTROOSMOSIS IN STRAIGHT CONDUCTING NANOCHANNELS

5.2.1 NANOFLUIDIC SYSTEM DESIGN AND PROBLEM FORMULATION

The nanofluidic system design is presented in Figure 5.1. The parallel-plate nanochannel with a length of L and a height of 2h is fabricated on an insulating substrate, and the conducting wall can be formed by coating conducting materials, such as diamond-like carbon and Au, on the nanochannel walls (Evtukh et al., 2006; Piruska et al., 2008; Piruska et al., 2010). Electric wires connect the two power sources, the two driving electrodes (with the right driving electrode grounded) and the two conducting nanochannel walls (a.k.a. gate electrodes). There are two DC power sources in the nanofluidic system, power source 1 is used to set up the external electric field for driving the flow along the nanochannel, and power source 2 is designed to perform the DCGC to regulate the charge content and polarity inside the nanochannel. When the switch is off, the conducting nanochannel walls are floating in the external driving electric field, while when the switch is on, the electric potential on the conducting wall can be adjusted and so are the charge content and polarity

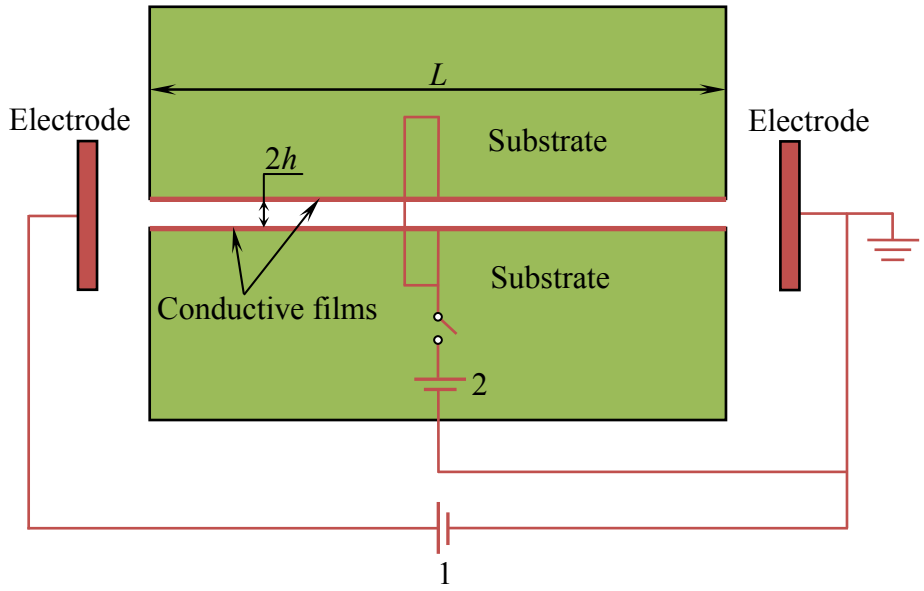

Figure 5.1 Schematics of the nanofluidic system equipped with the DCGC. The nanochannel with dimension of L×2h is formed in an insulating substrate and then the walls are coated with conductive (ideally polarizable) films. There are two power sources in the circuit, power source 1 is used to set up the external driving electric field for the flow inside the nanochannel and power source 2 is used to adjust the wall potential of the conducting nanochannel. Moreover, the two power sources are connected to the same ground. When the switch is in off-state, the conductive nanochannel walls float in the external driving electric field. When the switch is in on-state, the potential on conductive nanochannel walls can be arbitrarily controlled.

inside the nanochannel. The nanochannel is connected to two reservoirs filled with the KCl solution with a bulk concentration, c_0. We will restrict our analyses to cases with equal concentrations of ions, c_0, in both reservoirs, thus eliminating any contribution of osmosis to the nanofluidic system.

For the purpose of nondimensionalizing the governing equations, we respectively introduce the following reference quantities for electric potential, velocity, pressure, electric current density, electric current and surface charge density

$$\varphi = \frac{k_B T}{e},\ u_{ref} = \frac{\varepsilon_0 \varepsilon_r \varphi_{ref}^2}{\mu L_{ref}},\ p_{ref} = \mu \frac{u_{ref}}{L_{ref}},\ i_{ref} = N_A e u_{ref} c_{ref},\ I_{ref} = N_A e u_{ref} c_{ref} L_{ref},$$

$$q_{ref} = \varepsilon_0 \varepsilon_r \frac{\varphi_{ref}}{L_{ref}} \tag{5.1}$$

as well as Reynolds number for liquid flow and Peclet number for ionic species transport

$$Re = \frac{\rho u_{ref} L_{ref}}{\mu} \qquad Pe = \frac{u_{ref} L_{ref}}{D_{ref}} \tag{5.2}$$

where L_{ref}, c_{ref} and D_{ref} denote the reference length, the reference ionic concentration and the reference ionic diffusion coefficient, respectively. All of these reference scales are to be specified later. φ_{ref} is the so-called thermal voltage with a value of 25.7mV at the room temperature. In equations (5.1) and (5.2), e is the elementary charge, k_B is the Boltzmann constant, N_A is the Avogadro constant, ε_r, ρ and μ are the dielectric constant, density and dynamic viscosity of the electrolyte solution, respectively. T and ε_0 represent the absolute temperature and electric permittivity of free space, respectively.

The electric potential and the net charge density are related by the Poisson equation which can be expressed in the nondimensional form as

$$\nabla^2 \varphi = -\frac{1}{2}\left(\kappa L_{ref}\right)^2 \sum_{i=1,2} z_i c_i \tag{5.3}$$

where c_i and z_i are the dimensionless concentration and valence of ions (i=1 corresponds to cations and i=2 corresponds to anions), respectively. κ is the inverse of Debye length given by

$$\kappa = \sqrt{\frac{2 c_{ref} N_A e^2}{\varepsilon_0 \varepsilon_r k_B T}} \tag{5.4}$$

The Nernst-Plank equation governs the ionic transport in electrolyte solution domain. At the steady sate, it can be written in the dimensionless form for ions as

$$Pe\left(\mathbf{u}\bullet\nabla c_i\right) = D_i\nabla^2 c_i + D_i z_i\nabla\bullet\left(c_i\nabla\varphi\right) \tag{5.5}$$

where $\mathbf{u}$ is the velocity vector and has two components (u, v) respectively along x and y directions.

The steady state flow field in the fluid domain is governed by the continuity and Navier–Stokes equations which can be written in dimensionless forms as

$$\nabla\bullet\mathbf{u} = 0 \tag{5.6}$$

$$Re\left(\mathbf{u}\bullet\nabla u\right) = -\nabla p + \nabla^2\mathbf{u} - \frac{1}{2}\left(\kappa L_{ref}\right)^2\nabla\varphi\sum_{i=1,2} z_i c_i \tag{5.7}$$

where p is the pressure and the third term on the right-hand side of equation (5.7) represents the electrostatic body force due to the non-electroneutrality in the electrolyte solution. Although the Reynolds number in nanofluidics is vanishingly small (estimated as $\mathrm{Re}\sim 10^{-4}$ in this work), the convection term of momentum transport on the left-hand side of equation (5.7) is still retained for completeness. Besides, we would highlight that electrothermal effect on the flow (Ramos et al., 1998) is left out here to just concentrate on the induced-charge effect.

If the concentration field for the ionic species and the velocity field for electrolyte solution are known, the dimensionless ionic current density vector of the ion species i can then be expressed as

$$\mathbf{i}_i = \mathbf{u}z_i c_i - \frac{1}{Pe} z_i D_i\nabla c_i - \frac{\nabla\varphi}{Pe} z_i^2 D_i c_i \tag{5.8}$$

where i=1 (2) corresponds to cations (anions).

And the total electric current for the ionic species i can be obtained by integrating the current density over the cross section of nanochannel

$$I_i = \int_{s_1} i_{i,x} ds_1 \tag{5.9}$$

where $i_{i,x}$ denotes the x component of the current density vector given in equation (5.8) and s_1 is the surface element for the cross section of the nanochannel. The nanochannel shows cations selective function when $|I_1| > |I_2|$ and anions selective function when $|I_1| < |I_2|$, while $I_1 = I_2$ corresponds to a nonselective nanochannel (Vlassiouk et al., 2008a, b).

It should be noted that momentum and ionic transport problems and the electric problem are strongly coupled via the governing equations (5.3), (5.5)and (5.7). The complete model presents a general mathematical description of electrokinetic phenomena and is valid for any thickness of EDL, any kind of electrolyte and any values of surface charge density. The model requires one to simultaneously solve the coupled equations including the Poisson equation(5.3), the Nernst–Planck equation (5.5) and the Navier-Stokes equation (5.7). The similar complete model has been successfully adopted to characterize ionic transport behavior in nanochannels (Daiguji et al., 2003; Daiguji et al., 2004; Qian et al., 2007; White and Bund, 2008) and ICEO mixing in microchannels (Jain et al., 2009).

5.2.2 DESCRIPTION OF THE SIMULATION DOMAIN AND THE BOUNDARY CONDITIONS

The whole system shown in Figure 5.1 is symmetric with respect to the nanochannel center line (y=0). In order to reduce the computational cost, only the lower half of the nanochannel is simulated, see Figure 5.2. We consider the symmetric electrolyte KCl with z_1=-z_2=1 in the simulations. c_{ref} is set to be the bulk ionic concentrations inside the reservoirs, c_0. L_{ref} is chosen as the half channel height h. The reference ionic diffusion coefficient D_{ref} is chosen as 10^{-9} m^2/s and then the normalized ionic diffusion coefficients for two ionic species are D_1= 1.957 and D_2= 2.032 (Masliyah and Bhattacharjee, 2006), respectively. The solution is the room-temperature (T=298K) water, then it can be calculated that Pe=5.10 ×10^{-1} and Re=5.66×10^{-4}. In all the simulations, we set L/h=200 and the electrokinetic parameter $\kappa L_{ref} = \kappa h = 1$, which indicates that the channel dimension is comparable to the thickness of the Debye length and is in nanometric scale. These values of L/h and κh can be representative of a typical case in which we have a nanochannel of height 2h=30nm and length L=3μm with a bulk ionic concentration of c_0= 4.1×10^{-4} M inside two reservoirs and the nanochannel.

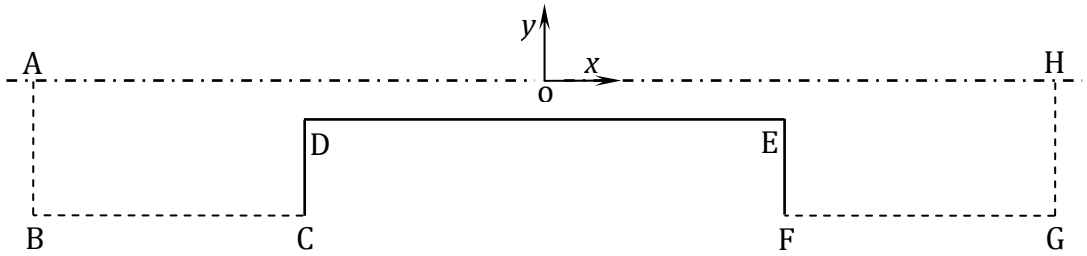

Figure 5.2 The simulated domain and the relevant boundaries. Due to the symmetry, only the lower half channel is simulated here to reduce the computational cost. The Cartesian coordinates (x, y) are normalized with respect to the half channel height h.

To complete the formulation, the relevant boundary conditions are needed for the Poisson equation, the Nernst-Planck equation and the Navier-Stokes

equation.

On the symmetric boundary AH, a symmetric boundary condition is used for the electric potential in the electrolyte solution (see Figure 5.2)

$$\mathbf{n}\cdot\nabla\varphi=0 \text{ on the boundary AH} \tag{5.10}$$

where **n** represents the unit outward normal to the corresponding planes.

Along the boundary AB, the electric potential is specified as

$$\varphi = \varphi_0 \text{ on the boundary AB} \tag{5.11}$$

and the potential, φ_0, is known a priori and can be adjusted by the power source 1 shown in Figure 5.1. Along the boundary GH, the potential is set to zero (i.e., grounded as shown in Figure 5.1) as the reference potential

$$\varphi = 0 \text{ on the boundary GH} \tag{5.12}$$

The surfaces of BC and FG are far away from the nanochannel and thus can be assumed to be in the bulk electrolyte solution. Besides, the walls of the reservoirs (planes CD and EF) do not carry fixed electric charge, so no charge boundary conditions for the potential are used

$$\mathbf{n}\cdot\nabla\varphi=0 \text{ on the boundaries BC, CD, EF and FG} \tag{5.13}$$

Along the conducting walls of the nanochannel, two kinds of boundary conditions are considered: (i) if the switch in Figure 5.1 is in off-state, the conducting wall floats in the electric field set up by the two driving electrodes inside two reservoirs. Then the floating boundary condition for the potential is used (Stratton, 1941)

$$\int_{s_2} (\mathbf{n} \bullet \nabla \varphi) ds_2 = Q \text{ on the boundary DE} \quad (5.14)$$

where Q is the overall dimensionless free surface charge acquired by the conductor surface before the application of the external electric field. Specifically, Q is normalized with respect to $\varepsilon_0 \varepsilon_r \varphi_{ref}$. s_2 stands for the surface element for the boundary DE and is normalized with respect to L_{ref}. Equation (5.14) constrains the total charge on the conducting surface. In the present work, the conducting wall of the nanochannel is uncharged and thus Q =0 is used. (ii) While when the switch is in on-state, the electric potential on the conducting wall is constrained by the power source 2, and the following boundary condition applies

$$\varphi = \varphi_1 \text{ on the boundary DE} \quad (5.15)$$

On the boundaries of AB and GH, the concentrations of two ionic species are identical to the bulk concentration of electrolyte solution in the reservoirs, namely

$$c_i = 1 \text{ on the boundaries AB and GH} \quad (5.16)$$

At the walls of two reservoirs the nanochannel (boundary segments CD, DE, and EF in Figure 5.2), ions cannot penetrate through the solid surfaces, and hence ionic fluxes (electric current) normal to the rigid walls are set to zero

$$\mathbf{n} \bullet \left(\mathbf{u} c_i - D_i \nabla c_i / Pe - D_i z_i c_i \nabla \varphi / Pe \right) = 0 \text{ on the boundaries CD, DE, and EF} \quad (5.17)$$

It is assumed that segments BC and FG are far from the nanochannel inlet (outlet) and in the bulk electrolyte solution. Consequently, zero normal flux is used for the Nernst–Planck equations

$$\mathbf{n}\cdot\left(\mathbf{u}c_i - D_i\nabla c_i / Pe - D_i z_i c_i \nabla\varphi / Pe\right) = 0 \text{ on the boundaries BC and FG} \quad (5.18)$$

On the symmetric boundary AH, a symmetric boundary condition applies to the Nernst–Planck equations

$$\mathbf{n}\cdot\left(\mathbf{u}c_i - D_i\nabla c_i / Pe - D_i z_i c_i \nabla\varphi / Pe\right) = 0 \text{ on the boundary AH} \quad (5.19)$$

Finally, boundary conditions for the hydrodynamic problem governed by equations (5.6) and (5.7) are prescribed. On the solid walls of the nanochannel and the reservoirs (boundary segments CD, DE, and EF in Figure 5.2), the liquid sticks on the solid surfaces and thus nonslip boundary conditions (i.e., u = v = 0) are specified. Normal pressure with p =0 is set on the boundaries AB and GH because there is no externally applied pressure difference between two reservoirs. A symmetric boundary condition is used along the boundary of symmetry, AH. Finally, because boundaries BC and FG are in the bulk electrolyte solution and are not affected by the nanochannel inlet and outlet, slip boundary conditions are then used on these boundaries to indicate that there are no viscous drag effects at these boundaries.

It should be noted that the floating boundary condition and the fixed potential boundary condition are used on the conducting wall of nanochannel for the Poisson equation, instead of the surface charge density boundary condition used for the classic electrokinetics in nanochannels. Potentials on the left driving electrode and the conducting wall are denoted as φ_0 and φ_1, respectively. All the governing equations are strongly coupled and thus solved with the commercial finite element software package Comsol Multiphysics 3.4, and the details of numerical method and model validation are provided in Appendix B.

5.2.3 RESULTS AND DISCUSSION

5.2.3.1 ELECTROOSMOSIS IN CONDUCTING NANOCHANNELS WITH FLOATING WALLS (MODE 1)

Under this situation, the switch in Figure 5.1 is in off-state and the conducting walls float in the external driving field set by φ_0. Figure 5.3 depicts the electric potential and ionic concentrations along the nanochannel axis for the case of floating conducting wall when the system is positively biased with $\varphi_0 = 6$. It is observed that the electric potential drops along the axial direction and two potential barriers exist at the two junctions connecting the nanochannel and the two reservoirs. Furthermore, Cl^- is depleted to be slightly less concentrated than the bulk ionic species right after the left nanochannel-reservoir junction. In the nanochannel, the concentration of Cl^- increases to reach its maximum, and then

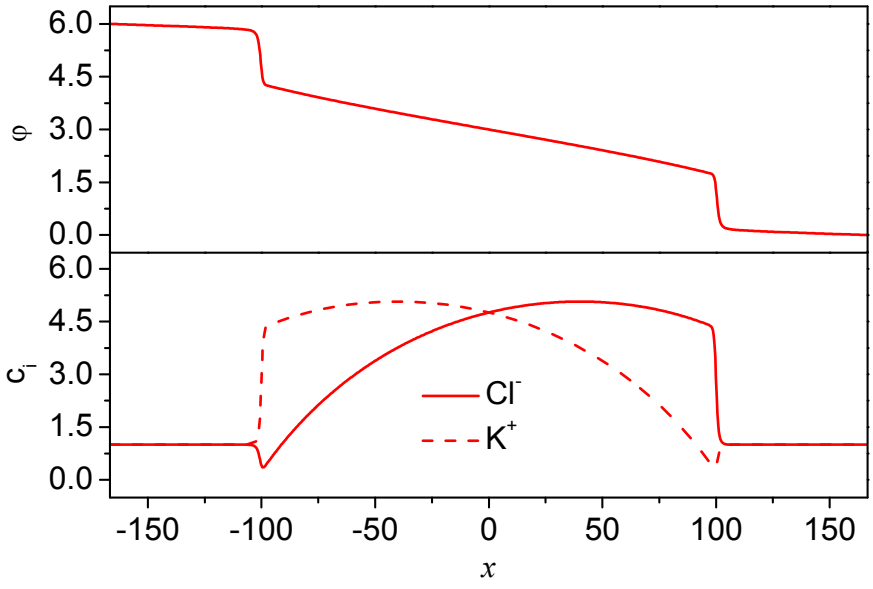

Figure 5.3 Electric potential φ and ion concentration c profiles along the nanochannel axis (y=0) for mode 1 when the conducting walls are floating under a positively electric bias of $\varphi_0 = 6$.

gradually decreases. At the right nanochannel-reservoir junction, the concentration of Cl^- reduces sharply to the bulk ionic concentration. For K^+, the concentration distribution can be seen as a mirror image of the concentration distribution for Cl^- with respect to x=0. It is also manifested that in the right half of the nanochannel, the concentration of the anions is higher than that of the cations; while in the left half of the nanochannel, the concentration of the cations is higher than that of the anions. At the middle point of the nanochannel (x=0), the cations and the anions have the same concentration. In the two reservoirs, the solution is electrically neural and the cations and anions are with the same scaled bulk concentration of unity. The corresponding flow characteristics inside the nanochannel are shown in Figure 5.4. The pressure in Figure 5.4 (a) exhibits a symmetric distribution with respect to the middle of nanochannel (x=0) where the pressure also attains its maximum. Figure 5.4 (b) indicates two flow circulations inside the nanochannel, one in the right half of the nanochannel and the other in the left half of the channel, which suggests a stagnant plane at the middle of the nanochannel. These features lead to no net flow through the nanochannel. In addition, Figure 5.5 is prepared to interpret the physics involved in Figure 5.3 and Figure 5.4. If the nanochannel is positively biased as shown in Figure 5.5 (b), upon imposing the external electric field, the conducting nanochannel wall is simultaneously polarized with the right-half of the wall surface acquiring positive charges and the left-half of the wall surface acquiring negative charges (see Figure 5.5 (a)). These induced surface charges can also play the roles of the natural physiochemical bound surface charges in conventional electrokinetics (Bazant and Squires, 2004; Squires and Bazant, 2004). Then in order to neutralize these induced surface charges, in the solution

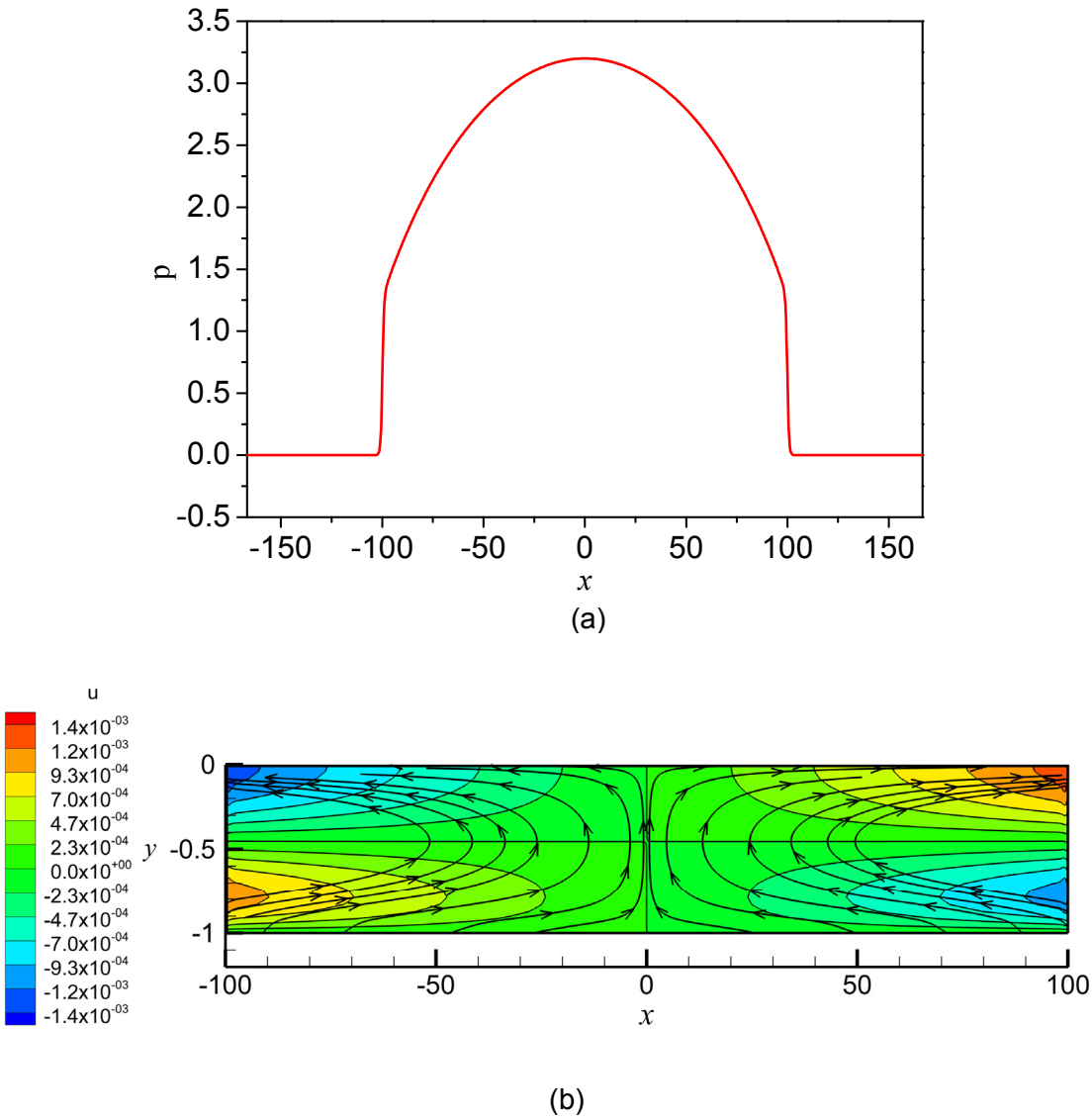

Figure 5.4 Flow characteristics in conducting nanochannels with floating walls when the electric bias $\varphi_0 = 6$. (a) Pressure p distribution along the nanochannel axis (y=0) and (b) the contour plot for the velocity component in the x direction, u. The solid lines in (b) with arrows are the stream lines.

domain, the anions predominate inside the right-half of the channel and the cations predominate inside the left-half of the channel. The interactions of the external electric field with the nonzero charge densities inside two halves of the nanochannel give rise to two net electric body forces which both point to the middle of the nanochannel. These two body forces drive the liquid solution to move towards the middle of the channel, so two opposite pressure gradients in

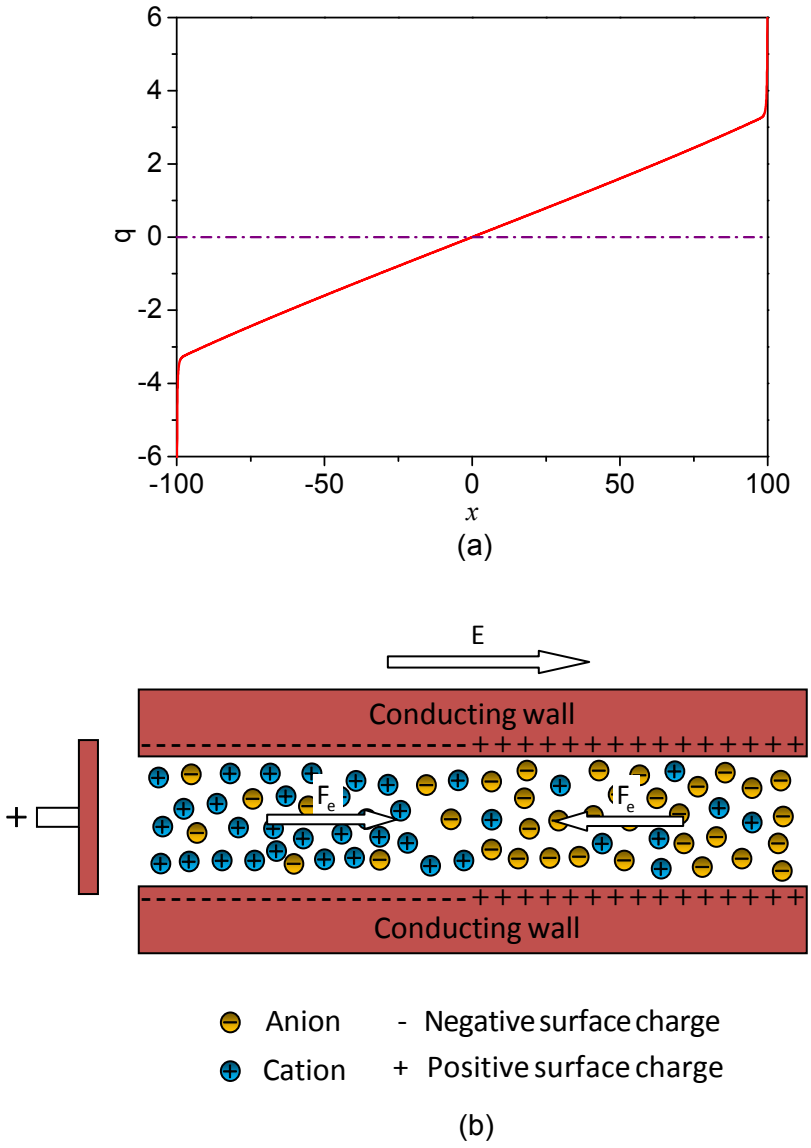

Figure 5.5. Physical interpretation of the results presented in Figure 5.3 and Figure 5.4. (a) The induced surface charge density q from the computation due to the polarization along the floating conducting nanochannel walls for positively biased case of $\varphi_0 = 6$. (b). Schematics of the simple model for the interpretation of induced-charge electrokinetics in a nanochannel with its conducting walls floating in an external driving electric field. As soon as the system is positively biased (see from the left to the right), the conducting walls are simultaneously polarized with positive induced surface charge on the right half of the channel walls and negative induced surface charge on the left half of the channel walls. To neutralize these surface charges, there should be surplus anions inside the right half of the nanochannel and surplus cations inside the left half of the nanochannel. Then the interactions of the external electric field E with the nonzero charge densities inside two halves of the nanochannel result in two identical electrostatic body forces Fe on the electrolyte solution which both direct to the right middle of the nanochannel.

the two halves of the nanochannel shown in Figure 5.4 (a) must be induced to maintain the mass continuity. Finally, the induced pressure gradients push the solution away from the middle of the channel to form the two flow circulations. The flow characteristics under the negatively biased situation ($\varphi_0 = -6$) are shown to be identical to those under the positively biased situation ($\varphi_0 = 6$). For the negatively biased situation provided in Appendix B, it can be seen from Figure B. 2 (b) that the polarization of the conducting wall reverses as compared with the positively biased case, and so do the direction of external electric field and the predominant charge polarities inside the two halves of the nanochannel (see Figure B.2 (a)). Hence both the magnitude and direction of two net electric body forces remain the same as those in the positively biased case. Consequently, the identical flow field is repeated for the negatively biased case.

5.2.3.2 ELECTROOSMOSIS IN CONDUCTING NANOCHANNELS WITH WALL POTENTIAL CLOSER TO φ_0 (MODE 2)

In mode 1, the potential on the wall is constrained by the floating boundary condition. According to electrostatics, it is known that the uncharged floating conducting walls are equipotential and the potential on the walls reads exactly $\varphi_0/2$. In addition, the uncharged floating conducting wall is exactly half negatively polarized and exactly half positively polarized. Alternatively, one can intentionally control the voltage on the conducting wall φ_1 through power source 2 to deviate from $\varphi_0/2$, and consequently the symmetry in the polarization of the conducting all (as shown in Figure 5.5(a)) is broken with longer portion of the channel wall positively (negatively) charged and the shorter portion of the channel wall negatively (positively) charged. Then if φ_1 is

set to be closer to φ_0, i.e., $|\varphi_0| > |\varphi_1| > |\varphi_0|/2$, one can expect that the operating characteristics of the nanofluidic system will differ from those in the situation of floating walls. Specifically, the positively biased case with $\varphi_1 = 4$ and $\varphi_0 = 6$ is demonstrated here, and the results for the corresponding negatively biased case ($\varphi_1 = -4$ and $\varphi_0 = -6$) are provided in Appendix B. For the positively biased case shown in Figure 5.6, the potential decreases along the nanochannel. Here the potential on the conducting wall is controlled to be closer to $\varphi_0 = 6$. Then the potential drop across the left nanochannel-reservoir junction is less significant than that across the right nanochannel-reservoir junction. Ionic concentrations for both cations and anions change drastically across two junctions connecting the nanochannel and the two reservoirs, and inside the two reservoirs the ionic concentrations for both ions reach the same bulk value of unity to ensure the electroneutrality of solution. Inside the longer right portion of the nanochannel, the concentration of anions (Cl^-) is higher that of cations (K^+), while only inside the relatively shorter left portion of the nanochannel, the cations have higher concentration. These ionic distribution characteristics can be quite understandable as a result of the surface charge density shown in Figure 5.6 (b). With the wall potential biased close to φ_0, the symmetric wall polarization in the floating case is modified with the shorter left portion of the wall negatively polarized and the longer right portion of the wall positively polarized. Compared to the symmetric flow characteristics in mode 1, the flow characteristics in mode 2 are asymmetric as shown in Figure 5.7. For example, the location with maximum pressure in Figure 5.7 (a) shits to the right of the middle point of the nanochannel (x=0). In addition, the pressure experiences more drastic drop

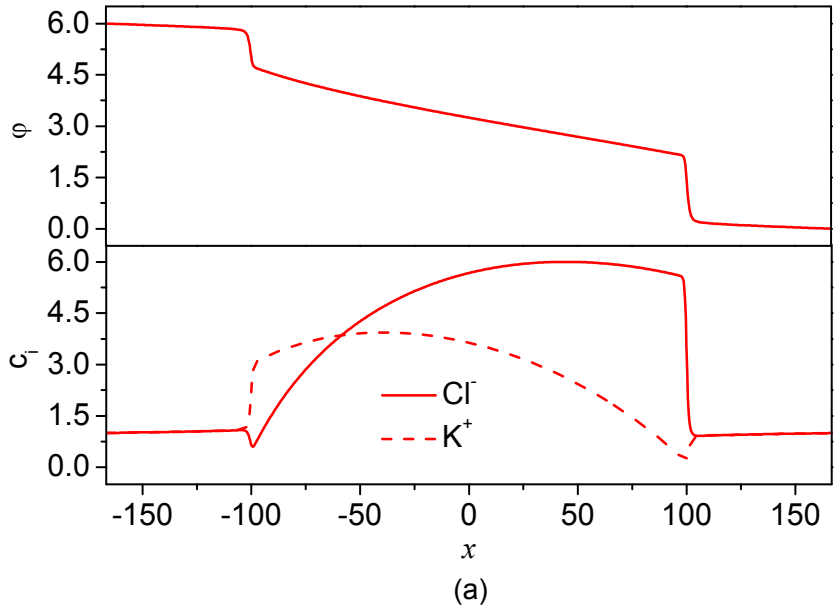

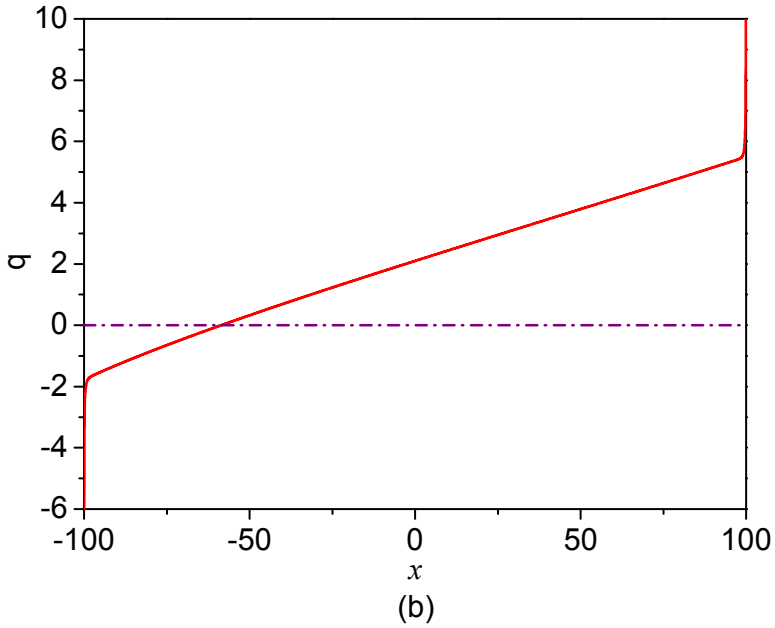

Figure 5.6 The results for mode 2 when the potential on the conducting walls is set to be closer to φ_0 for the positively biased case of $\varphi_0 = 6$, $\varphi_1 = 4$. (a) Electric potential φ and ion concentration c profiles along the nanochannel axis (y=0) and (b) Surface charge density q along the conducting wall.

at the right nanochannel-reservoir junction, and still remains zero inside two reservoir domains. Also witness that the solution flows in the negative x direction (Figure 5.7(b)) with a normalized flow rate (the reference flow rate

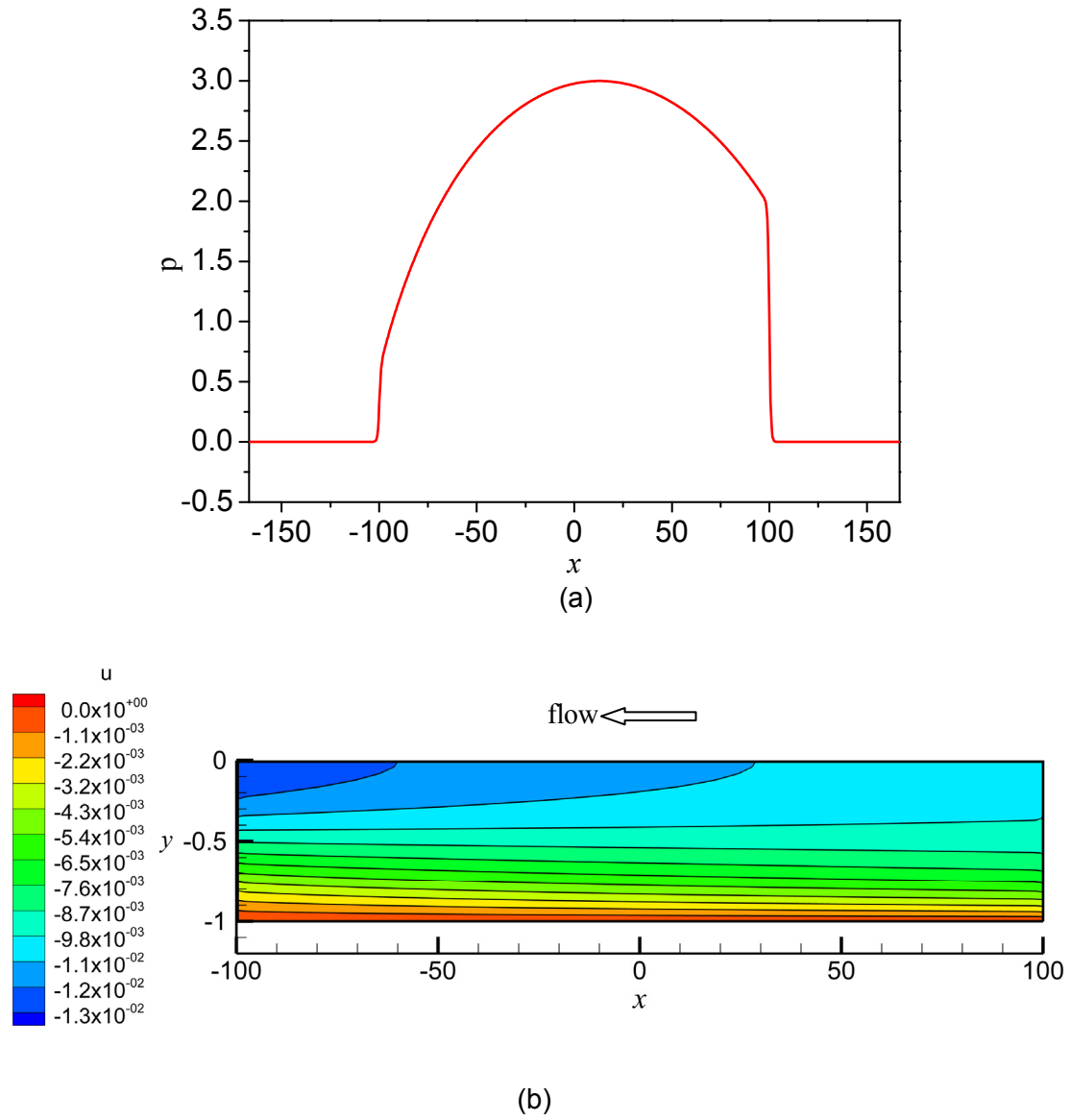

Figure 5.7 Flow characteristics in conducting nanochannels with wall potential closer to φ_0 for the positively biased case of $\varphi_0 = 6$, $\varphi_1 = 4$. (a) Pressure p distribution along the nanochannel axis (y=0) and (b) the contour plot for the velocity component in the x direction, u.

is chosen as $u_{ref}h$) of 7.94×10^{-3}. It is also found that the flow characteristics under the positively biased case ($\varphi_1 = 4$ and $\varphi_0 = 6$) and the negatively biased case ($\varphi_1 = -4$ and $\varphi_0 = -6$) are identical. Overall, inside the nanochannel the anions predominate for the positively biased case while the cations predominate for the negatively biased case (see Figure B.3 (a)). However, considering the reversion

of direction of the electric fields under these two cases, the net body forces for these two cases are exactly the same (with the same magnitude and both point to the negative *x* direction), which explains the same flow characteristics under the positively and negatively biased cases.

5.2.3.3 ELECTROOSMOSIS IN CONDUCTING NANOCHANNELS WITH WALL POTENTIAL CLOSER TO THE GROUND (MODE 3)

Similarly, if φ_1 is set to be closer to the ground, i.e., $|\varphi_0|/2 > |\varphi_1| > 0$, it is also expected that the symmetries for ionic distributions and flow field in the situation of floating walls (mode 1) are to be broken. Specifically, this mode also has two scenarios, the positively biased case and the corresponding negatively biased case. Here, again only the simulation results for a positive biased case ($\varphi_1 = 2$, $\varphi_0 = 6$) are presented, and the results for the corresponding negative biased case ($\varphi_1 = -2$, $\varphi_0 = -6$) are provided in Appendix B. As displayed in Figure 5.8 (a), the potential for the positively biased case decreases along the nanochannel, which is similar to that depicted in Figure 5.6 (a) for mode 2. Since the potential on the wall is controlled to be closer to the ground in this case, the potential drop across the right nanochannel-reservoir junction is less significant than that across the left nanochannel-reservoir junction. Similar to mode 2, cationic and anionic concentration profiles become asymmetric. Inside the longer left portion of the nanochannel, the concentration of cations is higher than that of anions, and only inside the relatively shorter right portion of the nanochannel, the cations have lower concentration. In addition, the induced surface charge density on the conducting wall is presented in Figure 5.8 (b). The longer left portion of the wall is negatively polarized, while the relatively shorter

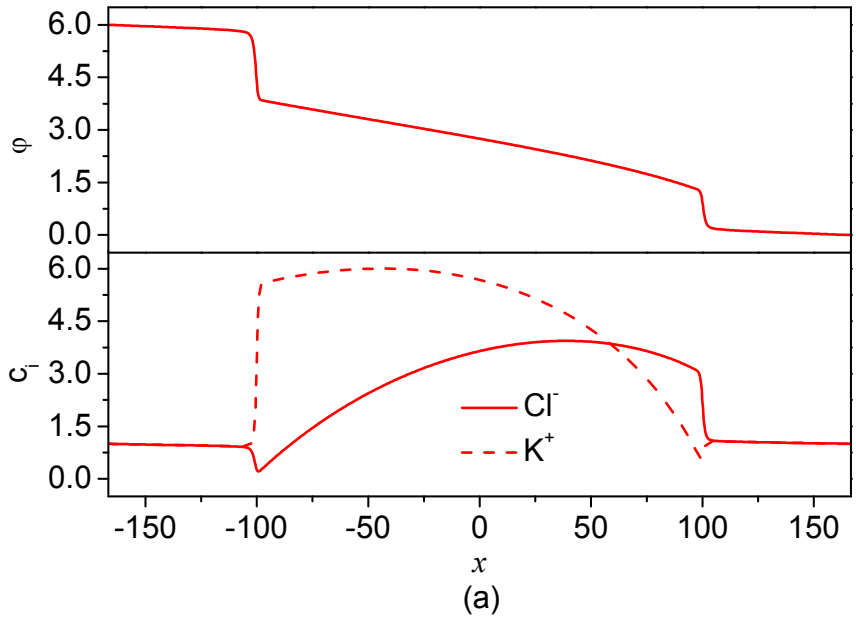

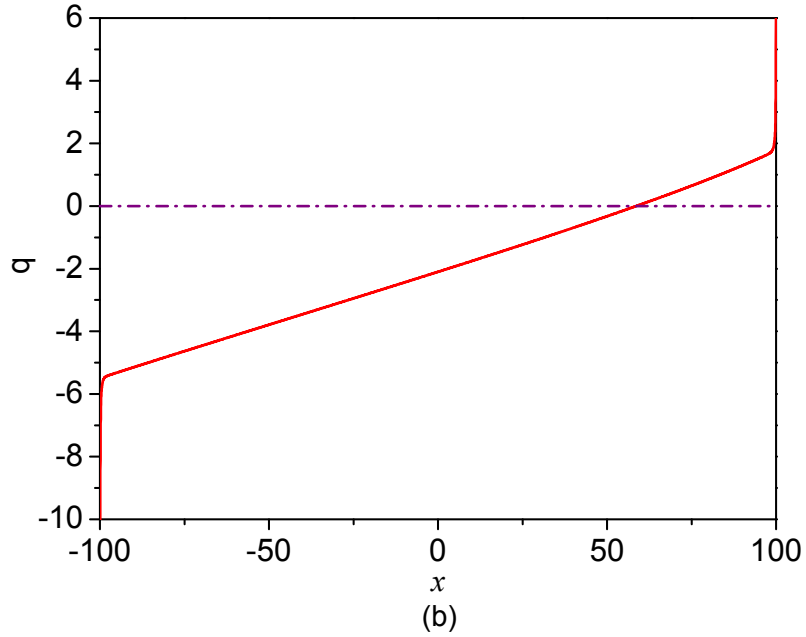

Figure 5.8 The results for mode 3 when the potential on the conducting walls is set to be closer to the ground for the positively biased case of $\varphi_0 = 6$, $\varphi_1 = 2$. (a) Electric potential φ and ion concentration c profiles along the nanochannel axis (y=0) and (b) Surface charge density q along the conducting wall.

right portion of the wall is positively polarized. It is clear that such surface charge density is responsible for aforementioned characteristics of ionic distribution.

The corresponding flow characteristics are presented in Figure 5.9 from which we identify that the symmetries in Figure 5.4 are also broken. As shown in Figure 5.9 (a), the location with the maximum pressure inside the nanochannel shifts to the left of the middle point (x=0), and there exists a net flow is in the positive x direction with a same normalized flow rate of 7.94×10^{-3} as in mode 2

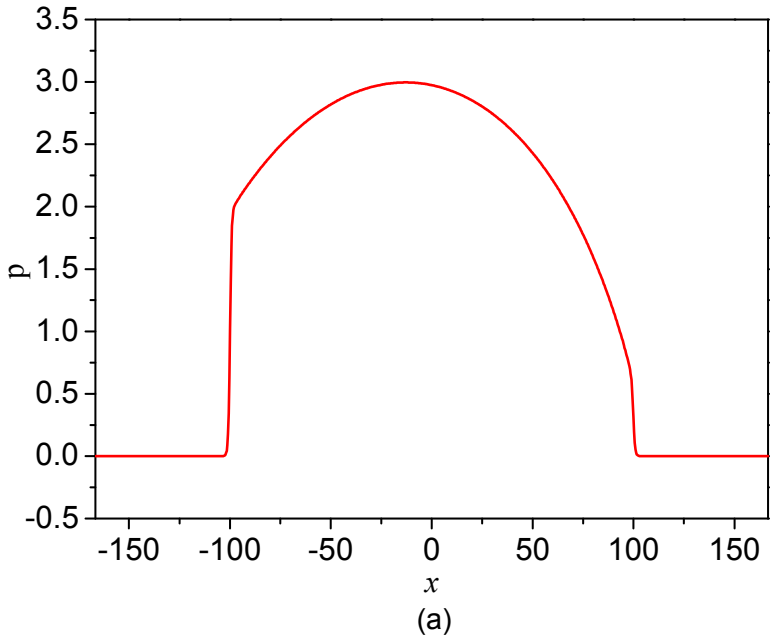

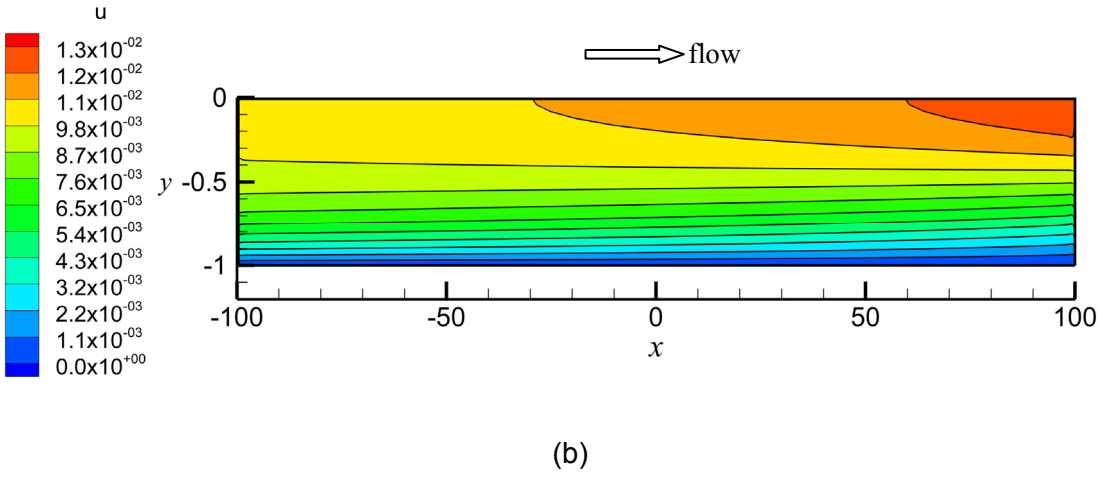

Figure 5.9 Flow characteristics in conducting nanochannels with wall potential biased closer to the ground for the positively biased case of $\varphi_0 = 6$, $\varphi_1 = 2$. (a) Pressure p distribution along the nanochannel axis (y=0) and (b) the contour plot for the velocity component in the x direction, u.

(see Figure 5.9(b)). All these flow characteristics in Figure 5.9 can be seen as the mirror images of those presented in Figure 5.7 for mode 2. In mode 3, the cations predominate inside the whole nanochannel for the positively biased case, and the anions predominate inside the whole nanochannel for the negatively biased case (see Figure B.4 (a)). These features are contrary to mode 2. Consequently, the net body forces for two cases in mode 3 both point to the positive x direction, which results in the flow reversion in mode 3 as compared to mode 2. Similarly, the flow characteristics are the same for the positively biased case and the negatively biased case in mode 3.

At last, to gain an in-depth quantitative understanding of ionic transport in the nanochannel with conducting walls, we summarize both cationic and anionic currents in Table 5.1 for three different operating modes. In the mode 1, the normalized ionic currents are in positive x direction for the positively biased case and in negative x direction for the negatively biased case. The magnitudes of the anionic currents are slightly larger than those of the cationic currents in both cases, indicating a weak anion selectivity of the nanochannel. This is caused by inequality of the diffusion coefficients of K^+ and Cl^-. More specifically, the diffusion coefficient of anion (Cl^-) is slightly larger than that of cation (K^+). If two types of ions have identical diffusion coefficient, the resultant two currents should be identical and the nanochannel would be nonselective. In modes 2 and 3, the positively biased case in mode 2 and the negatively biased case in mode 3 both exhibit anion selective characteristics, while the former selective process is in positive x direction and the latter selective process is in negative x direction. Similarly, the negatively biased case in mode 2 and the positively biased case in

mode 3 all exhibit cation selective characteristics, and the only difference is that the directions of the selective processes under these two operating conditions are opposite. We also note that, all the cation selective processes in modes 2 and 3 follow the flow, while anion selective processes resist the flow.

Table 5.1 Summary of the normalized ionic currents for both cations and anions under different operating conditions

Operating conditions \ Ionic currents		I_1	I_2
Mode 1	Positively biased	0.272	0.282
	Negatively biased	-0.272	-0.282
Mode 2	Positively biased	0.154	0.466
	Negatively biased	-0.451	-0.161
Mode 3	Positively biased	0.451	0.161
	Negatively biased	-0.154	-0.466

5.3 ELECTROOSMOSIS IN TAPERED CONDUCTING NANOCHANNELS

5.3.1 MODEL DESCRIPTIONS

We consider a two dimensional tapered nanochannel with a length L , the height of right opening $2h_2$ and the height of left opening $2h_1$, as shown in Figure 5.10. The nanochannel is fabricated on an insulating substrate, and the conducting wall can be formed by coating conducting materials, such as diamond-like carbon and Au, on the insulating substrate. The right driving electrode is grounded, and the potential on the left driving electrode is adjustable by a DC power source, which sets up the external electric field for

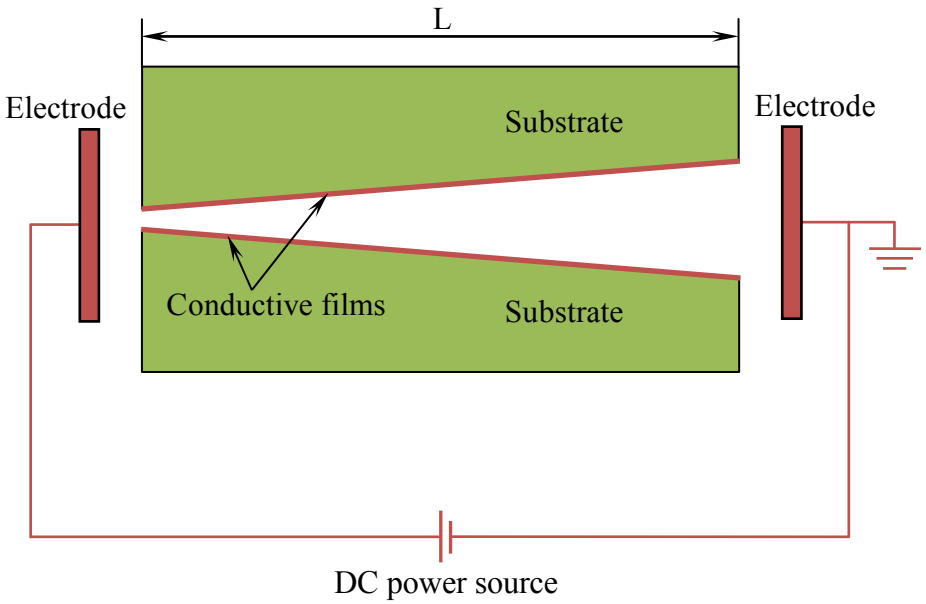

Figure 5.10 Schematics of the nanofluidic system with a conducting tapered nanochannel. The tapered nanochannel is formed in an insulating substrate and then the walls are coated with conductive (ideally polarizable) films. The length of the tapered nanochannel is L, the height of the left opening of the channel is $2h_1$ and the height of the right opening is $2h_2$.The power source is used to set up the external driving electric field for the flow inside the nanochannel. The right electrode is grounded and the driving electric field can be adjusted by changing the applied voltage on the left electrode. The conductive nanochannel walls float in the external driving electric field and is simultaneously polarized.

driving the flow along the nanochannel. The conducting nanochannel walls floating in the external driving electric field are polarized to acquire surface charges which can play the roles of physiochemical bond charges in the traditional electrokinetics (Bazant and Squires, 2004; Squires and Bazant, 2004). At each opening, the nanochannel is connected to a reservoir filled with the KCl solution with a bulk concentration, c_0. The electrolyte concentrations in two reservoirs are equal and thus osmosis is absent from the present system.

The governing equations are the same as those presented in section 5.2.1. Particularly, the ion selectivity of a single nanochannel is defined as (Vlassiouk et al., 2008a, b)

$$S = \frac{|I_1| - |I_2|}{|I_1| + |I_2|} \tag{5.20}$$

which ranges from -1 to 1. When S is in the range of (-1, 0), the channel show anion selective function, while when S is in the range of (0, 1), the channel shows cation selective function. Thus S would be 1 (-1) for a nanochannel that is perfectly cation (anion) selective and S=0 would correspond to a nonselective nanochannel. I_1 and I_2 represent the electric currents of cations and anions, respectively, and both of them can be calculated from equation (5.9).

5.3.2 DESCRIPTIONS OF THE SIMULATION DOMAIN AND THE BOUNDARY CONDITIONS

Since the whole system is symmetric with respect to the nanochannel center line, only the lower half of the nanochannel is simulated as sketched in Figure 5.11. The solvent is the room-temperature (T=298K) water and the solute is symmetric electrolyte KCl with z_1=-z_2=1. The reference ionic diffusion coefficient D_{ref} is chosen as 10^{-9} m^2/s and then the normalized ionic diffusion coefficients for two ionic species are D_1= 1.957 and D_2= 2.032 (Masliyah and Bhattacharjee, 2006), respectively. Then we can calculate that Pe=5.10 ×10^{-1} and Re=5.66×10^{-4}. Furthermore, c_{ref} is set to be the bulk ionic concentrations inside the reservoirs, c_0, and L_{ref} is chosen as the half height of the right opening h_2. In all the simulations, we set L/h_2=200 and the electrokinetic parameter $\kappa L_{ref} = \kappa h_2 = 1$, which ensures that the channel dimension is comparable to the thickness of EDL and is in nanometer scale. These nondimensional values of L/h_2 and κh_2 together with h_2/h_1=5 can represent a nanochannel system with geometric dimensions of $2h_1$=6nm, $2h_2$=30nm and L=3 μm, and a bulk ionic concentration of c_0= 4.1×10^{-4}

M in two reservoirs and the nanochannel.

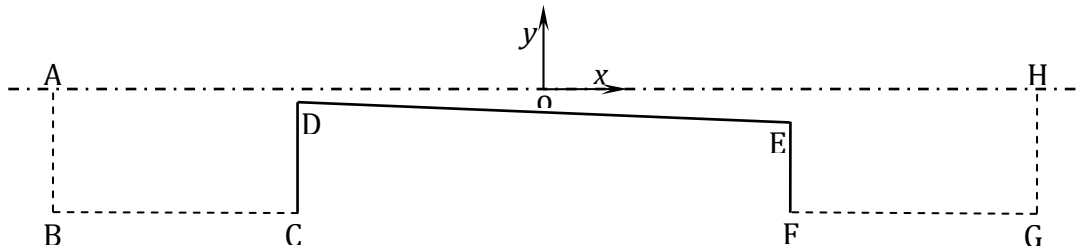

Figure 5.11 The sketch of simulated domain. The Cartesian coordinates (x, y) are normalized with respect to the half height of the right opening h_2.

For all boundary conditions associated with the hydrodynamic and electrostatic problems, they all are similar to those in section 5.2.2. The only difference is that the potential on the conducting wall is not actively controlled for the tapered nanochannel considered here; instead the conducting boundary DE in Figure 5.11 floats in the electric field and only the floating boundary condition (5.14) is used for the Poisson equation (5.3).

5.3.3 RESULTS AND DISCUSSION

5.3.3.1 ELECTROOSMOSIS IN CONDUCTING TAPERED NANOCHANNELS WITH FLOATING WALLS

Figure 5.12 depicts the electric potential and ionic concentrations along the centerline of nanochannel with floating conducting walls when the system is forwardly biased ($\varphi_0 = 6$) and reversely biased ($\varphi_0 = -6$) for $h_1/h_2 = 0.2$. For the forward bias situation in Figure 5.12 (a), the electric potential drops along the axial direction and two potential barriers exist at the two junctions connecting the nanochannel and the two reservoirs. Furthermore, the barrier at the narrow nanochannel-reservoir junction is more significant than that at the wide nanochannel-reservoir junction. It is also manifested that in the right half of the nanochannel, the concentration of the anions is slightly higher than that of the

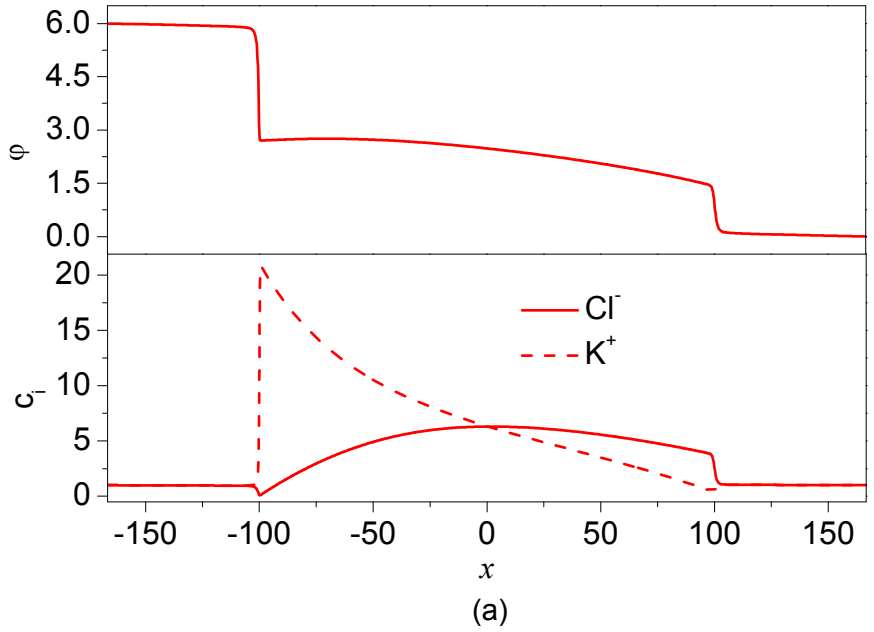

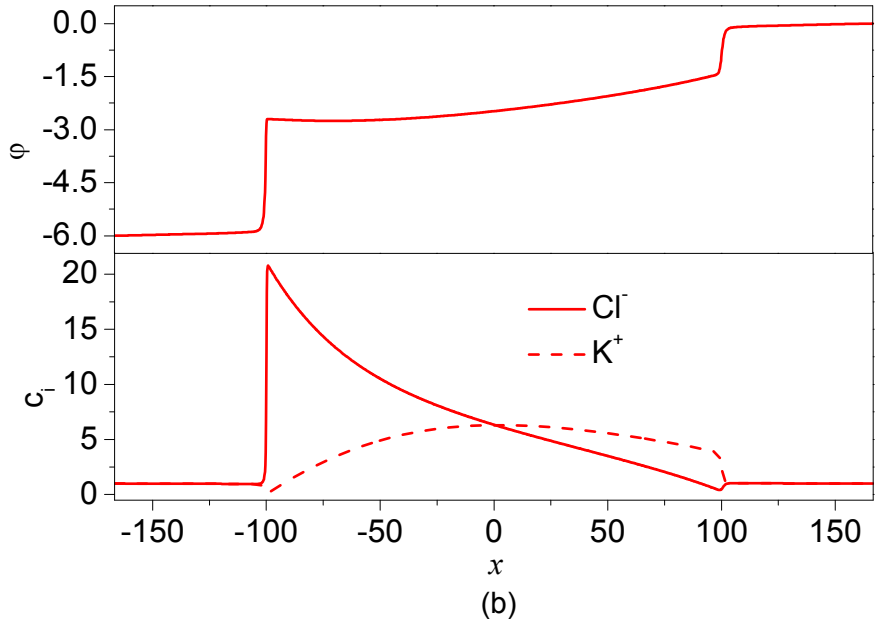

Figure 5.12 Electric potential φ and ion concentration c profiles along the nanochannel axis (y=0) when the conducting walls float in the externally applied electric field for (a) the forward biased case with electric potential φ_0=6 and (b) the reversely biased case with electric potential φ_0 = -6 .

cations; while in the left half of the nanochannel, the concentration of the cations is much higher than that of the anions. In the middle of the nanochannel, both the cations and the anions have the same concentration. In the two reservoirs, the

solution is electrically neural and thus the cations and the anions are with the same scaled bulk concentration of unity. When the system is reversely biased (Figure 5.12(b)), the electric potential grows along the axial direction and there are also two potential barriers at the junctions connecting the nanochannel and the two reservoirs. The ionic distributive characteristics inside the nanochannel can be obtained by simply interchanging the profiles of K^+ and Cl^- presented in Figure 5.12 (a). The corresponding flow characteristics inside the nanochannel are presented in Figure 5.13. It is found that the flow characteristics under the forward biased and reversely biased situations are identical. The pressure shown in Figure 5.13 (a) increases steeply from zero to its maximum at the left nanochannel-reservoir junction and then nonlinearly decreases along the nanochannel to the bulk value of zero in the right reservoir. As shown in Figure 5.13 (b), the axial velocity component u inside the whole nanochannel domain is positive, suggesting that the net flow is always from the narrow end to the wide end. This feature produces a same net flow through the nanochannel for electric biases of both polarities. If an alternating current bias is used to energize such nanofluidic system, the fluid stays flowing in the positive x direction at all instant times. By analogy with the full wave rectification in electricity(Nair, 2004) which converts both polarities of the input waveform to direct current, the present nanofluidic device functions effectively as a full-wave flow rectifier.

Furthermore, the induced surface charge density on the conducting wall of the tapered nanochannel is shown in Figure 5.14, which sheds light on the physics involved in Figure 5.12 and Figure 5.13. It can be seen that the conducting wall is half negatively polarized and half positively polarized for

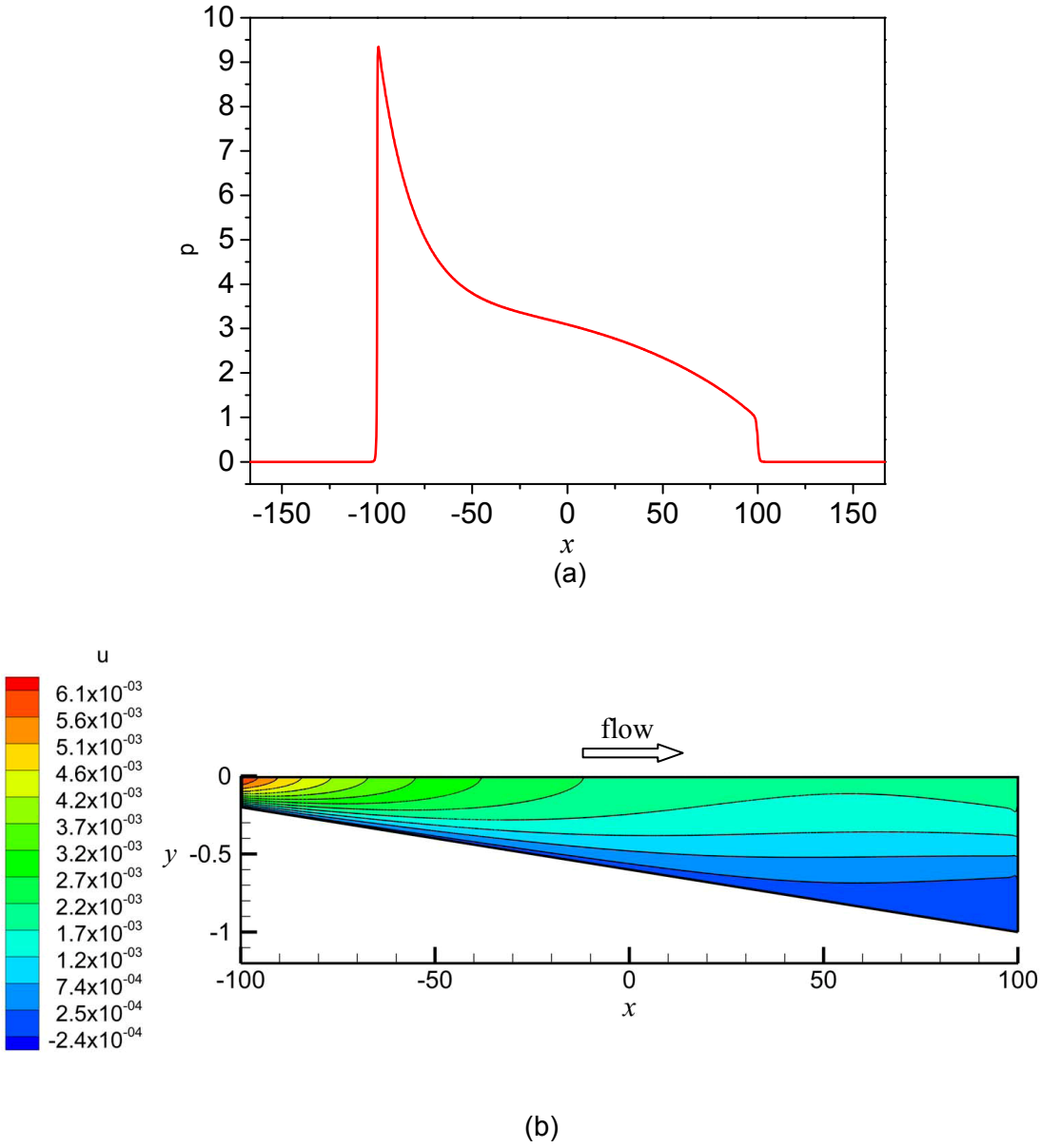

Figure 5.13 Flow characteristics in conducting tapered nanochannels with floating walls when the magnitude of the biased potential, $|\varphi_0| = 6$ (either forward biased or reversely biased). (a) Pressure p distribution along the nanochannel axis (y=0) and (b) the contour plot for the velocity component in the x direction, u.

electric biases of both polarities. These polarized surface charges will play the roles of the physiochemical bond surface charges in conventional fixed-charge linear electrokinetics. In other words, if the surface charge density depicted in Figure 5.14 is prescribed for the channel wall in the conventional fixed-charge electrokinetics, the resulting situation emulates the ICEK phenomena

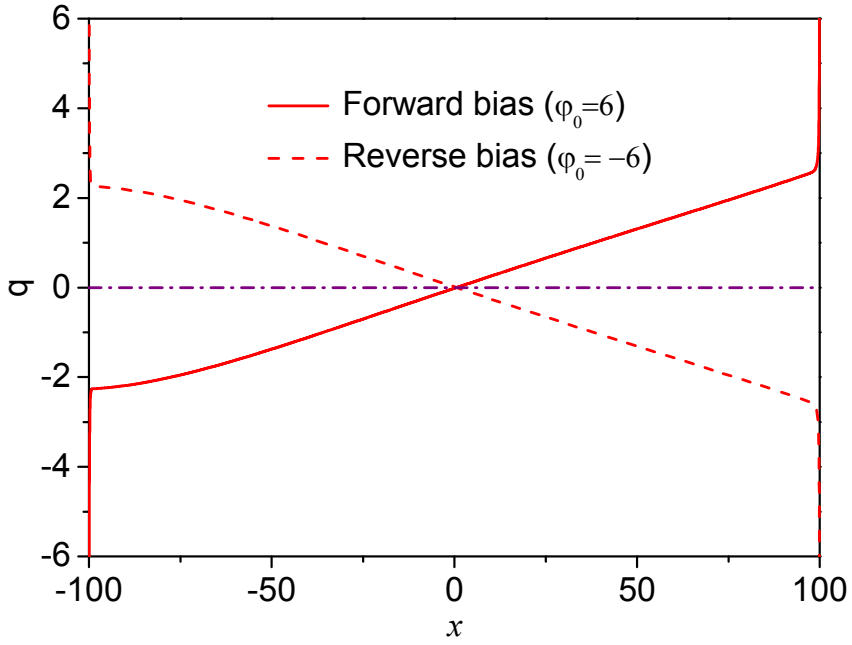

Figure 5.14 The induced surface charged density q along the conducting wall due to the polarization caused by the externally applied electric field for the forward bias of φ_0 = 6 and the reverse bias of φ_0 = -6 .

with the floating electric boundary condition on the conducting wall of tapered nanochannel. Subsequently, the forward biased case is interpreted to unveil the mechanism of ICEK inside the tapered nanochannel with conducting walls. Upon switching on the forward electric bias, the conducting nanochannel wall is instantaneously polarized with the right half of the wall surface acquiring positive charges and the left half of the wall acquiring negative charges. Then in order to neutralize these induced surface charges, in the solution domain, the anions predominate in the right half of the channel and the cations predominate in the left half of the channel. Due to the asymmetry of the nanochannel, the resulting positive net charge density in the left half of the narrower nanochannel outcompetes the negative net charge density in the right half of the wider nanochannel. The interactions of the external electric field with these two unequal charge densities inside two halves of the nanochannel give rise to a net

body force which directs to the positive x direction. This net body force drives the liquid solution to move from the narrow end to the wide end. For the reversely biased situation, the polarization of the conducting wall also reverses as shown in Figure 5.14, and so do the external electric field and the signs of charge densities inside the two halves of the nanochannel. It should be noted that the electric body force is a product of the electric field strength and the charge density, so simultaneous reversions of the direction of electric field and the sign of charge density do not affect both the direction and magnitude of the net electric body force. Consequently, the same flow field as the forward bias can be expected.

5.3.3.2 IONIC TRANSPORT AND FLOW CHARACTERISTICS INSIDE TAPERED CONDUCTING NANOCHANNELS

Figure 5.15 presents the effect of electric bias on the ionic transport characteristics and the flow rate. It is seen from Figure 5.15 (a) that, although the total ionic current shows no rectification, the corresponding cationic current and anionic current do exhibit rectifying behaviors. More specifically, the magnitude of the cationic current for the forward bias is larger than that for the reserve bias; while the magnitude of the anionic current for the forward bias is smaller than that for the reverse bias. Also identify from Figure 5.15 (a) that the cationic current is larger than the anionic current under the forwardly biased condition, which indicates a cation selective behavior, while the situation is completely contrary under the reversely biased condition where an anion selective behavior is exhibited. At last, to gain an in-depth quantitative understanding of ionic selective characteristics of the tapered nanochannel with conducting walls, the characteristics of ionic selectivity defined in equation (5.20) is depicted in

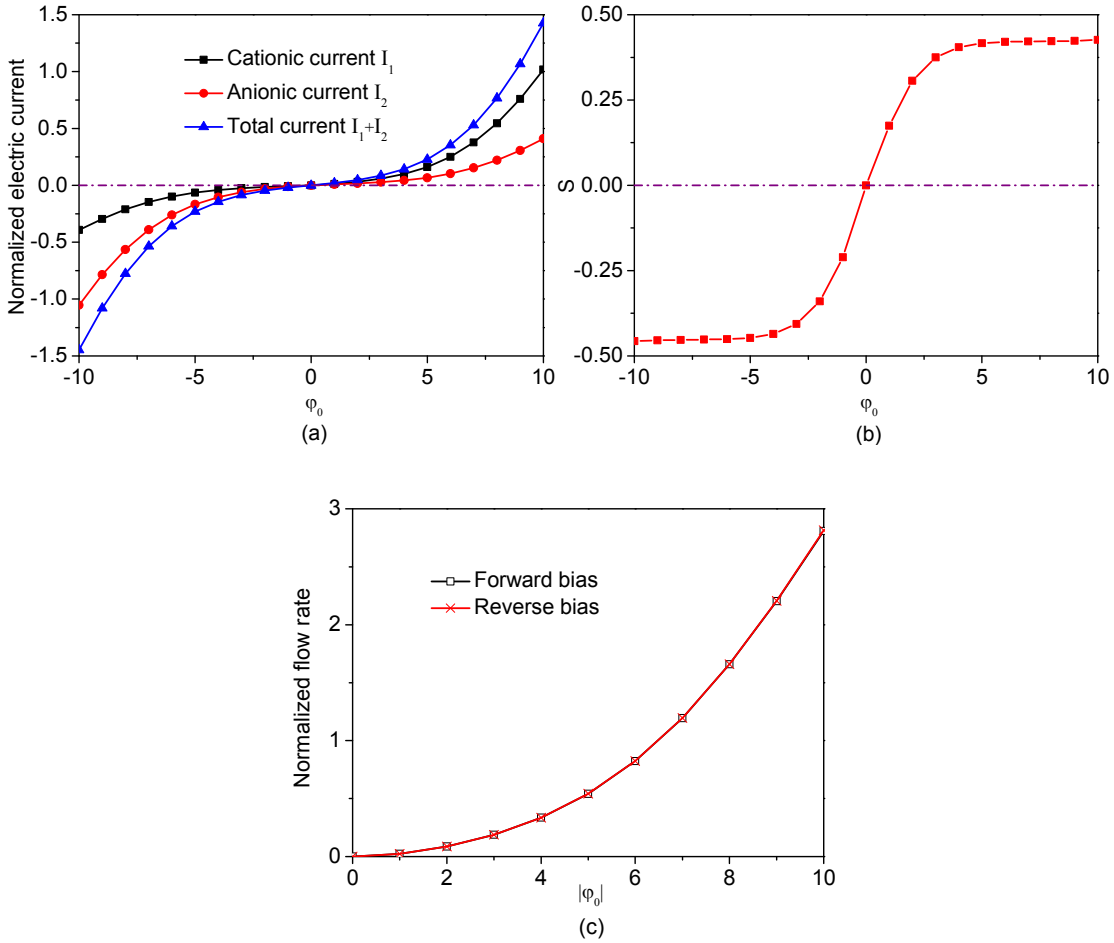

Figure 5.15 Dependence of ionic transport and flow rate on the electric bias for a straight nanochannel (h_1/h_2=1). (a) Variation of cationic current, anionic current and total current with the electric bias. (b) Variation of the ionic selectivity, S, with the electric bias. (c) Variation of the flow rate with the electric bias.

Figure 5.15 (b). Generally, the tapered conducting nanochannel is nonselective when the bias is zero, cation selective when it is forwardly biased, and anion selective when it is reversely biased. At relatively low voltages, magnitudes of both anionic selectivity and cationic selectivity increase significantly with the increase of the magnitude of applied electric bias. At high voltages (say larger than 4), the magnitude of selectivity however increases very slow and tends to saturation. This behavior at large magnitudes of electric bias is reminiscent of the similar phenomena in the electrodialysis across membranes (Rubinstein,

1984, 1990) where bulk concentration gradients (concentration polarization) were identified as the cause for such saturation behavior. The details of concentration polarization inside two reservoirs are to be discussed in the next section. It is also noted that the cation selective processes follow the flow, while the anion selective processes resist the flow. Figure 5.15 (c) is the plot for the variation of scaled flow rate through the nanochannel with the magnitudes of the electric bias. As discussed previously, for the same magnitude of electric biases, reversion of the electric field direction does not change the flow field, so reverse bias and forward bias with the same magnitude produce the flow rates with the same magnitude, and the net flow is always from the narrow end to the wide end. It is shown that the flow rate increases nonlinearly with the increase of the magnitude of electric biases. This intrinsic nonlinearity differentiates ICEK from the conventional electrokinetics in which the flow rate is linearly proportional to the applied biases.

The effect of taper angle of the nanochannel on the ionic transport and the flow rate is presented in Figure 5.16. In the present analysis, the smallest h_1/h_2 is chosen as 0.02 and all the predictions for $h_1/h_2=0$ are based on physical aspects of the nanofluidic system. It is clear from Figure 5.16(a) that both cationic current and anionic current increase with the increase of h_1/h_2. It is reasonable to believe that all the currents should vanish at the limit of $h_1/h_2=0$ because both cationic and anionic species cannot go through the nanochannel to conduct currents. Also available from this plot is that the anionic current increases much faster than the cationic current. When h_1/h_2 is very near unity, the anionic current slightly surpasses the cationic current. As long as the height of the left

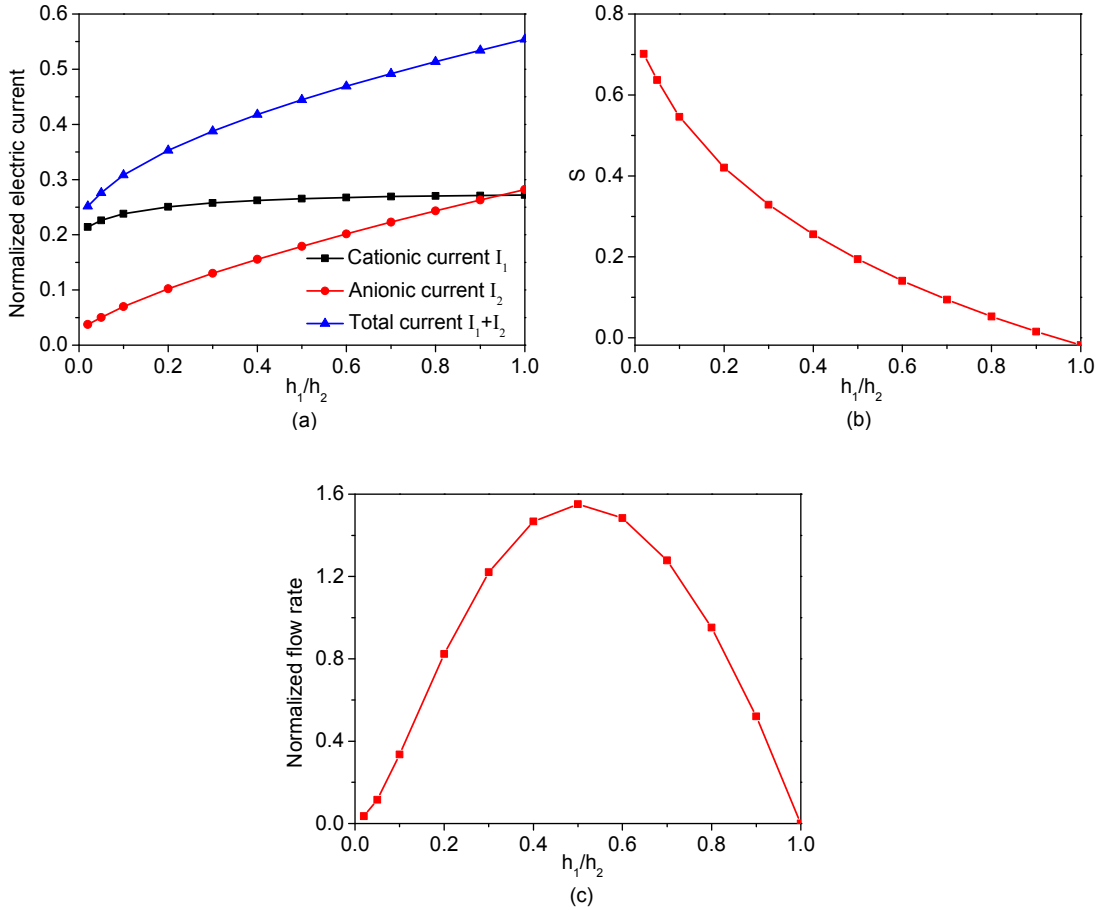

Figure 5.16 Dependence of ionic transport and flow rate on taper angle of the channel wall when $\varphi_0 = 6$. (a) Variation of cationic current, anionic current and total current with h_1/h_2. (b) Variation of the ionic selectivity, S, with h_1/h_2 (c) Variation of the flow rate with h_1/h_2.

opening is not zero, the ionic selectivity (see Figure 5.16(b)) monotonically decreases with the increase of h_1/h_2, which can be explained by the characteristics of ionic currents depicted in Figure 5.16(a). When $h_1/h_2=1$ (straight nanochannels), the channel exhibits very weak anion selective characteristics, which is due to the larger diffusion anionic coefficient as pointed out in section 5.2.3.3. It also should be pointed out that the selectivity is indefinite when $h_1/h_2=0$ since the denominator and the numerator in equation (5.20) are both zero. For the flow rate shown in Figure 5.16 (c), it is clear that there exists an optimal height for the left opening at which the flow rate reaches

the maximum value. In this particular case, the optimal height for the left opening is around $h_1=0.5h_2$. When $h_1 < 0.5h_2$, the flow rate increases with the increase of h_1/h_2, while when $h_1 > 0.5h_2$, the flow rate decreases with the increase of h_1/h_2. At two extreme limits, i.e., $h_1/h_2=0$ and $h_1/h_2=1$, net flow rates are both zero. When $h_1=0$, the height of the left opening is zero and consequently the flow cannot go through the nanochannel. For the straight channel ($h_1=h_2$), two symmetrical vortices exist inside the nanochannel (see Figure 5.4(b)), which also causes a nearly zero net flow rate. Therefore, there is certainly a competition between the flow enhancement due to increasing h_1/h_2 and the flow reduction due to vortical flows. When $h_1 < 0.5h_2$, the flow enhancement due to increasing h_1/h_2 is more significant than the flow reduction caused by vortical flows, while when $h_1 > 0.5h_2$, the flow reduction due to vortical flows becomes dominant.

5.3.3.3 CONCENTRATION POLARIZATION IN THE RESERVOIRS

Another fundamental aspect of a cation selective or anion selective nanochannel is the generation of bulk electrolyte gradients, usually known as concentration polarization. The reason for this has been recently attributed to the dominant surface conduction in nanochannels (Dydek et al., 2011). Figure 5.17 shows the details of concentration polarization inside two reservoirs for various values of electric bias. It should be pointed out that only the electroneutral regions (with equal concentration of K^+ and Cl^+) are the bulk concentration polarization zones, and the charged regions very near the nanochannel inlet and outlet are so-called space charge zones. The formation of these two zones inside the reservoirs is universal for ion selective nanochannels or membranes. Thus it would be quite expected that the ion selective process in

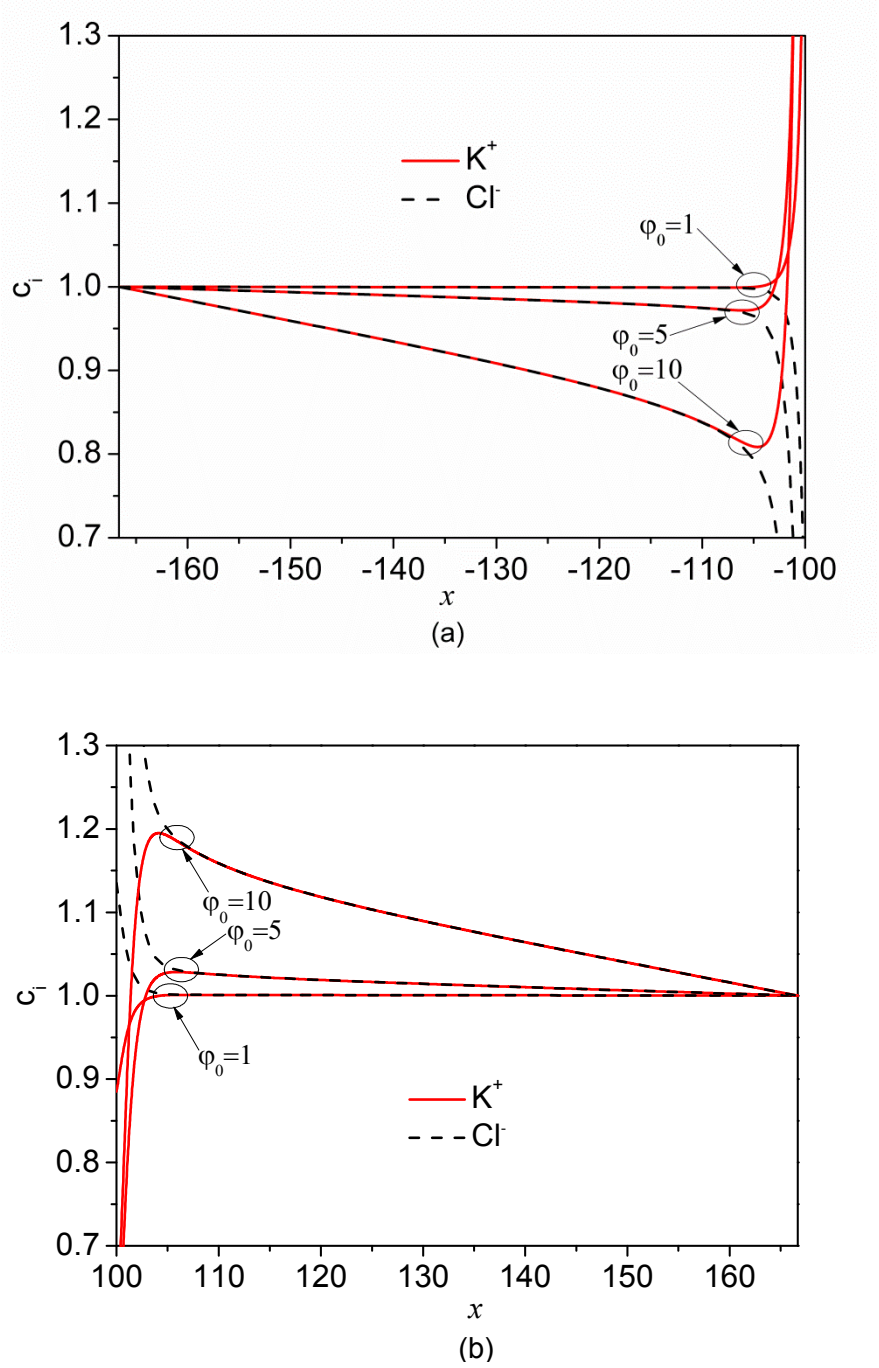

Figure 5.17 Concentration polarization inside the two reservoirs for three different values of electric bias. (a) Ionic concentration profiles along the nanochannel axis (y=0) inside the left (inlet) reservoir. (b) Ionic concentration profiles along the nanochannel axis (y=0) inside the right (outlet) reservoir.

conducting tapered nanochannel due to induced-charge electrokinetics also induces two zones in the reservoirs. For three cation selective processes shown in Figure 5.17, the bulk electrolyte concentration decreases along the channel

axis inside both left and right reservoirs. These characteristics of concentration polarization for conducting tapered nanochannels are similar to those for cation selective nanochannels with uniform natural surface charge as shown in Schoch et al. (2008) (see their Figure 18). It is also evident from Figure 5.17 that the intensity of the concentration polarization increases with the increase of the magnitude of electric bias, and the space charged zone tends to occupy a much larger portion of the reservoir as the magnitude of electric bias increases. With a larger forward electric bias applied, preferential transfer of cations through the nanochannel would significantly deplete cations near the inlet of nanochannel in the left reservoir, so that a concentration gradient must form inside the bulk reservoir at equilibrium to maintain an appreciably lower concentration of electrolyte near the nanochannel inlet. Such change in the ionic concentration is equivalent to the reduction of the effective bulk concentration of electrolyte which manifests as a tendency for ionic selectivity saturation (Rubinstein, 1990). When the magnitude of electric bias is large enough to completely deplete both cations and anions near nanochannel inlet, the electric current reaches its high limiting value (so-called limiting current) (Schoch et al., 2008), and thus the selectivity approaches its saturation value. In the present technique, ion selective function is achieved by the induced-charge electrokinetics in the conducting nanochannel. The high DC electric bias however would engender some negative effects, such as dissolution of conducting films and Faradaic reactions, which are beyond the scope of this thesis. Therefore, limiting behaviors of concentration polarization and ionic selectivity at high voltages are not included in this thesis.

5.4 SUMMARY

This chapter presents the first attempt to extend the induced-charge electrokinetics for nanofluidic applications. Specifically, two prototypes of nanofluidic systems featuring the active modulation of surface charge density are analyzed, and their operating characteristics for manipulations of both ionic flow and fluid flow are presented. Main conclusions can be summarized for straight conducting nanochannels and tapered conducting nanochannels respectively as follows:

(i) Based on the theory of induced-charge electrokinetics, a novel nanofluidic DCGC technique is proposed for flexible modulations of both ionic transport and flow directions inside straight conducting nanochannels. Three basic operating modes are identified for the proposed nanofluidic system, i.e., (a) the conducting walls are floating, (b) the conducting walls are biased close to φ_0 and (c) the conducting walls are biased close to the ground. These three modes result in zero net flow, backward flow and forward flow through the nanochannel, respectively. As for ionic transport through the nanochannels, weak anion selectivity operates in the first mode due to the unequal diffusion coefficients of cations and anions. Cation selectivity operates in the second mode for the negatively biased case and in the third mode for the positively biased case, while anion selectivity operates in the second mode for the positively biased case and in the third mode for the negatively biased case. The gate electrode (conductive nanochannel wall) is in direct contact with the electrolyte solutions and only very low voltages (a few times thermal voltage) are needed to adjust the ionic concentration and polarity inside the nanochannel. Another advantage of the proposed nanofluidic DCGC is that both ionic selectivity and flow direction can be adjusted at will by simply

controlling the potential imposed on the conducting nanochannel walls, which allows for the easy integration with external controlling circuits to realize full automatization, thus negating the need for the conventional way of surface treatment for modifications of the surface charge on channel walls. The DCGC strategy is attractive also because the gate electrodes are patternable and can be individually addressed, which can readily fulfill independent controls of fluid flow and ionic species transport at multiple points in the nanofluidic systems.

(ii) The second part of this chapter presents the analyses of induced-charge electrokinetics in tapered conducting nanochannels. The presented technique takes advantage of induced-charge electrokinetics for flexible modulations of surface charges which governs the ionic species transport inside the nanochannels. A numerical model including the Poisson equation, the Nernst-Planck equation and the Navier-Stokes equation is formulated to describe characteristics of the fluid flow and the ionic transport in a tapered conducting nanochannel. The results indicate a full-wave flow rectification of the tapered conducting nanochannel that the fluid always flows from the narrow end of the nanochannel to the wide end under electric biases of both negative and positive polarities. It is also interesting to note that the flow rate is nonlinearly dependent on the externally applied bias. This distinctive feature defines the nonlinear characteristics of induced-charge electrokinetics, and stands in stark contrast to the conventional electrokinetic pumping for which the flow rate depends linearly on the externally applied bias. For ionic transport through the tapered nanochannels, although the total ionic current does not show any rectification, the corresponding cationic current and anionic current do exhibit rectifying

effects, which makes the tapered conducting nanochannel cation selective when the system is forwardly biased and anion selective when the system is reversely biased. More significantly, the ionic selectivity is tunable through adjustment of the magnitude of external applied bias, which leads ionic selections to a higher level of controllability. Finally, if the taper angles of the conducting walls, i.e., the asymmetry of the tapered conducting nanochannel, is altered, so are the polarization of the conducting walls and the induced surface charge distribution on the conducting walls. It is found out that the ionic selectivity increases monotonically with the increase of taper angle of the nanochannel, while there exists an optimal taper angel at which the flow rate attains it maximum value.

CHAPTER 6: TRAPING OF COLLOIDAL PARTICLES VIA INDUCED-CHARGE ELECTROKINETICS

6.1 INTRODUCTION

Manipulation of particulate matters in micro- and nanofluidics is a fast growing research field because of its direct applications in cell handling, virus detection, biomacromolecule concentration and colloidal particle assembly etc. Extensive efforts have been made to devise various particle manipulation techniques. In the literature, optical tweezing, electrophoresis, and dielectrophoresis are certainly the most popular and well-established techniques for particle manipulations. However, these techniques have their respective limitations. Optical tweezing is mainly designed for trapping individual particles and thus suffers from its low throughput. Furthermore, the system must be equipped with sophisticated and expensive laser systems and other optical components. Electrophoresis can only be applied to handle naturally charged particles. As for dielectrophoresis, cares must be taken to tune electric properties of both particles and surrounding media to achieve the desired tasks, such as separation and trapping. Besides, complicated electrode designs are required to create nonuniform electric fields for dielectrophoretic manipulation of particles.

In Chapter 3 and Chapter 4, the ICEO flows over polarizable blocks are analytically and numerically studied, respectively. It was shown that the basic feature for ICEO is the generation of vortices over the surfaces of polarizable media. These kind of nonlinear vortical flows naturally lend themselves to the mixing enhancement in microfluidic devices (Jain et al., 2009; Wu and Li, 2008a;

Wu and Li, 2008b; Zhao and Bau, 2007). Other than the microfluidic mixing, the applications of induced-charge electrokinetics in microfluidics are very rare. In this chapter, a novel and high-throughput technique relying on the induced-charge electrokinetics is devised for simultaneous trapping and concentration of submicron- to micron-sized particles. The microfluidic device is simply composed of a straight channel and a floating conducting patch sitting on the bottom wall of the channel. Under DC-biased AC electric driving voltages, the trapping and concentration of particle over the edge of the conducting patch are demonstrated and tested. Moreover, systematic studies are performed to investigate the effects of relevant factors (such as AC frequency, AC amplitude, DC offset and particle size) on the performance of trapping and concentration. In addition, a numerical model based on the effective boundary conditions presented in Chapter 3 is developed to explain the underlying mechanism of particle trapping and concentration.

6.2 EXPERIMENTAL SECTION

6.2.1 MICROFLUIDIC DEVICE DESIGN AND FABRICATION

The microfluidic device designed for particle trapping consists of two parts (as shown in Figure 6.1): a PDMS microchannel and a glass slide deposited with a conducting patch. The dimensions of the PDMS channel and the conducting patch are illustrated in Figure 6.1(b). The depth of microchannel is 40 μm and two cylindrical reservoirs are punched using the puncher (Uni-Core, Harris) in the PDMS with radii of 6 mm. To minimize the possible dissolution of conducting patch due to electrochemical reactions during the experiment, noble meal gold is chosen as the material for the conducting patch. In experiments, the gold

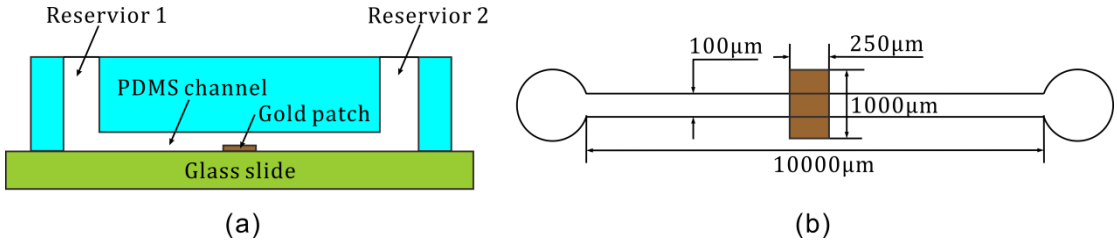

Figure 6.1 Details of the microfluidic device for particle trapping. (a) Cross-sectional view of the microchannel along the depth direction. (b) Top view of the device and dimensions of the channel and the gold patch.

conducting patch floats in an external electric field and, then electric charge is induced on the conducting patch and associated induced-charge electrokinetic phenomena occur over the conducting patch to trap the particles. A similar microfluidic device was recently used to study the induced-charge electroosmotic flow (Pascall and Squires, 2010).

The standard photolithographic technique was adopted to fabricate the PDMS channel. At first, a silicon wafer was sequentially cleaned in the piranha solution (70% H_2SO_4:30% H_2O_2) and the deionized (DI) water. Then the wafer was spin-coated with a layer of negative photoresist (SU-8 50) with a uniform thickness of 40 µm. After soft-baking, UV light exposure was conducted to transfer the channel pattern from the mask to the SU-8 layer. Subsequently, post-baking was performed to further remove the solvent in the SU-8 layer and enhance the cross-linking of exposed SU-8. Finally, a master mold of microchannels was formed by removing the unexposed SU-8 in the SU-8 developer. To form the PDMS channel, Sylgard 184 Silicone Elastomer (Dow corning, Midland, USA) and the curing agent were mixed with a ratio of 10:1 (wt/wt), and then the mixture was thoroughly stirred. Because of unwanted bubble generation during the stirring, the mixture was placed in a vacuum

chamber for 40 minutes for degassing. Finally, the mixture was poured on the wafer with the channel mould and then was cured in an oven at 80°C for 1 hour. The PDMS channels after curing were peeled off from the wafer and ready for bonding with glass slides sputtered with conducting patches.

The fabrication of the conducting patch was achieved using the standard lift-off process. Similarly, a glass slide was cleaned by using the piranha solution and the DI water. Then the positive photoresist (AZ9260) was spin-coated onto the glass slide (75mm×50mm, Corning) to form a uniform thickness around 10μm, followed by the baking at 110°C for 4 min. Subsequently, the UV exposure is performed to define the structure of the conducting patch. After developing process, the exposed portion of AZ layer was removed and cavities defining the structure of the conducting patch form on the glass sidle. Finally, the sputtering process was performed using a coxial magnetron sputter to fully coat the glass slides and the cavities with a 53nm-thick titanium film and a 300nm-thick gold layer. Then the coated glass slide was immersed in acetone for 6h to remove the unwanted photoresist and obtain the desired pattern of conducting patch on the glass slide.

In final step, the PDMS channel and the glass slide with the patterned gold conducting patch were placed into a plasma cleaner (Harrick Plasma Cleaner PDC-32G) for the oxygen plasma treatment of 30s. After the treatment, the PDMS channel and the glass slide were brought into contact to form an irreversible bonding. In addition, the conducting patch was precisely aligned to the center of the microchannel under a microscope (020-520.008 DM/LM, Leica) during the bonding process. A schematic view of the fabricated microfluidic device for

experiments is shown in Figure 6.1 (a).

6.2.2 PREPARATION OF PARTICLE SAMPLES

In experiments, green fluorescent polymer microspheres (Thermoscientic, USA) of five different sizes (0.3μm, 0.5 μm, 0.7μm, 1μm and 1.9 μm) were used. The original particle solutions were all diluted with the 10^{-4}M KCl solution for 250 times, and the final particle concentration in the solution is 0.04 ‰ wt for all cases. Before loading the tested particle solution into the microchannel, the particle suspensions were well mixed and thoroughly stirred in an ultrasonic cleaner (Elmasonic E30H, Elma®) to ensure an excellent homogeneity.

6.2.3 EXPERIMENTAL SETUP, DETECTION AND IMAGE ANALYSIS

The entire experimental system is shown in Figure 6.2. Experiments were carried out with a fluorescence microscope (Axiostar Plus 1169-149, Carl Zeiss) equipped with a long-working-distance 20×objective, a mercury arc lamp (Leistungselektronik mbq 52 AC-Z/ HBO 50 AC), and an appropriate filter set (excitation, 546 ± 12 nm, emission, 600 ± 40 nm). All images were acquired by using a CCD camera (SamBa EZ-140c, Sensovation AG) of 8-bit, 696×520 pixels with a frame grabber (Sensovation SamBa EZ-series IEEE 1394a). The exposure time for CCD camera was set to 33ms for all experiments. To obtain a combined AC and DC voltage for trapping the particles, a function generator (AFG3102, Tektronix) was used to generate a DC-biased AC signal which was then amplified to the desired combination of AC and DC voltage by a customized three channel voltage amplifier (OPT3-AC800-DC1.5K, Optrobio, Singapore). At the same time, the signal of DC-biased AC voltage after amplification was monitored by an oscilloscope (HM 1008-2, HAMEG Instruments).

The tested chip is placed under the microscope for monitoring the particle trapping, with two platinum wires (0.5 mm in diameter, Sigma-Aldrich) placed in each reservoir to apply the amplified voltages (Figure 6.2(b)). The left platinum electrode was supplied with a DC-biased AC voltage ($V_0+V_1\cos(2\pi ft)$, where f is the frequency of AC voltage, V_1 is the amplitude of AC voltage and V_0 is the DC component of the voltage) and the right platinum electrode was grounded. At the beginning of each experiment, two reservoirs were carefully balanced to eliminate the pressure-driven flows. To clearly show the structure of the tested section, a microscopic view of the microchannel loaded with the solution of 500nm fluorescent particles is presented in Figure 6.2(c).

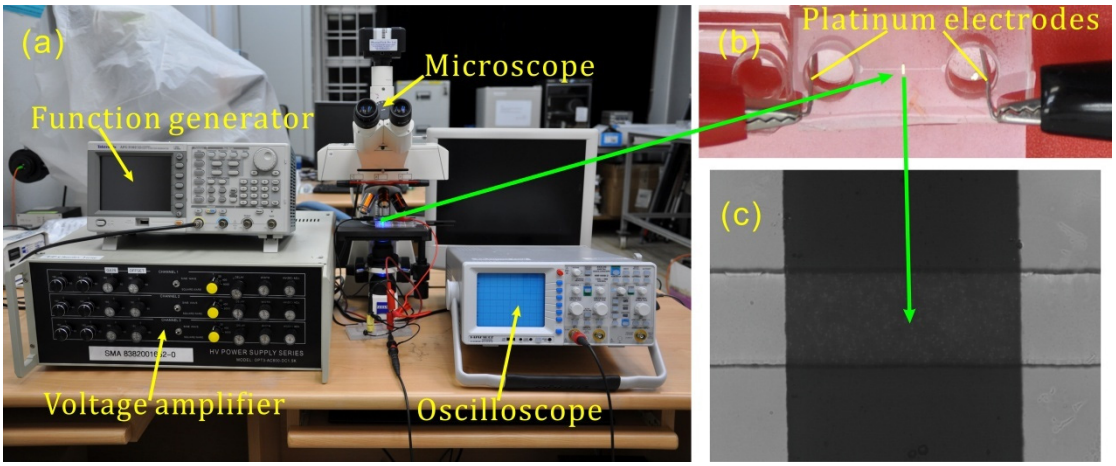

Figure 6.2(a) Experimental setup.(b) Overview of the microchannel with two reservoirs in which two platinum wires are used to supply the driving electric field. In the experiment, a combination of AC and DC voltage is applied on the left electrode and the right electrode is grounded. (c) Microscopic image of the microchannel loaded with the solution of 500nm fluorescent particles.

During experiments, the background was blackened and the green fluorescence particles were illuminated by the blue light from the mercury lamp. The CCD camera was set to the continuous mode to capture the entire process of particle trapping and releasing, thus providing multi images for a certain period of time. The time internal between two successive frames is about 67 ms. Lastly,

the captured images were recorded in a personal computer for further analyses. The fluorescent intensity was extracted from the images by using an open source image processing software (ImageJ 1.45) developed at the National Institutes of Health.

6.3 RESULTS AND DISCUSSION

6.3.1 TRAPPING OF PARTICLES OF VARIOUS SIZES

The snapshots in Figure 6.3 show the transient trapping of 500nm fluorescent polymer particles over the right edge of the conducting patch under a combined AC and DC electric field (DC V_0=36V, AC amplitude V_1=368V and AC frequency f=4kHz). It is obvious that more and more particles get trapped over the right edge of the conducting patch as time elapses. The trapped particles form a line defined by the edge of the conducting patch. The trapping involves two scenarios: at first, the particles are transported from the left to the right by the joint effect of electrophoresis and electroosmotic flow (as denoted by the arrow) due to the DC voltage (note that the AC field does not generate any net flow or particle motion). When the particles reach the right edge of the conducting patch, the induced-charge electrokinetic flow there together with the electrophoresis and dielectrophoresis traps the particles. It is believed that the vortical flow due to induced-charge electrokinetics is the dominant mechanism for the particle trapping. The later theoretical analysis shows that the microvortex forms a stagnant zone where the particles transported from the upstream are accumulated. The presented microfluidic device consists of only a straight microchannel and a conducting patch on its bottom wall, thus does not involve complicated microfluidic designs. Furthermore, it is also reasonable to

believe that the present technique demonstrates flexible controllabilities. Trapping locations can be controlled by altering the location of patterned conducting patch, and also trapping at multiple locations can be readily realized by sputtering multiple conducting patches along the microchannel wall.

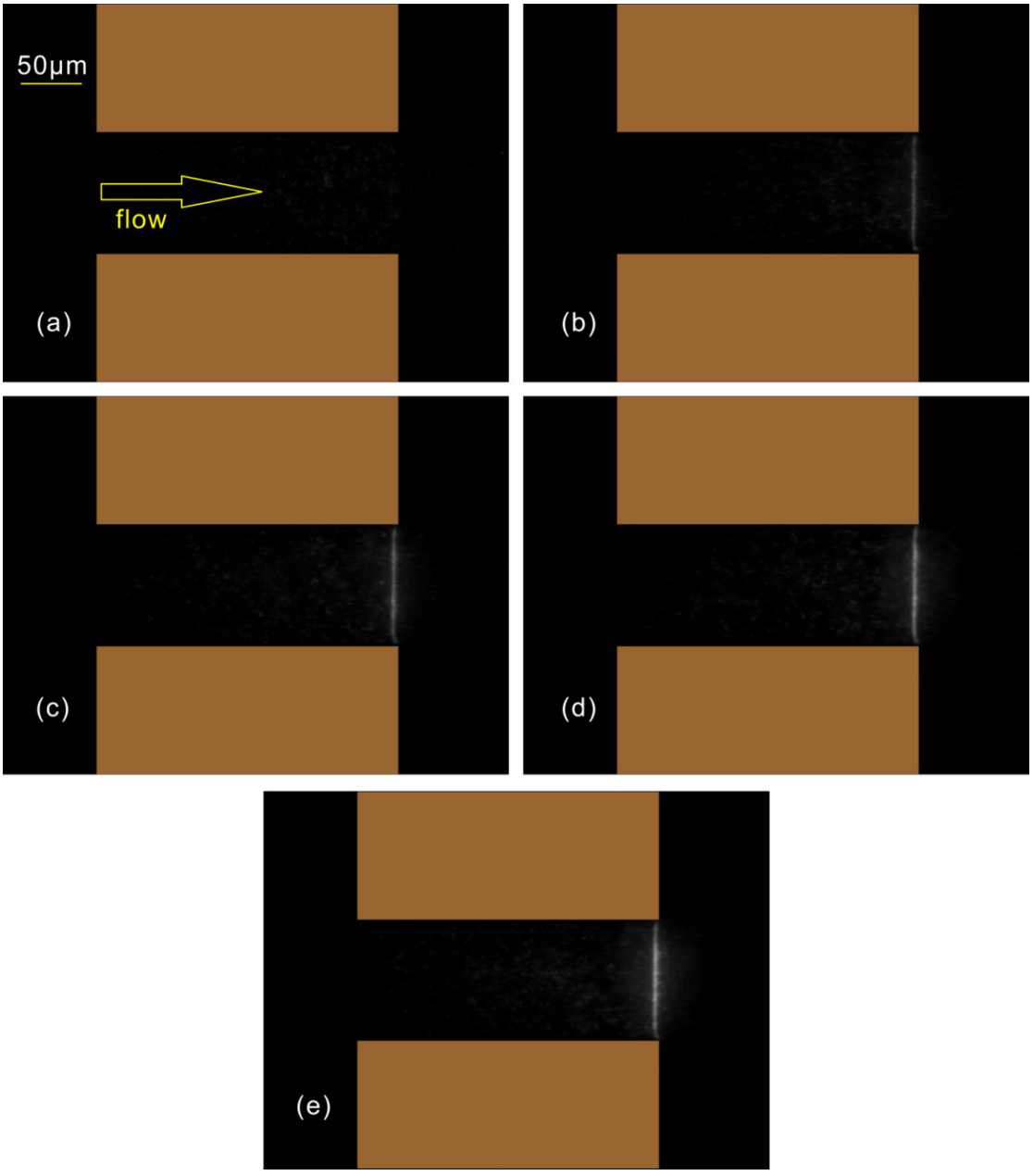

Figure 6.3 Transient trapping of 500nm fluorescent particles over the right edge of the conducting patch when V_0=36V, V_1=368V and f=4 kHz, (a) t=0s, (b) t=5s, (c) t=10s, (d) t=20s and (e) t=30s. t=0 is the instant right before the field is turned on. Two rectangles in each picture define the location of the conducting patch, in between the rectangles there is the microchannel.

After the external driving field is removed, the particles trapped over the right edge of the conducting patch are released as shown in Figure 6.4. Additionally, the released particles are advected backwards by the flow driven by a pressure gradient which results from the reservoir liquid level difference induced during the transient trapping process. As indicated in Figure 6.4, the pressure driven flow is in the opposite direction of the electroosmotic flow during the trapping process to re-balance the reservoirs, since the two reservoirs are carefully balanced to eliminate any flow before the experiment.

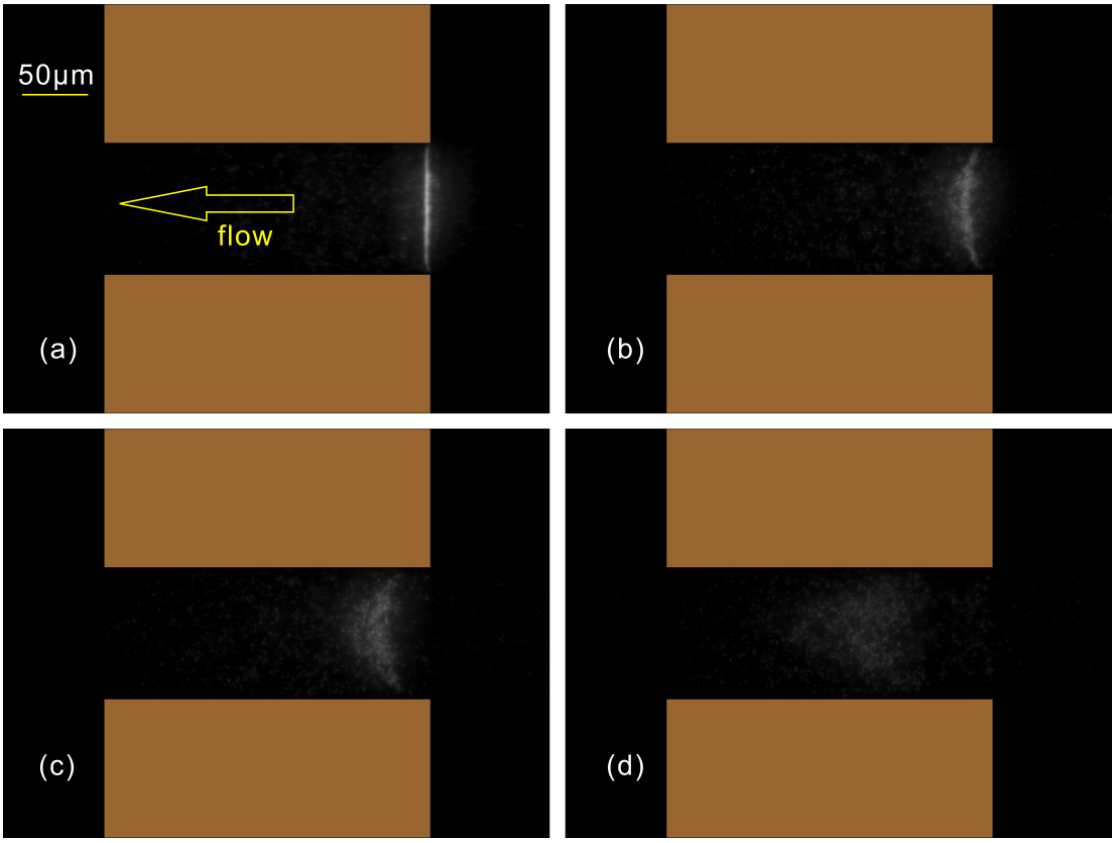

Figure 6.4 Transient releasing of 500nm fluorescent particles from the right edge of conducting patch after removing the combined AC and DC electric field (V_0=36V, V_1=368V and f=4kHz) due to the induced pressure-driven flow, (a) t=0s,(b)t=1s,(c)t=2s, (d)t=5s. Here, t=0s denote the instant right before the electric field is removed. Two rectangles in each picture define the location of the conducting patch, in between the rectangles there is the microchannel.

Trapping of particles of various sizes is demonstrated in Figure 6.5. The results show that the proposed method can achieve stable trapping of particle from 0.3μm to 1 μm. It is shown that the trapped particles for 0.3 μm, 0.7 μm and 1 μm form straight lines which are defined by the right edge of conducting patch. For 1.9 μm particles, trapped particles are more spread as compared to other three smaller sizes. This could be due to the fact that induced-charge electrokinetic vortices are not strong enough to catch such large particles. Along with the later demonstration of the potential in nanoparticle trapping, one can see that the presented method is very effective for trapping submicron particles and even nanoparticles which is however quite challenging for other trapping

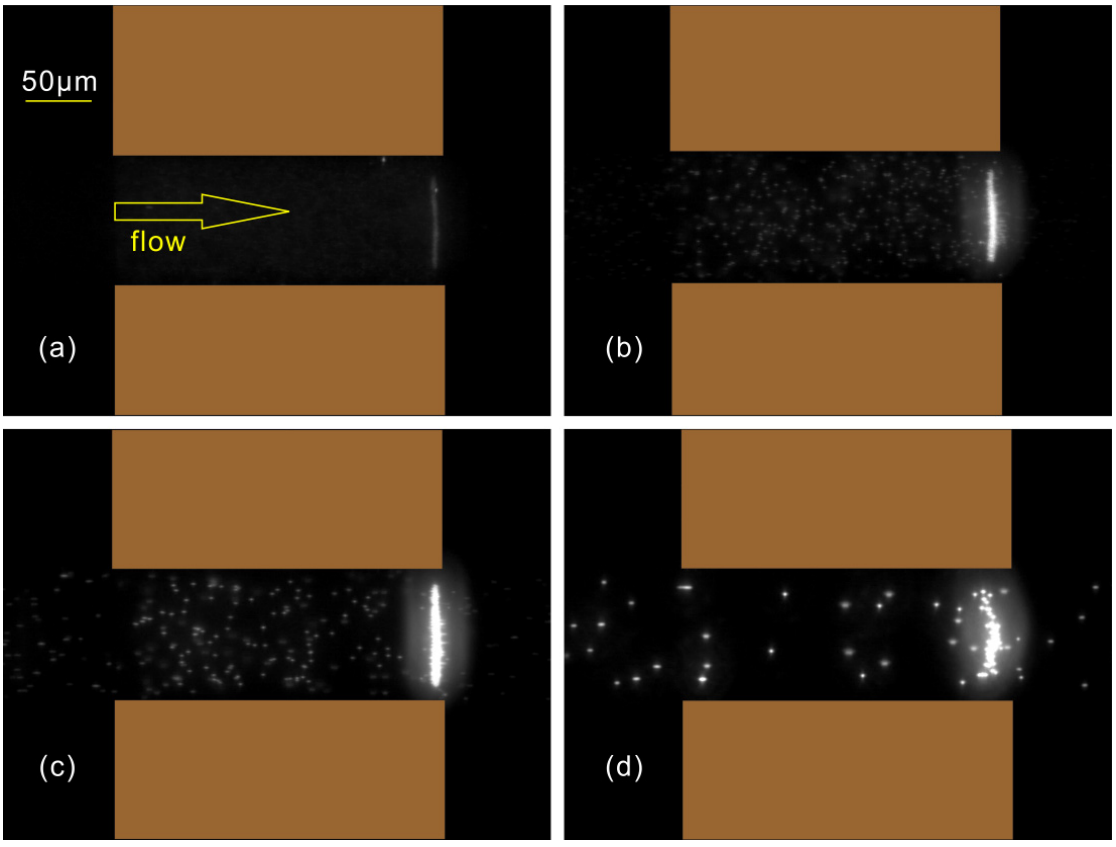

Figure 6.5 Trapping of fluorescent particles of various sizes over the right edge of the conducting patch after switch on the electric field (V_0=36V, V_1=368V and f=4 kHz) for 30s. (a) 0.3μm, (b) 0.7μm, (c) 1μm, (d) 1.9μm. Two rectangles in each picture define the location of the conducting patch, in between the rectangles there is the microchannel.

techniques, such as optical tweezing and dielectrophoresis.

6.3.2 EFFECTS OF RELEVANT PARAMETERS ON THE TRAPPING PERFORMANCE

Figure 6.6 presents the effects of combined AC and DC field on the trapping performance. The vertical axis in each plot denotes the fluorescent intensity which is an indication of the particle concentration. The higher the fluorescence intensity is, the higher the particle concentration is. As shown in Figure 6.6(a), the band of trapped particles under a lower AC frequency is more spread. As the AC frequency increases, the band of trapped particles is compressed to the right edge of the conducting patch. It is clear that there exists an optimal frequency at which the band accumulates the most particles. The effect of the AC amplitude on the trapping performance is monotonic, as can be seen from Figure 6.6(b). The band of trapped particles becomes narrower and darker as the AC amplitude decreases. With the DC offset increasing, the electroosmotic flow becomes stronger, which pushes the band of trapped particles to the right edge of the conducting patch (see Figure 6.6(c)). The investigation also predicts an optical DC offset under which the band traps the most particles. This should be understandable, because if the DC offset is mall, electroosmotic flow is not strong enough to transport sufficient particles to the trapping zone; while if the DC offset is too high, electroosmotic flow is so strong that the trapped particles are washed off from the edge of the conducting patch.

6.3.3 POTENTIAL APPLICATIONS IN NANOPARTICLE TRAPPING

Trapping of nanoparticle are currently a subject of intensive research due to a broad range of potential applications in nanotechnology, as well as biomedical, optical, electronic, material and environmental sciences. Nanoparticles are

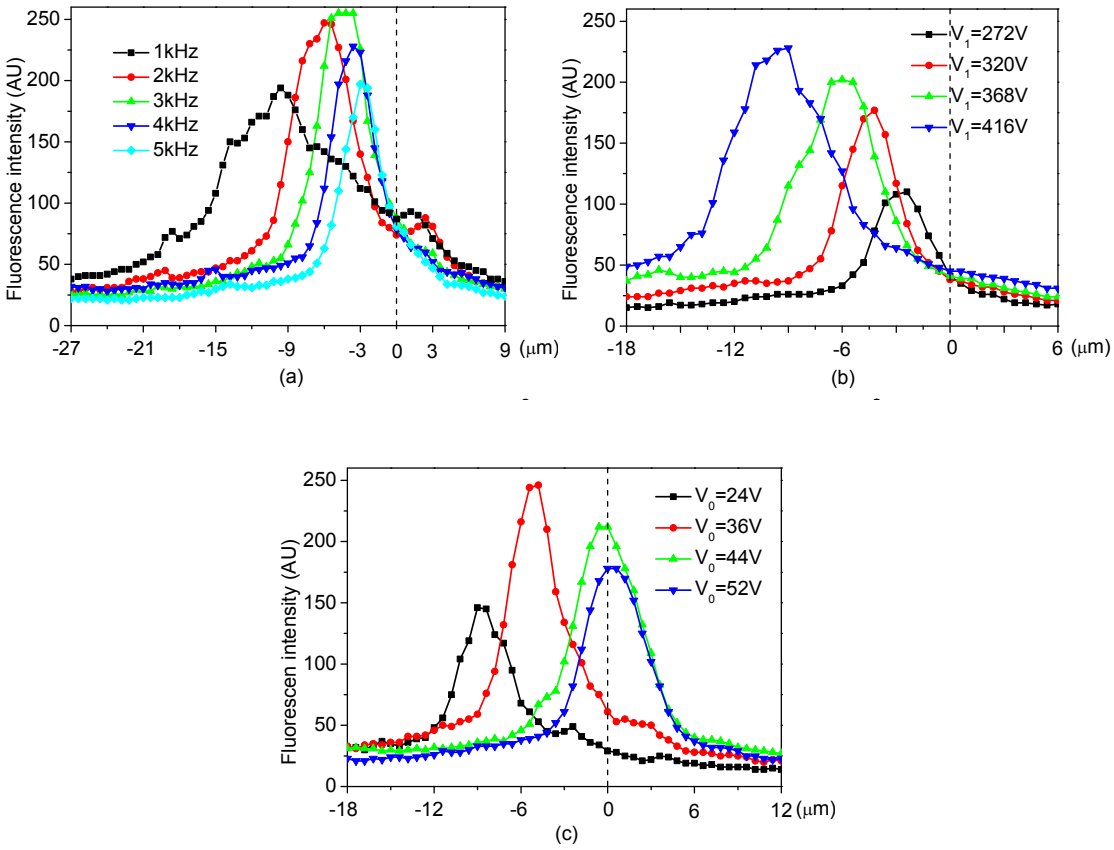

Figure 6.6 Effects of the combined AC and DC electric field on the steady-state trapping of 500nm fluorescent particles. All fluorescence intensity profiles are along the center line of the 100 μm wide microchannel. Vertical dash lines represent the right edge of the conducting patch. (a) Effect of AC frequency on the particle trapping when DC V_0=36V and AC amplitude V_1=368V. (b) Effect of AC amplitude on the particle trapping when DC V_0=36V and AC frequency *f*=4 kHz. (c) Effect of DC offset on the particle trapping when AC amplitude V_1=368V and AC frequency *f*=4 kHz.

generally considered to have radii from 1nm to 100 nm. The well-established techniques for trapping micron-sized particles mostly are inefficient for trapping nanoparticles due to the following three reasons: first, it is very difficult to overcome the Brownian motion for nanoparticles; second, the trapping force usually scales as the volume of the particle or the cube of particle radius; third, the real-time detection of the nanoparticle trapping at present is still a challenge, especially for non-fluorescent nanoparticles.

In our experiment, the trapping is mainly due to the flow circulation which confines the particles in a stagnant zone (see details in the theoretical modeling part in section 6.4), and not due to the volumetric force as in the optical and dielectrophoretic trapping. The present method is thus likely extended for nanoparticle trapping. Figure 6.7 (a) shows the trapping of 50nm particles over the right edge of the conducting patch, though the throughput is not as high as the submicron particle trapping presented earlier. Similarly, the trapped nanoparticles are released from the right edge of the conducting patch after turning off the electric field and transported backwards due to the back pressure induced flow, as indicated in Figure 6.7(b).

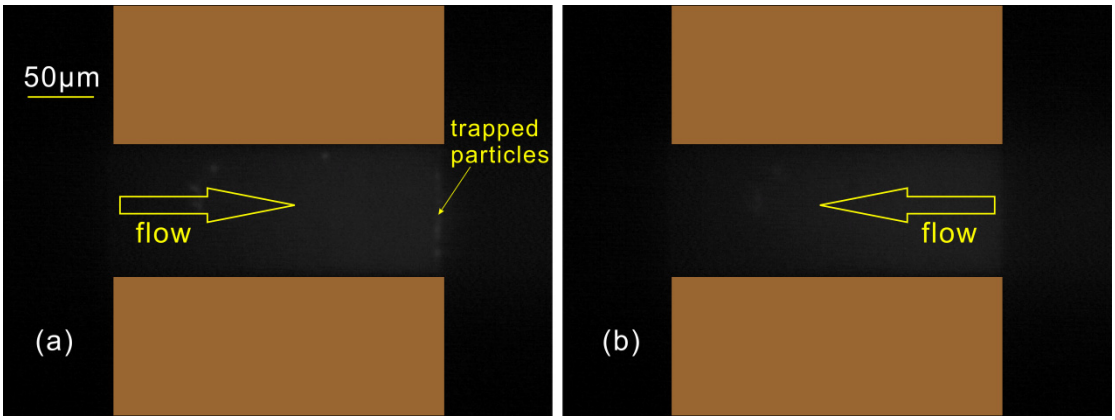

Figure 6.7 (a) Trapping of 50nm fluorescent particles over the right edge of the conducting patch after turning on the electric field (V_0=36V, V_1=368V and f=4kHz) for 30s. (b) Releasing after turning off the field for 1s. Two rectangles in each picture define the location of the conducting patch, in between the rectangle there is the microchannel.

6.4 THEORETICAL MODELING OF PARTICLE TRAPPING DUE TO INDUCED-CHARGE ELECTROKINETICS

6.4.1 MODELING DOMAIN

Because of the multiphysical processes involved in the particle trapping, a numerical method has to be developed to simulate the complex phenomena. In

the present study, the finite-element software (Comsol Multiphysics 3.4) is used to simulate the particle trapping due to induced-charge electrokinetics. Since the channel width (100μm) in the experiment is 2.5 times of the channel depth (40 μm), the simulation domain can be effectively represented by a rectangular domain shown in Figure 6.8 (a two dimensional cross-section along the depth direction of the microchannel). Specifically, the segment CD with length of 2L at the center of the lower boundary denotes the conducting patch, segments BC and DE are the glass walls, and segment AF is the PDMS wall. In the simulation, BC and DC are chosen to be at least 10L long to minimize the effects of inlet and outlet boundaries (AB and FE) on the simulation results.

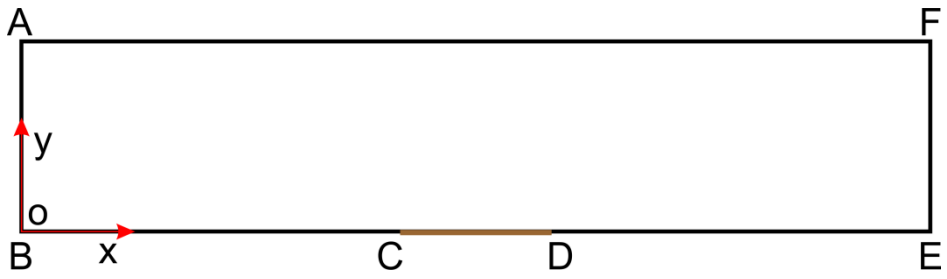

Figure 6.8 Sketch of the modeling domain. Segment CD represents the gold conducting patch, BC and DE are the lower glass walls and AF is the upper PDMS wall.

6.4.2 FORMULATION OF THE PROBLEM

There should be tree governing equations in the model development, one is for evaluation of the induced zeta potential on the conducting surface, one is for evaluation of the induced-charge electrokinetic flow field and another one is for evaluation of the mass transport of particles.

For the model development, we consider a conducting patch immersed in an infinite electrolyte solution domain and simultaneously floating in an external electric field without contact with the driving electrodes. In addition, we

introduce the following scales for the nondimensionalization of the governing equations

$$[x, y] = L\,,\ [\phi] = \frac{k_B T}{ze} \tag{6.1}$$

where L is half width of the conducting patch, k_B is the Boltzmann constant, T is temperature, e is elementary charge, and z is the valence of electrolyte ions.

In the experiment, the electric field is given as a combination of AC and DC electric fields. Therefore, the electric problem can be formulated in terms of phasor variables. The dimensionless complex amplitude of electric potential in the bulk fluid satisfies Laplace's equation

$$\nabla^2 \phi_f = 0 \tag{6.2}$$

The boundary condition over the surface of floating conductor can be obtained from equations (3.75) and (3.76) in Chapter 3 as

$$\phi_f - \phi_c = \frac{d\phi_f}{dy} \frac{1}{j\omega\tau\sqrt{1 + j\omega\tau\left(\lambda_D / L\right)}} \tag{6.3}$$

Note that $\tau=\lambda_D L/D_i$ represents the characteristic time scale for the double layer changing over the conducting patch, or the so-called "RC time" in the terminology of the equivalent circuit. In the definition of τ, D_i is ionic diffusivity, and λ_D is the Debye length and is defined for a symmetric (z:z) electrolyte as $\lambda_D = \sqrt{\varepsilon_0 \varepsilon_f k_B T / \left(2 n_\infty e^2 z^2\right)}$, where $\varepsilon_0\varepsilon_f$ is the electric permittivity of the electrolyte solution and n_∞ represents the bulk ion concentration. $\omega=2\pi f$ is the angular frequency of the electric field. It should be noted that for a floating conductor with perfect polarizability, it is polarized instantaneously after the application of

external electric field and remains equipotential with ϕ_c in the entire charging process of the electric double layer.

Then the total potential drop across the double layer, or equivalently the zeta potential over the conducting surface, can be evaluated as

$$\zeta = \phi_c - \phi_f \tag{6.4}$$

Once the double layer around the conductor is charged, the externally applied field exerts a body force on ionic charge in the double layer, driving the ions and then the liquid into motion. For the thin EDL situation considered here, the resultant electrokinetic flow appears to slip just outside the double layer and the slip velocity varies proportionally to the local electric field strength and is given by the Helmholtz–Smoluchowski equation

$$\mathbf{u} = \left\langle \zeta \nabla \phi_f \right\rangle \tag{6.5}$$

where $\langle \cdots \rangle$ denotes the time averaging. Equation (6.5) is the boundary condition over the conducting patch and the channel walls for the time averaged flow field.

Usually, the flows considered in microsystem are usually of creeping type due to very small Reynolds number, and then the equations governing the ICEK flow of an incompressible liquid are the continuity equation and the Stokes equation

$$\nabla \bullet \mathbf{u} = 0 \tag{6.6}$$

$$-\nabla p + \nabla^2 \mathbf{u} = 0 \tag{6.7}$$

together with slip velocity boundary condition on the solid surface as given by equation (6.5).

Velocity and pressure is made dimensionless by following natural scales

$$[\mathbf{u}] = \frac{\varepsilon_0 \varepsilon_f [\phi]^2}{\mu L} \qquad [p] = \varepsilon_0 \varepsilon_f \frac{[\phi]^2}{L^2} \tag{6.8}$$

where μ is the dynamic viscosity of the electrolyte solution.

There are generally two methods for modeling of particle behavior, namely the Lagrangian method and the Eulerian method. The Lagrangian method relies on tracking the trajectories of individual particles. It is a simple approach, but inefficient for the situation with a very large number of particles. The Eulerian method however can be readily used to analyze the behavior of a collection of particles in terms of particle concentration. To investigate trapping of particles, the Eulerian method is chosen in the present investigation. It is further assumed that the microchannel wall does not adsorb particles and there is no interaction among the particles, between the particles and the electrolyte components and between the particles and the walls of channel. Therefore, the particle concentration can be governed by the mass transport equation. In addition, beside the ICEK flow, other electrokinetic forces (electrophoresis and dielectrophoresis) also contribute to particle transport. Under this circumstance, the transport of particles can be modified as

$$\frac{\partial c}{\partial t} + Pe \nabla \bullet \left[\left(\mathbf{u} + \mathbf{u}_{ep} + \mathbf{u}_{dep} \right) c \right] = \nabla^2 c \tag{6.9}$$

in which the scales of time, particle concentration and the Peclet number are defined as

$$[t] = \frac{L^2}{D_p} \quad [c] = c_0 \quad Pe = \frac{[\mathbf{u}] L}{D_p} = \frac{\varepsilon_0 \varepsilon_f [\phi]^2}{\mu D_P} \tag{6.10}$$

In equation (6.10), the concentration scale c_0 refers to the initial particle concentration, and D_p refers to the mass diffusivity (or diffusion coefficient) of the particle, which can be estimated from the Stokes-Einstein relation

$$D_p = \frac{k_B T}{6\pi\mu a} \tag{6.11}$$

where a is the radius of the particle.

Electrophoresis results from the interaction of the electric field with the charged particles. For a negatively charged particle in a bulk fluid, the electrophoretic force drags the particle from the cathode side of the electric field to the anode side of the electric field. For particles with thin EDLs, the time averaged electrophoretic velocity is expressed as

$$\mathbf{u}_{ep} = -\zeta_p \left\langle \nabla \phi_f \right\rangle \tag{6.12}$$

where ζ_p is the dimensionless zeta potential for particles.

The presence of the floating conducting patch can perturb the electric field locally, and creates a nonuniform electric field around the conducting patch. Dielectrophoretic force is then induced due to the interaction of such non-uniform electric field with the dipole moment induced by the same field inside a polarizable particle. The resulting dielectrophoretic force can transport the particle from high (low) electric field strength to low (high) electric field strength, depending on electric properties of particles and surrounding media. The time averaged dielectrophoretic velocity of the particle $\mathbf{u}_{dep}$ can be expressed as

$$\mathbf{u}_{dep} = \frac{1}{3}\left(\frac{a}{L}\right)^2 \mathrm{Re}\left[\underline{K}(\omega)\big|_{\omega\to 0}\right]\nabla\left(\left\langle\nabla\phi_f\right\rangle\bullet\left\langle\nabla\phi_f\right\rangle\right) + \frac{1}{3}\left(\frac{a}{L}\right)^2 \mathrm{Re}\left[\underline{K}(\omega)\right]\nabla\left[\left\langle\left(\nabla\phi_f - \left\langle\nabla\phi_f\right\rangle\right)\bullet\left(\nabla\phi_f - \left\langle\nabla\phi_f\right\rangle\right)\right\rangle\right] \tag{6.13}$$

where the Clausius-Mossotti (CM) factor is defined as $\underline{K}(\omega) = \left(\underline{\varepsilon}_p - \underline{\varepsilon}_f\right)/\left(\underline{\varepsilon}_p + 2\underline{\varepsilon}_f\right)$. The complex dielectric permittivities of the particle and fluid medium (electrolyte solution) are $\underline{\varepsilon}_p = \varepsilon_0\varepsilon_p - j\sigma_p/\omega$ and $\underline{\varepsilon}_f = \varepsilon_0\varepsilon_f - j\sigma_f/\omega$, respectively, with $j = \sqrt{-1}$. The particle has an electric permittivity of $\varepsilon_0\varepsilon_p$ and a conductivity of σ_p. The conductivity of particle consists of the bulk conductivity and the surface conductivity ($2\sigma_s/a$). For latex particles, the bulk conductivity is usually taken to be zero and the surface conductance σ_s ranges from 0.2 to 2.1nS (Arnold et al., 1987; Morgan and Green, 2003). The first term in equation (6.13) denotes the dielectrophoretic velocity of particle due to the DC component of the electric field and the second term is the dielectrophoretic velocity of particle due to the AC component of the electric field.

6.4.3 INITIAL AND BOUNDARY CONDITIONS

The similar model was also adopted previously for analyzing the concentration of solute and particles (Ge, 2011; Ge et al., 2010), and the time scale analysis suggested that concentration field dominates the transient characteristics of the whole system. Therefore, the transient term is only present in the mass transport equation. The electric and flow problems can be treated as pseudo-steady. At the initial state, the microchannel is filled with a uniform particle dispersion with a normalized concentration of c=1.0.

Due to linearity, the electric problem can be separated into two parts: one part represents the DC electric field and another one represents the AC part. For the DC electric field, the boundary condition on the CD segment (conducting patch) reduces to the insulation boundary, i.e., $d\phi_f / dy\big|_{y=0} = 0$ (which is actually the DC limit of equation(6.3)). After solving the AC and DC electric fields separately, one can add these two solutions to obtain the total electric field due to the combined AC and DC electric field. Table 6.1 summarizes the boundary conditions specified for solving three governing equations. Only the boundary conditions for solving AC component of the electric field are included in this table. The AC amplitude is imposed at the inlet segment AB ($\phi_f = V_1$), while the outlet segment FE is grounded ($\phi_f = 0$). Since there is no electric current leakage from channel walls, the electric insulation boundary condition is assigned to all the channel wall surfaces (BC, DE and AF), i.e., $d\phi_f / dy\big|_{y=0} = 0$. To account for the charging of EDL on the conducting patch (segment CD), the boundary condition expressed in equation (6.3) applies.

The electrolyte solution carrying particles is purely driven by the external electric field and certainly there is no pressure gradient applied along the microchannel axial direction. So at the inlet and outlet boundaries (AB and FE), the pressure is given as zero, i.e. $p = 0$. The slip velocity condition given by equation (6.5) is applied on the channel walls and the conducting patch. It should be pointed out that the flow generated on the conducting patch observed in the present experiment is actually reversed as compared to the theoretical prediction from equation (6.3). Such flow reversal at high AC frequency was

Table 6.1 Summary of the boundary conditions for governing equations of electric problem, flow problem and mass transport problem

Governing equations / Boundary segments	Electric problem	Flow problem	Mass transport
AB	Specified voltage	Zero pressure	Specified concentration
BC	Insulation	Slip velocity	Impermeable
CD	Charging of EDL defined by equation (6.3)	Slip velocity	Impermeable
DE	Insulation	Slip velocity	Impermeable
FE	Grounded	Zero pressure	Convective flux
AF	Insulation	Slip velocity	Impermeable

also observed by many other researchers as reviewed by Bazant et al. (2009), and the underlying mechanism for such flow reversal is still an open question at the present stage. In the modeling, it is assumed that the flow reversal is due to the sign change of induced zeta potential over the conducting patch.

Since the particles are transported into the microchannel from the inlet boundary, the particle concentration should be maintained the same as the initial particle concentration at segment AB, i.e. $c = 1$. At the outlet boundary (FE), it is assumed that the particles are only transported convectively and thus a

convective flux boundary condition is applied. Furthermore, the particles cannot penetrate through the channel walls and the conducting patch, and thus zero mass flux boundary conditions are specified at these segments (BC, CD, DE, and AF).

The whole computational domain was meshed with triangular elements, and the mesh near the conducting patch CD was the finest to capture large gradients in this area. The grid independence was also tested before using the model. The governing equations for electrical potential, flow field and particle concentration are decoupled, which allows us to solve these three equations separately. The electric problem and the flow problem were first solved sequentially using the stationary UMFPACK solver with a relative tolerance of 10^{-6}. The particle concentration was then solved using the converged results of the electric and velocity fields by a time-dependent BDF solver.

6.4.4 COMPARISON OF THE SIMULATION WITH THE EXPERIMENT

In this section, theoretical analyses are conducted to investigate the underlying mechanisms responsible for the particle trapping, and the steady sate trapping of 500nm particles are chosen for such purpose. Figure 6.9 presents the numerical predictions of three different hypothetical cases for trapping of 500nm particles at the steady state. Figure 6.9(a) presents the first hypothetical case without the floating conducting patch. It is expected that the typical flow field under this case is an electroosmotic plug flow in the microchannel. The particle transport in this case is due to the joint effect of electroosmotic plug flow and particle electrophoresis. It is seen that the particle concentration is uniform in the entire channel domain, with its initial normalized value of unity. Figure

6.9(b) depicts the second hypothetical case with the induced-charge electrokinetic flow but without consideration of the particle dielectrophoresis. In this situation, two vortices over two edges of the conducting patch are generated because of induced-charge effects. There is still no trapping of particles as illustrated in Figure 6.9(b). Only when both induced-charge electrokinetic flow and dielectrophoresis are effective (Figure 6.9(c)), the particles can be trapped and concentrated in a region defined by the ICEK microvortex over the right edge of conducting patch. The results from the three hypothetical cases suggest that ICEK flow and particle dielectrophoresis are both crucial for successful trapping of particles. Based on this picture, the trapping mechanism can be understood as

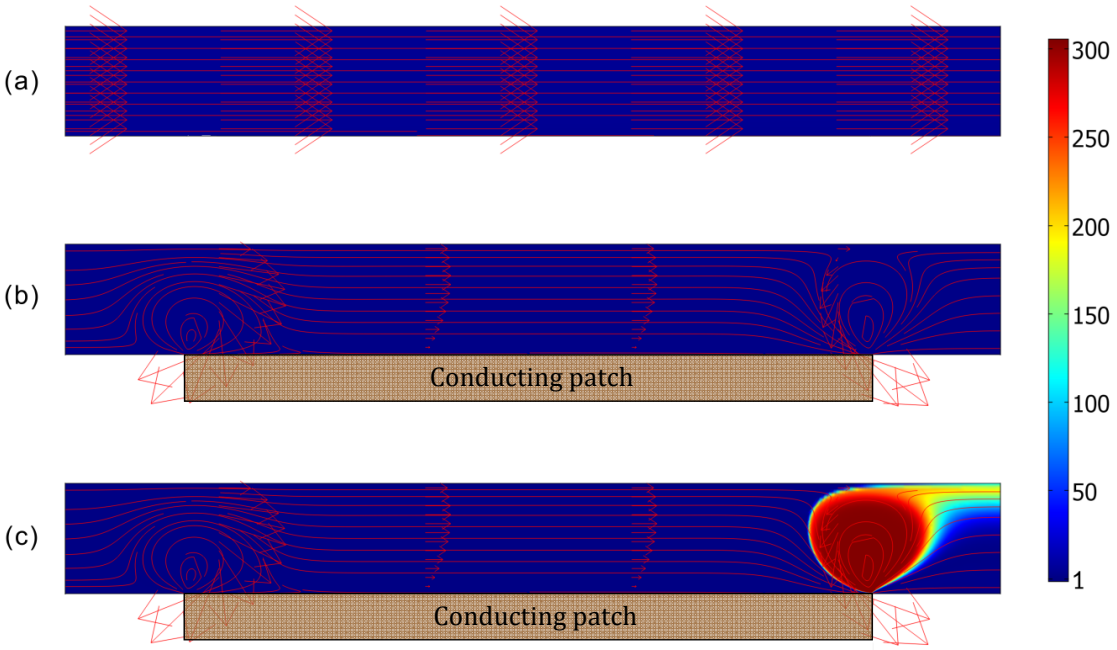

Figure 6.9 Numerical predictions for the steady-state trapping of 500nm particles under a combined AC and DC electric field (V_0=36 V, V_1=368 V and f=4 kHz). (a) Without the conducting patch (i.e., without ICEK flow and dielectrophoresis), (b) Without dielectrophoresis and with ICEK flow, (c) With both ICEK flow and dielectrophoresis. The arrows and lines give details of flow field and the contour plots give the normalized particle concentration field c.

follows: the dielectrophoresis only takes effect very near the edges of conducting path and try to trap the particles on the edge of the conducting path (Note that 500nm particle experience positive dielectrophoretic force which pushes particles to the edges of conducting patch). Subsequently, induced-charge electrokinetic flow entrains these trapped particles into the vortex, leading to the final trapping of particles as shown in Figure 6.9(c). Interestingly, the trapping of particles only occurs inside the right vortex, which can be attributed to the DC field driven electroosmotic flow from the insulating channel which breaks the symmetric configuration of two vortices generated by pure ICEK. In the modeling, it is found that the trapping location shifts to the left vortex if the polarity of the DC field is reversed, which is also consistent with our experimental observations.

To carry out a quantitative comparison against experiments, the theoretical concentration of particles is averaged along the channel depth direction. In addition, the experimentally measured fluorescence intensity can be readily converted to particle concentration enhancement, since the calibration suggests a linear relationship between the fluorescent intensity and the concentration of 500nm particles. Figure 6.10 provides a detailed comparison of particle concentration enhancement between the numerical prediction and the experimental measurement for an entire transient trapping process. Generally, the numerical simulation can qualitatively predict the transient trapping of particles over the right edge of the conducting patch. Quantitatively, it is seen that the theoretically predicted enhancement of particle concentration is more-than 300 fold at 30s, and the band of trapped particles forms a near-rectangular zone. However, the experimental measurements only achieve around 120 fold

enhancement of the particle concentration at 30s, and the band of trapped particles exhibits a triangular shape. Moreover, the measured trapping band is much smaller than that of theoretical prediction.

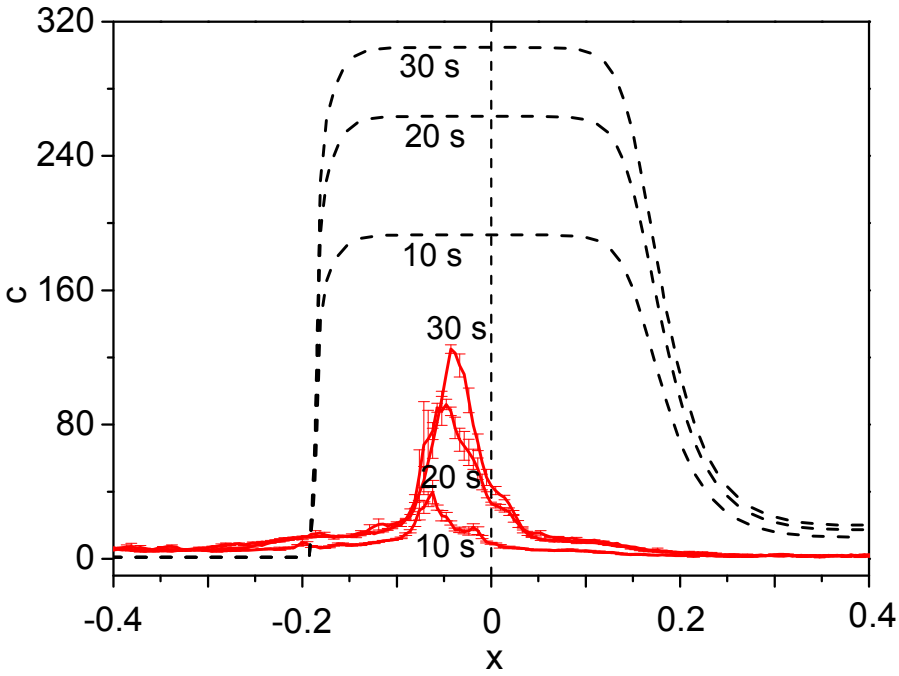

Figure 6.10 Quantitative comparison between experimental results and numerical results for the transient trapping of 500nm particles under a combined AC and DC electric field (V_0=36V, V_1=368V and f=4 kHz). The dashed lines are the averaged concentration profile across the microchannel depth direction predicted by the theoretical model and the solid lines with the error bars are the concentration profile along the centerline of microchannel from the experimental observation. The vertical dashed line denotes the right edge of conducting patch.

In summary, the presented model can only give qualitative prediction of the particle trapping. Those discrepancies shown in Figure 6.10 can be possibly explained from three aspects: first, for the theoretical prediction of induced-charge electrokinetics flow, the velocity from the experiment is universally lower than that from the theory in most existing literature, sometimes even by orders of magnitudes (Bazant et al., 2009). The reason for this may be manifold, such as

ion crowding in the EDL, surface contamination and increased viscosity of the solution near the solid surface. Second, in the modeling of particle transport, the mass flux of particles due to other colloidal forces, such as EDL forces among particles, EDL force between particles and channel walls, van der Waals force among particles as well as van der Walls force between particles and channel walls, were neglected. These forces are especially important when the interparticle distance and the particle-wall distance are very small. For example, when the particles are concentrated in the microvortex domain as shown Figure 6.9(c), the interparticle distance could be small enough to induce these colloidal forces. Third, a constant dynamic viscosity for the solution was assumed in solving the flow field. However, for the solution dispersed with particles, the viscosity may not be a constant value and usually has direct relation with the size and local volume fraction of particles. Especially, the viscosity of solution in the trapping zone is expected to be strikingly different from that of pure solution.

6.5 SUMMARY

Utilizing the induced-charge electrokinetics, a novel method for high-throughput particle trapping is devised and tested. The device for particle trapping simply consists of a microchannel and a conducting patch on the bottom wall of the channel. When a particle solution is continuously transported through the microchannel under a combined AC and DC electric field, the particles get trapped around one edge of the conducting patch, and form a particle line which is defined by the edge of conducting patch. It is demonstrated that the proposed method is capable of trapping particles with size ranging from 50nm to 1.9 μm. Particularly, the experimental demonstration of 50nm particle trapping implies

that the present method could be particularly efficient for trapping nanoparticles which is still a challenge for most of other trapping techniques.

In addition, a multiphysical model was established to illustrate the trapping mechanism due to the induced-charge electrokinetics. The model utilizes the effective boundary conditions presented in Chapter 3 for predictions of the induced zeta potential on the conducting surface and then the induced-charge electrokinetic flow. The particle transport due to the induced flow, electrophoresis and dielectrophoresis is solved to obtain the particle concentration field. It is shown that the induced-charge electrokinetic flow circulation and dielectrophoresis over the edge of the conducting patch are indispensable to the successful trapping of particles, and there would be no trapping if either of them disappears. Only a qualitative agreement between the theoretical predictions and experimental results is achieved because of assumptions and limitations embedded in the model, and more advanced models will be required to reach a closer agreement.

CHAPTER 7: CONCLUSIONS AND FUTURE STUDIES

7.1 CONTRIBUTIONS

In comparison with the conventional linear electrokinetic phenomena, induced-charge electrokinetic phenomena can achieve the active control of zeta potential or surface charge, which is much desired in microfluidic and nanofluidic applications. This thesis presents theoretical advancements of induced-charge electrokinetics and its several potential applications in microfluidics and nanofluidics. The findings from the present thesis research can serve as the guidance for incorporating induced-charge electrokinetic techniques into microfluidic and nanofluidic devices. To be more specific, four major contributions during the course of my PhD study can be summarized below:

1. **Derivation of effective electric boundary conditions for evaluation of induced zeta potentials on solid surfaces with arbitrary electric properties**. In the existing literature, two extreme categories of electrokinetics have been studied. The first is the classic linear electrokinetics over completely insulating (nonpolarizable) surfaces bearing fixed physiochemical bond charge. The second is the induced-charge nonlinear electrokinetics over perfectly polarizable surfaces (conductors) acquiring charge due to the electric polarization. Electrokinetics over solid surfaces with finite electric properties represents a more general situation and certainly bridges the gap between the above two extreme categories. When electric properties of solid surface go to one extreme (completely insulating or nonpolarizable) and another extreme (good conductivity or perfectly polarizable), the above two extreme categories can be

recovered from the general situation, respectively. Therefore, the focus of this thesis has been placed on the general situation and two types of effective electric boundary conditions for evaluation of induced zeta potentials on solid surfaces are derived. The first type of boundary conditions assumes that the solid is purely dielectric and no free charge carriers exist inside such solid. The interface between the liquid electrolyte and the solid consists of only an EDL inside the electrolyte solution. The derived boundary conditions quantifying the contribution of the polarizability of the solid to zeta potential are applicable to solid surfaces with arbitrary dielectric constants. To demonstrate the application of such boundary conditions, the DC field driven induced-charge electroosmotic flow in a microchannel embedded with a pair of polarizable dielectric blocks is analytically studied, and the results show that the perfectly polarizable conductor induces strongest vortices above the conducting block surface. The second type of boundary conditions assumes that the solid is leaky-dielectric. Then free charge carriers (electrons and holes) do exist inside the solid. The interface between the electrolyte and the solid consists of an SCL in the solid and an EDL in the liquid electrolyte. It is shown that this type of boundary conditions is the generalized boundary conditions dealing with AC field driven induced-charge electrokinetic phenomena over solid surfaces with arbitrary dielectric constants and conductivities. At last, an analytical study is presented to calculate the flow field around a leaky-dielectric cylinder by using the proposed boundary conditions. The flow pattern basically contains four vortices around the cylinder which become stronger as the conductivity and/or dielectric constant of the cylinder increase.

2. Development of a comprehensive model for analyzing the transient behaviors of EDL charging and electrokinetic flow around polarizable dielectrics. Most of previous theoretical analyses of the dynamic induced-charge electrokinetics involved various assumptions including thin EDL, perfectly polarizable surfaces, decoupling of the flow and the ionic transport, negligible surface conduction, symmetric electrolyte and equal diffusion coefficients of cations and anions, etc, which can be sometimes violated in practical applications. In view of this, a comprehensive model including the Poisson equation for electric potential, the Nernst-Planck equation for concentration of ionic species and the Navier-Stokes equation for velocity field is developed and solved numerically in a fully coupled manner to abolish the above assumptions. Consequently, our model is valid for arbitrary thickness of EDL and thus can reveal the details inside EDL which are necessary for understanding induced-charge electrokinetic phenomena around polarizable dielectrics with nanometer scales. Finally, the developed model is applied to simulate dynamic behaviors of the EDL charging and the associated electrokinetic flow around arbitrarily polarizable dielectrics. The model substantiates two time scales in the EDL charging reported in previous works, i.e., the RC charging time scale and the bulk diffusion time scale. Apparently, the present model certainly extends the previous analyses to more general cases with finite EDL thickness and finitely polarizable surface. More importantly, the details inside the EDL during the charging process are resolved for the first time and the induced flow accompanying the charging of EDL is investigated in details.

3. Extension of induced-charge electrokinetics from microfluidics to nanofluidics for active and flexible control of both ionic transport and fluid

flow. In nanofluidic channel, the surface charge on the channel wall governs the transport of charged species, such as ions, molecules and virus etc. The ability to modify the surface charge is crucial for active control of the transport of these species through nanochannels. We have presented two nanofluidic systems based on the induced-charge electrokinetics for active modification of the surface charge on the nanochannel walls. In the system with straight conducting nanochannels, there is no net flow and the channel does not show preferential transport of ions when the walls float in an external electric field. However, when the wall potential is actively controlled by the DCGC technique, the nanofluidic system can be readily tuned to be cation selective or anion selective, and the flow direction can be readily controlled to be forward or reverse by control of the wall voltage. For the system with tapered conducting nanochannels, the ionic selectivity can be reversed by the reversion of the direction of external driving field and the flow in the nanochannel however always goes from the narrow end to the wide end regardless of the direction of the driving field. It is then expected that such system can generate net flow even under an AC driving electric field. Another way of tuning the ionic selectivity and the fluid flow can be realized by altering the taper angle of the conducting wall.

4. Development of a novel and high-throughput method based on induced-charge electrokinetics for particle trapping. The proposed method for particle trapping relies on induced-charge electrokinetic phenomena over a conducting patch floating in combined AC and DC electric fields. The ability of presented method for trapping of micron particles, submicron particles and even nano particles has been successfully demonstrated by experiments. The present method has numerous advantageous features over other established particle

trapping methods: it can achieve high-throughput trapping and does not require sophisticated laser systems as compared to optical tweezing; it does not involve complex electrode design as compared to the dielectrophoretic trapping. Furthermore, a theoretical model based on effective electric boundary conditions presented in Chapter 3 is constructed to simulate the particle trapping phenomenon. The theoretical analyses show that the trapping of particles is mainly due to the combined effects of dielectrophoresis and induced-charge electrokinetics over the floating conducting patch, and the experimental results are in qualitative agreement with the theoretical modeling. The discrepancy between the numerical predictions and the experimental observations is likely due to several limitations of the theory of induced-charge electrokinetics and the neglect of complex colloidal forces in the modeling of particle transport.

7.2 RECOMMENDATIONS FOR FUTURE RESEARCH

7.2.1 EXPERIMENTAL VALIDATION OF EFFECTIVE ELECTRIC BOUNDARY CONDITIONS ON SOLID-ELECTROLYTE INTERFACE

The effective electric boundary conditions presented in Chapter 3 are of fundamental importance to induced-charge electrokinetics. These boundary conditions can be used to predict the induced zeta potentials on surfaces with arbitrary electric properties. Although they have been rigorously derived, experimental investigations are required to verify such boundary conditions. However, the validation of these boundary conditions is not straightforward, because these boundary conditions predict the potential drop across the liquid-electrolyte interface, and direct measurement of such potential drop is usually difficult. The induced zeta potential can be related to the induced flow field via

the Helmholtz-Smoluchowski velocity, which provides us an alternative way of validation. In the future study, the micro-PIV technique will be utilized to measure the induced-charge electrokinetic flow around solids with finite electric properties. Once the flow field is obtained, the induced zeta potential can be retrieved from the Helmholtz-Smoluchowski velocity. Then a comparison between the retrieved induced zeta potential and the induced zeta potential predicted from our model fulfills an indirect validation of the derived effective electric boundary conditions.

7.2.2 EXPERIMENTAL REALIZATION OF THE DIRECT CONTACT GATE CONTROL NANOFLUIDIC SYSTEM

Two prototypes of nanofluidic systems utilizing induced-charge electrokinetics have been proposed in Chapter 5. Both of them demonstrate a high level of flexibility for control of both the charged species transport and the fluid flow. The current state-of-the-art micro- and nano-fabrication technologies allow us to fabricate such two nanofluidic systems. Nanochannels with dimensions ranging from several nanometers to several tens of nanometers can be fabricated on silicon substrates by using the reactive ion etching or wet etching (Duan and Majumdar, 2010; Mao and Han, 2005), and then the nanochannel walls can be made conductive by coating them with thin conducting films (such as gold or platinum) using the sputtering process or electron beam evaporation process. In the next step, these systems will be fabricated and the performance of such systems for control of ionic transport and fluid flow will be experimentally tested. Moreover, a comparison between the experimental results and the theoretical predictions will be carried out.

7.2.3 EXTENSION TO TRAPPING OF BIOPARTICLES WITH MULTIPLE FLOATING CONDUCTING PATCHES

In the experimental work presented in Chapter 6, only one floating conducting patch is used for trapping and concentration of polystyrene beads. However, in more advanced applications, trapping and concentration at multiple locations in microfluidic devices are sometimes required. Considering the trapping mechanism of the proposed technique, trapping at multiple locations needs the introduction of multiple vortices to the system. It is expected that the sputtering of multiple floating conducting patches on glass substrate can induce multiple vortices and then the trapping at multiple locations can be readily fulfilled. In addition, polystyrene beads were used in the original experiment. More practically, microfluidic systems handle bioparticles, such as cells, biomacromolecules and bacteria etc. Consequently, the proposed microfluidic method will be extended for trapping and concentration of bioparticles at multiple locations in the future.

7.2.4 FURTHER IMPROVEMENT OF EFFECTIVE ELECTRIC BOUNDARY CONDITIONS ON SOLID-ELECTROLYTE INTERFACE WITH CONSIDERATION OF ION SIZE EFFECTS

In dilute electrolyte solutions, the Poisson-Boltzmann equation relates the concentration of ionic species and the electric potential in the diffuse part of EDL at a charged surface. In classical linear electrokinetic phenomena, the potential drop across the EDL is usually comparable to the thermal voltage (k_BT/e). However, induced-charge nonlinear electrokinetic phenomena under large driving voltages frequently involve large induced zeta potentials which could be significantly larger than the thermal voltage. Consequently, the Poisson-

Boltzmann theory becomes invalid under this circumstance because it predicts an absurdly high concentration of counterions on the solid surface. This is attributed to the assumption of pointlike ions embedded in the classic Passion-Boltzmann equation. More realistically, ions have finite sizes which were already shown to have important implications on EDL charging (Kilic et al., 2007a, b) and ACEO pumping (Storey et al., 2008). If a solid surface gets heavily charged due to electric polarization, a very larger number of counterions in the electrolyte solution are attracted to the surface and thus the EDL near the solid surface becomes highly crowded with these counterions. Under this circumstance, the finite ion size must be accounted for by using more advanced theoretical approaches instead of the classic Poisson-Boltzmann equation. Definitely, the significant crowding of ions inside the EDL would affect the magnitude of the potential drop across the EDL (or the so-called induced zeta potential). Therefore, the derived effective electric boundary conditions in Chapter 3 must be modified to include the ion size effects for the situation of large applied electric fields and/or highly polarizable surfaces. The theoretical modifications of these boundary conditions are to be carried out in the future.

Appendix A: Validation of the numerical model for transient induced-charge electrokinetics

The numerical model presented in Chapter 4 for characterizing the transient dynamics of induced-charge electrokinetics consists of a set of highly coupled governing equations, and we solved this strongly coupled system with finite element software package Comsol Multiphysics 3.4 which is suitable for modeling phenomena arising from the interplay of multiple physical effects. In order to carry out the simulation, the simulated domain should be meshed first. The characteristics of the coupled solutions must be considered when meshing the simulated domain. Near the cylinder surface inside the EDL, gradients of electric potential, ionic concentration and velocity are extremely pronounced, and thus the simulation domain near the cylinder surface was finest meshed to capture these large gradients. Specifically, in our calculations, the mesh near the conducting surface has more than 10 elements inside the EDL. Since the accuracy of the numerical model is usually dependent on the mesh size, dependence of the results to mesh size was excluded by comparing the results obtained from different numbers of mesh elements. The results presented in this work were all obtained using a mesh containing 87,000 finite elements which ensures that all results are independent of measurable influence of mesh size.

When an uncharged conducting cylinder immersed in electrolyte a solution is suddenly subjected to an external electric field, this cylinder is instantaneously polarized to acquire surface charge on its surface. Such surface charge breaks the local electroneutrality near the cylinder surface and induces an EDL around the conductor surface to restore the overall electroneutrality of the system. During

the transient formation of the EDL around the conducting cylinder, the tangential component of the external electric field exerts an electrostatic force on the induced EDL. This force drives the electrolyte solution in the EDL to move, resulting in an transient induced-charge electroosmotic slip velocity over the cylinder surface, $u_s = 2E_0^2 \sin(2\theta)\left(1 - e^{-2t}\right)^2$ (Squires and Bazant, 2004). The velocity, electric field strength and time in the above formula have been nondimensionalized by using the reference quantities defined in Chapter 4. The derivation of such transient slip velocity employs several assumptions including the Debye Hückel linearity, no surface conduction, no convective ionic transport and thin EDL approximation. In the numerical model, none of these assumptions were made. Then the comparison of the numerical solution and the analytical solution is not straightforward. However, if we choose a case with large values of κa (thin EDL) and low driving voltages, these assumptions should hold properly.

In view of this point, we ran a transient numerical simulation for a large value of κa =500 and a small electric bias of φ_0=1.0 from the initial state to the steady state. In the numerical simulations, the location where the magnitude of the tangential velocity reaches its maximum is treated as the outer edge of the EDL, and the velocity there is chosen as the slip velocity. Comparison of the numerical and analytical slip velocities at the outer edge of the EDL for five different instants is shown in Figure A1. At first three instants (i.e., t=0.01, 0.1 and 0.5), the numerical results agrees very well with the theoretical predictions. At the last two time instants (i.e., t=1.0 and ∞), the numerical predictions slightly underestimate the theoretical predictions. Such difference could be due to the assumptions embedded in the analytical formula mentioned above. Although a

case of very thick EDL (κa=500) was chosen in the numerical simulation, the analytical formula is derived under the assumption of vanishing thickness of EDL (κa→∞). Overall, the finite element model constructed in Comsol can well reproduce the analytical results and thus is ready for use to investigate the transient behaviors of EDL charging and induced-charge electrokinetic flow around dielectric objects in Chapter 4.

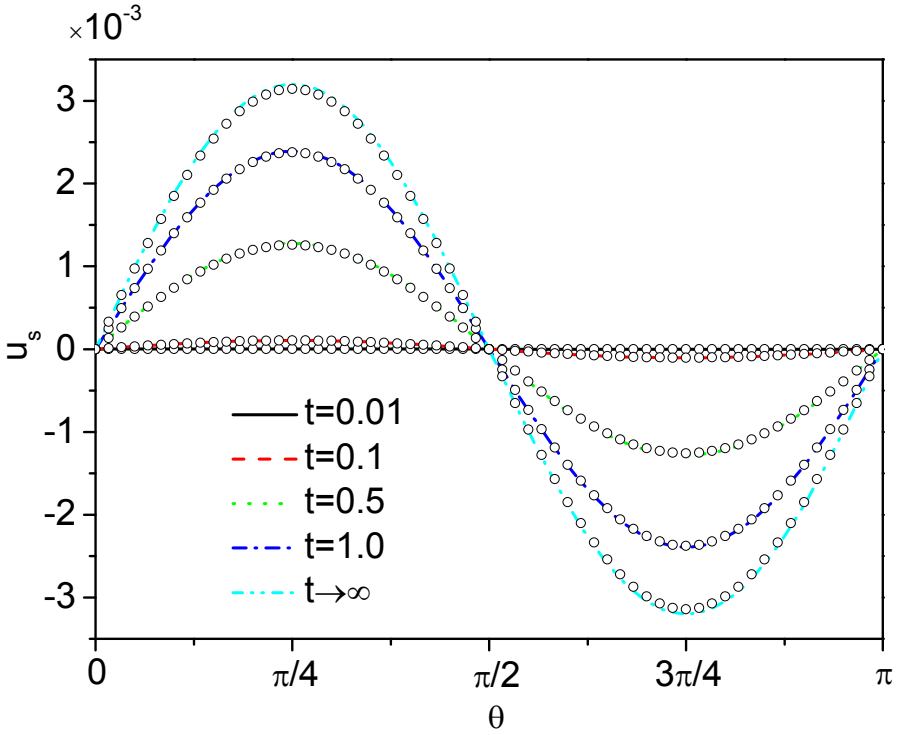

Figure A.1 Transient development of induced-charge electroosmotic slip velocity over the upper half of the cylinder surface. The solid lines are the solutions from the analytical formula, $u_s = 2E_0^2 \sin(2\theta)\left(1 - e^{-2t}\right)^2$ (Squires and Bazant, 2004). The circles are the results from the finite element model in Comsol.

Appendix B: Model validation and supplemental results for induced-charge electrokinetics in conducting nanochannels

B.1 Numerical method and validation

The presented model is different from most of the previous relevant studies on induced-charge electrokinetic phenomena around microscale conducting surfaces (Bazant and Squires, 2004; Squires and Bazant, 2004), because in these studies the ionic concentrations conform to the Boltzmann distribution. Then the electric potential is governed by the Poisson–Boltzmann equation, and the electrostatic and hydrodynamic problems are decoupled. However, the Boltzmann distribution is only valid to describe the ionic distribution over charged surfaces in contact with an infinitely large quiescent liquid medium. In the current study, the channel is in nanometric scale, and the EDLs around the walls of the nanochannel overlap. Furthermore, the ionic species are also transported convectively by the flow. Evidently, distributions of ionic species do not exactly follow the Boltzmann distribution, and hence the Poisson-Boltzmann equation cannot give a precise description of the electric potential. Overall, the electrostatic problem, the hydrodynamic problem and the ionic transport in our case are highly coupled, and then the numerical method is resorted to for tackling this coupled system.

The strongly coupled system presented in Chapter 5 was solved using the commercial finite element software package Comsol Multiphysics 3.4. The simulated domain is fairly regular in shape, and nonuniform meshes were

employed with a larger number of mesh elements within the nanochannel. Furthermore, to capture the details inside the EDL on the wall (segment DE) of the nanochannel, the region near the wall was finely meshed with more than 20 mesh elements inside the EDL. In addition, the solutions obtained for different numbers of mesh elements were compared to ensure that the results are independent of the size of finite element mesh. The results presented in this work were all obtained using a mesh system containing 210,000 elements. The direct solver UMFPACK was used for solving all governing equations and the relative tolerance was set to 10^{-8}. Reservoirs with different sizes were also considered in the simulations. It is found that the results depend marginally on the reservoir size. Hence, predictions for reservoir size of 67h×67h are presented in this work. Before we are confident to start using the above numerical model, we simulated a conventional electroosmosis with fixed surface charge density on the channel walls and compared the numerical results with the bench mark solutions to ensure the validity of the numerical model.

We reminisce about a benchmark for the conventional electroosmosis in an insulating microchannel with a fixed surface charge density q on the walls. Then the dimensionless axial velocity takes the form (Keh and Tseng, 2001; Stein et al., 2004; Zhao et al., 2008)

$$u = -q\frac{E_x}{\kappa h}\frac{\cosh(\kappa h)}{\sinh(\kappa h)}\left[1-\frac{\cosh(\kappa h y)}{\cosh(\kappa h)}\right] \tag{B1}$$

where q is the dimensionless surface charge density normalized with $\varepsilon_0\varepsilon_r\varphi_{ref}/h$ and E_x is the dimensionless electric field strength along the channel axial direction and is normalized with φ_{ref}/h.

The derivation of the analytical formula (B1) employs several assumptions including the Debye-Hückel linearization of Poisson–Boltzmann equation, the linear superposition of external and EDL electric fields, no variation of axial ionic concentration and the neglect of entrance/exit effects. Because these assumptions were not made for the present numerical model, comparison of the numerical and analytical results is not straightforward. Nevertheless, if one focuses on the mid-section of the channel (corresponding to x =0, sufficiently far from the channel inlet and outlet), the numerical results would be astonishingly close to those existing in an infinitely long channel (Mansouri et al., 2005). Therefore, we compared the axial velocity profile obtained from the numerical simulation at x =0 with the corresponding velocity profile obtained using equation (B1). It also should be noted that one needs to take value of E_x in equation (B1) to be identical to the numerical solution of the parameter at the mid-plane when comparing the velocity profiles. The numerical simulations for κh =5, and 10 were conducted using a constant surface charge of q = -1 at the capillary wall and a voltage difference of 1000 between the two driving electrodes (i.e., φ_0 = 1000). From the steady state numerical solution, the value of E_x at x=0 and y=0 is obtained. This value of E_x is then substituted in equation (B1) to calculate the analytical velocity profiles. Figure B.1 shows the comparison between the numerical and analytical velocity profiles. It is evident that the velocity profiles at the mid-section of the channel (x=0) obtained from the numerical simulation agrees excellently with the velocity profiles obtained for an infinitely long channel using the analytical formula given by equation (B1).

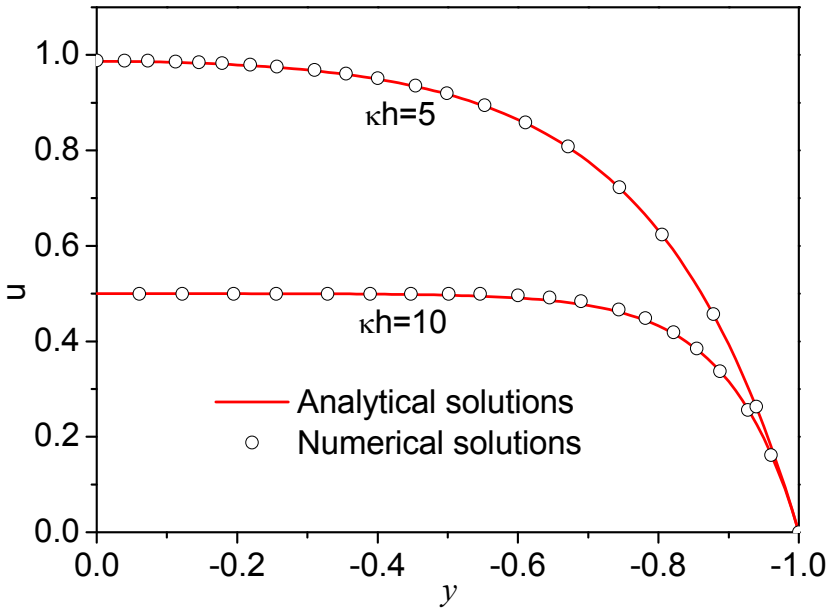

Figure B. 1 Comparison of velocity profiles obtained from present numerical model and the analytical formula equation (B1) for electroosmosis with a uniform natural surface charge density of q=-1 on the channel walls. In comparisons, the velocity profiles are obtained at the cross section of x=0 and two values of κh are chosen, viz., κh =5, 10.

B.2 Supplemental results for negatively biased cases under three operating modes

B.2.1 Electroosmosis in conducting nanochannels with floating walls (Mode1)

When the system is negatively biased (φ_0 = -6), it is seen from Figure B.2 (a) that the electric potential grows along the axial direction and there are also two identical potential barriers at the junctions connecting the nanochannel and the two reservoirs. The ionic distributive characteristics inside the nanochannel can be obtained by simply interchanging the profiles of K^+ and Cl^- presented in Figure 5.3 for the positively biased case (φ_0 = 6). The wall polarization shown in Figure B.2 (b) reverses as compared to the positively biased case shown in Figure 5.5 (a).

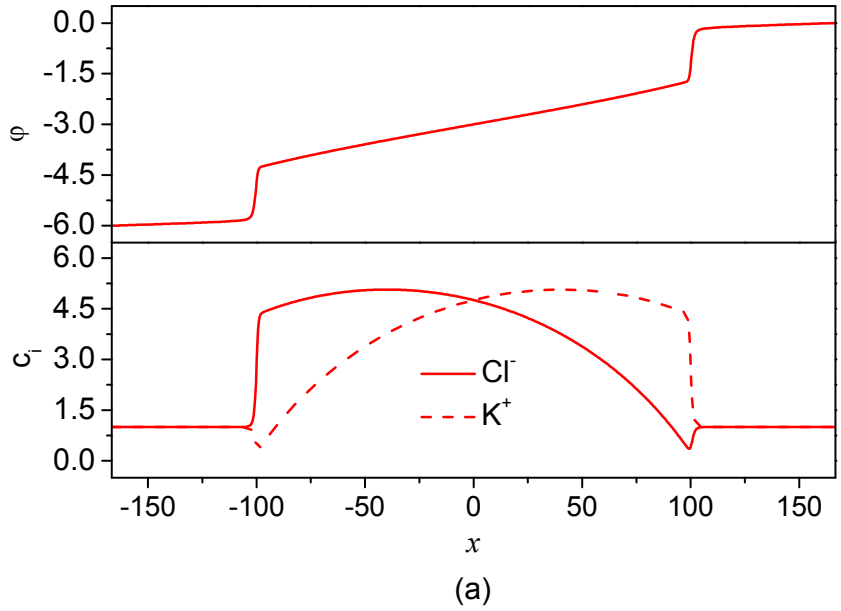

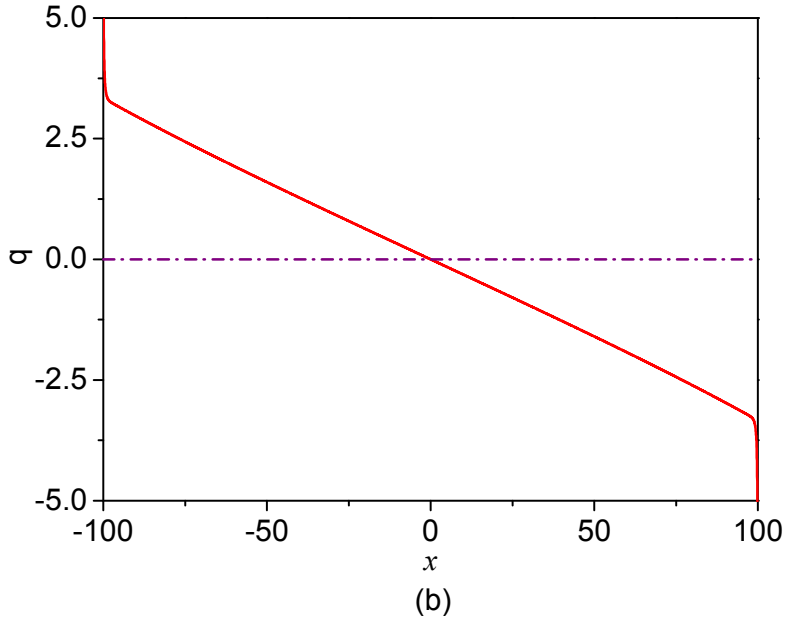

Figure B.2 The results for mode 1 when the conducting walls are floating for a negatively electric bias of φ_0 = -6 . (a) Electric potential φ and ion concentration c profiles along the nanochannel axis (y=0) and (b) Surface charge density q along the conducting wall.

B.2.2 Electroosmosis in conducting nanochannels with wall potential closer to φ_0 (Mode 2)

For the negatively biased case ($\varphi_0 = -6, \varphi_1 = -4$), Figure B.3 (a) shows that the electric potential increases from -6 to 0 along the nanochannel and the potential rise across the left nanochannel-reservoir junction is less significant because the conducting wall is biased much closer to $\varphi_0 = -6$. The ionic concentration profiles can be obtained by interchanging the profiles of anions and cations depicted in Figure 5.6 (a) for the positively based case ($\varphi_0 = 6, \varphi_1 = 4$). Contrary to the positively biased case, the cations predominate inside the longer right portion of the nanochannel while the anions predominate inside the relatively shorter left portion of the nanochannel. In addition, it can be concluded from the Figure B.3 (b) that the wall polarization also reverses as compared to the positively biased case shown in Figure 5.6 (b).

B.2.3 Electroosmosis in conducting nanochannels with wall potential closer to the ground (Mode 3)

In the negatively biased case ($\varphi_1 = -2$, $\varphi_0 = -6$) depicted in Figure B.4 (a), similar to that shown in Figure B.3 (a), the electric potential also grows from -6 to 0, while the potential rise at the right nanochannel-reservoir junction is less significant. And the ion distributions in Figure B.4 (a) can also be similarly obtained via interchanging profiles of K^+ and Cl^- presented in Figure 5.8 (a) for the positively biased case ($\varphi_1 = 2$, $\varphi_0 = 6$). In addition, the wall polarization presented in Figure B.4 (b) also reverses as compared to the positively biased case shown in Figure 5.8 (b).

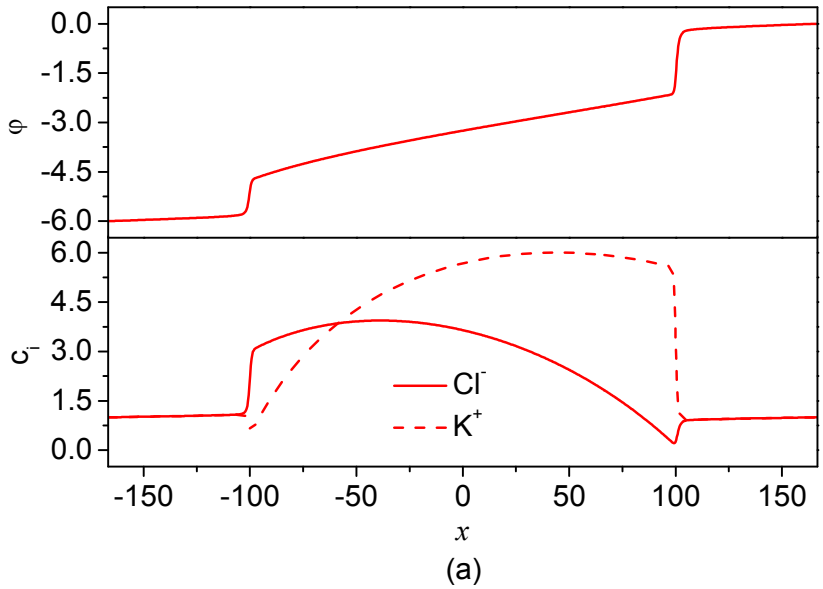

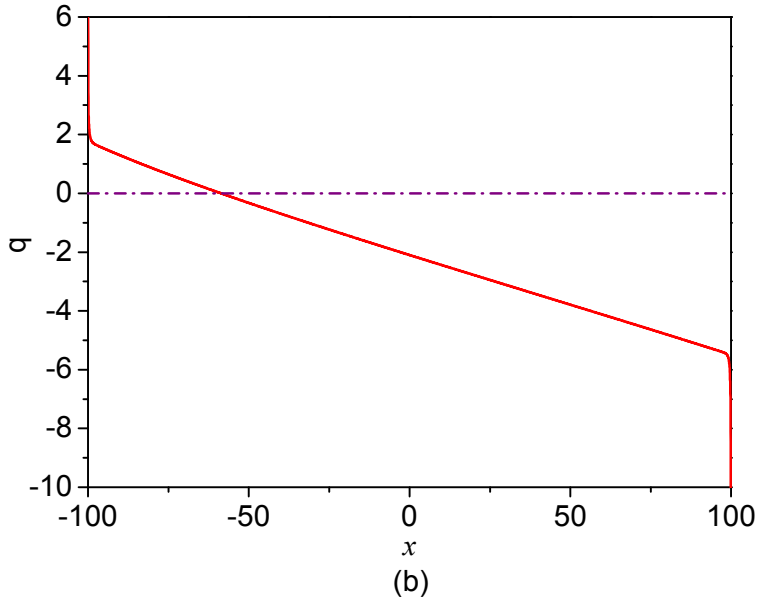

Figure B.3 The results for mode 2 when the potential on the conducting walls is set to be closer to φ_0 for the negatively biased case of $\varphi_0 = -6, \varphi_1 = -4$. (a) Electric potential φ and ion concentration c profiles along the nanochannel axis (y=0) and (b) Surface charge density q along the conducting wall.

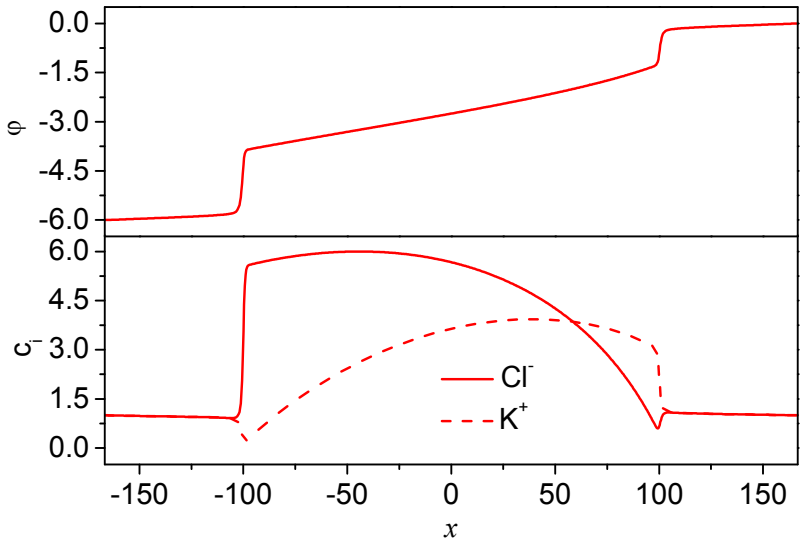

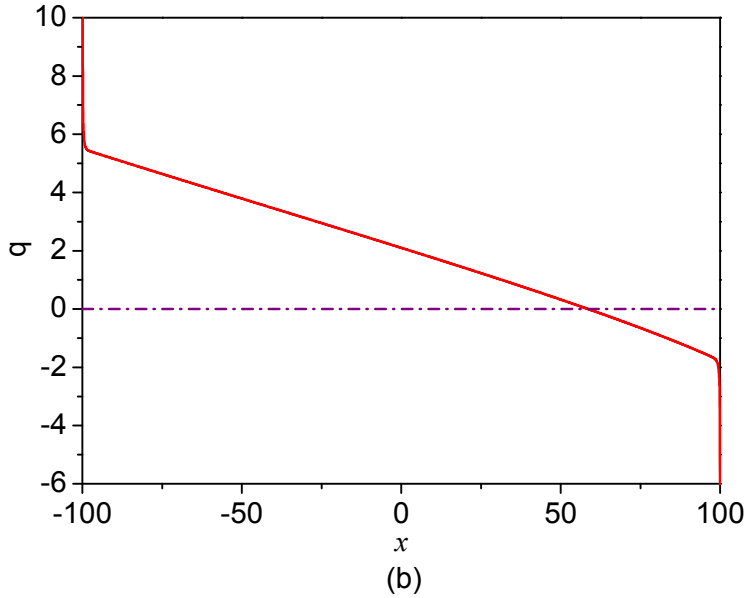

Figure B.4 The results for mode 3 when the potential on the conducting walls is set to be closer to the ground for the negatively biased case of φ_0 = -6, φ_1 = -2. (a) Electric potential φ and ion concentration c profiles along the nanochannel axis (y=0) and (b) Surface charge density q along the conducting wall.

References

Ajdari A (1995) Electro-osmosis on inhomogeneously charged surfaces. Physical Review Letters 75: 755-758

Ajdari A (2000) Pumping liquids using asymmetric electrode arrays. Physical Review E 61: R45-R48

Anderson JL (1985) Effect of nonuniform zeta potential on particle movement in electric fields. Journal of Colloid and Interface Science 105: 45-54

Anderson JL (1989) Colloid Transport by Interfacial Forces. Annual Review of Fluid Mechanics 21: 61-99

Anderson JL, Idol WK (1985) Electroosmosis through pores with nonuniformly charged walls. Chemical Engineering Communications 38: 93-106

Arnold WM, Schwan HP, Zimmermann U (1987) Surface conductance and other properties of latex particles measured by electrorotation. The Journal of Physical Chemistry 91: 5093-5098

Barany S, Mishchuk NA, Prieve DC (1998) Superfast Electrophoresis of Conducting Dispersed Particles. Journal of Colloid and Interface Science 207: 240-250

Bardeen J (1947) Surface states and rectification at a metal semi-conductor contact. Physical Review 71: 717-727

Basuray S, Chang H-C (2007) Induced dipoles and dielectrophoresis of nanocolloids in electrolytes. Physical Review E 75: 060501

Bazant M, Chu K, Bayly B (2005) Current-Voltage Relations for Electrochemical Thin Films. SIAM Journal on Applied Mathematics 65: 1463-1484

Bazant MZ (2008) Nonlinear Electrokinetic Phenomena. In: Li D (ed) Encyclopedia of Microfluidics and Nanofluidics. Springer, New York

Bazant MZ, Ben Y (2006) Theoretical prediction of fast 3D AC electro-osmotic pumps. Lab on a Chip 6: 1455-1461

Bazant MZ, Kilic MS, Storey BD, Ajdari A (2009) Towards an understanding of induced-charge electrokinetics at large applied voltages in concentrated solutions. Advances in Colloid and Interface Science 152: 48-88

Bazant MZ, Squires TM (2004) Induced-Charge Electrokinetic Phenomena: Theory and Microfluidic Applications. Physical Review Letters 92: 066101

Bazant MZ, Squires TM (2010) Induced-charge electrokinetic phenomena. Current Opinion in Colloid & Interface Science 15: 203-213

Bazant MZ, Thornton K, Ajdari A (2004) Diffuse-charge dynamics in electrochemical systems. Physical Review E 70: 021506

Ben Y, Chang HC (2002) Nonlinear smoluchowski slip velocity and micro-vortex generation. Journal of Fluid Mechanics 461: 229-238

Ben Y, Demekhin EA, Chang HC (2004) Nonlinear electrokinetics and "superfast" electrophoresis. Journal of Colloid and Interface Science 276: 483-497

Biesheuvel PM, van Soestbergen M, Bazant MZ (2009) Imposed currents in galvanic cells. Electrochimica Acta 54: 4857-4871

Bockris JOM, Reddy AKN (2004) Modern Electrochemistry 2B : Electrodics in Chemistry, Engineering, Biology, and Environmental Science. Kluwer academic publishers, New York

Bockris JOM, Reddy AKN, Gamboa-Aldeco ME (2002) Modern Electrochemistry 2A : Fundamentals of Electrodics. Kluwer academic publishers, New York

Bonnefont A, Argoul F, Bazant MZ (2001) Analysis of diffuse-layer effects on time-dependent interfacial kinetics. Journal of Electroanalytical Chemistry 500: 52-61

Brotherton CM, Davis RH (2004) Electroosmotic flow in channels with step changes in zeta potential and cross section. Journal of Colloid and Interface Science 270: 242-246

Castellanos A, Ramos A, González A, Green NG, Morgan H (2003) Electrohydrodynamics and dielectrophoresis in microsystems: Scaling laws. Journal of Physics D: Applied Physics 36: 2584-2597

Chen JK, Weng CN, Yang RJ (2009) Assessment of three AC electroosmotic flow protocols for mixing in microfluidic channel. Lab on a Chip 9: 1267-1273

Chu KT, Bazant MZ (2006) Nonlinear electrochemical relaxation around conductors. Physical Review E 74: 011501

Daghighi Y, Gao Y, Li D (2011) 3D numerical study of induced-charge electrokinetic motion of heterogeneous particle in a microchannel. Electrochimica Acta 56: 4254-4262

Daiguji H, Oka Y, Shirono K (2005) Nanofluidic Diode and Bipolar Transistor. Nano Letters 5: 2274-2280

Daiguji H, Yang P, Majumdar A (2003) Ion Transport in Nanofluidic Channels. Nano Letters 4: 137-142

Daiguji H, Yang P, Szeri AJ, Majumdar A (2004) Electrochemomechanical energy conversion in nanofluidic channels. Nano Letters 4: 2315-2321

Debnath L, Bhatta D (2007) Integral transforms and their applications Chapman & Hall/CRC, Boca Raton

Deen WM (1998) Analysis of Transport Phenomena. Oxford University Press, New York

Delgado ÁV, Arroyo FJ (2002) Electrokinetic phenomena and their experimental determination: an overview. In: Delgado ÁV (ed) Interfacial Electrokinetics and Electrophoresis Marcel Dekker, New York

Duan C, Majumdar A (2010) Anomalous ion transport in 2-nm hydrophilic nanochannels. Nature Nanotechnology 5: 848-852

Dukhin AS (1986) Pair Interaction of Disperse Particles in Electric Field. 3. Hydrodynamic Interaction of Ideally Polarizable Metal Particles and Dead Biological Cells. Colloid journal of the USSR 48: 376-381

Dukhin AS, Murtsovkin VA (1986) Pair Interaction of Particles in Electric Field. 2. Influence of Polarization of Double Layer of Dielectric Particles on Their Hydrodynamic Interaction in a Stationary Electric Field. Colloid journal of the USSR 48: 203-209

Dukhin SS (1991) Electrokinetic phenomena of the second kind and their applications. Advances in Colloid and Interface Science 35: 173-196

Dukhin SS (1993) Non-equilibrium electric surface phenomena. Advances in Colloid and Interface Science 44: 1-134

Dukhin SS, Shilov VN (1969) Theory of the static polarization of the diffuse part of the thin double layer of spherical particles. Colloid journal of the USSR 31: 564-570

Dukhin SS, Tarovskii AA, Baran AA (1989) Electrophoresis of the second kind for metallic particles. Colloid journal of the USSR 50: 1058-1059

Dydek EV, Zaltzman B, Rubinstein I, Deng DS, Mani A, Bazant MZ (2011) Overlimiting Current in a Microchannel. Physical Review Letters 107: 118301

Evtukh A, Litovchenko V, Semenenko M, Yilmazoglu O, Mutamba K, Hartnagel HL, Pavlidis D (2006) Formation of conducting nanochannels in diamond-like carbon films. Semiconductor Science and Technology 21: 1326-1330

Fan R, Huh S, Yan R, Arnold J, Yang P (2008) Gated proton transport in aligned mesoporous silica films. Nature Materials 7: 303-307

Fan R, Yue M, Karnik R, Majumdar A, Yang P (2005) Polarity switching and transient responses in single nanotube nanofluidic transistors. Physical Review Letters 95: 086607

Flores-Rodriguez N, Markx GH (2006) Anomalous dielectrophoretic behaviour of barium titanate microparticles in concentrated solutions of ampholytes. Journal of Physics D: Applied Physics 39: 3356-3361

Gamayunov NI, Mantrov GI, Murtsovkin VA (1992) Study of flows induced in the vicinity of conducting particles by an external electric-field. Colloid journal of the USSR 54: 20-23

Gamayunov NI, Murtsovkin VA, Dukhin AS (1986) Pair Interaction of Particles in Electric Field. 1. Features of Hydrodynamic Interaction of Polarized Particles. Colloid journal of the USSR 48: 197-203

Gangwal S, Cayre OJ, Bazant MZ, Velev OD (2008) Induced-charge electrophoresis of metallodielectric particles. Physical Review Letters 100: 058302

García-Sánchez P, Ramos A, Green NG, Morgan H (2008) Traveling-wave electrokinetic micropumps: Velocity, electrical current, and impedance measurements. Langmuir 24: 9361-9369

Ge Z (2011) Microfluidic Temperature Gradient Focusing by Electrokinetically Induced Joule Heating. Divison of Thermal Fluids Engineering, vol Doctor of Philosophy. Nanyang Technological University

Ge Z, Yang C, Tang G (2010) Concentration enhancement of sample solutes in a sudden expansion microchannel with Joule heating. International Journal of Heat and Mass Transfer 53: 2722-2731

Ghosal S (2003) The effect of wall interactions in capillary-zone electrophoresis. Journal of Fluid Mechanics: 285-300

Ghosal S (2004) Fluid mechanics of electroosmotic flow and its effect on band broadening in capillary electrophoresis. Electrophoresis 25: 214-228

Ghowsi K, Gale RJ (1991) Field effect electroosmosis. Journal of Chromatography A 559: 95-101

Girault HH, Schiffrin DJ (1985) In: Bard AJ (ed) Electroanalytical Chemistry, vol 15. Marcel Dekker, New York,, p 1

Gitlin I, Stroock AD, Whitesides GM, Ajdari A (2003) Pumping based on transverse electrokinetic effects. Applied Physics Letters 83: 1486-1487

González A, Ramos A, Green NG, Castellanos A, Morgan H (2000) Fluid flow induced by nonuniform ac electric fields in electrolytes on microelectrodes. II. A linear double-layer analysis. Physical Review E 61: 4019-4028

Green NG (2005) Interactions of electric fields with fluids. Anal. Bioanal.Chem. 382: 891-893

Green NG, Ramos A, González A, Morgan H, Castellanos A (2000) Fluid flow induced by nonuniform ac electric fields in electrolytes on

microelectrodes. I. Experimental measurements. Physical Review E 61: 4011-4018

Green NG, Ramos A, González A, Morgan H, Castellanos A (2002) Fluid flow induced by nonuniform ac electric fields in electrolytes on microelectrodes. III. Observation of streamlines and numerical simulation. Physical Review E 66: 026305

Halpern D, Wei HH (2007) Electroosmotic Flow in a Microcavity with Nonuniform Surface Charges. Langmuir 23: 9505-9512

Harnett CK, Templeton J, Dunphy-Guzman KA, Senousy YM, Kanouff MP (2008) Model based design of a microfluidic mixer driven by induced charge electroosmosis. Lab on a Chip 8: 565-572

Heldal T, Volden T, Auerswald J, Knapp H (2007) Embeddable low-voltage micropump using electroosmosis of the second kind. 2007 NSTI Nanotechnology Conference and Trade Show - NSTI Nanotech 2007, Technical Proceedings, vol 3, Santa Clara, California, U.S.A, pp 268-271

Herr AE, Molho JI, Santiago JG, Mungal MG, Kenny TW, Garguilo MG (2000) Electroosmotic capillary flow with nonuniform zeta potential. Analytical Chemistry 72: 1053-1057

Hoffman PD, Zhu Y (2008) Double-layer effects on low frequency dielectrophoresis-induced colloidal assembly. Applied Physics Letters 92: 224103

Huang C-C, Bazant MZ, Thorsen T (2010a) Ultrafast high-pressure AC electro-osmotic pumps for portable biomedical microfluidics. Lab on a Chip 10: 80-85

Huang SH, Hsueh HJ, Hung KY (2010b) Configurable AC electroosmotic generated in-plane microvortices and pumping flow in microchannels. Microfluidics and Nanofluidics 8: 187-195

Hunter RJ (1981) Zeta Potential in Colloid Science. Academic Press, New York

Jain M, Yeung A, Nandakumar K (2009) Efficient micromixing using induced-charge electroosmosis. Journal of Microelectromechanical Systems 18: 376-384

Jeffrey A (2006) Complex analysis and applications. Taylor & Francis, Boca Raton, FL

Joshi P, Smolyanitsky A, Petrossian L, Goryll M, Saraniti M, Thornton TJ (2010) Field effect modulation of ionic conductance of cylindrical silicon-on-insulator nanopore array. Journal of Applied Physics 107: 054701

Karnik R, Castelino K, Majumdar A (2006) Field-effect control of protein transport in a nanofluidic transistor circuit. Applied Physics Letters 88: 123114

Karnik R, Fan R, Yue M, Li D, Yang P, Majumdar A (2005) Electrostatic control of ions and molecules in nanofluidic transistors. Nano Letters 5: 943-948

Keh HJ, Tseng HC (2001) Transient Electrokinetic Flow in Fine Capillaries. Journal of Colloid and Interface Science 242: 450-459

Kilic MS, Bazant MZ (2011) Induced-charge electrophoresis near a wall. Electrophoresis 32: 614-628

Kilic MS, Bazant MZ, Ajdari A (2007a) Steric effects in the dynamics of electrolytes at large applied voltages. I. Double-layer charging. Physical Review E 75: 021502

Kilic MS, Bazant MZ, Ajdari A (2007b) Steric effects in the dynamics of electrolytes at large applied voltages. II. Modified Poisson-Nernst-Planck equations. Physical Review E 75: 021503

King BV, Freund F (1984) Surface charges and subsurface space-charge distribution in magnesium oxides containing dissolved traces of water. Physical Review B 29: 5814-5824

Kivanc FC, Litster S (2011) Pumping with electroosmosis of the second kind in mesoporous skeletons. Sensors and Actuators B: Chemical 151: 394-401

Kovarik ML, Jacobson SC (2009) Nanofluidics in Lab-on-a-Chip Devices. Analytical Chemistry 81: 7133-7140

Kumar A, Qiu Z, Khusid B, Yeksel M, Acrivos A (2005) Strong DC and low-frequency AC fields for the manipulation of particles and fluids in microfluidics. 2005 NSTI Nanotechnology Conference and Trade Show - NSTI Nanotech 2005 Technical Proceedings, Anaheim, California, U.S.A., pp 191-193

Lacoste D, Menon GI, Bazant MZ, Joanny JF (2009) Electrostatic and electrokinetic contributions to the elastic moduli of a driven membrane. European Physical Journal E 28: 243-264

Lee CS, Blanchard WC, Wu CT (1990) Direct control of the electroosmosis in capillary zone electrophoresis by using an external electric field. Analytical Chemistry 62: 1550-1552

Lee D-H, Farouk B, Noh H (2011) 3-D Simulations of Electroosmotic Sample Migration in Microchannels: Effects of Surface and Solution Property Variations. Separation Science and Technology 46: 1377-1387

Lee YK, Lee LM, Hau WLW, Zohar Y (2007) Two-dimensional analysis of electrokinetically driven out-of-plane vortices in a microchannel liquid flow using patterned surface charge. Journal of Microelectromechanical Systems 16: 58-67

Leinweber FC, Eijkel JCT, Bomer JG, Van Den Berg A (2006) Continuous flow microfluidic demixing of electrolytes by induced charge electrokinetics in structured electrode arrays. Analytical Chemistry 78: 1425-1434

Leinweber FC, Tallarek U (2004) Nonequilibrium electrokinetic effects in beds of ion-permselective particles. Langmuir 20: 11637-11648

Levich VG (1962) Physicochemical Hydrodynamics. Prentice-Hall, N.J.

Levitan JA, Devasenathipathy S, Studer V, Ben Y, Thorsen T, Squires TM, Bazant MZ (2005) Experimental observation of induced-charge electro-osmosis around a metal wire in a microchannel. Colloids and Surfaces A 267: 122-132

Long D, Ajdari A (1998) Symmetry properties of the electrophoretic motion of patterned colloidal particles. Physical Review Letters 81: 1529-1532

Long D, Stone HA, Ajdari A (1999) Electroosmotic flows created by surface defects in capillary electrophoresis. Journal of Colloid and Interface Science 212: 338-349

Lyklema J (1995) Fundamentals of Interface and Colloid Science Vol.2. Academic Press, London

MaCdonald JR (1970) Double layer capacitance and relaxation in electrolytes and solids. Transactions of the Faraday Society 66: 943-958

Mansouri A, Scheuerman C, Bhattacharjee S, Kwok DY, Kostiuk LW (2005) Transient streaming potential in a finite length microchannel. Journal of Colloid and Interface Science 292: 567-580

Mao P, Han J (2005) Fabrication and characterization of 20 nm planar nanofluidic channels by glass-glass and glass-silicon bonding. Lab on a Chip 5: 837-844

Masliyah JH, Bhattacharjee S (2006) Electrokinetic and Colloid Transport Phenomena Wiley-Interscience, Hoboken, N.J.

Miloh T (2008) A unified theory of dipolophoresis for nanoparticles. Physics of Fluids 20: 107105

Mishchuk N, F, Gonzalez C, Takhistov P (2001) Electroosmosis of the second kind and current through curved interface. Colloids and Surfaces A 181: 131-144

Mishchuk NA, Heldal T, Volden T, Auerswald J, Knapp H (2009) Micropump based on electroosmosis of the second kind. Electrophoresis 30: 3499-3506

Mittal M, Lele PP, Kaler EW, Furst EM (2008) Polarization and interactions of colloidal particles in ac electric fields. The Journal of Chemical Physics 129: 064513

Monroe CW, Daikhin LI, Urbakh M, Kornyshev AA (2006) Electrowetting with Electrolytes. Physical Review Letters 97: 136102

Monroe CW, Urbakh M, Kornyshev AA (2009) Double-Layer Effects in Electrowetting with Two Conductive Liquids. Journal of Electrochemistry Society 156: P21-P28

Moorthy J, Khoury C, Moore JS, Beebe DJ (2001) Active control of electroosmotic flow in microchannels using light. Sensors and Actuators B: Chemical 75: 223-229

Morgan H, Green NG (2003) AC Electrokinetics:colloids and nanoparticles. Research Studies Press, Philadelphia, Pa.

Morin FO, Gillot F, Fujita H (2007) Modeling the mechanisms driving ac electro-osmotic flow on planar microelectrodes. Applied Physics Letters 91: 064103

Morrison FA (1970) Electrophoresis of a particle of arbitrary shape. Journal of Colloid and Interface Science 34: 210-214

Mpholo M, Smith CG, Brown ABD (2003) Low voltage plug flow pumping using anisotropic electrode arrays. Sensors and Actuators B: Chemical 92: 262-268

Mruetusatorn P, Mahfouz MR, Wu J (2009) Low-voltage dynamic control for DC electroosmotic devices. Sensors and Actuators A :Physical 153: 237-243

Murtsovkin VA (1996) Nonlinear flows near polarized disperse particles. Colloid Journal of the Russian Academy of Sciences: Kolloidnyi Zhurnal 58: 341-349

Nadal F, Argoul F, Hanusse P, Pouligny B, Ajdari A (2002a) Electrically induced interactions between colloidal particles in the vicinity of a conducting plane. Physical Review E 65: 061409

Nadal F, Argoul F, Kestener P, Pouligny B, Ybert C, Ajdari A (2002b) Electrically induced flows in the vicinity of a dielectric stripe on a conducting plane. European Physical Journal E 9: 387-399

Nair BS (2004) Electronic Devices and Applications. PHI Learning Pvt. Ltd, New Delhi

Ng WY, Goh S, Lam YC, Yang C, Rodriguez I (2009) DC-biased AC-electroosmotic and AC-electrothermal flow mixing in microchannels. Lab on a Chip 9: 802-809

Nishizawa M, Menon VP, Martin CR (1995) Metal nanotubule membranes with electrochemically switchable ion-transport selectivity. Science 268: 700-705

Paris DT, Hurd FK (1969) Basic electromagnetic theory McGraw-Hill New York

Pascall AJ, Squires TM (2010) Induced Charge Electro-osmosis over Controllably Contaminated Electrodes. Physical Review Letters 104: 088301

Perry JM, Zhou K, Harms ZD, Jacobson SC (2010) Ion Transport in Nanofluidic Funnels. ACS Nano 4: 3897-3902

Piruska A, Branagan S, Cropek DM, Sweedler JV, Bohn PW (2008) Electrokinetically driven fluidic transport in integrated three-dimensional microfluidic devices incorporating gold-coated nanocapillary array membranes. Lab on a Chip 8: 1625-1631

Piruska A, Branagan SP, Minnis AB, Wang Z, Cropek DM, Sweedler JV, Bohn PW (2010) Electrokinetic control of fluid transport in gold-coated nanocapillary array membranes in hybrid nanofluidic–microfluidic devices. Lab on a Chip 10: 1237 - 1244

Plecis A, Schoch RB, Renaud P (2005) Ionic transport phenomena in nanofluidics: Experimental and theoretical study of the exclusion-enrichment effect on a chip. Nano Letters 5: 1147-1155

Plecis A, Tazid J, Pallandre A, Martinhon P, Deslouis C, Chen Y, Haghiri-Gosnet AM (2010) Flow field effect transistors with polarisable interface for EOF tunable microfluidic separation devices. Lab on a Chip 10: 1245 - 1253

Probstein RF (1994) Physicochemical Hydrodynamics: An Introduction. John Wiley and Sons, New York

Qian S, Das B, Luo X (2007) Diffusioosmotic flows in slit nanochannels. Journal of Colloid and Interface Science 315: 721-730

Ramos A, González A, Castellanos A, Green NG, Morgan H (2003) Pumping of liquids with ac voltages applied to asymmetric pairs of microelectrodes. Physical Review E 67: 056302

Ramos A, González A, García-Sánchez P, Castellanos A (2007) A linear analysis of the effect of Faradaic currents on traveling-wave electroosmosis. Journal of Colloid and Interface Science 309: 323-331

Ramos A, Morgan H, Green NG, Castellanos A (1998) Ac electrokinetics: A review of forces in microelectrode structures. Journal of Physics D: Applied Physics 31: 2338-2353

Ramos A, Morgan H, Green NG, Castellanos A (1999) AC electric-field-induced fluid flow in microelectrodes. Journal of Colloid and Interface Science 217: 420-422

Rathore AS, Horvath C (1997) Capillary electrochromatography: theories on electroosmotic flow in porous media. Journal of Chromatography A 781: 185-195

Ristenpart WD, Aksay IA, Saville DA (2003) Electrically guided assembly of planar superlattices in binary colloidal suspensions. Physical Review Letters 90: 128303

Ristenpart WD, Aksay IA, Saville DA (2007) Electrohydrodynamic flow around a colloidal particle near an electrode with an oscillating potential. Journal of Fluid Mechanics 575: 83-109

Rose KA, Meier JA, Dougherty GM, Santiago JG (2007) Rotational electrophoresis of striped metallic microrods. Physical Review E 75: 011503

Rubinstein I (1984) Effect of concentration polarization upon the valency-induced counterion selectivity of ion-exchange membranes. Journal of the Chemical Society, Faraday Transactions 2: Molecular and Chemical Physics 80: 335-344

Rubinstein I (1990) Theory of concentration polarization effects in electrodialysis on counter-ion selectivity of ion-exchange membranes

with differing counter-ion distribution coefficients. Journal of the Chemical Society, Faraday Transactions 86: 1857-1861

Rubinstein SM, Manukyan G, Staicu A, Rubinstein I, Zaltzman B, Lammertink RGH, Mugele F, Wessling M (2008) Direct Observation of a Nonequilibrium Electro-Osmotic Instability. Physical Review Letters 101: 236101

Russel WB, Saville DA, Schowalter WR (1989), Colloidal Dispersions

Saintillan D, Darve E, Shaqfeh ESG (2006) Hydrodynamic interactions in the induced-charge electrophoresis of colloidal rod dispersions. Journal of Fluid Mechanics 563: 223-259

Sasaki N, Kitamori T, Kim HB (2006) AC electroosmotic micromixer for chemical processing in a microchannel. Lab on a Chip 6: 550-554

Schasfoort RBM, Schlautmann S, Hendrikse J, Van Den Berg A (1999) Field-effect row control for microfabricated fluidic networks. Science 286: 942-945

Schoch RB, Han J, Renaud P (2008) Transport phenomena in nanofluidics. Reviews of Modern Physics 80: 839-883

Selvadurai APS (2000) Partial Differential Equations in Mechanics: Fundamentals, Laplace's equation, diffusion equation, wave equation. Springer, Berlin

Sharp K, Yazdi S, Davison S (2011) Localized flow control in microchannels using induced-charge electroosmosis near conductive obstacles. Microfluidics and Nanofluidics 10: 1257-1267

Simonov IN, Dukhin SS (1973) Theory of electrophoresis of solid conducting particles in case of ideal polarization of a thin diffuse double-layer. Colloid Journal of the Russian Academy of Sciences: Kolloidnyi Zhurnal 35: 173-176

Siwy Z, Heins E, Harrell CC, Kohli P, Martin CR (2004) Conical-Nanotube Ion-Current Rectifiers: The Role of Surface Charge. Journal of the American Chemical Society 126: 10850-10851

Sniadecki NJ, Lee CS, Sivanesan P, DeVoe DL (2004) Induced Pressure Pumping in Polymer Microchannels via Field-Effect Flow Control. Analytical Chemistry 76: 1942-1947

Soni G, Squires TM, Meinhart CD (2007) Nonlinear phenomena in induced charge electroosmosis. Proceedings of IMECE2007, ASME International Mechanical Engineering Congress and Exposition, Seattle, Washington, USA

Sparreboom W, van den Berg A, Eijkel JCT (2009) Principles and applications of nanofluidic transport. Nature Nanotechnology 4: 713-720

Squires TM, Bazant MZ (2004) Induced-charge electro-osmosis. Journal of Fluid Mechanics 509: 217-252

Squires TM, Bazant MZ (2006) Breaking symmetries in induced-charge electro-osmosis and electrophoresis. Journal of Fluid Mechanics 560: 65-101

Squires TM, Quake SR (2005) Microfluidics: Fluid physics at the nanoliter scale. Review of Modern Physics 77: 977-950

Stein D, Kruithof M, Dekker C (2004) Surface-Charge-Governed Ion Transport in Nanofluidic Channels. Physical Review Letters 93: 035901

Storey BD, Edwards LR, Kilic MS, Bazant MZ (2008) Steric effects on ac electro-osmosis in dilute electrolytes. Physical Review E 77: 036317

Stratton JA (1941) Electromagnetic Theory. McGraw - Hill, New York

Stroock AD, Weck M, Chiu DT, Huck WTS, Kenis PJA, Ismagilov RF, Whitesides GM (2000) Patterning Electro-osmotic Flow with Patterned Surface Charge. Physical Review Letters 84: 3314-3317

Su B, Abid J-P, Fermín DJ, Girault HH, Hoffmannová H, Krtil P, Samec Z (2003) Reversible Voltage-Induced Assembly of Au Nanoparticles at Liquid|Liquid Interfaces. Journal of the American Chemical Society 126: 915-919

Swaminathan TN, Hu HH (2009) Effect of induced-charge double layer on dielectrophoretic motion of particles. Mechanics Research Communications 36: 46-54

Takhistov P, Duginova K, Chang HC (2003) Electrokinetic mixing vortices due to electrolyte depletion at microchannel junctions. Journal of Colloid and Interface Science 263: 133-143

Teubner M (1982) The motion of charged colloidal particles in electric fields. Journal of Chemical Physics 76: 5564-5573

Thamida SK, Chang HC (2002) Nonlinear electrokinetic ejection and entrainment due to polarization at nearly insulated wedges. Physics of Fluids 14: 4315-4328

Trau M, Saville DA, Aksay IA (1996) Field-Induced Layering of Colloidal Crystals. Science 272: 706-709

Trau M, Saville DA, Aksay IA (1997) Assembly of colloidal crystals at electrode interfaces. Langmuir 13: 6375-6381

Uppalapati M, Huang YM, Jackson TN, Hancock WO (2008) Microtubule alignment and manipulation using AC electrokinetics. Small 4: 1371-1381

Van Der Wouden EJ, Hermes DC, Gardeniers JGE, Van Den Berg A (2006) Directional flow induced by synchronized longitudinal and zeta-potential controlling AC-electrical fields. Lab on a Chip 6: 1300-1305

Vlassiouk I, Siwy ZS (2007) Nanofluidic Diode. Nano Letters 7: 552-556

Vlassiouk I, Smirnov S, Siwy Z (2008a) Ionic Selectivity of Single Nanochannels. Nano Letters 8: 1978-1985

Vlassiouk I, Smirnov S, Siwy Z (2008b) Nanofluidic Ionic Diodes. Comparison of Analytical and Numerical Solutions. ACS Nano 2: 1589-1602

White HS, Bund A (2008) Ion Current Rectification at Nanopores in Glass Membranes. Langmuir 24: 2212-2218

Wu J, Ben Y, Battigelli D, Chang HC (2005) Long-range AC electroosmotic trapping and detection of bioparticles. Industrial and Engineering Chemistry Research 44: 2815-2822

Wu Z, Li D (2008a) Micromixing using induced-charge electrokinetic flow. Electrochimica Acta 53: 5827-5835

Wu Z, Li D (2008b) Mixing and flow regulating by induced-charge electrokinetic flow in a microchannel with a pair of conducting triangle hurdles. Microfluidics and Nanofluidics 5: 65-76

Yan R, Liang W, Fan R, Yang P (2009) Nanofluidic Diodes Based on Nanotube Heterojunctions. Nano Letters 9: 3820-3825

Yariv E (2005) Induced-charge electrophoresis of nonspherical particles. Physics of Fluids 17: 051702

Yeh SR, Seul M, Shraiman BI (1997) Assembly of ordered colloidal aggregates by electric-field-induced fluid flow. Nature 386: 57-59

Yossifon G, Chang HC (2008) Selection of nonequilibrium overlimiting currents: Universal depletion layer formation dynamics and vortex instability. Physical Review Letters 101: 254501

Yossifon G, Frankel I, Miloh T (2006) On electro-osmotic flows through microchannel junctions. Physics of Fluids 18: 117108

Yossifon G, Frankel I, Miloh T (2007) Symmetry breaking in induced-charge electro-osmosis over polarizable spheroids. Physics of Fluids 19: 068105

Yossifon G, Frankel I, Miloh T (2009) Macro-scale description of transient electro-kinetic phenomena over polarizable dielectric solids. Journal of Fluid Mechanics 620: 241-262

Yusko EC, An R, Mayer M (2009) Electroosmotic Flow Can Generate Ion Current Rectification in Nano- and Micropores. ACS Nano 4: 477-487

Zaltzman B, Rubinstein I (2007) Electro-osmotic slip and electroconvective instability. Journal of Fluid Mechanics 579: 173-226

Zhang P, Qiu HH (2008) Investigation of the patterned surface modification on 3D vortex flow generation in a micropipe. Journal of Micromechanics and Microengineering 18: 115030

Zhao C, Yang C (2009) Analysis of induced-charge electro-osmotic flow in a microchannel embedded with polarizable dielectric blocks. Physical Review E 80: 046312

Zhao C, Yang C (2011a) AC field induced-charge electroosmosis over leaky dielectric blocks embedded in a microchannel. Electrophoresis 32: 629-637

Zhao C, Yang C (2011b) Erratum: Analysis of induced-charge electro-osmotic flow in a microchannel embedded with polarizable dielectric blocks [Phys. Rev. E 80, 046312 (2009)]. Physical Review E 83: 019904

Zhao C, Zholkovskij E, Masliyah JH, Yang C (2008) Analysis of electroosmotic flow of power-law fluids in a slit microchannel. Journal of Colloid and Interface Science 326: 503-510

Zhao H, Bau HH (2007) Microfluidic chaotic stirrer utilizing induced-charge electro-osmosis. Physical Review E 75: 066217

Zhao H, Bau HH (2009) The polarization of a nanoparticle surrounded by a thick electric double layer. Journal of Colloid and Interface Science 333: 663-671

Ziebert F, Bazant MZ, Lacoste D (2010) Effective zero-thickness model for a conductive membrane driven by an electric field. Physical Review E 81: 031912